micromachines

Micro/Nano-Chip Electrokinetics, Volume III

Edited by
Xiangchun Xuan and Shizhi Qian

Printed Edition of the Special Issue Published in *Micromachines*

www.mdpi.com/journal/micromachines

MDPI

Micro/Nano-Chip Electrokinetics, Volume III

Micro/Nano-Chip Electrokinetics, Volume III

Editors

Xiangchun Xuan
Shizhi Qian

MDPI • Basel • Beijing • Wuhan • Barcelona • Belgrade • Manchester • Tokyo • Cluj • Tianjin

Editors

Xiangchun Xuan
Department of Mechanical Engineering,
Clemson University
USA

Shizhi Qian
Department of Mechanical and Aerospace Engineering,
Old Dominion University
USA

Editorial Office
MDPI
St. Alban-Anlage 66
4052 Basel, Switzerland

This is a reprint of articles from the Special Issue published online in the open access journal *Micromachines* (ISSN 2072-666X) (available at: https://www.mdpi.com/journal/micromachines/special_issues/micro_nano_chip_electrokinetics_v3).

For citation purposes, cite each article independently as indicated on the article page online and as indicated below:

LastName, A.A.; LastName, B.B.; LastName, C.C. Article Title. *Journal Name* **Year**, *Volume Number*, Page Range.

ISBN 978-3-0365-0048-5 (Hbk)
ISBN 978-3-0365-0049-2 (PDF)

Contents

About the Editors . . . . . **vii**

Shizhi Qian and Xiangchun Xuan
Editorial for the Special Issue on Micro/Nano-Chip Electrokinetics, Volume III
Reprinted from: *Micromachines* **2020**, *11*, 482, doi:10.3390/mi11050482 . . . . . **1**

Juan Eduardo Sosa-Hernández, Angel M. Villalba-Rodríguez, Kenya D. Romero-Castillo, Mauricio A. Aguilar-Aguila-Isaías, Isaac E. García-Reyes, Arturo Hernández-Antonio, Ishtiaq Ahmed, Ashutosh Sharma, Roberto Parra-Saldívar and Hafiz M. N. Iqbal
Organs-on-a-Chip Module: A Review from the Development and Applications Perspective
Reprinted from: *Micromachines* **2018**, *9*, 536, doi:10.3390/mi9100536 . . . . . **5**

Aminul Islam Khan and Prashanta Dutta
Analytical Solution of Time-Periodic Electroosmotic Flow through Cylindrical Microchannel with Non-Uniform Surface Potential
Reprinted from: *Micromachines* **2019**, *10*, 498, doi:10.3390/mi10080498 . . . . . **25**

Zi Ye, Renchang Zhang, Meng Gao, Zhongshan Deng and Lin Gui
Development of a High Flow Rate 3-D Electroosmotic Flow Pump
Reprinted from: *Micromachines* **2019**, *10*, 112, doi:10.3390/mi10020112 . . . . . **39**

Jie Li, Dilin Chen, Jian Ye, Lai Zhang, Teng Zhou and Yi Zhou
Direct Numerical Simulation of Seawater Desalination Based on Ion Concentration Polarization
Reprinted from: *Micromachines* **2019**, *10*, 562, doi:10.3390/mi10090562 . . . . . **49**

Du-Soon Choi, Sungchan Yun and WooSeok Choi
An Exact Solution for Power-Law Fluids in a Slit Microchannel with Different Zeta Potentials under Electroosmotic Forces
Reprinted from: *Micromachines* **2018**, *9*, 504, doi:10.3390/mi9100504 . . . . . **61**

Dilin Chen, Jie Li, Haiwen Chen, Lai Zhang, Hongna Zhang and Yu Ma
Electroosmotic Flow Behavior of Viscoelastic LPTT Fluid in a Microchannel
Reprinted from: *Micromachines* **2019**, *10*, 881, doi:10.3390/mi10120881 . . . . . **73**

Lanju Mei and Shizhi Qian
Electroosmotic Flow of Viscoelastic Fluid in a Nanochannel Connecting Two Reservoirs
Reprinted from: *Micromachines* **2019**, *10*, 747, doi:10.3390/mi10110747 . . . . . **87**

Kai Du, Jingni Song, Weiyu Liu, Ye Tao and Yukun Ren
Multifrequency Induced-Charge Electroosmosis
Reprinted from: *Micromachines* **2019**, *10*, 447, doi:10.3390/mi10070447 . . . . . **97**

Tianyi Jiang, Ye Tao, Hongyuan Jiang, Weiyu Liu, Yansu Hu and Dewei Tang
An Experimental Study of 3D Electrode-Facilitated Particle Traffic Flow-Focusing Driven by Induced-Charge Electroosmosis
Reprinted from: *Micromachines* **2019**, *10*, 135, doi:10.3390/mi10020135 . . . . . **123**

Kai Du, Weiyu Liu, Yukun Ren, Tianyi Jiang, Jingni Song, Qian Wu and Ye Tao
A High-Throughput Electrokinetic Micromixer via AC Field-Effect Nonlinear Electroosmosis Control in 3D Electrode Configurations
Reprinted from: *Micromachines* **2018**, *9*, 432, doi:10.3390/mi9090432 . . . . . **137**

Shizhi Qian, Wenxiang Shi, Huai Zheng and Zhaohui Liu
Tunable-Focus Liquid Lens through Charge Injection
Reprinted from: *Micromachines* **2020**, *11*, 109, doi:10.3390/mi11010109 . . . . . **159**

Jie Liu and Sheng Liu
Dynamics Behaviors of Droplet on Hydrophobic Surfaces Driven by Electric Field
Reprinted from: *Micromachines* **2019**, *10*, 778, doi:10.3390/mi10110778 . . . . . **169**

Monsur Islam, Devin Keck, Jordon Gilmore and Rodrigo Martinez-Duarte
Characterization of the Dielectrophoretic Response of Different Candida Strains Using 3D Carbon Microelectrodes
Reprinted from: *Micromachines* **2020**, *11*, 255, doi:10.3390/mi11030255 . . . . . **185**

Adriana Coll De Peña, Nurul Humaira Mohd Redzuan, Milky K. Abajorga, Nicole Hill, Julie A. Thomas and Blanca H. Lapizco-Encinas
Analysis of Bacteriophages with Insulator-Based Dielectrophoresis
Reprinted from: *Micromachines* **2019**, *10*, 450, doi:10.3390/mi10070450 . . . . . **197**

Danfen Yin, Xiaoling Zhang, Xianwei Han, Jun Yang and Ning Hu
Multi-Stage Particle Separation based on Microstructure Filtration and Dielectrophoresis
Reprinted from: *Micromachines* **2019**, *10*, 103, doi:10.3390/mi10020103 . . . . . **207**

About the Editors

Xiangchun Xuan is currently a Professor of Mechanical Engineering at Clemson University. He obtained his PhD degree from University of Toronto in 2006 and his bachelor degree from University of Science and Technology of China in 1995. His research and teaching interests lie in the general area of thermal and fluid sciences, with a special emphasis on microfluidic devices.

Shizhi Qian is currently an Associate Professor in Department of Mechanical and Aerospace Engineering at Old Dominion University. He obtained his PhD degree from University of Pennsylvania in 2004 and his bachelor degree from Huazhong University of Science and Technology in 1994. His research and teaching interests include transport phenomena and colloidal science, with a special emphasis in micro and nanoscale applications.

micromachines

MDPI

Editorial

Editorial for the Special Issue on Micro/Nano-Chip Electrokinetics, Volume III

Shizhi Qian [1,*] and Xiangchun Xuan [2]

[1] Department of Mechanical and Aerospace Engineering, Old Dominion University, Norfolk, VA 23529, USA
[2] Department of Mechanical Engineering, Clemson University, Clemson, SC 29634, USA; xcxuan@clemson.edu
* Correspondence: sqian@odu.edu; Tel.: +1-757-683-3304

Received: 6 May 2020; Accepted: 6 May 2020; Published: 8 May 2020

With the support from contributors and the help from peer reviewers, the Special Issue on Micro/Nano-Chip Electrokinetics (Volume III) published fourteen regular research articles and one review article. Based on the involved electrokinetic phenomena, these papers can be classified into the following six groups as summarized below.

(1) **Organs-on-a-chip (1 paper).** The review on organs-on-a-chip [1] reviewed the principles, fabrication techniques, and recent progress of organs-on-chip, which aims to achieve a complete functionality including the inclusion of specific conditions for the organ or tissue such as pressure, flow rate, pH, osmotic pressure, nutrient content, toxins presence, among other properties. Electrokinetic phenomena, such as electroosmotic pumps, can be applied to the organs-on-chip applications.

(2) **Newtonian Electroosmotic Flow (EOF) (3 papers).** EOF has been widely used to pump fluids in micro/nanofluidic applications. Khan and Dutta [2] derived an analytical solution of time-periodic EOF through a microtube with heterogeneous distribution of zeta potential. Ye et al. [3] developed a low-voltage high flow rate 3D EOF pump, which achieved a flow rate of 5.69 nL/min at a driving voltage of 2 V. Li et al. [4] numerically simulated EOF and ionic mass transport in a microchannel with an ion exchange membrane (IEM), and investigated the performance of seawater desalination of the system. Newtonian fluid was considered in these studies.

(3) **Non-Newtonian Electroosmotic Flow (EOF) (3 papers).** Choi et al. [5] derived an analytical solution of EOF of power-law fluid in a slit microchannel with different zeta potentials at the top and bottom walls. Chen et al. [6] simulated EOF of viscoelastic Linear Phan–Thien–Tanner (LPTT) fluid in a microchannel under various conditions, and found out that EOF of viscoelastic fluid was higher than that of Newtonian fluid under the same conditions. Mei and Qian [7] also numerically simulated EOF of LPTT fluid through a nano-slit connecting two reservoirs on both sides, and significant enhancements of both flow rate and ionic conductance were observed for viscoelastic fluid compared to Newtonian fluid.

(4) **Induced-Charge Electroosmosis (ICEO) (3 papers).** Du et al. [8] developed a unique concept of multifrequency induced-charge electroosmosis (MICEO) on ideally polarizable surfaces of a series of parallelly-placed metal strips. The proposed MICEO combines the transverse AC electroosmotic vortex flow and the axial traveling-wave electroosmotic pump motion under external dual-Fourier-mode AC electric fields. Jiang et al. [9] used ICEO in 3D composite electrode layouts to concentrate particles. Du et al. [10] utilized the ICEO flow controlled by AC field-effect transistor to generate secondary flow for mixing enhancement.

(5) **Electrohydrodynamics (EHD) (2 papers)**. Qian et al. [11] proposed a simple and easily implemented method for achieving tunable-focus liquid lenses. By corona discharge in the air, electro-pressure with a magnitude of 10 Pa was generated at the interface between liquid silicone and air, and

the resulting electro-pressure was utilized to tune liquid-lens. Liu and Liu [12] numerically investigated the EHD phenomena of sessile droplets on hydrophobic surfaces under non-uniform electric fields using the phase field method. They analyzed the dynamic behaviors of the electro-driven deformation and motion of water droplets in the oil phase.

(6) **Dielectrophoresis (DEP) (3 papers)**. Islam et al. [13] characterized the DEP response of *Candida albicans*, *Candida tropicalis* and *Candida parapsilosis* using 3D carbon microelectrodes. Peña et al. [14] demonstrated the first time use of insulator-based dielectrophoresis (iDEP) to study bacteriophages, possibly the most abundant and genetically diverse biological entities on earth. Yin et al. [15] integrated DEP and microstructure filtration to achieve multi-stage particle and cell separation.

We appreciate the contributors who submitted their articles to this Special Issue. We would like to thank many reviewers for taking time and effort to review manuscripts submitted to this Special Issue. We also acknowledge many assistant editors from Micromachines Editorial Office, and we could not have the third volume without their help and support. The first, second, and third volumes of the Special Issue on Micro/Nano-Chip Electrokinetics can be accessed through the following links:

Volume I

https://www.mdpi.com/journal/micromachines/special_issues/micro_nano_chip_electrokinetics

Volume II

https://www.mdpi.com/journal/micromachines/special_issues/micro_nano_chip_electrokinetics_v2

Volume III

https://www.mdpi.com/journal/micromachines/special_issues/micro_nano_chip_electrokinetics_v3

Conflicts of Interest: The authors declare no conflict of interest.

References

1. Sosa-Hernández, J.E.; Villalba-Rodríguez, A.V.; Romero-Castillo, K.D.; Aguilar-Aguila-Isaías, M.A.; García-Reyes, I.E.; Hernández-Antonio, A.; Ahmed, I.; Sharma, A.; Parra-Saldívar, R.; Iqbal, R.M.N. Organs-on-a-chip Module: A Review from the development and applications perspective. *Micromachines* **2018**, *9*, 536. [CrossRef] [PubMed]
2. Khan, A.I.; Dutta, P. Analytical solution of time-periodic electroosmotic flow through cylindrical microchannel with non-uniform surface potential. *Micromachines* **2019**, *10*, 498. [CrossRef] [PubMed]
3. Ye, Z.; Zhang, R.; Gao, M.; Deng, Z.; Gui, L. Development of a high flow rate 3-d electroosmotic flow pump. *Micromachines* **2019**, *10*, 112. [CrossRef] [PubMed]
4. Li, J.; Chen, D.; Ye, J.; Zhang, L.; Zhou, T.; Zhou, Y. Direct numerical simulation of seawater desalination based on ion concentration polarization. *Micromachines* **2019**, *10*, 562. [CrossRef] [PubMed]
5. Choi, D.-S.; Yun, S.; Choi, W. An exact solution for power-law fluids in a slit microchannel with different zeta potentials under electroosmotic forces. *Micromachines* **2018**, *9*, 504. [CrossRef] [PubMed]
6. Chen, D.; Li, J.; Chen, H.; Zhang, L.; Zhang, H.; Ma, Y. Electroosmotic flow behavior of viscoelastic lptt fluid in a microchannel. *Micromachines* **2019**, *10*, 881. [CrossRef] [PubMed]
7. Mei, L.; Qian, S. Electroosmotic flow of viscoelastic fluid in a nanochannel connecting two reservoirs. *Micromachines* **2019**, *10*, 747. [CrossRef] [PubMed]
8. Du, K.; Song, J.; Liu, W.; Tao, Y.; Ren, Y. Multifrequency induced-charge electroosmosis. *Micromachines* **2019**, *10*, 447. [CrossRef] [PubMed]
9. Jiang, T.; Tao, Y.; Jiang, H.; Liu, W.; Hu, Y.; Tan, D. An experimental study of 3d electrode-facilitated particle traffific flow-focusing driven by induced-charge electroosmosis. *Micromachines* **2019**, *10*, 135. [CrossRef] [PubMed]
10. Du, K.; Liu, W.; Ren, Y.; Jiang, T.; Song, J.; Wu, Q.; Tao, Y. A high-throughput electrokinetic micromixer via ac field-effect nonlinear electroosmosis control in 3d electrode confifigurations. *Micromachines* **2018**, *9*, 432. [CrossRef] [PubMed]

11. Qian, S.; Shi, W.; Zhen, H.; Liu, Z. Tunable-focus liquid lens through charge injection. *Micromachines* **2020**, *11*, 109. [CrossRef] [PubMed]
12. Liu, J.; Liu, S. Dynamics behaviors of droplet on hydrophobic surfaces driven by electric field. *Micromachines* **2019**, *10*, 778. [CrossRef] [PubMed]
13. Islam, M.; Keck, D.; Gilmore, J.; Martinez-Duarte, R. Characterization of the dielectrophoretic response of different candida strains using 3d carbon microelectrodes. *Micromachines* **2020**, *11*, 255. [CrossRef] [PubMed]
14. Coll De Peña, A.; Redzuan, N.H.M.; Abajorga, M.K.; Hill, N.; Thomas, J.A.; Lapizco-Encinas, B.H. Analysis of bacteriophages with insulator-based dielectrophoresis. *Micromachines* **2019**, *10*, 450. [CrossRef] [PubMed]
15. Yin, D.; Zhang, X.; Han, X.; Yang, J.; Hu, N. Multi-stage particle separation based on microstructure filtration and dielectrophoresis. *Micromachines* **2019**, *10*, 103. [CrossRef] [PubMed]

micromachines

MDPI

Review

Organs-on-a-Chip Module: A Review from the Development and Applications Perspective

Juan Eduardo Sosa-Hernández [1], Angel M. Villalba-Rodríguez [1], Kenya D. Romero-Castillo [1], Mauricio A. Aguilar-Aguila-Isaías [1], Isaac E. García-Reyes [1], Arturo Hernández-Antonio [1], Ishtiaq Ahmed [2], Ashutosh Sharma [3], Roberto Parra-Saldívar [1] and Hafiz M. N. Iqbal [1,*]

1 Tecnologico de Monterrey, School of Engineering and Sciences, Campus Monterrey, Ave. Eugenio Garza Sada 2501, Monterrey CP 64849, N.L., Mexico; eduardo.sosa@itesm.mx (J.E.S.-H.); angel.vr@itesm.mx (A.M.V.-R.); a00823430@itesm.mx (K.D.R.-C.); a00816656@itesm.mx (M.A.A.-A.-I.); a00824289@itesm.mx (I.E.G.-R.); heran@itesm.mx (A.H.-A.); r.parra@itesm.mx (R.P.-S.)

2 School of Medical Science, Understanding Chronic Conditions Program, Menzies Health Institute Queensland, Griffith University (Gold Coast Campus), Parklands Drive, Southport, QLD 4222, Australia; i.ahmed@griffith.edu.au

3 Tecnologico de Monterrey, School of Engineering and Sciences, Campus Queretaro, Epigmenio Gonzalez 500, Queretaro CP 76130, Mexico; asharma@itesm.mx

* Correspondence: hafiz.iqbal@itesm.mx; Tel.: +52-(81)-83582000 (ext. 5679)

Received: 15 August 2018; Accepted: 19 October 2018; Published: 22 October 2018

Abstract: In recent years, ever-increasing scientific knowledge and modern high-tech advancements in micro- and nano-scales fabrication technologies have impacted significantly on various scientific fields. A micro-level approach so-called "microfluidic technology" has rapidly evolved as a powerful tool for numerous applications with special reference to bioengineering and biomedical engineering research. Therefore, a transformative effect has been felt, for instance, in biological sample handling, analyte sensing cell-based assay, tissue engineering, molecular diagnostics, and drug screening, etc. Besides such huge multi-functional potentialities, microfluidic technology also offers the opportunity to mimic different organs to address the complexity of animal-based testing models effectively. The combination of fluid physics along with three-dimensional (3-D) cell compartmentalization has sustained popularity as organ-on-a-chip. In this context, simple humanoid model systems which are important for a wide range of research fields rely on the development of a microfluidic system. The basic idea is to provide an artificial testing subject that resembles the human body in every aspect. For instance, drug testing in the pharma industry is crucial to assure proper function. Development of microfluidic-based technology bridges the gap between in vitro and in vivo models offering new approaches to research in medicine, biology, and pharmacology, among others. This is also because microfluidic-based 3-D niche has enormous potential to accommodate cells/tissues to create a physiologically relevant environment, thus, bridge/fill in the gap between extensively studied animal models and human-based clinical trials. This review highlights principles, fabrication techniques, and recent progress of organs-on-chip research. Herein, we also point out some opportunities for microfluidic technology in the future research which is still infancy to accurately design, address and mimic the in vivo niche.

Keywords: organ-on-a-chip; biosensors; biomedical; microfluidics; in vivo models; applications

1. Introduction

In 1990, Manz et al. [1] coined the term "miniaturized total chemical analysis systems (μTAS)" for performing small-volume related reactions. Later, μTAS also encompassed other areas of biology and chemistry. With ever-increasing scientific knowledge and technology advancement,

a broader term—so-called "microfluidics"—came into existence and is now often used in addition to μTAS [2]. Microfluidics has been defined as a science and technology which deals with the behavior, precise control and manipulation of fluids through micro-channels. Generally, the fluids are geometrically constrained to a small (10^{-9} to 10^{-18} litters) amount using channels with tens to hundreds of micrometers in dimensions [3]. In microfluidics, the "Lab-on-a-Chip" is an adaptation from microchips to miniaturize laboratory experiments. Following that, other applications appear, and new organs-on-a-chip concept has become very popular among researchers around the globe. This concept developed quickly because its applications to biology and medicine provide tools that are portable, cost-effective, reduce time and can also provide better mimicking of environment for cells. In general, organs-on-a-chip allows the performance of in vitro experiments with more controlled parameters. Although the domain of the device, other equipment is required, such as pumps, incubators, microscopes, and specific target experiment tools. The handling equipment needed for microfluidic devices make it a laboratory tool that cannot leave laboratory facilities. The significant advances in microfluidics began with research about physics and involved handling very low sample volumes, typically a volume range from microliters to femtoliters. For example, the comparison of bulk flow at microscale is remarkable. For instance, turbulent flow only exists in macroscales, and laminar flow is dominant in microscale (see Figure 1), subject to the Reynolds number. The Reynolds number is a critical dimensionless quantity in fluid mechanics used to predict flow patterns in different fluid flow situations as shown in Figure 1. Reynolds number is the ratio of internal force to viscous force. The internal forces tend to move the particles away from the layer, whereas, viscous forces tend to keep the layers moving smoothly one over the other. At low Reynolds numbers, i.e., smaller than 500, viscous forces dominate, and the flow tends to be laminar (sheet-like) [4]. A series of parallel layers can represent laminar flows without any mixing between them. While, at high Reynolds numbers, i.e., larger than 2000, turbulent forces dominate that results in differences in the fluid's speed and direction, thus, the flow is fully turbulent [4]. Under these conditions, there are lateral and vertical exchanges between the liquid veins which may sometimes intersect or even move counter to the overall direction of the flow (eddy currents).

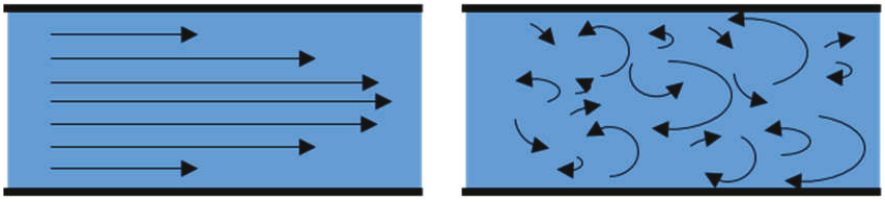

Figure 1. Schematic representation of flow lines in microscale and macroscale. Flow lines follow straight paths in microscale with a parabolic profile; contrary to macroscale, flow lines follow crossing paths with no defined pattern.

Laminar flow, diffusion, fluidic resistance, surface area to volume ratio and surface tension are among the main physical parameters. These parameters change as a consequence of small scales that require a new understanding of the physical and chemical phenomena. Bulk conditions, namely mesoscale and macroscale, are different from microscale, for instance (detailed information on the phenomena related are presented elsewhere [1–3]). Herein, we discuss the microfluidics and its application as a versatile tool to construct an organs-on-a-chip module which in turn mimics its counterpart inside the body. The first part of the review focuses on the manufacturing techniques along with the material used to fabricate microfluidic devices/systems. Following that, electrokinetic phenomena with a detailed description of the electrokinetic theory and its role in the applications towards microfluidics are discussed. The last half of the review mainly focuses on different organs-on-a-chip, and describes the most relevant research in the past few years. The last

part highlights the current state-of-the-art whole human-on-chip model. Towards the end, we provide concluding remarks and comment on future perspectives.

2. Microfluidics Techniques

In the beginning, microfluidics was implemented by industrial processes such as gas chromatography and printing machines to handle small volumes to perform fast analysis with high precision [3]. Later, lithography from microelectronics was adapted to construct devices with medical potentialities using various types of biocompatible materials. Verpoorte and De Rooij [2] reviewed developments that have emerged from the increasing interaction between the microelectromechanical systems (MEMS) and microfluidics worlds. The incorporation of MEMS techniques to fluidic device fabrication using photo-sensible polymers allows producing molds by shading patterns with UV light. This mold is then used to cast the pattern using a biocompatible polymer. The principal characteristics of polydimethylsiloxane (PDMS) are transparency, flexibility, biocompatible, gas permeable, etc. Through the high attention attracted towards microfluidics in the last two decades led to the development of novel fabrication processes and the use of other materials [5–9]. Despite the significant involvement of physics, the integration of other research areas such as chemistry, biology, and medicine to labs-on-a-chip confronted researchers with new problems which made them develop new microfluidic platforms [8]. Replica molding, along with procedures such as micro-contact printing, casting, injection molding, and embossing, encompass the techniques for manipulating elastomeric structures [10,11]. Some of the first approaches have used micro-contact printing, replica molding, micro-transfer molding, micro-molding in the capillary, solvent assisted micro-molding, phase-shifting edge lithography, nano-transfer printing, decal transfer lithography, and nano-skiving. Since most techniques use polymeric or organic matter known by physics as soft matter, all together these techniques are known as soft-lithography [9]. Soft-lithography is a rapid prototyping technique applied to generate micro and nanostructures. Generally, a low-cost polymer is used to build the desired pattern.

Advantages and Challenges: Traditional vs. Microfluidic Cell Culture Approach

Cell culture refers to the cell growth and maintenance of influencing parameters in a controlled environment. In cell related experimental biological research at large, and cell culture technology, in particular, in vitro cell culture models are considered the backbone of the field [12]. Based on literature evidence, several traditional approaches, i.e., (1) culture in the flasks, (2) culture in the dishes and (3) well-plates, etc. have been developed and have gone through heuristic optimization. The modern cell culture techniques such as microfluidics-based cell culture approach offer unique potentialities to culture, maintain, and analyze the cultures in a more sophisticated manner at micro-level. These interactions are not easily replicated or controlled in the traditional cell culture formats [13]. As compared to the traditional cell culture methods, microfluidics-based cell culture approach reveals a clear understanding of an interplay between cell culture parameters and the microenvironmental elements which traditional cell culture methods fails to demonstrate on their own. Furthermore, it is also believed that the controlled operational conditions at microenvironmental level by microfluidic approach will further accelerate and advance the cell culture technology [14]. With a variety of cost and resource benefits such as reduced consumption of reagents, smaller volume, and reduced contamination risk, microfluidics-based cell culture offers a unique platform for efficient high throughput experimentation [13]. The microfluidics-based cell culture approach has several advantages over traditional or macroscopic cell culture. However, both suffer from some considerable challenges. Figure 2 illustrates a comparative overview of significant advantages and challenges of microfluidics-based cell culture approach vs traditional/macroscopic cell culture [12].

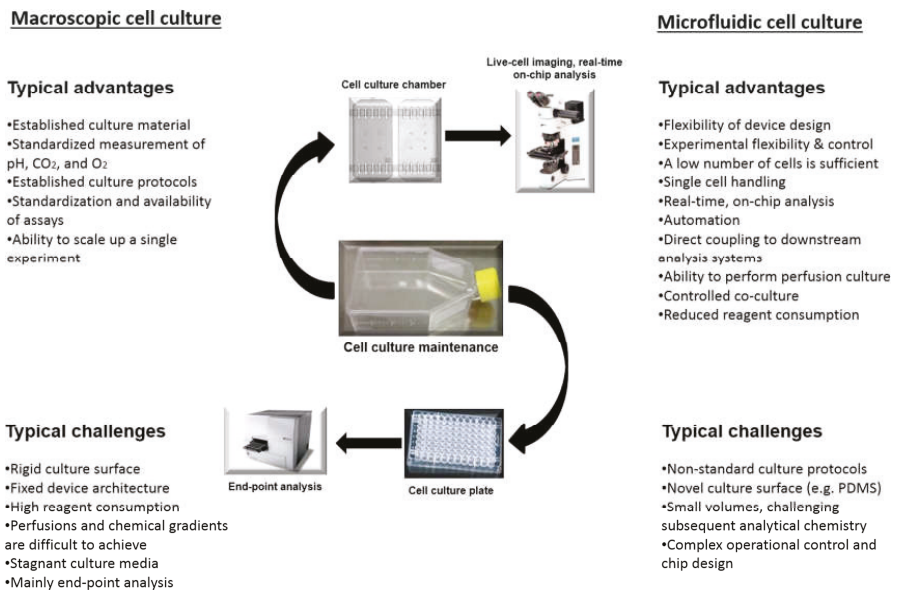

Figure 2. Overview of the advantages and challenges of both macroscopic and microfluidic cell culture. Reproduced from Halldorsson et al. [12], with permission from Elsevier.

3. Three-Dimensional (3-D) Printed Microfluidics

Owing to key scientific advancements, three-dimensional (3-D) (bio)-printing technology has drawn significant research interests. As compared to other microfluidic approaches such as soft-lithography (as discussed above), 3-D printing technology has simplified the fabrication process of microfluidic devices to a single step [15]. As mentioned earlier, facile sample preparation and handling, separation of liquids, detection and fluid manipulation, or indeed the device fabrication itself are some of the key functions of microfluidic technology [9,15]. A detailed description of each specific function from fabrication to implementation can be found in a paper by Ahmed et al. [9]. Additionally, 3-D printing technology also has numerous other considerable advantages over conventional fabrication of microfluidic devices. For instance, the capability to incorporate multi-(bio)-materials such as living cells and growth factors, aligned embedding of tissue scaffold with controlled porosity, highly defined device generation with high resolution, defined pore structure and distribution into the device, etc. [15,16]. The historical perspective and potential impact of 3-D printing technology on biotechnology and the chemical sciences, both, have been well covered and reviewed by Gross et al. [16], thus are not the focus of current work. From the industrial and commercial markets perspectives, so far, different 3-D printing techniques have been introduced. For instance, stereolithography (SLA), Digital Micromirror Device-based Projection Printing (DMD-PP), Fused Deposition Method (FDM), Two-photon-polymerisation (2PP), inkjet printing, Electron Beam Melting (EBM) or bio-printers, etc. have been exploited to develop microfluidic devices using photocurable resin, photopolymers, thermoplastic polymers, or materials-based hydrogels as their starting materials [15]. However, among these 3-D printing methods, SLA and extrusion-based system dominate the current market [17]. More detailed information on SLA, DMD-PP. FDM, 2PP, EBM, and bio-printers can be found in a paper by Ho et al. [15]. In summary, 3-D printing technology has an enormous potential to revolutionize the way we print/engineer devices with particular reference to bio-printing, and also perceive the challenges of experimental designs, and fabrication of engineered 3-D biological tissues with particular

reference to biological studies where spatial control of samples or cells is critical to integrate into 3-D printed microfluidic devices.

4. Potential Materials and Fabrication Techniques

Among potential materials, PDMS, polymethylmethacrylate (PMMA), polycarbonate (PC), polystyrene (PS), polyvinyl chloride (PVC), polyimide (PI), and the family of cyclic olefin polymers have been widely used in microfluidics [9,18–20]. The overall characteristics have made them successful in laboratories around the world. Undoubtedly, the unique characteristics of PDMS allow the generation of the precise micro-channels network to develop a microfluidic device [9]. It is essential to be aware that potential candidate materials (See Table 1) are continuously developed and open new possibilities which need to be explored in microfluidic applications.

Table 1. Potential materials used in microfluidics.

Material	Relevant Property	Proposed Application	Reference
Collagen (Chitosan)	Biocompatibility, versatile control of structure and chemistry	Bio-sensing, film assembly	[21,22]
Silkworm (*Bombyx mori*)	Biocompatibility, mechanically robust, flexibility, high mechanical modulus, and toughness	Fabrication of microfluidic channel	[23,24]
Agarose hydrogel	Lox cytotoxicity, biodegradability, mechanical stability at low solid fractions	Cell culture, sensors, and actuators	[25–27]
Teflon	Ease of fabrication with maximum chemical resistance	High precision assay, super clean tools, valves, and pumps fabrication	[28]
Acrylonitrile Butadiene Styrene (ABS)	High resolution, excellent surface finish	Making of the master mold, microfluidics interface (MI), pathogen detection, biological assay	[29–34]
Photocurable resin/polymer	Very high resolution with small features	Biology observation of cell growth	[35,36]
ABS, polycarbonate, polyphenylsulfone, elastomers	Cheap material, ease of support removal	Pathogen detection of bacteria and viruses	[37,38]
Polyamide	Fast build speed, multi-material printing, very durable and high-temperature stable material	Making of the master mold	[39,40]
Hydrogels	Swelling and contraction, act as sensors and actuators	Self-regulating valves, microlens arrays, drug release systems, binding of antigens and proteins and glucose. Flow sensors pH regulators, flooding cooling devices.	[29,41,42]
Polyurethane-methacrylate (PUMA)	Economical to manufacture, biocompatible, nontoxic, strong electroosmotic mobility	High-aspect-ratio microstructures	[43]
Polyethylene glycols (PEGs)	Relatively inexpensive, available in a wide variety of molecular weights, biocompatible, negligible cytotoxicity	Microfluidic valves, Channel cover to improve the microfluidic lifetime	[44,45]
Polyhydroxyalkanoates (PHAs)	Biocompatibility, tunable biodegradability	Microfilm barrier for vapor and oxygen	[46]

Table 1. *Cont.*

Material	Relevant Property	Proposed Application	Reference
Gelatin methacrylate (gel-MA)	Photopolymerizable, porous membrane	Mechanistic vascular and valvular biology cell support matrix	[47,48]
Polylactic acid (PLA) and Polyglycolic acid (PGA)	Tunable biodegradation	Porous scaffold for cell culture with better adhesion	[49]
Poly(polyol sebacate) (PPS)	Biocompatibility, design adaptability, mechanical compliance, low cytotoxicity, degradability	3-D microfluidic system, Microbioreactor	[50]
Poly(ethylene glycol) diacrylate (PEGDA) and gelatin methacryloyl (GelMA)	Biocompatibility, neovascularization potential, multi-material fabrication capability at a high spatial resolution	Tissue engineering, regenerative medicine, and bio-sensing	[51]
Poly(methyl methacrylate)	Favorable mechanical and thermal resistance, chemical compatibility	Genomic analysis	[52]
Styrene Ethylene Butylene Styrene (SEBS)	Biocompatibility, Rheological characteristics	Fabrication of complex and more sophisticated microfluidic networks (μFNs)	[53]
Styrene Ethylene Butylene Styrene (SEBS)	Electrical surface properties, stable and relatively high zeta potential magnitude	Microdevices for Electrokinetic Applications	[54]
Styrene Ethylene Butylene Styrene (SEBS)	Reduced drug absorption, Optical transmittance, Mechanical performance	Cell culture	[55]

From the fabrication viewpoint, several methods have been developed and exploited to construct microfluidic systems. Among them, the (1) hot embossing and (2) injection molding methods are considered two major ones. The first (hot embossing) is very similar to thermal nanoimprint lithography (NIL) and characteristically used to fabricate microfluidic-based products and lab-on-a-chip components. It is a low-cost and flexible fabrication method with unique potentialities to build nanoimprint patterns with high-aspect-ratio microstructures. However, in the injection molding method, the microfluidic device is produced by injecting molten material into a mold where it cools and hardens subject to the mold configuration [56]. A range of materials that include metals, glasses, elastomers, thermoplastic and thermo-setting-based polymers have been used to fabricate micro-channels. Generally, the materials with relatively low viscosity in the solution form are preferred because, during injection, they can lead to good contact with the mold resulting in distinct features [57]. Furthermore, injection-based molding methods have also been used, with an advantage, to construct or fabricate plastic based microfluidic channels using PMMA and PC type materials [58]. However, each fabrication method has specific limitations with regard to the properties of the material. For example, in case of above-mentioned major fabrication methods, i.e., hot embossing and injection molding, the characteristics like materials melting temperature, glass transition temperature, and thermal expansion coefficient are considered most influential for a successful fabrication [57]. These parameters are not only crucial for successful manufacturing but also play a vital role in the sealing process where materials are thermally bonded, e.g., in hot embossing method.

5. Electrokinetic Phenomena: Theory and Microfluidic Applications

Electrokinetic effects occur in the presence of an interfacial double layer of charges. The phenomena appear when an external force produce a tangential motion of fluid, liquid

electrolytes, with respect to an adjacent charged surface. Classically, the electric force used to drive fluid flow, and particle motion [59]. For microfluidic technology, it is fundamental to pump and mix fluids, electrokinetic offers an option to avoid mechanical pumps with electro-osmosis [60]. Additionally, separation of phases or heterogeneous solutions can be done with electrophoresis and dielectrophoresis [61,62]. A principles representation of the main electrokinetic phenomena is presented in Figure 3.

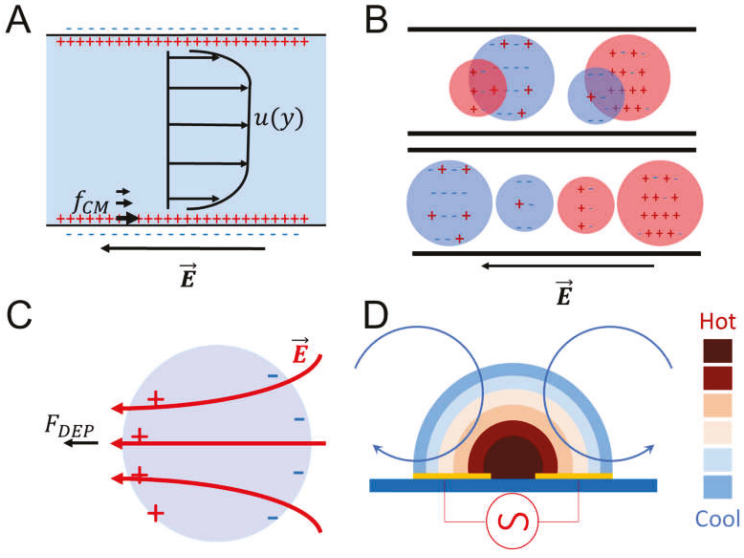

Figure 3. A schematic representation of electrokinetic phenomena. (**A**) electro-osmosis, (**B**) electrophoresis, (**C**) dielectrophoresis, and (**D**) electrothermal in alternate current.

Electro-osmosis (Figure 3A) is used to move and mix fluid charged in electrolytic solutions with specific microfluidic designs as presented in the work of Bazant and Squires. The parallel slip flow $u_{||}$ due to the electric field $E_{||}$ is given by the Herlmholtz–Smoluchowski equation,

$$u_{||} = -\frac{\varepsilon\zeta}{\eta}E_{||}$$

In terms of permittivity ε and viscosity η of the fluid, and the zeta potential ζ which can be constant or non-uniform. The result in an aqueous solution gives a speed of 70 μm/s with an electrical field of 100 V/cm and zeta potential of 10 mV [63].

For electrophoresis (Figure 3B), the mechanism is the same as electro-osmosis. However, the objective is to move small particles with an electrical charge. As a consequence, different sized and electrical charged particles are displaced at a different speed and can be separated. Lapizco's group was able to segregate three different microorganisms with microns' diameter variations in a microfluidic device [64]. Another application in microfluidic is the use of Janus particles of different sizes to mix fluids thanks to the electrophoretic phenomena [65].

Dielectrophoresis (Figure 3C) is a phenomenon driven by polarized particles with or without electrical charge immerse in a non-uniform electric field. The electric field can be applied in alternate current and direct current. This method is widely used for dielectrophoretic analysis of macromolecules, viruses, submicron particulates and recently to separate particles with a different shape, size, and dielectric properties [62]. Polarizability of particles expressed with the Clausius–Mossotti factor estimated with the particle ε_p^* and suspension media ε_m^* complex permittivity, $\varepsilon^* = \varepsilon - (j\sigma/\omega)$,

$$f_{CM} = \frac{\varepsilon_p^* - \varepsilon_m^*}{\varepsilon_p^* + 2\varepsilon_m^*},$$

where σ and ω are the conductivity and angular frequency of the potential. Dielectrophoresis can be positive or negative and it depends of the coefficient expressed before. In case of low frequency of alternate current and direct current, the factor is approximately to the same equation using switching the complex permittivity with the real conductivities. Force and velocity imposed by the dielectrophoretic effect is described by the equations:

$$F_{DEP} = 2\pi\varepsilon_m r_p^3 f_{CM} \nabla E^2,$$

and,

$$v_{DEP} = \mu_{DEP} \nabla E^2 = \frac{r_p^3 \varepsilon_m^*}{3\eta} Re[f_{CM}] \nabla E^2,$$

where, μ_{DEP} is the mobility, η is the suspension viscosity and ∇E^2 is the electric field gradient used to separate trap and isolate particles [64]. Other electrokinetic phenomena is the electrothermal (Figure 3D), which is a consequence of the Joule heating effect. Electrolytes with conductivities bigger than 0.2 S/m exposed to non-uniform alternate current electric field generates temperature, permittivity and conductivity gradients. The result of the formed gradients induces a force f_{et}, this electro thermal force is calculated by the following equation:

$$\langle f_{et} \rangle = -0.5 \left[\left(\frac{\nabla\sigma}{\sigma} - \frac{\nabla\epsilon}{\epsilon} \right) \cdot E \frac{\epsilon E}{1 + (\omega\tau)^2} + 0.5|E|^2 \nabla\epsilon \right],$$

where ω and τ are the frequency and the relaxation time [66].

Electrokinetic phenomena in microfluidics potentize achievement of higher milestones in lab-on-a-chip, point-of-care and organs-on-a-chip. A review focused on mixing through electrokinetics microfluidics summarizes extensive research and designs. The most significant advantages are miniaturized and straightforward design, no vibration and fatigue, integration with other microfluidic devices, low hydrodynamic dispersion, high speed and efficiency [67]. Microvalve is one of the applications of electrokinetics solved by using a Janus particle and electro-osmosis to control the flow in different channels presented in Li's work [68]. Very recently, Shaegh et al. [69] developed a novel rapid prototyping method to fabricate microfluidic chips from thermoplastic materials with embedded microvalves using laser ablation and thermal fusion bonding. A CO_2-assisted laser micromachining method was employed to engrave and cut PMMA sheets, together with thermoplastic polyurethane (TPU) film. Aiming to generate a gas-actuated microvalve, the authors have used an unfocused CO_2 laser beam to fabricate semi-circular fluid channels. Likewise, in another recent study [70], the whole-thermoplastic microfluidic functional elements, including a pneumatic (gas-actuated) normally closed microvalve, a micro-check valve, and a pneumatic dual-phase micropump have been fabricated for lab-on-a-chip applications [70]. Analytical microfluidics in the fields of protein, DNA, bacteria and virus and cells uses electrokinetics to sort, separate, concentrate and fix them for their analysis [71]. More details about alternate current electrokinetics microfluidic designs and theory applied to physiological fluids can be found in Reference [72].

In microfluidics, fluids or fluids-based sample pumping is an essential function for biological fluid handling for lab-on-a-chip and μTAS applications [73,74]. However, subject to a specific application, microscale pumping needs vary over a broader range with certain specifications. For instance, fluids or fluids-based sample pumping from low-power mode to high-power, low-flow-rate to high-flow-rate, and/or low-pressure-flow to high-pressure-flow, etc. To fulfill these demanding requisites for a given application, a variety of fluid driving pumps have been developed and roughly classified into two categories, i.e., (1) mechanical micropumps with moving parts, and (2) non-mechanical micropumps without moving parts [73]. Both categories have been further

sub-classified subject to various actuation principles. For instance, the mechanical micropumps can be sub-divided and mainly include (i) piezoelectric, (ii) pneumatic, (iii) thermopneumatic, (iv) electrostatic, (v) electromagnetic and (vi) bimetallic SMA micropumps, among others. Non-mechanical micropumps can be sub-divided and mainly include (i) electrokinetic, (ii) electroosmotic, (iii) magnetohydrodynamic (MHD), (iv) electrochemical, (v) acoustic-wave and surface tension and (vi) capillary micropumps, among others [73,75]. A detailed overview and working mode of the above-categorized micropumps has been comprehensively achieved [73,75], thus these are not the focus of the current research.

6. Microfluidic: Lab-on-a-Chip

Use of microfluidics on lab-on-a-chip (LOC) is inherent in the handling of very low volumes. Lab-on-a-chip was used mostly for analysis and biochemical detections, but recently it is aimed at diagnostics. Progress towards a portable diagnostic system is becoming possible as new advances in technologies evolve. As mentioned above, alongside microfluidic systems it is necessary to create integrated pumps, electrodes, valves, electrical fields, and microelectronics. Other examples of applications for lab-on-a-chip are for molecular biology, proteomics, cell biology, among others. A recent study focused on flow cytometry [76] addresses the main problems related to LOC microsystems that require other components to provide independent functionality to achieve point-of-care (POC) chips. They implemented a cytometer that identifies and classifies cells with an electromagnetic field. The chip includes electrodes in channels that separate the cell by dielectrophoresis. However, other components are still needed to achieve the desired goal. Similar to the flow cytometer, a lab-on-a-chip designed to perform a liquid biopsy is presented in Reference [77].

7. Microfluidic: Organ-on-a-Chip

Organs-on-a-chip aim to reproduce the function of biological organs or tissues as realistic models. Cells are grown inside the chambers and channels to generate tissues or complete organs to emulate its biology, and integrative physiology [78]. Achieving a complete functionality involves the inclusion of specific conditions for the organ or tissue such as pressure, flow rate, pH, osmotic pressure, nutrient content, toxins presence, among other properties. Through LOC it has been possible to reproduce several organs-on-a-chip (OoC). Outstanding research to perform in vitro models of cardiovascular, respiratory, nervous, digestive, endocrine and integumentary systems are mentioned in this summary. A general set-up representation of OoC is shown in Figure 4.

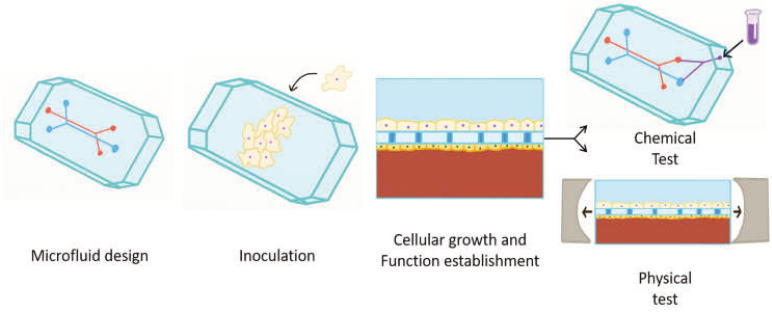

Figure 4. The process to produce different OoCs is in principle the same, taking into account the application. First, the design must address the properties to emulate and measure. Second, different cells must be incubated into the device. Third, cellular growth, differentiation and function are established in order for the chip to operate like an organ. Fourth, data is obtained through chemical and physical testing.

7.1. Lung-on-a-Chip

Huh et al. [79] constructed a biomimetic microsystem that reconstitutes the critical functional alveolar–capillary interface of the human lung, which is the fundamental functional unit of the living lung. As a proof of principle for a biomimetic microsystems approach, authors have engineered a multifunctional microdevice that reproduces key structural, functional, and mechanical properties of the human alveolar–capillary interface. It was based on a microfluidic system containing two closely apposed micro-channels separated by a thin (10 μm), porous, flexible membrane made of PDMS. The achieved system allowed visualization and characterization of inflammatory processes and response to bacteria [79]. Recently, a bioinspired lung-on-a-chip was capable of reproducing parenchyma by the construction of a thin alveolar barrier in respiratory dynamics. The primary objective to reproduce a lung is to growth epithelial and endothelial cells in cyclic stress that mimics the respiration diaphragm movement of an in vivo model. A bronchial epithelial human cell line from a patient was used, leading to a demonstration of how mechanical stress affects the epithelial barrier permeability. Additionally, there was an improvement of the cell culture in the dynamical model compared to a static one [80].

Including a hydrogel micro-layer in the lung-on-a-chip allowed the growth of smooth muscle cells and their interaction with epithelial cells. The combination of type 1 collagen and Matrigel for the hydrogel production was favorable to epithelial cell adhesion. Young's group was able to incorporate the smooth muscle cells with epithelial cells to evaluate chronic lung diseases [81]. Platforms have been developed to mimic physiological barriers in different systems; a recent review focuses on that matter with microfluidics [82]. Clinical tests for specific diseases can be reproduced with high accuracy in the biochemical reaction chains. A therapeutic model for intravascular thrombosis was set up recently in lung alveolus by Ingber's group [83]. The model helps to access different drugs; specifically, this group tested antagonist to protease-activated receptor-1 leading to the dissection of complex responses towards antithrombotic drug development.

7.2. Liver-on-a-Chip

The liver, with its high metabolic activity, is crucial to life. Its tissue is highly regenerative but suffers major damage from chronic diseases and viral infections. In order to investigate hepatocytes interactions, a microfluidic device was designed to grow hepatic cell cultures in a three-dimensional fashion. This liver-on-a-chip was able to sustain monocultures and co-cultures of hepatocytes and hepatic stellate cells to study its interaction with and without flow [84]. Several other studies are mentioned in the recent review [85] where the liver-on-a-chip applications perform drug analysis, toxicity and screening, pathophysiology and human physiology.

Monitoring metabolic function is an issue to the current in vivo models that only resemble the final result. Therefore, the integration of microfluidics systems like organ and sensors offers an advantage to follow the steps in a biological process. The liver and sensor coupling in the work of Bavli et al. [86] have led to the tracking of the adaptation to mitochondrial dysfunction. The sensor was designed to observe changes in glucose and lactate. Another micro-engineered liver chip was developed to test drug toxicity. The work focused on reconstructing 3-D cellular structure to represent the hepatic sinusoid. The hepatocyte culture was prolonged until 4 weeks and allowed screening cytotoxicity of new drugs [87].

7.3. Kidney-on-a-Chip

The kidney is one of the most complex organs to mimic since the integration of several tissues with the correct environmental characteristics is highly difficult. The kidney is formed by glomerular cells, proximal tubule cells, a loop of Henle cells, thick ascending limb cells, distal tubule cells, collecting duct cells, interstitial kidney cells, and renal endothelial cells. However, with four different tissue cells co-cultured in an organization that facilitates their function along with their physicochemical

conditions, the kidney can be mimicked. The four tissue types are glomerular, proximal and distal tubule, and collecting duct. One of the most recent studies succeeds in generating a OoC model with glomerular function by using human induced pluripotent stem (hiPS) cells into podocytes and generating glomerular basement-membrane collagen to reproduce tissue–tissue interaction with human glomerular endothelial cells. As a result, they were able to produce an in vitro model to glomerular filtration wall physiology and replicate pharmacologically induced podocyte injury and albuminuria as it occurs in patients [88]. Similar work was done to reproduce the proximal kidney tube for drug and nephrotoxicity probes [89]. Recently, Wilmer et al. [90] reviewed significant aspects of a kidney-on-a-chip development technology for drug-induced nephrotoxicity screening that are crucial for improving the early prediction of drug-induced kidney injury (DIKI).

7.4. Gut-on-a-Chip

Human in vitro models usually fail to represent human gut physiology because of the lack of its natural mechanical microenvironment. The normal gut conditions consist of fluid flow in a complex dynamic caused by its cyclic peristaltic motion. A recent study was able to develop a human gut-on-a-chip with Caco-2 intestinal epithelial cells in flexible microfluidic channels that reproduced the fluidic dynamics and its peristaltic movement. With the described conditions they were able to produce undulating epithelium columns with polarized Caco-2 cells and multiple differentiated intestinal cell types. This work was able to reproduce enteroendocrine cells, Paneth cells, and differentiated Goblet cells that secrete large amounts of mucus found in living small intestine [91,92]. Subsequent work by the same group followed the intestinal inflammation produced by bacterial overgrowth. The project let them to study pathophysiology over a time lapse of weeks, which is an outstanding model for several medical applications [93].

Exposure to ionizing gamma radiation through treatment leads to intestinal hemorrhage, sepsis, and death [94]. The radiation of cells from murine models to test damage and measure reactive oxygen species is used to test the properties of the drugs. The gut-on-a-chip application for modeling gamma radiation injury provides an alternative to in vitro testing, and prevents loss of junction continuity and demonstrates similar results [95].

The replication of the coxsackievirus B (CVB1) virus infection is another application of the gut-on-a-chip model. The CVB1 virus causes myocarditis, infects the pancreas and liver, and produces severe problems for neonatal cases [96]. Studies in this field with cells from human lines are a pressing issue, since the use of the human chip to mimic the microenvironment in the dynamic system allows the successfully testing of a polarized infection. The work of Villenave et al. shows how this model can be used for other enterovirus test and the relevance for complex systems to establish better than static cell cultures [97].

7.5. Skin-on-a-Chip

The biggest human organ is the skin, which protects the entire body from external conditions. This is one of the most accessible cells for several stress factors causing several reactions. Experiments to test almost every imaginable condition have a great impact on the use of in vitro and in vivo models models, and some of these are not efficient in humans. To reduce animal use and better approach the impact on human skin it is important to provide a better alternative. Skin-on-a-chip is becoming the main in vitro model. An example is a model with epidermal, dermal and endothelial layers developed to reproduce inflammation and edema treated with dexamethasone as a drug testing model [98] (similar work was presented in Reference [99]). The skin is more complex than a general division of epidermis and dermis. Wrinkles are one of the phenomena that happen over time and through external stress. Ultraviolet light, chemicals, physical stimuli, and other processes cause wrinkles. Recent work was able to reproduce wrinkled skin-on-a-chip with the use of magnetic stretching. This work can help to test products for cosmetics and pharmaceutics with a more realistic approximation [100]. The work done by Sriram et al. offers a full-thickness skin chip with novel fibrin-based dermal matrix support

for 3-D culture. Additionally, they surpassed problems like inconsistent seeding, epithelial damage, and contraction of the dermal matrix [101].

7.6. Brain-on-a-Chip

Human brain function and genetics are very different from animal models. Animal models only provide a basic knowledge of the brain, comparing the human brain/neuronal diseases are not equal, and human models are not an option. A series of research efforts have been directed on producing brain-on-a-chip devices to reproduce fundamental interactions and test applications. Basic research has focused on the principles that command brain formation with high complexity and interconnectivity with other organs. Applications of brain cell function and interaction with drugs for pharmacological proposals to attack degenerative diseases.

The first example is a multilayer device where pluripotent human cells were grown to mimic the central neuron system and incorporate the blood-brain barrier. The complete system was used to analyze the cellular interaction between human fetal neural progenitor cells and the mature model. Then, a chemotactic gradient was included significant for neurodevelopmental studies, neurotoxicology, neuroregeneration, and neuro-oncology research [102]. In the second work, an Alzheimer's disease in vitro model was reproduced on a chip. The group was able to grow neurospheroids with flow control. Changes in flow led to complex neural network and neural differentiation. Then, amyloid-β toxic effects and treatment were recorded with and without flow. The conclusion was that dynamic conditions provided a better development of the neurospheroids [103]. Similarly, another group was able to generate a multiregional brain-on-a-chip implementing in vivo characteristics. Their chip can develop a particular disease model, evaluating direct electrode signals from specific brain region cells and the network activity [104].

7.7. Heart-on-a-Chip

Cardiovascular in vitro models usually generate a monolayer tissue culture under static conditions and inside a considerable geometry. With the standard considerations already discussed, the tissue grows with random cell orientation, no flow conditions, and in a flat layer resulting in different physiology than the in vivo conditions. At the beginning of heart-on-a-chip, similar conditions were used but the physiology was improved step-by-step as mentioned in Reference [105]. One of the newest works is a platform where micro-engineered cardiac tissues (μECTs) was created to support a three-dimensional beating tissue from human cardiomyocytes. The mechanical and electrical response showed a high coupling response. During culture, the platform provided mechanical stimuli which resulted in better cell maturation and increased the mechanical and electrical coupling. The device was also used to test several concentrations of isoprenaline [106]. The influence of perfusion condition and microsystem geometry helps to develop cell proliferation with high alignment and morphology [107].

A mussel-inspired 3-D chip was developed thought engineered nanomaterials to test cardiac contractility. The materials used were gelatin as extracellular matrix and titanium oxide and silver nanoparticles. The device can measure in vitro contractile effects by cardiotoxicity of nanoparticles that affect calcium signal to sarcomere [108]. Cardiomyocytes clusters in spheroid geometry are part of an experiment for drug testing in a microfluidic device. The work demonstrates the potential to do studies in the long-term by applying compound concentrations. A 48 hour test was used as a non-invasive assay for quality control in pharmacological applications [109]. In this way, preclinical tests may be used for testing drug efficacy and safety. Kamei et al. built an Integrated Heart/Cancer on a-Chip (iHCC) using human cells. The microfluidic device included micropump and pneumatic valves to reproduce heart dynamics and test the anti-cancer drug doxorubicin (DXR) [110].

8. Human-on-a-Chip

Human-on-a-chip refers to an in vitro model of mimicking either normal or pathological whole human physiology within a microfluidic system that has high measurement accessibility and control

(Figure 5). Biomedical and pharmaceutical sectors will greatly benefit from multi-organ-on-a-chip and ultimately human-on-a-chip models, in terms of drug development and testing, the reliability of results, overall cost-effective ratio and working efficacy, etc. As discussed earlier, multi-organ-on-a-chip and ultimately human-on-a-chip models are promising alternatives to the animal-based testing model which have been a debating issue for a long time. Another considerable advantage is a low-throughput screening along with a high content screening at a small scale which is often not economical and sustainable on a macroscopic level [111]. Moreover, microfluidics-based chip technology is currently in a mature state and offers exceptional control over culture conditions along with other conditions, i.e., spatial homogeneity, chemical gradients, time-dependent biochemical stimulations, and substrate mechanical properties, etc. [111–114].

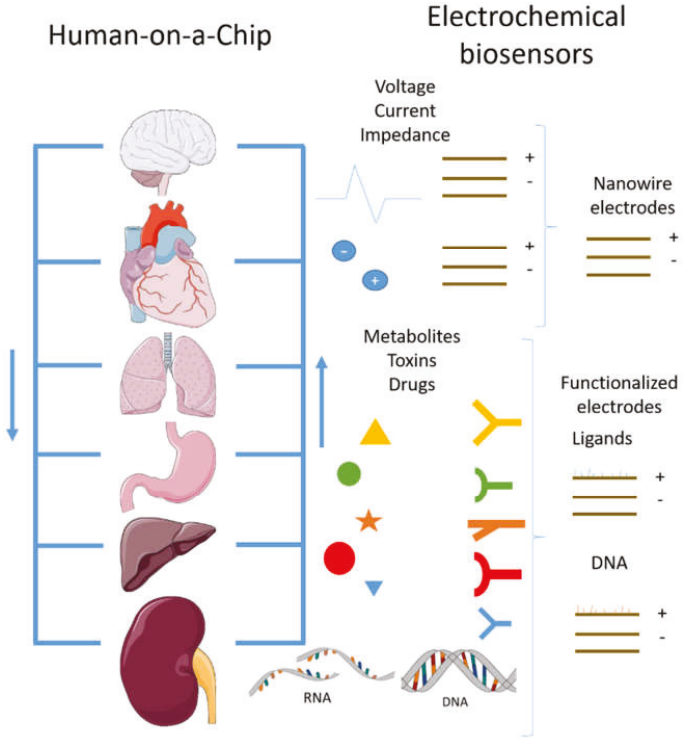

Figure 5. Organs-sensors-on-a-chip microfluidic representation.

Research is underway around the globe to study the next level of complexity to get insight into the interplay between tissues physically separated in vivo but the circulation-mediated interaction of which could be important for their mutual functionality. Therefore, it is most requisite to construct novel microfluidic designs where tissues must be able to perform the function required to support the other tissues. In order to succeed first, the single organ tissue has been studied separately, and now multi-organ-on-a-chip research has begun with successful results. First by pairs, such as liver-fibroblast, gut-liver, and liver-pancreas, and subsequently by incorporating more organs with an integration factor that includes single and recirculation perfusions, since organ systems communicate by secreting chemical factors and vesicles [115]. Despite the current advancement in technology, some critical challenges for the integration of all the organs in a chip still need to be addressed. For instance, biological challenges include appropriate organ scaling, vascularization of tissues, the inclusion of immune components, the creation of a universal media, induced pluripotent stem cells (iPSCs)

sourcing, and consideration of circadian and other cycles on cells, etc. Likewise, technical challenges include connection of platforms to maintain sterility and avoid bubbles, drug adsorption and binding to PDMS, flow rate differences between platforms, and creating ideal oxygenation and nutrient levels for different organs, etc.

Despite the challenges mentioned above, this growing field of multi-organ-on-a-chip will also help human health care programs around the world [116]. A four-organ-chip system that enables maintain high cell viability and discrete physiological tissue architecture over the entire co-culture period was designed to support absorption, distribution, metabolism, and excretion (ADME). The profiling of substances, along with repeated dose systemic toxicity testing of drug candidates, demonstrates the integrity and functionality of the intestine and the biological barriers of the kidney at a physiologically relevant organ scale. The arrangement enables physiological absorption, first path metabolism in the liver tissue, secondary metabolism and finally excretion through the kidney model and evaluation of pharmacokinetic and pharmacodynamics [117]. A recent review focused on the design parameters to develop a physiologically based pharmacokinetic (PBPK) model used with pharmacodynamics for drug development. This review establishes the basic parametric equations set to represent the human physiology of the human-on-a-chip and considers the critical parameters to be satisfied, along with its limitations [118].

9. Concluding Remarks and Future Perspectives

In conclusion, herein we summarize the recent progress in the development of microfluidic-based systems including LOC and multi-organs-on-a-chip. A plethora of microfluidic-based systems has been developed in the past few years with an ultimate aim to facilitate the predictive in vitro and in vivo models. Moreover, comparative to traditional cell culture methods, i.e., (1) culture in flasks, (2) culture in dishes and (3) well-plates, etc. microfluidics-based cell culture approach reveals a clear understanding of an interplay between cell culture parameters and the microenvironmental elements which traditional cell culture methods fail to demonstrate on their own. The versatile multifunctional features of microfluidics—such as precise control over microenvironmental elements—opens up new avenues not only for tissue engineering areas but also for next-generation drug testing sectors. Furthermore, the notable capability of microfluidics to biomimetic the micron-scale structures along with fluidic manipulation under microenvironment demonstrates it to be a powerful tool to engineer products with multifunctional applications.

One of the most significant targets for research tools development is the human-on-a-chip to replace animal models in research test and pharmaceutical industry. The human-on-a-chip tool offers the opportunities for growth through the incorporation of more tissues with proper function and without external aid. For this proposal, a completely independent system requires that all tissue can adequately provide its physiological function. First, it is needed to sustain cell viability for an extended time. The communication between tissues must offer a similar approach to the in vivo capacity, and not just by the microfluidic channels. For that, a high quantity of cell types must be developed, as shown by some of the presented works, where up to four cell types were grown from stem cells with the correct order and shape. Moreover, a proportional tissue, organ, volume, and whole mass must be sustained to provide a normal scaled human physiology. In our opinion, a new trend would be to incorporate electrochemical biosensors in a human-on-a-chip platform to merge tools (Figure 5). This approach would add a new layer in research studies, allowing innovative experiments on processes such as cancer behavior, congenital diseases, brain function, tissue development, and differentiation. As well as the correct physiology implementations, it is important to consider the design from a physics point of view; for example the inclusion of relevant parameters in the flow system and the biochemical equations. It is necessary to recognize the limitations of these in vitro models through their intrinsic value and exploit their benefits. Current research has been able to get closer to the idea of human-on-a-chip [119], and besides the mainstream of research for drug design and physiology, other novel applications are possible, including sensors development towards the detection of toxins, drugs, and hormones [120].

Through building a human reproductive tract it became possible to demonstrate that the biophysical environment helps sperm to reach the ovule. The cancer model is another critical issue, where an implementation of a human-on-a-chip has let researchers study metastasis, tumor growth, and its physiology. In summary, to fully elucidate and appreciate the potential of human-on-a-chip models as strategic measuring tools to test clinical trials on chips, correlations must be established between human in vitro measurements and traditional in vivo parameters. This will also act as a bridge between conventional cell cultures and new standardized clinical trial procedures without using animal-based models.

Author Contributions: Conceptualization, J.E.S.-H. and H.M.N.I.; Literature review, J.E.S.-H., A.M.V.-R., K.D.R.-C., M.A.A.-A.-I., and I.E.G.-R.; Validation, J.E.S.-H. and A.M.V.-R.; Writing-Original Draft Preparation, J.E.S.-H., A.M.V.-R., K.D.R.-C., M.A.A.-A.-I., and I.E.G.-R.; Figures, J.E.S.-H., M.A.A.-A.-I., and I.E.G.-R.; Tables, K.D.R.-C. and H.M.N.I.; Writing-Review & Editing, A.H.-A., I.A., A.S., R.P.-S. and H.M.N.I.; Revisions & Final editing, I.A., A.S., and H.M.N.I.; Supervision, H.M.N.I.; and APC Funding Acquisition, H.M.N.I.

Funding: This research received no external funding.

Acknowledgments: The literature facilities provided by Tecnologico de Monterrey, Mexico are thankfully acknowledged. The APC was funded by MDPI, St. Alban-Anlage 66, 4052 Basel, Switzerland.

Conflicts of Interest: The authors declare no conflicts of interest.

References

1. Manz, A.; Graber, N.; Widmer, H.Á. Miniaturized total chemical analysis systems: A novel concept for chemical sensing. *Sens. Actuators B Chem.* **1990**, *1*, 244–248. [CrossRef]
2. Verpoorte, E.; De Rooij, N.F. Microfluidics meets MEMS. *Proc. IEEE* **2003**, *91*, 930–953. [CrossRef]
3. Whitesides, G.M. The Origins and the Future of Microfluidics. *Nature* **2006**, *442*, 368–373. [CrossRef] [PubMed]
4. Bravard, J.P.; Petit, F. Geomorphology of Streams and Rivers. In *Encyclopedia of Inland Waters*; Elsevier: Amsterdam, The Netherlands, 2009; pp. 387–395.
5. Mohammed, M.I.; Zainal Alam, M.N.H.; Kouzani, A.; Gibson, I. Fabrication of Microfluidic Devices: Improvement of Surface Quality of CO_2 Laser Machined Poly(Methylmethacrylate) Polymer. *J. Micromech. Microeng.* **2017**, *27*, 015021. [CrossRef]
6. Hong, T.-F.; Ju, W.-J.; Wu, M.-C.; Tai, C.-H.; Tsai, C.-H.; Fu, L.-M. Rapid Prototyping of PMMA Microfluidic Chips Utilizing a CO2 Laser. *Microfluid. Nanofluid.* **2010**, *9*, 1125–1133. [CrossRef]
7. Owens, C.E.; Hart, A.J. High-Precision Modular Microfluidics by Micromilling of Interlocking Injection-Molded Blocks. *Lab Chip* **2018**, *18*, 890–901. [CrossRef] [PubMed]
8. Mark, D.; Haeberle, S.; Roth, G.; von Stetten, F.; Zengerle, R. Microfluidic Lab-on-a-Chip Platforms: Requirements, Characteristics and Applications. *Chem. Soc. Rev.* **2010**, *39*, 1153. [CrossRef] [PubMed]
9. Ahmed, I.; Iqbal, H.M.N.; Akram, Z. Microfluidics Engineering: Recent Trends, Valorization, and Applications. *Arab. J. Sci. Eng.* **2018**, *43*, 23–32. [CrossRef]
10. Whitesides, G.M.; Ostuni, E.; Takayama, S.; Jiang, X.; Ingber, D.E. Soft lithography in biology and biochemistry. *Annu. Rev. Biomed. Eng.* **2001**, *3*, 335–373. [CrossRef] [PubMed]
11. Sia, S.K.; Whitesides, G.M. Microfluidic devices fabricated in poly (dimethylsiloxane) for biological studies. *Electrophoresis* **2003**, *24*, 3563–3576. [CrossRef] [PubMed]
12. Halldorsson, S.; Lucumi, E.; Gómez-Sjöberg, R.; Fleming, R.M. Advantages and challenges of microfluidic cell culture in polydimethylsiloxane devices. *Biosens. Bioelectron.* **2015**, *63*, 218–231. [CrossRef] [PubMed]
13. Sackmann, E.K.; Fulton, A.L.; Beebe, D.J. The present and future role of microfluidics in biomedical research. *Nature* **2014**, *507*, 181–189. [CrossRef] [PubMed]
14. Paguirigan, A.L.; Beebe, D.J. Microfluidics meet cell biology: Bridging the gap by validation and application of microscale techniques for cell biological assays. *Bioessays* **2008**, *30*, 811–821. [CrossRef] [PubMed]
15. Ho, C.M.B.; Ng, S.H.; Li, K.H.H.; Yoon, Y.J. 3D printed microfluidics for biological applications. *Lab Chip* **2015**, *15*, 3627–3637. [CrossRef] [PubMed]
16. Gross, B.C.; Erkal, J.L.; Lockwood, S.Y.; Chen, C.; Spence, D.M. Evaluation of 3D printing and its potential impact on biotechnology and the chemical sciences. *Anal. Chem.* **2014**, *86*, 3240–3253. [CrossRef] [PubMed]

17. Serex, L.; Bertsch, A.; Renaud, P. Microfluidics: A New Layer of Control for Extrusion-Based 3D Printing. *Micromachines* **2018**, *9*, 86. [CrossRef]
18. Tsao, C.-W. Polymer Microfluidics: Simple, Low-Cost Fabrication Process Bridging Academic Lab Research to Commercialized Production. *Micromachines* **2016**, *7*, 225. [CrossRef]
19. Ahmed, I.; Akram, Z.; Bule, M.H.; Iqbal, H.M.N. Advancements and Potential Applications of Microfluidic Approaches—A Review. *Chemosensors* **2018**, *6*, 46. [CrossRef]
20. Edington, C.D.; Chen, W.L.K.; Geishecker, E.; Kassis, T.; Soenksen, L.R.; Bhushan, B.M.; Valdez, J. Interconnected Microphysiological Systems for Quantitative Biology and Pharmacology Studies. *Sci. Rep.* **2018**, *8*, 4530. [CrossRef] [PubMed]
21. Yi, H.; Wu, L.-Q.; Ghodssi, R.; Rubloff, G.W.; Payne, G.F.; Bentley, W.E. Signal-Directed Sequential Assembly of Biomolecules on Patterned Surfaces. *Langmuir* **2005**, *21*, 2104–2107. [CrossRef] [PubMed]
22. Yi, H.; Wu, L.-Q.; Bentley, W.E.; Ghodssi, R.; Rubloff, G.W.; Culver, J.N.; Payne, G.F. Biofabrication with Chitosan. *Biomacromolecules* **2005**, *6*, 2881–2894. [CrossRef] [PubMed]
23. Bettinger, C.J.; Cyr, K.M.; Matsumoto, A.; Langer, R.; Borenstein, J.T.; Kaplan, D.L. Silk Fibroin Microfluidic Devices. *Adv. Mater.* **2007**, *19*, 2847–2850. [CrossRef] [PubMed]
24. Pérez-Rigueiro, J.; Viney, C.; Llorca, J.; Elices, M. Mechanical Properties of Single-Brin Silkworm Silk. *J. Appl. Polym. Sci.* **2000**, *75*, 1270–1277. [CrossRef]
25. Ling, Y.; Rubin, J.; Deng, Y.; Huang, C.; Demirci, U.; Karp, J.M.; Khademhosseini, A. A Cell-Laden Microfluidic Hydrogel. *Lab Chip* **2007**, *7*, 756–762. [CrossRef] [PubMed]
26. Masuda, K.; Sah, R.L.; Hejna, M.J.; Thonar, E.J.-M.A. A Novel Two-Step Method for the Formation of Tissue-Engineered Cartilage by Mature Bovine Chondrocytes: The Alginate-Recovered-Chondrocyte (ARC) Method. *J. Orthop. Res.* **2003**, *21*, 139–148. [CrossRef]
27. Rahfoth, B.; Weisser, J.; Sternkopf, F.; Aigner, T.; von der Mark, K.; Bräuer, R. Transplantation of Allograft Chondrocytes Embedded in Agarose Gel into Cartilage Defects of Rabbits. *Osteoarthr. Cartil.* **1998**, *6*, 50–65. [CrossRef] [PubMed]
28. Grover, W.H.; Von Muhlen, M.G.; Manalis, S.R. Teflon Films for Chemically-Inert Microfluidic Valves and Pumps. *Lab Chip* **2008**, *8*, 913–918. [CrossRef] [PubMed]
29. Dong, L.; Jiang, H. Autonomous Microfluidics with Stimuli-Responsive Hydrogels. *Soft Matter* **2007**, *3*, 1223. [CrossRef]
30. Rogers, C.I.; Qaderi, K.; Woolley, A.T.; Nordin, G.P. 3D Printed Microfluidic Devices with Integrated Valves. *Biomicrofluidics* **2015**, *9*, 016501. [CrossRef] [PubMed]
31. Shallan, A.I.; Smejkal, P.; Corban, M.; Guijt, R.M.; Breadmore, M.C. Cost-Effective Three-Dimensional Printing of Visibly Transparent Microchips within Minutes. *Anal. Chem.* **2014**, *86*, 3124–3130. [CrossRef] [PubMed]
32. Han, N.; Shin, J.H.; Han, K.-H. An On-Chip RT-PCR Microfluidic Device, That Integrates MRNA Extraction, CDNA Synthesis, and Gene Amplification. *RSC Adv.* **2014**, *4*, 9160. [CrossRef]
33. Lee, H.; Han, N.; Choi, I.-H.; Han, K.-H. A High-Speed, High-Performance on-Chip Integrated Reverse Transcription (RT)-Microchip. *Biomed. Microdevices* **2013**, *15*, 9–15. [CrossRef] [PubMed]
34. Zhu, F.; Macdonald, N.P.; Cooper, J.M.; Wlodkowic, D. Additive Manufacturing of Lab-on-a-Chip Devices: Promises and Challenges. In *Micro/Nano Materials, Devices, and Systems*; Friend, J., Tan, H.H., Eds.; International Society for Optics and Photonics: Melbourne, Australia, 2013; Volume 8923, p. 892344.
35. Sugioka, K.; Hanada, Y.; Midorikawa, K. 3D microstructuring of glass by femtosecond laser direct writing and application to biophotonic microchips. *Prog. Electromagn. Res. Lett.* **2008**, *1*, 181–188. [CrossRef]
36. Hanada, Y.; Sugioka, K.; Shihira-Ishikawa, I.; Kawano, H.; Miyawaki, A.; Midorikawa, K. 3D Microfluidic Chips with Integrated Functional Microelements Fabricated by a Femtosecond Laser for Studying the Gliding Mechanism of Cyanobacteria. *Lab Chip* **2011**, *11*, 2109–2115. [CrossRef] [PubMed]
37. Chudobova, D.; Cihalova, K.; Skalickova, S.; Zitka, J.; Rodrigo, M.A.M.; Milosavljevic, V.; Hynek, D.; Kopel, P.; Vesely, R.; Adam, V.; et al. 3D-Printed Chip for Detection of Methicillin-Resistant *Staphylococcus Aureus* Labeled with Gold Nanoparticles. *Electrophoresis* **2015**, *36*, 457–466. [CrossRef] [PubMed]
38. Krejcova, L.; Nejdl, L.; Rodrigo, M.A.M.; Zurek, M.; Matousek, M.; Hynek, D.; Zitka, O.; Kopel, P.; Adam, V.; Kizek, R. 3D Printed Chip for Electrochemical Detection of Influenza Virus Labeled with CdS Quantum Dots. *Biosens. Bioelectron.* **2014**, *54*, 421–427. [CrossRef] [PubMed]

39. King, P.H.; Jones, G.; Morgan, H.; de Planque, M.R.R.; Zauner, K.-P. Interdroplet Bilayer Arrays in Millifluidic Droplet Traps from 3D-Printed Moulds. *Lab Chip* **2014**, *14*, 722–729. [CrossRef] [PubMed]
40. Becker, H.; Gärtner, C. Polymer Microfabrication Technologies for Microfluidic Systems. *Anal. Bioanal. Chem.* **2008**, *390*, 89–111. [CrossRef] [PubMed]
41. Miller, J.S.; Stevens, K.R.; Yang, M.T.; Baker, B.M.; Nguyen, D.-H.T.; Cohen, D.M.; Toro, E.; Chen, A.A.; Galie, P.A.; Yu, X.; et al. Rapid Casting of Patterned Vascular Networks for Perfusable Engineered Three-Dimensional Tissues. *Nat. Mater.* **2012**, *11*, 768–774. [CrossRef] [PubMed]
42. Bertassoni, L.E.; Cecconi, M.; Manoharan, V.; Nikkhah, M.; Hjortnaes, J.; Cristino, A.L.; Barabaschi, G.; Demarchi, D.; Dokmeci, M.R.; Yang, Y.; et al. Hydrogel Bioprinted Microchannel Networks for Vascularization of Tissue Engineering Constructs. *Lab Chip* **2014**, *14*, 2202–2211. [CrossRef] [PubMed]
43. Kuo, J.S.; Ng, L.; Yen, G.S.; Lorenz, R.M.; Schiro, P.G.; Edgar, J.S.; Zhao, Y.; Lim, D.S.W.; Allen, P.B.; Jeffries, G.D.M.; et al. A New USP Class VI-Compliant Substrate for Manufacturing Disposable Microfluidic Devices. *Lab Chip* **2009**, *9*, 870–876. [CrossRef] [PubMed]
44. Rogers, C.I.; Oxborrow, J.B.; Anderson, R.R.; Tsai, L.-F.; Nordin, G.P.; Woolley, A.T. Microfluidic Valves Made from Polymerized Polyethylene Glycol Diacrylate. *Sens. Actuators B Chem.* **2014**, *191*, 438–444. [CrossRef] [PubMed]
45. Plegue, T.J.; Kovach, K.M.; Thompson, A.J.; Potkay, J.A. Stability of Polyethylene Glycol and Zwitterionic Surface Modifications in PDMS Microfluidic Flow Chambers. *Langmuir* **2018**, *34*, 492–502. [CrossRef] [PubMed]
46. Cherpinski, A.; Torres-Giner, S.; Vartiainen, J.; Peresin, M.S.; Lahtinen, P.; Lagaron, J.M. Improving the Water Resistance of Nanocellulose-Based Films with Polyhydroxyalkanoates Processed by the Electrospinning Coating Technique. *Cellulose* **2018**, *25*, 1291–1307. [CrossRef]
47. Chen, M.B.; Srigunapalan, S.; Wheeler, A.R.; Simmons, C.A. A 3D Microfluidic Platform Incorporating Methacrylated Gelatin Hydrogels to Study Physiological Cardiovascular Cell–cell Interactions. *Lab Chip* **2013**, *13*, 2591–2598. [CrossRef] [PubMed]
48. Shim, K.; Kim, S.H.; Lee, D.; Kim, B.; Kim, T.H.; Jung, Y.; Choi, N.; Sung, J.H. Fabrication of Micrometer-Scale Porous Gelatin Scaffolds for 3D Cell Culture. *J. Ind. Eng. Chem.* **2017**, *50*, 183–189. [CrossRef]
49. Zamboni, F.; Keays, M.; Hayes, S.; Albadarin, A.B.; Walker, G.M.; Kiely, P.A.; Collins, M.N. Enhanced Cell Viability in Hyaluronic Acid Coated Poly(Lactic-Co-Glycolic Acid) Porous Scaffolds within Microfluidic Channels. *Int. J. Pharm.* **2017**, *532*, 595–602. [CrossRef] [PubMed]
50. Mogosanu, D.-E.; Verplancke, R.; Dubruel, P.; Vanfleteren, J. Fabrication of 3-Dimensional Biodegradable Microfluidic Environments for Tissue Engineering Applications. *Mater. Des.* **2016**, *89*, 1315–1324. [CrossRef]
51. Miri, A.K.; Nieto, D.; Iglesias, L.; Goodarzi Hosseinabadi, H.; Maharjan, S.; Ruiz-Esparza, G.U.; Shin, S.R. Microfluidics-Enabled Multimaterial Maskless Stereolithographic Bioprinting. *Adv. Mater.* **2018**, *30*, 1800242. [CrossRef] [PubMed]
52. Bertana, V.; Potrich, C.; Scordo, G.; Scaltrito, L.; Ferrero, S.; Lamberti, A.; Marasso, S.L. 3D-printed microfluidics on thin poly (methyl methacrylate) substrates for genetic applications. *J. Vac. Sci. Technol. B Nanotechnol. Microelectron. Mater. Process. Meas. Phenom.* **2018**, *36*, 01A106. [CrossRef]
53. Roy, E.; Geissler, M.; Galas, J.C.; Veres, T. Prototyping of microfluidic systems using a commercial thermoplastic elastomer. *Microfluid. Nanofluid.* **2011**, *11*, 235–244. [CrossRef]
54. Borysiak, M.D.; Yuferova, E.; Posner, J.D. Simple, low-cost styrene-ethylene/butylene-styrene microdevices for electrokinetic applications. *Anal. Chem.* **2013**, *85*, 11700–11704. [CrossRef] [PubMed]
55. Domansky, K.; Sliz, J.D.; Wen, N.; Hinojosa, C.; Thompson, G.; Fraser, J.P.; Ingber, D.E. SEBS elastomers for fabrication of microfluidic devices with reduced drug absorption by injection molding and extrusion. *Microfluid. Nanofluid.* **2017**, *21*, 107. [CrossRef]
56. Todd, R.H.; Allen, D.K.; Alting, L. *Manufacturing Processes Reference Guide*; Industrial Press Inc.: New York, NY, USA, 1994.
57. Becker, H.; Locascio, L.E. Polymer microfluidic devices. *Talanta* **2002**, *56*, 267–287. [CrossRef]
58. Kellogg, G.J.; Arnold, T.E.; Carvalho, B.L.; Duffy, D.C.; Sheppard, N.F. Centrifugal microfluidics: Applications. In *Micro Total Analysis Systems*; Springer: Dordrecht, The Netherland, 2000; pp. 239–242.
59. Anderson, J.L. Colloid Transport by Interfacial Forces. *Annu. Rev. Fluid Mech.* **1989**, *21*, 61–99. [CrossRef]
60. Garza-García, L.D.; Pérez-González, V.H.; Pérez-Sánchez, O.A.; Lapizco-Encinas, B.H. Electrokinetic Mobilities Characterization and Rapid Detection of Microorganisms in Glass Microchannels. *Chem. Eng. Technol.* **2011**, *34*, 371–378. [CrossRef]

61. Polniak, D.V.; Goodrich, E.; Hill, N.; Lapizco-Encinas, B.H. Separating Large Microscale Particles by Exploiting Charge Differences with Dielectrophoresis. *J. Chromatogr. A* **2018**, *1545*, 84–92. [CrossRef] [PubMed]
62. Romero-Creel, M.; Goodrich, E.; Polniak, D.; Lapizco-Encinas, B. Assessment of Sub-Micron Particles by Exploiting Charge Differences with Dielectrophoresis. *Micromachines* **2017**, *8*, 239. [CrossRef]
63. Squires, T.M.; Bazant, M.Z. Induced-Charge Electro-Osmosis. *J. Fluid Mech.* **2004**, *509*, 217–252. [CrossRef]
64. Saucedo-Espinosa, M.A.; Rauch, M.M.; Lalonde, A.; Lapizco-Encinas, B.H. Polarization Behavior of Polystyrene Particles under Direct Current and Low-Frequency (<1 KHz) Electric Fields in Dielectrophoretic Systems. *Electrophoresis* **2016**, *37*, 635–644. [CrossRef] [PubMed]
65. Gangwal, S.; Cayre, O.J.; Bazant, M.Z.; Velev, O.D. Induced-Charge Electrophoresis of Metallodielectric Particles. *Phys. Rev. Lett.* **2008**, *100*, 1–4. [CrossRef] [PubMed]
66. Lang, Q.; Wu, Y.; Ren, Y.; Tao, Y.; Lei, L.; Jiang, H. AC Electrothermal Circulatory Pumping Chip for Cell Culture. *ACS Appl. Mater. Interfaces* **2015**, *7*, 26792–26801. [CrossRef] [PubMed]
67. Rashidi, S.; Bafekr, H.; Valipour, M.S.; Esfahani, J.A. A Review on the Application, Simulation, and Experiment of the Electrokinetic Mixers. *Chem. Eng. Process. Process Intensif.* **2018**, *126*, 108–122. [CrossRef]
68. Li, M.; Li, D. Microvalve Using Electrokinetic Motion of Electrically Induced Janus Droplet. *Anal. Chim. Acta* **2018**, *1021*, 85–94. [CrossRef] [PubMed]
69. Shaegh, S.A.M.; Pourmand, A.; Nabavinia, M.; Avci, H.; Tamayol, A.; Mostafalu, P.; Zhang, Y.S. Rapid prototyping of whole-thermoplastic microfluidics with built-in microvalves using laser ablation and thermal fusion bonding. *Sens. Actuators B Chem.* **2018**, *255*, 100–109. [CrossRef]
70. Pourmand, A.; Shaegh, S.A.M.; Ghavifekr, H.B.; Aghdam, E.N.; Dokmeci, M.R.; Khademhosseini, A.; Zhang, Y.S. Fabrication of whole-thermoplastic normally closed microvalve, micro check valve, and micropump. *Sens. Actuators B Chem.* **2018**, *262*, 625–636. [CrossRef]
71. Chen, X.; Zhang, S.; Zhang, L.; Yao, Z.; Chen, X.; Zheng, Y.; Liu, Y. Applications and Theory of Electrokinetic Enrichment in Micro-Nanofluidic Chips. *Biomed. Microdevices* **2017**, *19*, 19. [CrossRef] [PubMed]
72. Lu, Y.; Liu, T.; Lamanda, A.C.; Sin, M.L.Y.; Gau, V.; Liao, J.C.; Wong, P.K. AC Electrokinetics of Physiological Fluids for Biomedical Applications. *J. Lab. Autom.* **2015**, *20*, 611–620. [CrossRef] [PubMed]
73. Zhang, C.; Xing, D.; Li, Y. Micropumps, microvalves, and micromixers within PCR microfluidic chips: Advances and trends. *Biotechnol. Adv.* **2007**, *25*, 483–514. [CrossRef] [PubMed]
74. Wang, X.; Cheng, C.; Wang, S.; Liu, S. Electroosmotic pumps and their applications in microfluidic systems. *Microfluid. Nanofluid.* **2009**, *6*, 145–162. [CrossRef] [PubMed]
75. Iverson, B.D.; Garimella, S.V. Recent advances in microscale pumping technologies: A review and evaluation. *Microfluid. Nanofluid.* **2008**, *5*, 145–174. [CrossRef]
76. Carminati, M.; Ferrari, G.; Vahey, M.D.; Voldman, J.; Sampietro, M. Miniaturized Impedance Flow Cytometer: Design Rules and Integrated Readout. *IEEE Trans. Biomed. Circuits Syst.* **2017**, *11*, 1438–1449. [CrossRef] [PubMed]
77. Mathew, B.; Alazzam, A.; Khashan, S.; Abutayeh, M. Lab-on-Chip for Liquid Biopsy (LoC-LB) Based on Dielectrophoresis. *Talanta* **2017**, *164*, 608–611. [CrossRef] [PubMed]
78. Wikswo, J.P. The relevance and potential roles of microphysiological systems in biology and medicine. *Exp. Biol. Med.* **2014**, *239*, 1061–1072. [CrossRef] [PubMed]
79. Huh, D.; Matthews, B.D.; Mammoto, A.; Montoya-Zavala, M.; Hsin, H.Y.; Ingber, D.E. Reconstituting Organ-Level Lung Functions on a Chip. *Science* **2010**, *328*, 1662–1668. [CrossRef] [PubMed]
80. Stucki, A.O.; Stucki, J.D.; Hall, S.R.R.; Felder, M.; Mermoud, Y.; Schmid, R.A.; Geiser, T.; Guenat, O.T. A Lung-on-a-Chip Array with an Integrated Bio-Inspired Respiration Mechanism. *Lab Chip* **2015**, *15*, 1302–1310. [CrossRef] [PubMed]
81. Humayun, M.; Chow, C.-W.; Young, E.W.K. Microfluidic Lung Airway-on-a-Chip with Arrayable Suspended Gels for Studying Epithelial and Smooth Muscle Cell Interactions. *Lab Chip* **2018**, *18*, 1298–1309. [CrossRef] [PubMed]
82. Yu, F.; Selva Kumar, N.D.; Choudhury, D.; Foo, L.C.; Ng, S.H. Microfluidic Platforms for Modeling Biological Barriers in the Circulatory System. *Drug Discov. Today* **2018**, *23*, 815–829. [CrossRef] [PubMed]
83. Jain, A.; Barrile, R.; van der Meer, A.; Mammoto, A.; Mammoto, T.; De Ceunynck, K.; Aisiku, O.; Otieno, M.; Louden, C.; Hamilton, G.; et al. Primary Human Lung Alveolus-on-a-Chip Model of Intravascular Thrombosis for Assessment of Therapeutics. *Clin. Pharmacol. Ther.* **2018**, *103*, 332–340. [CrossRef] [PubMed]

84. Lee, S.-A.; No, D.Y.; Kang, E.; Ju, J.; Kim, D.-S.; Lee, S.-H. Spheroid-Based Three-Dimensional Liver-on-a-Chip to Investigate Hepatocyte–hepatic Stellate Cell Interactions and Flow Effects. *Lab Chip* **2013**, *13*, 3529–3537. [CrossRef] [PubMed]
85. Yoon No, D.; Lee, K.-H.; Lee, J.; Lee, S.-H. 3D Liver Models on a Microplatform: Well-Defined Culture, Engineering of Liver Tissue and Liver-on-a-Chip. *Lab Chip* **2015**, *15*, 3822–3837. [CrossRef] [PubMed]
86. Bavli, D.; Prill, S.; Ezra, E.; Levy, G.; Cohen, M.; Vinken, M.; Vanfleteren, J.; Jaeger, M.; Nahmias, Y. Real-Time Monitoring of Metabolic Function in Liver-on-Chip Microdevices Tracks the Dynamics of Mitochondrial Dysfunction. *Proc. Natl. Acad. Sci. USA* **2016**, *113*, E2231–E2240. [CrossRef] [PubMed]
87. Delalat, B.; Cozzi, C.; Rasi Ghaemi, S.; Polito, G.; Kriel, F.H.; Michl, T.D.; Harding, F.J.; Priest, C.; Barillaro, G.; Voelcker, N.H. Microengineered Bioartificial Liver Chip for Drug Toxicity Screening. *Adv. Funct. Mater.* **2018**, *28*, 1801825. [CrossRef]
88. Musah, S.; Mammoto, A.; Ferrante, T.C.; Jeanty, S.S.F.; Hirano-Kobayashi, M.; Mammoto, T.; Roberts, K.; Chung, S.; Novak, R.; Ingram, M.; et al. Mature Induced-Pluripotent-Stem-Cell-Derived Human Podocytes Reconstitute Kidney Glomerular-Capillary-Wall Function on a Chip. *Nat. Biomed. Eng.* **2017**, *1*, 0069. [CrossRef] [PubMed]
89. Jang, K.-J.; Mehr, A.P.; Hamilton, G.A.; McPartlin, L.A.; Chung, S.; Suh, K.-Y.; Ingber, D.E. Human Kidney Proximal Tubule-on-a-Chip for Drug Transport and Nephrotoxicity Assessment. *Integr. Biol.* **2013**, *5*, 1119–1129. [CrossRef] [PubMed]
90. Wilmer, M.J.; Ng, C.P.; Lanz, H.L.; Vulto, P.; Suter-Dick, L.; Masereeuw, R. Kidney-on-a-chip technology for drug-induced nephrotoxicity screening. *Trends Biotechnol.* **2016**, *34*, 156–170. [CrossRef] [PubMed]
91. Kim, H.J.; Huh, D.; Hamilton, G.; Ingber, D.E. Human Gut-on-a-Chip Inhabited by Microbial Flora That Experiences Intestinal Peristalsis-like Motions and Flow. *Lab Chip* **2012**, *12*, 2165–2174. [CrossRef] [PubMed]
92. Kim, H.J.; Ingber, D.E. Gut-on-a-Chip Microenvironment Induces Human Intestinal Cells to Undergo Villus Differentiation. *Integr. Biol.* **2013**, *5*, 1130–1140. [CrossRef] [PubMed]
93. Kim, H.J.; Li, H.; Collins, J.J.; Ingber, D.E. Contributions of Microbiome and Mechanical Deformation to Intestinal Bacterial Overgrowth and Inflammation in a Human Gut-on-a-Chip. *Proc. Natl. Acad. Sci. USA* **2016**, *113*, E7–E15. [CrossRef] [PubMed]
94. Singh, V.K.; Romaine, P.L.; Newman, V.L. Biologics as Countermeasures for Acute Radiation Syndrome: Where Are We Now? *Expert Opin. Biol. Ther.* **2015**, *15*, 465–471. [CrossRef] [PubMed]
95. Jalili-Firoozinezhad, S.; Prantil-Baun, R.; Jiang, A.; Potla, R.; Mammoto, T.; Weaver, J.C.; Ferrante, T.C.; Kim, H.J.; Cabral, J.M.S.; Levy, O.; et al. Modeling Radiation Injury-Induced Cell Death and Countermeasure Drug Responses in a Human Gut-on-a-Chip. *Cell Death Dis.* **2018**, *9*, 223. [CrossRef] [PubMed]
96. Wikswo, M.E.; Khetsuriani, N.; Fowlkes, A.L.; Zheng, X.; Peñaranda, S.; Verma, N.; Shulman, S.T.; Sircar, K.; Robinson, C.C.; Schmidt, T.; et al. Increased Activity of Coxsackievirus B1 Strains Associated with Severe Disease among Young Infants in the United States, 2007–2008. *Clin. Infect. Dis.* **2009**, *49*, e44–e51. [CrossRef] [PubMed]
97. Villenave, R.; Wales, S.Q.; Hamkins-Indik, T.; Papafragkou, E.; Weaver, J.C.; Ferrante, T.C.; Bahinski, A.; Elkins, C.A.; Kulka, M.; Ingber, D.E. Human Gut-On-A-Chip Supports Polarized Infection of Coxsackie B1 Virus In Vitro. *PLoS ONE* **2017**, *12*, e0169412. [CrossRef] [PubMed]
98. Wufuer, M.; Lee, G.; Hur, W.; Jeon, B.; Kim, B.J.; Choi, T.H.; Lee, S. Skin-on-a-Chip Model Simulating Inflammation, Edema and Drug-Based Treatment. *Sci. Rep.* **2016**, *6*, 37471. [CrossRef] [PubMed]
99. Mori, N.; Morimoto, Y.; Takeuchi, S. Skin Integrated with Perfusable Vascular Channels on a Chip. *Biomaterials* **2017**, *116*, 48–56. [CrossRef] [PubMed]
100. Lim, H.Y.; Kim, J.; Song, H.J.; Kim, K.; Choi, K.C.; Park, S.; Sung, G.Y. Development of Wrinkled Skin-on-a-Chip (WSOC) by Cyclic Uniaxial Stretching. *J. Ind. Eng. Chem.* **2018**. [CrossRef]
101. Sriram, G.; Alberti, M.; Dancik, Y.; Wu, B.; Wu, R.; Feng, Z.; Ramasamy, S.; Bigliardi, P.L.; Bigliardi-Qi, M.; Wang, Z. Full-Thickness Human Skin-on-Chip with Enhanced Epidermal Morphogenesis and Barrier Function. *Mater. Today* **2018**, *21*, 326–340. [CrossRef]
102. Park, J.; Lee, B.K.; Jeong, G.S.; Hyun, J.K.; Lee, C.J.; Lee, S.-H. Three-Dimensional Brain-on-a-Chip with an Interstitial Level of Flow and Its Application as an in Vitro Model of Alzheimer's Disease. *Lab Chip* **2015**, *15*, 141–150. [CrossRef] [PubMed]

103. Kilic, O.; Pamies, D.; Lavell, E.; Schiapparelli, P.; Feng, Y.; Hartung, T.; Bal-Price, A.; Hogberg, H.T.; Quinones-Hinojosa, A.; Guerrero-Cazares, H.; et al. Brain-on-a-Chip Model Enables Analysis of Human Neuronal Differentiation and Chemotaxis. *Lab Chip* **2016**, *16*, 4152–4162. [CrossRef] [PubMed]
104. Dauth, S.; Maoz, B.M.; Sheehy, S.P.; Hemphill, M.A.; Murty, T.; Macedonia, M.K.; Greer, A.M.; Budnik, B.; Parker, K.K. Neurons Derived from Different Brain Regions Are Inherently Different in Vitro: A Novel Multiregional Brain-on-a-Chip. *J. Neurophysiol.* **2017**, *117*, 1320–1341. [CrossRef] [PubMed]
105. Jastrzebska, E.; Tomecka, E.; Jesion, I. Heart-on-a-Chip Based on Stem Cell Biology. *Biosens. Bioelectron.* **2016**, *75*, 67–81. [CrossRef] [PubMed]
106. Marsano, A.; Conficconi, C.; Lemme, M.; Occhetta, P.; Gaudiello, E.; Votta, E.; Cerino, G.; Redaelli, A.; Rasponi, M. Beating Heart on a Chip: A Novel Microfluidic Platform to Generate Functional 3D Cardiac Microtissues. *Lab Chip* **2016**, *16*, 599–610. [CrossRef] [PubMed]
107. Kobuszewska, A.; Tomecka, E.; Zukowski, K.; Jastrzebska, E.; Chudy, M.; Dybko, A.; Renaud, P.; Brzozka, Z. Heart-on-a-Chip: An Investigation of the Influence of Static and Perfusion Conditions on Cardiac (H9C2) Cell Proliferation, Morphology, and Alignment. *SLAS Technol.* **2017**, *22*, 536–546. [CrossRef] [PubMed]
108. Ahn, S.; Ardoña, H.A.M.; Lind, J.U.; Eweje, F.; Kim, S.L.; Gonzalez, G.M.; Liu, Q.; Zimmerman, J.F.; Pyrgiotakis, G.; Zhang, Z.; et al. Mussel-Inspired 3D Fiber Scaffolds for Heart-on-a-Chip Toxicity Studies of Engineered Nanomaterials. *Anal. Bioanal. Chem.* **2018**, 1–14. [CrossRef] [PubMed]
109. Christoffersson, J.; Meier, F.; Kempf, H.; Schwanke, K.; Coffee, M.; Beilmann, M.; Zweigerdt, R.; Mandenius, C.-F. A Cardiac Cell Outgrowth Assay for Evaluating Drug Compounds Using a Cardiac Spheroid-on-a-Chip Device. *Bioengineering* **2018**, *5*, 36. [CrossRef] [PubMed]
110. Kamei, K.; Kato, Y.; Hirai, Y.; Ito, S.; Satoh, J.; Oka, A.; Tsuchiya, T.; Chen, Y.; Tabata, O. Integrated Heart/Cancer on a Chip to Reproduce the Side Effects of Anti-Cancer Drugs in Vitro. *RSC Adv.* **2017**, *7*, 36777–36786. [CrossRef]
111. Luni, C.; Serena, E.; Elvassore, N. Human-on-chip for therapy development and fundamental science. *Curr. Opin. Biotechnol.* **2014**, *25*, 45–50. [CrossRef] [PubMed]
112. Schwarz, U.S.; Bischofs, I.B. Physical determinants of cell organization in soft media. *Med. Eng. Phys.* **2005**, *27*, 763–772. [CrossRef] [PubMed]
113. Weibel, D.B.; Whitesides, G.M. Applications of microfluidics in chemical biology. *Curr. Opin. Chem. Biol.* **2006**, *10*, 584–591. [CrossRef] [PubMed]
114. Luni, C.; Feldman, H.C.; Pozzobon, M.; De Coppi, P.; Meinhart, C.D.; Elvassore, N. Microliter-bioreactor array with buoyancy-driven stirring for human hematopoietic stem cell culture. *Biomicrofluidics* **2010**, *4*, 034105. [CrossRef] [PubMed]
115. Ronaldson-Bouchard, K.; Vunjak-Novakovic, G. Organs-on-a-Chip: A Fast Track for Engineered Human Tissues in Drug Development. *Cell Stem Cell* **2018**, *22*, 310–324. [CrossRef] [PubMed]
116. Jiang, B.; Zheng, W.; Zhang, W.; Jiang, X. Organs on Microfluidic Chips: A Mini Review. *Sci. China Chem.* **2014**, *57*, 356–364. [CrossRef]
117. Maschmeyer, I.; Lorenz, A.K.; Schimek, K.; Hasenberg, T.; Ramme, A.P.; Hübner, J.; Lindner, M.; Drewell, C.; Bauer, S.; Thomas, A.; et al. A Four-Organ-Chip for Interconnected Long-Term Co-Culture of Human Intestine, Liver, Skin and Kidney Equivalents. *Lab Chip* **2015**, *15*, 2688–2699. [CrossRef] [PubMed]
118. Abaci, H.E.; Shuler, M.L. Human-on-a-Chip Design Strategies and Principles for Physiologically Based Pharmacokinetics/Pharmacodynamics Modeling. *Integr. Biol.* **2015**, *7*, 383–391. [CrossRef] [PubMed]
119. Coppeta, J.R.; Mescher, M.J.; Isenberg, B.C.; Spencer, A.J.; Kim, E.S.; Lever, A.R.; Mulhern, T.J.; Prantil-Baun, R.; Comolli, J.C.; Borenstein, J.T. A Portable and Reconfigurable Multi-Organ Platform for Drug Development with Onboard Microfluidic Flow Control. *Lab Chip* **2017**, *17*, 134–144. [CrossRef] [PubMed]
120. Kim, J.; Abdulwahab, S.; Choi, K.; Lafrenière, N.M.; Mudrik, J.M.; Gomaa, H.; Ahmado, H.; Behan, L.-A.; Casper, R.F.; Wheeler, A.R. A Microfluidic Technique for Quantification of Steroids in Core Needle Biopsies. *Anal. Chem.* **2015**, *87*, 4688–4695. [CrossRef] [PubMed]

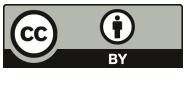

micromachines

MDPI

Article

Analytical Solution of Time-Periodic Electroosmotic Flow through Cylindrical Microchannel with Non-Uniform Surface Potential

Aminul Islam Khan and Prashanta Dutta *

School of Mechanical and Materials Engineering, Washington State University, Pullman, WA 99164-2920, USA
* Correspondence: prashanta@wsu.edu; Tel.: +1-509-335-7989

Received: 1 July 2019; Accepted: 23 July 2019; Published: 26 July 2019

Abstract: Time-periodic electroosmotic flow (EOF) with heterogeneous surface charges on channel walls can potentially be used to mix species or reagent molecules in microfluidic devices. Although significant research efforts have been placed to understand different aspects of EOF, its role in the mixing process is still poorly understood, especially for non-homogeneous surface charge cases. In this work, dynamic aspects of EOF in a cylindrical capillary are analyzed for heterogeneous surface charges. Closed form analytical solutions for time-periodic EOF are obtained by solving the Navier–Stokes equation. An analytical expression of induced pressure is also obtained from the velocity field solution. The results show that several vortices can be formed inside the microchannel with sinusoidal surface charge distribution. These vortices change their pattern and direction as the electric field change its strength and direction with time. In addition, the structure and strength of the vorticity depend on the frequency of the external electric field and the size of the channel. As the electric field frequency or channel diameter increases, vortices are shifted towards the channel surface and the perturbed flow region becomes smaller, which is not desired for effective mixing. Moreover, the number of vorticities depends on the periodicity of the surface charge.

Keywords: time-periodic electroosmotic flow; heterogeneous surface charge; cylindrical microchannel; stream function; micro-mixing

1. Introduction

Lab-on-a-chip microfluidic devices are utilized for numerous applications such as DNA sequencing, synthesis, crystallization, polymerization, and drug discovery. These applications require a number of unit operations such as pumping [1], mixing [2], etc. Among various functionalities, mixing in microfluidic devices is very challenging due to (ultra-low Reynolds number) creeping flow [3]. The quick mixing of species is key to reducing analysis time in a microfluidic device for its widespread application in the biomedical field [4]. To date, several mixing strategies have been proposed for microfluidic systems with different degrees of successes (see reviews [5–7]). Based on the methods used to achieve mixing, micromixers are generally classified as being passive or active. In passive micromixers, the mixing process depends entirely on diffusion; meanwhile, in active micromixers, the mixing process is accelerated by an external disturbance [6,8]. Although the passive mixing offers some benefits such as no external power requirements, it is not very effective in microfluidic devices because of the diffusion-based very slow mixing process. Active mixing has the potential to eliminate the inherent drawbacks of slow mixing using an acoustic, magnetic, or electrokinetic forcing [9]. Among various active micromixers (see reviews [2,5]), electrokinetic-based micromixers are preferred owing to their numerous advantages including ease of fabrication, no moving parts, ease of control, high reliability and repeatability, and quiet operation.

Electroosmotic mixing can be enhanced with an alternating electric field. Alternating electric field-based time-periodic electroosmotic flow (EOF) has been extensively studied with uniform surface charges for various types of channels such as parallel plate [10], circular [11], rectangular [12], and annulus [13] channels, etc. Oddy et al. [14] found that the rapid stretching and folding of fluid interfaces, induced by an alternating electric field, are able to stir fluid streams at a very low Reynolds number (Re < 1). Glasgow et al. [15] found that better mixing can be achieved in a T-junction channel with two out-of-phase alternating electric fields. The out-of-phase alternating electric field induces the oscillation of the fluid interface at the junction of the two inlet channels, which increases the contact surface area between the two fluid streams for significantly better mixing efficiency [16]. However, the alternating electric field-based EOF fails to take advantage of the vortex to enhance the mixing due to the unidirectional flow at any particular time.

The use of a nonhomogeneous channel surface is another way to improve electroosmotic mixing performance. The effects of a heterogeneous surface charge have also been extensively studied in direct current (DC) EOF. For example, Ajdari [17] theoretically showed that a surface with a sinusoidal charge can create vorticities within the bulk flow. Vortices formation within the bulk flow was also shown by Horiuchi et al. [18] for a step change in the surface charge in a DC EOF. Through a numerical investigation, Erickson and Li [19] showed that surface heterogeneity increases the mixing efficiency and reduces the required mixing length. Qian and Bau [20] presented a theoretical study of electroosmotic flows driven by a uniform electric field in a two-dimensional conduit with non-uniform surface potential distribution.

In microfluidic devices, surface heterogeneity can be introduced intentionally through micromanufacturing technology, such as microcontact printing or rapid prototyping. For instance, Biddiss et al. [4] manufactured several micromixers with heterogenous surface charge configurations by rapid prototyping for the quick mixing of species. Their analysis showed that heterogeneously charged micromixers significantly improve the mixing efficiency as compared to homogeneously charged micromixers. Strook et al. [21] also used microcontact printing to vary the surface charge in directions parallel and perpendicular to the applied electric field. They found that surface charge variation in the parallel direction generates recirculating flow, while surface charge variation in the perpendicular direction creates multidirectional flow. Electrokinetic characteristics of a microchannel surface can also be modulated through the dynamic or static coating of proteins, DNA, colloids, and/or nanosized particles on the surface. For example, Norde and Rouwendal [22] studied the change of surface charge by the protein adsorption on a glass surface. Wei et al. [23] generated non-uniform zeta potential distribution by periodically attaching DNA molecules in the microfluidic channel surface for increased DNA–DNA hybridization. The aforementioned studies showed that DC EOF with a heterogeneous surface charge can increase the mixing efficiency while reducing the mixing length by creating vorticity. However, a DC EOF fails to take advantages offered by an alternating electric field.

Thus, the primary focus of this work is to further increase the efficiency of electroosmotic mixing by introducing an alternating electric field in a heterogeneously charged channel. Through a numerical investigation, Lee et al. [24] demonstrated various kinds of flow circulation in a circular slit with time-periodic EOF for non-uniform zeta potential distribution along the microchannel walls. Luo [25] numerically investigated the transient electroosmotic flow induced by an alternating electric field with patch-wise surface heterogeneities in a planner microchannel. Tang et al. [26] studied the pulsating electroosmotic flow in a planar microchannel with non-uniform surface charges by the lattice Boltzmann method. These simulation results showed that time-periodic EOF with a heterogeneous surface can combine the advantages of the alternating electric field and the heterogeneous surface charge. However, no generalized analytical model exists for time-periodic EOF with non-uniform zeta potential in cylindrical systems. An analytical solution could help to find the optimum micromixer design. Motivated by the growing interest in time-periodic EOF as a reliable non-mechanical strategy to mix species in microfluidic devices, in this paper, a theoretical approach is presented. Specifically, we studied a time-periodic EOF field in a cylindrical microchannel with heterogeneous surface charge

distribution. A closed-form analytical solution was obtained for the time-periodic electroosmotic flow velocity by solving the Navier–Stokes equations. In addition, an expression for pressure distribution was also obtained for time-periodic electroosmotic flow.

2. Mathematical Model

2.1. Governing Equations for Time-Periodic EOF in a Cylindrical Microchannel

Figure 1 shows a schematic for time-periodic EOF in a cylindrical microchannel, where an alternating electric field is applied along the channel length. For generality, the model was developed such that the surface zeta potential can take any periodic distribution (e.g., sinusoidal, square) along the length of the channel, but there is no variation in zeta potential along the circumferential direction.

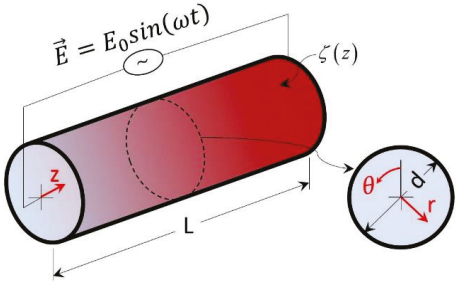

Figure 1. Schematic of a cylindrical microchannel with an associated polar coordinate system.

The application of a time-periodic external electric field results in a net body force on the free ions within the electric double layer (EDL), inducing a time-periodic bulk fluid motion. The motion of the fluid inside the channel can be governed by the incompressible Navier–Stokes equation [10]:

$$\rho\left[\frac{\partial \vec{V}}{\partial t} + \left(\vec{V}\cdot\nabla\right)\vec{V}\right] = -\nabla P + \mu\nabla^2\vec{V} + \rho_e\vec{E} \tag{1}$$

where ρ and μ are the density and viscosity of the fluid, respectively; P is the pressure; ρ_e is the charge density; and $\vec{E}$ is the applied electric field. The applied electric field can be expressed as $\vec{E} = E_z\hat{z} = E_0\sin(\omega t)\hat{z}$, where $\hat{z}$ is the unit vector in the axial (z) direction and E_0 is the reference electric field. In addition, the mass conservation equation can be expressed as:

$$\frac{\partial \rho}{\partial t} + \nabla\cdot\left(\rho\vec{V}\right) = 0. \tag{2}$$

In general, for an incompressible fluid, density is assumed to be a constant. Thus, for the axisymmetric flow scenario ($v_\theta = 0$) presented here, the mass conservation equation can be reduced to:

$$\frac{1}{r}\frac{\partial}{\partial r}(rv_r) + \frac{\partial v_z}{\partial z} = 0. \tag{3}$$

where v_r and v_z are the velocity components in the radial and axial direction, respectively. For the axisymmetric case, the radial and axial velocity can be related to the stream function, ψ as follows:

$$v_r = \frac{1}{r}\frac{\partial \psi}{\partial z}, v_z = -\frac{1}{r}\frac{\partial \psi}{\partial r}. \tag{4}$$

2.2. Analysis of Time-Periodic EOF in a Cylindrical Microchannel

Our next objective is to simplify the Navier–Stokes equations. In most microfluidic applications, the buffer solutions have a concentration of the order of mM, which results in a very thin EDL. The bulk fluid flow outside of the EDL region can be modeled by dropping the electroosmotic body force, $\rho_e \vec{E}$, and by introducing a Helmholtz–Smoluchowski slip boundary condition at the channel wall [24]:

$$\vec{V}_{r=r_0} = -\frac{\varepsilon \zeta(z)}{\mu} \vec{E} \tag{5}$$

where ε is the permittivity and $\zeta(z)$ is the surface potential distribution along the length of the conduit. This slip boundary condition was originally developed for steady-state EOF, but it can still be used for time-periodic EOF because the applied electric field frequency ($10^2 \sim 10^5$ Hz) is less than the charge relaxation frequency ($10^6 \sim 10^8 Hz$) [27]. Moreover, the Helmholtz–Smoluchowski formulation-based slip boundary condition is widely used for nonhomogeneous surface charges as well as time-periodic EOF analysis [3,24,28–30]. Thus by dropping the body force, the component form of equations of motion are:

$$\rho\left(\frac{\partial v_r}{\partial t} + v_r\frac{\partial v_r}{\partial r} + v_z\frac{\partial v_r}{\partial z}\right) = -\frac{\partial P}{\partial r} + \mu\left[\frac{\partial}{\partial r}\left\{\frac{1}{r}\frac{\partial}{\partial r}(rv_r)\right\} + \frac{\partial^2 v_r}{\partial z^2}\right], \tag{6a}$$

$$\rho\left(\frac{\partial v_z}{\partial t} + v_r\frac{\partial v_z}{\partial r} + v_z\frac{\partial v_z}{\partial z}\right) = -\frac{\partial P}{\partial z} + \mu\left[\frac{1}{r}\frac{\partial}{\partial r}\left(r\frac{\partial v_z}{\partial r}\right) + \frac{\partial^2 v_z}{\partial z^2}\right]. \tag{6b}$$

Here, the θ-component of the momentum equation is discarded due to axisymmetric flow, as there is no driving force in the θ-direction. In general, the advection effects are negligible in EOF due to the low Reynolds number [31,32]. For example, if water ($\rho = 1000$ kg·m^{-3} and $\mu = 0.001$ kg·m^{-1}·s^{-1}) flows through a 100 μm diameter cylindrical microchannel with an axial velocity of 1 mm·s^{-1}, the resulting Reynolds number would be $Re = 0.1$. Thus, by dropping the advective term, eliminating P between Equation (6), and introducing the stream function ψ, we get:

$$\left(D - \frac{1}{\vartheta}\frac{\partial}{\partial t}\right) D\psi = 0 \tag{7}$$

where ϑ is the kinetic viscosity and D denotes the following operator:

$$D \equiv \frac{\partial^2}{\partial r^2} - \frac{1}{r}\frac{\partial}{\partial r} + \frac{\partial^2}{\partial z^2}. \tag{8}$$

The commutative properties of operators D and $D - \frac{1}{\vartheta}\frac{\partial}{\partial t}$ lead us to separate the stream function, ψ, into two parts [32,33] as $\psi = \psi_1 + \psi_2$, where ψ_1 satisfies the equation

$$D\psi_1 = 0 \tag{9}$$

and ψ_2 satisfies

$$\left(D - \frac{1}{\vartheta}\frac{\partial}{\partial t}\right)\psi_2 = 0. \tag{10}$$

Considering periodic boundary conditions in the upstream ($z = 0$) and downstream ($z = L$) regions, we assume wave-like solutions of elliptic Equations (9) and (10), which can be given as:

$$\psi_1 = \sum_{n=-\infty}^{\infty} \varphi_{1,n}(r) e^{ik_n z} e^{i\omega t}, \tag{11a}$$

$$\psi_2 = \sum_{n=-\infty}^{\infty} \varphi_{2,n}(r) e^{ik_n z} e^{i\omega t}. \tag{11b}$$

Here, $\phi_{1,n}$ and $\phi_{2,n}$ are eigenfunctions, ω is the temporal angular frequency, and k_n is the eigenvalue for the spatially periodic process. Thus, Equation (11) provides a general solution for axially periodic boundary conditions [32,33]. The values of k_n can be given as $2\pi n/L$, where n is an integer and L is the length of the microfluidic conduit. The eigenfunctions $\phi_{1,n}$ and $\phi_{2,n}$ are solutions of the following differential equations:

$$\frac{d^2\varphi_{1,n}}{dr^2} - \frac{1}{r}\frac{d\varphi_{1,n}}{dr} - k_n^2\varphi_{1,n} = 0, \tag{12a}$$

$$\frac{d^2\phi_{2,n}}{dr^2} - \frac{1}{r}\frac{d\phi_{2,n}}{dr} - l_n^2\phi_{2,n} = 0, \tag{12b}$$

satisfying the boundary conditions at the tube wall. In Equation (12b), $l_n^2 = k_n^2 + i\omega/\vartheta$. The general solutions of Equation (12a,b) can be obtained as

$$\phi_{1,n} = r[A_{1,n}I_1(k_nr) + B_{1,n}K_1(k_nr)], \tag{13a}$$

$$\phi_{2,n} = r[A_{2,n}I_1(l_nr) + B_{2,n}K_1(l_nr)], \tag{13b}$$

respectively, where $I_1(r)$ and $K_1(r)$ are modified Bessel functions of the first and second kind of order 1; $A_{1,n}$, $A_{2,n}$, $B_{1,n}$, $B_{2,n}$ are coefficients. Thus, the stream function, ψ, can be given as follows:

$$\psi = \sum_{n=-\infty}^{\infty} r[A_{1,n}I_1(k_nr) + B_{1,n}K_1(k_nr) + A_{2,n}I_1(l_nr) + B_{2,n}K_1(l_nr)]\, e^{ik_nz}e^{i\omega t}. \tag{14}$$

From the stream function solution (Equation (14)), the radial and axial velocity components can be obtained using Equation (4):

$$v_r = \sum_{n=-\infty}^{\infty} [A_{1,n}I_1(k_nr) + B_{1,n}K_1(k_nr) + A_{2,n}I_1(l_nr) + B_{2,n}K_1(l_nr)]\, ik_ne^{ik_nz}e^{i\omega t}, \tag{15a}$$

$$v_z = \sum_{n=-\infty}^{\infty} [-k_nA_{1,n}I_0(k_nr) + k_nB_{1,n}K_0(k_nr) - l_nA_{2,n}I_0(l_nr) + l_nB_{2,n}K_0(l_nr)]\, e^{ik_nz}e^{i\omega t}. \tag{15b}$$

Our next objective is to find coefficients for velocity distribution. The velocity components v_r and v_z must be finite everywhere. This condition requires that the velocity components do not contain the function $K_1(k_nr)$; hence, $B_{1,n} = B_{2,n} = 0$. At the channel wall ($r = r_0 = d/2$), the boundary conditions for radial and axial velocity become no penetration to the wall ($v_r = 0$) and Helmholtz–Smoluchowski slip velocity ($v_z = -\varepsilon\zeta(z)E_0e^{i\omega t}/\mu$), respectively. The first boundary condition requires that $A_{2,n} = -A_{1,n}I_1(k_nr_0)/I_1(l_nr_0)$. Using the second Helmholtz–Smoluchowski boundary condition and applying complex Fourier analysis, one can find the remaining coefficient using the equation $A_{1,n} = -\frac{\varepsilon E_0 I_1(l_nr_0)}{\mu[-k_nI_0(k_nr_0)I_1(l_nr_0)+l_nI_1(k_nr_0)I_0(l_nr_0)]}\frac{1}{L}\int_0^L \zeta(z)e^{-ik_nz}dz$. Thus, the final forms of radial and axial velocity can be given as

$$v_r = \sum_{n=-\infty}^{\infty} A_{1,n}\left[I_1(k_nr) - \frac{I_1(k_nr_0)}{I_1(l_nr_0)}I_1(l_nr)\right] ik_ne^{ik_nz}e^{i\omega t}, \tag{16a}$$

$$v_z = \sum_{n=-\infty}^{\infty} A_{1,n}\left[-k_nI_0(k_nr) + l_n\frac{I_1(k_nr_0)}{I_1(l_nr_0)}I_0(l_nr)\right] e^{ik_nz}e^{i\omega t}, \tag{16b}$$

respectively. The imaginary part of these equations provides flow velocity corresponds to the external electric field, $\vec{E} = E_0sin(\omega t) = Im\left(E_0e^{i\omega t}\right)$, which we considered throughout the paper. Even though Equation (16) provides the analytical solution for time-periodic electroosmotic flow in a

heterogeneously charged circular shaped channel, it cannot be used for time-periodic electroosmotic flow in a homogeneously charged channel since we started our analysis for a general solution (Equation (11)) with periodicity in the axial (z) direction. Thus, to obtain time-periodic electroosmotic velocity in a homogenously charged microchannel, one has to drop the z-dependency in the general solution and governing equations (Equation (6)) and follow the method described in this work.

3. Results and Discussion

In this section, results are provided for a sinusoidal surface charge distribution, although the general solution presented in the aforementioned section can be applied for any periodic surface charge distribution along the tube. The sinusoidal surface charge distribution can be given as:

$$\zeta(z) = \zeta_0 \sin(qz) \tag{17}$$

where ζ_0 is the amplitude (reference) of the surface charge and q is the angular frequency of the surface charge distribution. With this charge distribution, the coefficient for Equation (16) can be found as follows:

$$A_{1,n} = -\frac{\varepsilon E_0 I_1(l_n r_0)}{\mu[-k_n I_0(k_n r_0) I_1(l_n r_0) + l_n I_1(k_n r_0) I_0(l_n r_0)]} \frac{\zeta_0}{L}\left[\frac{\{ik_n \sin(qL) + q\cos(qL)\}e^{-ik_n L} - q}{k_n^2 - q^2}\right] \tag{18}$$

Throughout this section, unless otherwise stated, the value of q is considered as $2\pi/L$, which corresponds to a single period in the surface charge distribution as shown in Figure 2.

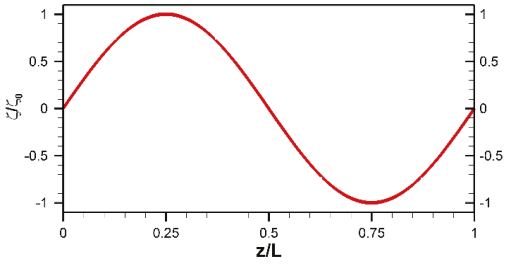

Figure 2. Schematic of the zeta potential distribution with a single period.

3.1. Velocity Profiles at Various Nondimensional Times

Figure 3 illustrates the velocity vector at different nondimensional times for a sinusoidal zeta potential distribution along the channel surface with a reference potential of −100 mV. When the zeta potential is changed along the channel wall, the driving force in electroosmotic flow is also changed. Consequently, a non-uniform flow field is developed along the channel (Figure 3). At $\omega t = \pi/2$, the electric field is positive. Thus, the fluids near the walls move in the positive x-direction in the left half of the channel, since the zeta potential is negative in the left half. In contrast, due to the positive surface charge in the right half of the channel, the fluids near the walls move in the negative x-direction. These two opposite directional flows create two counter-rotating vortices in the upper part ($0 \le r/r_0 \le 1$) of the channel (Figure 3a). In fact, two counter-rotating vortices are formed at any angle θ because of the axisymmetric conditions. In other words, for a single period of surface potential, two oppositely rotating vortices (each one extending one half of the total length) are formed within the tube. So, if the tube is filled with two fluids in such a way that each fluid fills the entire cross-section and one-fourth length of the channel in an alternative patch, this design will have strong potential to enhance the mixing efficiency. Figure 3b shows the vector plot of the flow field at a nondimensional time, $\omega t = 3\pi/4$. This yields similar results to the previous case (Figure 3a) due to

the similar conditions; however, the magnitude of the velocity components at the surface is reduced because of the reduced strength of the electric field. At $\omega t = \pi$, the slip velocity at the wall reaches zero due to the no applied electric field (Figure 3c). However, bulk fluid motion is still observed at the center part of the tube due to the phase lag between fluids in the electric double layer and bulk fluids. The phase lag occurs due to the finite time requirement for momentum diffusion from the surface to the center line of the tube. This out-of-phase behavior is clearly visible at time $\omega t = 5\pi/4$ (Figure 3d), where velocity is negligible at the centerline of the channel but slip velocity at the channel surface is moderate. The centerline velocity approaches zero at $\omega t = 1.26\pi$ and 2.26π. Based on these results, one can calculate the time lag as ~0.26π or 81.25 μs for an applied electric field frequency of 1.6 kHz.

When the electric field changes its direction, the velocity vector also switches its course (Figure 3d,e). For example, the distribution of velocity vectors at nondimensional time $\omega t = 3\pi/2$ appears to be opposite that at $\omega t = \pi/2$ (Figure 3e vs. Figure 3a). It has been found that in EOF, the net flow and its direction depend on the overall strength of the zeta potential:

$$\overline{\zeta} = \frac{\sum\limits_{i} \zeta_i \Delta L_i}{\sum\limits_{i} \Delta L_i} \tag{19}$$

where ζ_i and ΔL_i are the zeta potential and channel length at the i-th section, respectively [24]. Since the considered sinusoidal zeta potential has an overall strength of zero, the net flow in the current scenario is zero at any time.

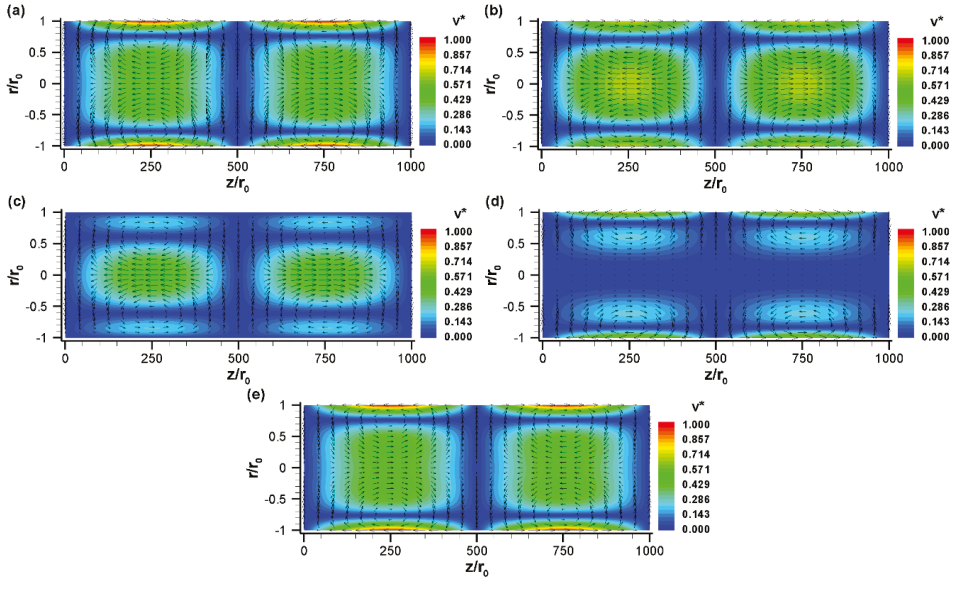

Figure 3. The normalized velocity, $\vec{v}^* = \vec{V}/u_{HS}$ (vector plot), and its magnitude, $v* = \left|\vec{V}\right|/u_{HS}$ (contour plot), with sinusoidal zeta potential distribution at various nondimensional times: (**a**) $\omega t = \pi/2$, (**b**) $\omega t = 3\pi/4$, (**c**) $\omega t = \pi$, (**d**) $\omega t = 5\pi/4$, and (**e**) $\omega t = 3\pi/2$. The vector plot shows the direction of fluid motion whereas the contour plot shows the magnitude of the velocity. Here, $u_{HS} = -\varepsilon\zeta E_0/\mu$, $E_0 = 10$ kV/m, $\zeta_0 = -100$ mV, $r_0 = 50$ μm, $L = 5$ cm, $q = 2\pi/L$, $f = 1.6$ kHz ($\Omega = 25$). Fluid properties are taken for water at 20 °C.

3.2. Effect of Nondimensional Frequency

Previous works have shown that both electric field frequency and channel height have a similar effect on electroosmotic vortices [3]. Thus, it is wise to combine these two parameters to obtain a nondimensional frequency as $\Omega = \omega r_0^2/\vartheta$. This nondimensional frequency represents the ratio of the diffusion time scale, $t_{diff} = r_0^2/\vartheta$, to the period of the external electric field, $t_p = 1/\omega$ [34]. The nondimensional frequency increases if either applied electric field frequency increases or the size of the tube increases.

The effect of nondimensional frequencies is shown in Figure 4 for the sinusoidal zeta potential distribution case presented in Figure 3. Velocity vectors are presented for four different nondimensional frequencies: (a) $\Omega = 2.5$, (b) $\Omega = 25$, (c) $\Omega = 125$, and (d) $\Omega = 250$ at $\omega t = \pi/2$. For a 100 μm diameter tube, these normalized frequencies correspond to $f = 0.16$, 1.6, 8 and 16 kHz. As the nondimensional frequency increases, the pattern of the flow field changes significantly (Figure 4). At a low value of Ω (e.g., 2.5), the diffusion time scale is on the same order of magnitude of the external electric field period. As a result, the flow has enough time to propagate from the surface to the center of the channel, resulting in large vortices which extend from the surface to the center region of the tube (Figure 4a). However, as Ω increases from 2.5 to 25, these vortices are slightly shifted toward the surface and the bulk fluid velocity diminishes slightly (Figure 4b). When Ω increases from 25 to 125, the vortices are mainly confined to near the surface and the bulk fluid motion reduces significantly, as shown in Figure 4c. At a very high value of Ω (250 or higher), the bulk fluids are virtually motionless, despite the very fast oscillating flow occurring near the channel surface (Figure 4d). Thus, it is obvious from Figure 4 that the perturbed flow regime becomes smaller at higher nondimensional frequencies. The effect of nondimensional frequency on the flow field can be represented by damped viscous waves traveling away from the wall.

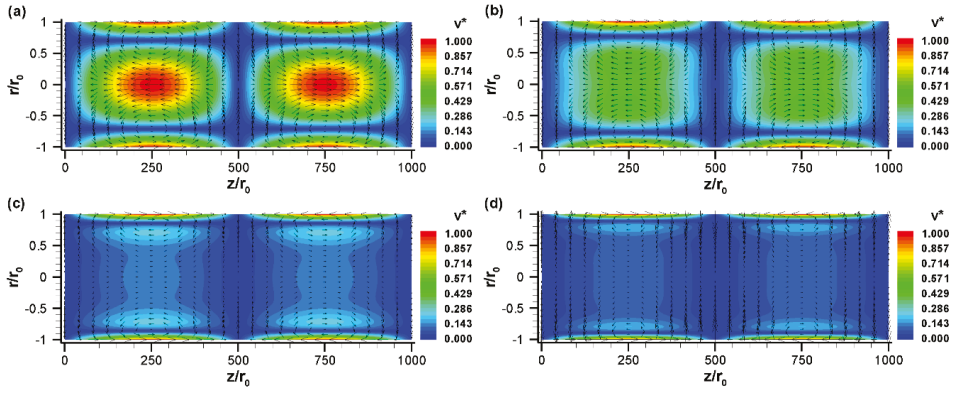

Figure 4. The normalized velocity, $\vec{v}^* = \vec{V}/u_{HS}$ (vector plot) and its magnitude, $v* = \left|\vec{V}\right|/u_{HS}$ (contour plot) with a sinusoidal zeta potential distribution for various nondimensional frequencies: (**a**) $\Omega = 2.5$ ($f = 160$ Hz), (**b**) $\Omega = 25$ ($f = 1.6$ kHz), (**c**) $\Omega = 125$ ($f = 8$ kHz), and (**d**) $\Omega = 250$ ($f = 16$ kHz) at $\omega t = \pi/2$. All other conditions are the same as those in Figure 3.

3.3. Effect of Surface Potential

Next, we studied the effect of surface potential distribution in the flow profile. As shown in Figure 5, the number of vortices formed within the channel can be controlled by the periodicity of the surface zeta potential distribution. With a half period ($q = \pi/L$), a large vortex is formed within the tube (Figure 5a), while with two periods ($q = 4\pi/L$), four smaller vortices (each one extending one-fourth of the total length) are formed within the length of the tube (Figure 5b). Thus, a reduction in the surface potential periodicity reduces the number of vortices but extends the size of the vortices. Even though

both scenarios (Figure 5a,b) provide an opportunity to enhance mixing through vortex formation, the higher periodicity case (Figure 5b) may be better for effective mixing because more vortices may yield a shorter mixing length. However, one has to be mindful about the sample loading to realize any positive outcome. For instance, in the case of half periodicity (Figure 5a), each mixing constituent needs to be loaded in each half of the channel. For example, fluid 1 should be loaded at length $0 \le z \le L/2$ and fluid 2 should be loaded at length $L/2 \le z \le L$. In contrast, in the case of double periodicity (Figure 5b), each mixing constituent needs to be loaded at one-eighth of the channel length in an alternative patch. For example, fluid 1 should be loaded at $0 \le z \le L/8$, $L/4 \le z \le 3L/8$, $L/2 \le z \le 5L/8$, and $3L/4 \le z \le 7L/8$, whereas fluid 2 should be loaded at $L/8 \le z \le L/4$, $3L/8 \le z \le L/2$, $5L/8 \le z \le 3L/4$, and $7L/8 \le z \le L$ for effective mixing. Thus, our analytical results show that one can precisely control the flow field to achieve the desired level of mixing by modifying the zeta potential patterning on the tube surface.

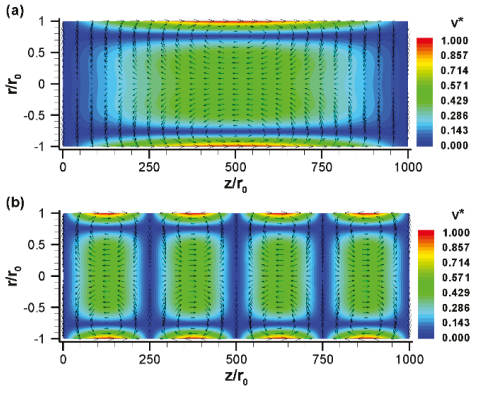

Figure 5. The normalized velocity, $\vec{v}^* = \vec{V}/u_{HS}$ (vector plot), and its magnitude, $v* = \left|\vec{V}\right|/u_{HS}$ (contour plot), with a sinusoidal zeta potential distribution with (**a**) $k = \pi/L$ and (**b**) $k = 4\pi/L$. Results are presented for $\omega t = \pi/2$. All other conditions are the same as those in Figure 3.

3.4. Pressure Distribution

Although no external pressure was imposed for our proposed micromixer, pressure can be induced inside the channel to ensure the constant flow rate between different regions with different zeta potentials on the wall. This induced pressure can be quantified from the velocity profile. An analytical expression for pressure can be obtained from the modified Navier–Stokes equations. For instance, in the absence of an advection term, one can replace the axial velocity, i.e., the z-directional velocity component (Equation (16b)), in the z-component of the Navier–Stokes equation (Equation (6b)) to obtain the z-directional pressure gradient:

$$\frac{\partial P}{\partial z} = \sum_{n=-\infty}^{\infty} A_{1,n}\left[i\rho\omega k_n I_0(k_n r) + \left(\mu l_n^3 - \mu l_n k_n^2 - i\rho\omega l_n\right)\frac{I_1(k_n r_0)}{I_1(l_n r_0)} I_0(l_n r)\right] e^{ik_n z} e^{i\omega t}. \tag{20}$$

The pressure distribution along the tube can be obtained by integrating with respect to z as follows:

$$P = \sum_{n=-\infty}^{\infty} A_{1,n}\left[i\rho\omega k_n I_0(k_n r) + \left(\mu l_n^3 - \mu l_n k_n^2 - i\rho\omega l_n\right)\frac{I_1(k_n r_0)}{I_1(l_n r_0)} I_0(l_n r)\right] \frac{1}{ik_n} e^{ik_n z} e^{i\omega t} + P_1(r,t) \tag{21}$$

where P_1 is an integration factor, which can be a fixed value or a function of r and t. Now, by manipulating Equations (6a), (16a), and (21), we obtain:

$$\frac{\partial P_1}{\partial r} = \sum_{n=-\infty}^{\infty} A_{1,n}\left[\left(-\rho\omega k_n + i\mu\frac{l_n^4}{k_n} - 2i\mu k_n l_n^2 + \rho\omega\frac{l_n^2}{k_n} + i\mu k_n^3\right)\frac{I_1(k_n r_0)}{I_1(l_n r_0)}I_1(l_n r)\right]e^{ik_n z}e^{i\omega t}. \tag{22}$$

The aforementioned equation indicates that $\partial P_1/\partial r$ might be a function of z, r, and t. However, following numerical evaluation with a sinusoidal surface charge distribution (Equation (17)) and applied electric field, $\vec{E} = E_0 sin(\omega t) = Im\left(E_0 e^{i\omega t}\right)$, it is found that $\partial P_1/\partial r$ is zero in space and time (data not shown). Thus, the integration of Equation (22) will yield P_1 equal to a constant. Since we are not seeking the absolute pressure, we can neglect that constant, and quantify the gauge pressure distribution from Equation (21):

$$P(r,t) = \sum_{n=-\infty}^{\infty} A_{1,n}\left[i\rho\omega k_n I_0(k_n r) + \left(\mu l_n^3 - \mu l_n k_n^2 - i\rho\omega l_n\right)\frac{I_1(k_n r_0)}{I_1(l_n r_0)}I_0(l_n r)\right]\frac{1}{ik_n}e^{ik_n z}e^{i\omega t}. \tag{23}$$

The distribution of pressure at various nondimensional times is shown in Figure 6. From this figure, it can be seen that the pressure varies mainly in the axial direction. The reason behind this is discussed shortly. Since the flow field varies with time, the induced pressure also varies accordingly. For any particular time, for instance, $\omega t = \pi/2$ (Figure 6a), an adverse (positive) pressure gradient is observed in the left half of the channel, while a favorable (negative) pressure gradient is formed in the right half of the channel. This induced positive pressure gradient tends to suppress electroosmotic flow, resulting in a mixed electroosmotic and pressure-driven flow, as shown in Figure 3a. This kind of velocity profile has also been obtained in an experimental study [35]. As the electric field direction switches, the flow field changes and, as a consequence, the pressure distribution is also switched, as shown in Figure 6b.

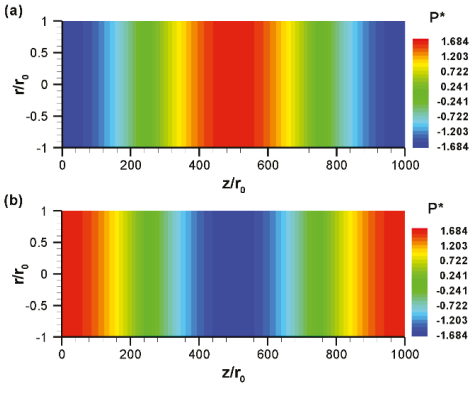

Figure 6. Distribution of normalized gauge pressure, $P* = Pr_0/\mu u_{HS}$, at different nondimensional times: (**a**) $\omega t = \pi/2$ and (**b**) $\omega t = 3\pi/2$. All other conditions are the same as those in Figure 3.

The axial variation of pressure is shown in Figure 7a for various nondimensional times, where pressure is obtained at the centerline of the tube. As seen from Figure 7a, for a sinusoidal variation of the zeta potential, the axial variation of pressure is also sinusoidal. However, there is a phase lag of 90° between the pressure distribution and zeta potential distribution. Thus, for a sine distribution of the zeta potential, the axial variation of induced pressure is cosine. At $\omega t = \pi/2$, an adverse pressure gradient is observed in the left half of the channel, whereas a favorable pressure gradient is observed in the right half of the channel. As the electric field changes, the pattern of pressure variation in the

axial direction also changes. For example, in contrast to $\omega t = \pi/2$, at $\omega t = 3\pi/2$ a favorable pressure gradient is observed in the left half of the channel while an adverse pressure gradient is observed in the right half of the channel. It should be noted that in this work, a pressure gradient was also observed in the radial direction, however, the variation was very small in comparison to the axial variation and, hence, it was not captured in the pressure contour plot (Figure 6). The radial directional variation of pressure is shown in Figure 7b by line plot for various nondimensional times, where pressure is obtained along the radial direction of the channel at the axial location $z/r_0 = 500$ ($z = L/2$). Since the radial variation of pressure is very small, instead of gauge pressure, its change from the center point ($r/r_0 = 0, \quad z/r_0 = 500$) is plotted in Figure 7b. This figure shows that the radial variation of pressure is several orders magnitude lower than that of the axial variation due to the low radial velocity. As the electric field changes direction, the pattern of pressure variation in the radial direction is also changed. For example, at $\omega t = \pi/2$, the pressure variation in the radial direction follows a concave parabolic curve; whereas at $\omega t = 3\pi/2$ the pressure variation in the radial direction becomes a convex parabolic curve (Figure 7b).

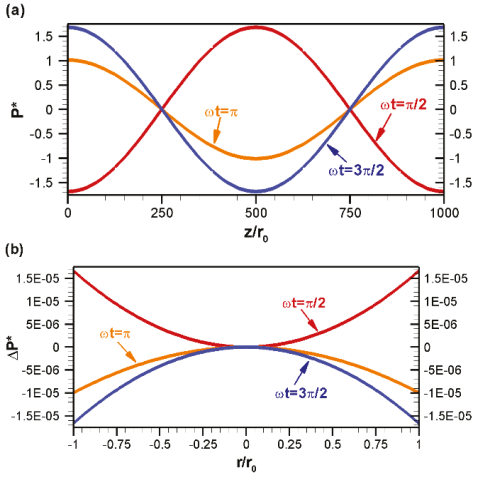

Figure 7. Distribution of gauge pressure, $P* = Pr_0/\mu u_{HS}$, at various nondimensional times: (**a**) Variation along the axial direction at $r/r_0 = 0$ and (**b**) along the radial direction at $z/r_0 = 500$, where $\Delta P* = P* - P*(r/r_0 = 0)$. All other conditions are same as those in Figure 3.

4. Conclusions

Motivated by the growing interest in electroosmosis as a reliable non-mechanical strategy to control fluid motion and mix species in microfluidic devices, we analytically studied the time-periodic electroosmotic flow in cylindrical microchannels with a heterogeneous surface charge distribution. The analytical solution was derived by solving a simplified Navier–Stokes equation with Helmholtz–Smoluchowski slip boundary conditions at the wall. Although the derived analytical solution is valid for any periodic surface charge distribution, only the sinusoidal surface charge case was analyzed in this paper. The induced pressure field was also obtained from the velocity profiles. The results show that several vortices are formed inside the microchannel with a sinusoidal surface charge. These vortices change their pattern and direction as the external electric field changes with time. In addition, the dominance of the vorticity depends on the frequency of the external electric field and the size of the channel. As the electric field frequency or channel diameter increases, vortices are shifted towards the channel surface and the perturbed flow regions become smaller. Unlike the homogenous surface charge case, velocity variation in the radial direction was also observed in this paper. The results also show that the number of vorticities can be changed easily by changing the

periodicity of the surface charge. Thus, the flow field can be precisely controlled with a specific surface pattern, which will provide the desired mixing efficiency.

Author Contributions: Methodology and formal analysis, A.I.K.; writing—original draft preparation, A.I.K.; conceptualization and supervision, P.D.; writing—review and editing, P.D.

Funding: This research was funded by the Washington State University through graduate assistantship program.

Acknowledgments: Authors would like to thank Hyunsung Kim for his valuable suggestions throughout the study.

Conflicts of Interest: The authors declare no conflict of interest.

References

1. Hossan, M.R.; Dutta, D.; Islam, N.; Dutta, P. Review: Electric field driven pumping in microfluidic device. *Electrophoresis* **2018**, *39*, 702–731. [CrossRef] [PubMed]
2. Capretto, L.; Cheng, W.; Hill, M.; Zhang, X.L. Micromixing Within Microfluidic Devices. *Microfluid. Technol. Appl.* **2011**, *304*, 27–68.
3. Kim, H.; Khan, A.I.; Dutta, P. Time-Periodic Electro-Osmotic Flow with Nonuniform Surface Charges. *J. Fluids Eng.* **2019**, *141*, 081201. [CrossRef]
4. Biddiss, E.; Erickson, D.; Li, D.Q. Heterogeneous surface charge enhanced micromixing for electrokinetic flows. *Anal. Chem.* **2004**, *76*, 3208–3213. [CrossRef] [PubMed]
5. Cai, G.Z.; Xue, L.; Zhang, H.L.; Lin, J.H. A Review on Micromixers. *Micromachines* **2017**, *8*, 274. [CrossRef] [PubMed]
6. Nguyen, N.T.; Wu, Z.G. Micromixers—A review. *J. Micromech. Microeng.* **2005**, *15*, R1–R16. [CrossRef]
7. Lee, C.Y.; Chang, C.L.; Wang, Y.N.; Fu, L.M. Microfluidic Mixing: A Review. *Int. J. Mol. Sci.* **2011**, *12*, 3263–3287. [CrossRef]
8. Wang, Y.; Zhe, J.; Dutta, P.; Chung, B.T. A microfluidic mixer utilizing electrokinetic relay switching and asymmetric flow geometries. *J. Fluids Eng.* **2007**, *129*, 395–403. [CrossRef]
9. Green, J.; Holdø, A.; Khan, A. A review of passive and active mixing systems in microfluidic devices. *Int. J. Multiphys.* **2007**, *1*, 1–32. [CrossRef]
10. Dutta, P.; Beskok, A. Analytical solution of time periodic electroosmotic flows: Analogies to Stokes' second problem. *Anal. Chem.* **2001**, *73*, 5097–5102. [CrossRef]
11. Kang, Y.J.; Yang, C.; Huang, X.Y. Dynamic aspects of electroosmotic flow in a cylindrical microcapillary. *Int. J. Eng. Sci.* **2002**, *40*, 2203–2221. [CrossRef]
12. Erickson, D.; Li, D.Q. Analysis of alternating current electroosmotic flows in a rectangular microchannel. *Langmuir* **2003**, *19*, 5421–5430. [CrossRef]
13. Jian, Y.J.; Yang, L.G.; Liu, Q.S. Time periodic electro-osmotic flow through a microannulus. *Phys. Fluids* **2010**, *22*, 042001. [CrossRef]
14. Oddy, M.H.; Santiago, J.G.; Mikkelsen, J.C. Electrokinetic instability micromixing. *Anal. Chem.* **2001**, *73*, 5822–5832. [CrossRef] [PubMed]
15. Glasgow, I.; Batton, J.; Aubry, N. Electroosmotic mixing in microchannels. *Lab Chip* **2004**, *4*, 558–562. [CrossRef] [PubMed]
16. Lim, C.Y.; Lam, Y.C.; Yang, C. Mixing enhancement in microfluidic channel with a constriction under periodic electro-osmotic flow. *Biomicrofluidics* **2010**, *4*, 014101. [CrossRef] [PubMed]
17. Ajdari, A. Electro-osmosis on inhomogeneously charged surfaces. *Phys. Rev. Lett.* **1995**, *75*, 755. [CrossRef] [PubMed]
18. Horiuchi, K.; Dutta, P.; Ivory, C.F. Electroosmosis with step changes in zeta potential in microchannels. *AIChE J.* **2007**, *53*, 2521–2533. [CrossRef]
19. Erickson, D.; Li, D.Q. Influence of surface heterogeneity on electrokinetically driven microfluidic mixing. *Langmuir* **2002**, *18*, 1883–1892. [CrossRef]
20. Qian, S.Z.; Bau, H.H. A chaotic electroosmotic stirrer. *Anal. Chem.* **2002**, *74*, 3616–3625. [CrossRef] [PubMed]
21. Stroock, A.D.; Weck, M.; Chiu, D.T.; Huck, W.T.S.; Kenis, P.J.A.; Ismagilov, R.F.; Whitesides, G.M. Patterning electro-osmotic flow with patterned surface charge. *Phys. Rev. Lett.* **2000**, *84*, 3314–3317. [CrossRef] [PubMed]

22. Norde, W.; Rouwendal, E. Streaming potential measurements as a tool to study protein adsorption-kinetics. *J. Colloid Interface Sci.* **1990**, *139*, 169–176. [CrossRef]
23. Wei, C.W.; Young, T.H.; Cheng, J.Y. Electroosmotic mixing induced by non-uniform zeta potential and application for dna microarray in microfluidic channel. *Biomed. Eng.-Appl. Basis Commun.* **2005**, *17*, 281–283. [CrossRef]
24. Lee, J.S.H.; Ren, C.L.; Li, D.Q. Effects of surface heterogeneity on flow circulation in electroosmotic flow in microchannels. *Anal. Chim. Acta* **2005**, *530*, 273–282. [CrossRef]
25. Luo, W.J. Transient electroosmotic flow induced by AC electric field in micro-channel with patchwise surface heterogeneities. *J. Colloid Interface Sci.* **2006**, *295*, 551–561. [CrossRef] [PubMed]
26. Tang, G.H.; Li, Z.; Wang, J.K.; He, Y.L.; Tao, W.Q. Electroosmotic flow and mixing in microchannels with the lattice Boltzmann method. *J. Appl. Phys.* **2006**, *100*, 094908. [CrossRef]
27. Green, N.G.; Ramos, A.; Gonzalez, A.; Morgan, H.; Castellanos, A. Fluid flow induced by nonuniform ac electric fields in electrolytes on microelectrodes. III. Observation of streamlines and numerical simulation. *Phys. Rev. E* **2002**, *66*, 026305. [CrossRef] [PubMed]
28. Potoček, B.; Gaš, B.; Kenndler, E.; Štědrý, M. Electroosmosis in capillary zone electrophoresis with non-uniform zeta potential. *J. Chromatogr. A* **1995**, *709*, 51–62. [CrossRef]
29. Chang, C.C.; Yang, R.J. A particle tracking method for analyzing chaotic electroosmotic flow mixing in 3D microchannels with patterned charged surfaces. *J. Micromech. Microeng.* **2006**, *16*, 1453–1462. [CrossRef]
30. Ajdari, A. Generation of transverse fluid currents and forces by an electric field: Electro-osmosis on charge-modulated and undulated surfaces. *Phys. Rev. E* **1996**, *53*, 4996. [CrossRef]
31. Yang, R.J.; Wu, C.H.; Tseng, T.I.; Huang, S.B.; Lee, G.B. Enhancement of electrokinetically-driven flow mixing in microchannel with added side channels. *Jpn. J. Appl. Phys.* **2005**, *44*, 7634–7642. [CrossRef]
32. Tomotika, S. On the instability of a cylindrical thread of a viscous liquid surrounded by another viscous fluid. *Proc. R. Soc. Lond. A* **1935**, *150*, 322–337.
33. Brenn, G. *Analytical Solutions for Transport. Processes: Fluid Mechanics, Heat and Mass Transfer*; Springer: Berlin/Heidelberg, Germany, 2017; pp. 1–300.
34. Moghadam, A.J. An exact solution of AC electro-kinetic-driven flow in a circular micro-channel. *Eur. J. Mech. B Fluids* **2012**, *34*, 91–96. [CrossRef]
35. Herr, A.; Molho, J.; Santiago, J.; Mungal, M.; Kenny, T.; Garguilo, M. Electroosmotic capillary flow with nonuniform zeta potential. *Anal. Chem.* **2000**, *72*, 1053–1057. [CrossRef] [PubMed]

micromachines

MDPI

Article

Development of a High Flow Rate 3-D Electroosmotic Flow Pump

Zi Ye [1,2], Renchang Zhang [1,2], Meng Gao [1,2], Zhongshan Deng [1,2] and Lin Gui [1,2,*]

[1] Key Laboratory of Cryogenics, Technical Institute of Physics and Chemistry, Chinese Academy of Sciences, 29 Zhongguancun East Road, Haidu District, Beijing 10019, China; yezi15@mails.ucas.ac.cn (Z.Y.); zhangrenchang15@mails.ucas.ac.cn (R.Z.); mgao@mail.ipc.ac.cn (M.G.); zsdeng@mail.ipc.ac.cn (Z.D.)

[2] School of Future Technology, University of Chinese Academy of Sciences, 19 Yuquan road, Shijingshan District, Beijing 100039, China

* Correspondence: lingui@mail.ipc.ac.cn

Received: 26 December 2018; Accepted: 2 February 2019; Published: 11 February 2019

Abstract: A low voltage 3D parallel electroosmotic flow (EOF) pump composed of two electrode layers and a fluid layer is proposed in this work. The fluid layer contains twenty parallel fluid channels and is set at the middle of the two electrode layers. The distance between fluid and electrode channels was controlled to be under 45 μm, to reduce the driving voltage. Room temperature liquid metal was directly injected into the electrode channels by syringe to form non-contact electrodes. Deionized (DI) water with fluorescent particles was used to test the pumping performance of this EOF pump. According to the experimental results, a flow rate of 5.69 nL/min was reached at a driving voltage of 2 V. The size of this pump is small, and it shows a great potential for implanted applications. This structure could be easily expanded for more parallel fluid channels and larger flow rate.

Keywords: multi-layer structure; electroosmotic flow (EOF) pump; parallel fluid channels; liquid metal electrodes

1. Introduction

Micropumps are one of the essential components in microfluidics systems [1]. The applications of micropumps include biological analysis [2–4], drug delivery [5], and micro-mixers [6]. For all these applications, micropumps are required to have wide range of flow rates, stable flow and biocompatibility. Electroosmotic flow (EOF) pumps have drawn much attention in recent years. They have the ability to generate constant flows, precisely control of flow rate, and can be easily integrated into lab-on-a-chip system because they have no moving parts [7]. Thus, they could offer a great solution to liquid delivery in microfluidics.

According to fluid channel type, EOF pumps can be divided into two categories: porous channel pumps and direct channel pumps. Porous channel EOF pumps could generate high flow rates at a relatively low voltage [8–10]. In some designs, particles with a diameter of a few microns are added into capillaries to form the fluid channel [8]. Also, both the porous membrane [9] and porous monolith [10] are used as fluid channels, and the flow rate of several mL/min would reach under 100 V. The fabrication process of these pumps is complicated, and pore diameter limits the sample size in the fluid. Cells and large particles are unable to go through these kinds of channels. This greatly limits their usage in biological analysis. On the other hand, direct channel EOF pumps have nothing blocking the channel, and could expand the usage of the pumps. One kind of direct channel EOF pump uses capillary as fluid channels [11]. Voltage as high as several thousand volts is applied directly on both sides of the capillary. The flow rate would reach several μL/min. As micro fabrication

develops, materials such as polydimethylsiloxane (PDMS) and polymethyl methacrylate (PMMA) are used to fabricate EOF pumps [12]. Solid electrodes are integrated in PDMS, and directly contact the microfluidic channel. Compared to single channel EOF pumps, parallel fluid channels could enhance the flow rate. With 10 parallel channels, flow rate would be increased compared to single channel pumps [13]. The electrodes in most of these pumps contact the fluid directly while pumping, and this would cause contamination to the fluid samples. Strong electrophoresis would happen with contact electrodes. Moreover, while working, bubbles and Joule heat would be a limitation of flow rates [14] and applications to these pumps.

To improve the bubble and joule heat problems in direct channel EOF pumps, and to reduce electrophoresis, several solutions are proposed: alternative current (AC) EOF pumps [15,16], bubbleless electrodes EOF pumps [17] and non-contact EOF pumps [1,18]. AC EOF pumps use asymmetric electrodes. Bubbleless electrodes such as vinylized fused silica capillary electrodes require high cost and complicated fabrication process. Non-contact EOF pumps, whose electrodes are not in direct contact with fluid channel, are ideal for EOF pumps. Room temperature liquid metal (gallium-base alloy) is used as electrodes and this EOF pump is able to generate fluid flow at a voltage less than 2 V [1]. Later, solid gallium metal electrodes were also used in non-contact EOF pumps in a similar pump structure, and the lowest pumping voltage is 650 V [18]. However, the flow rates of these pumps are relatively low, only several nanoliters per minute. In these 2-dementional designs, there could be only one or two fluid pumping channels. It is very difficult to increase the flow rate by using parallel fluid channel without increasing the pump size too much. To increase the flow rate, 3-dementional structure EOF micropump could be considered.

In this work, a low voltage three-dimensional non-contact EOF pump with new 3D structure is proposed. The pump is made of PDMS, and gallium-based alloy is used to form electrodes. This type of alloy is in liquid form in room temperature, and can be injected into channels directly by syringe. This alloy is also widely used as micro-electrode [19], biomaterial [20] and 3D printing material [21]. The structure and fabrication process of this pump is introduced below in detail. Then, we describe its performance, which we tested using deionized (DI) water with fluorescent particles for flow tracing. Experiment results are shown and discussed at the end of this paper.

2. Materials and Methods

2.1. Design of 3-Dimentional Non-Contact EOF Pump

Figure 1a,b shows the schematic of this stereoscopic pump. It contains 5 layers, including three channel layers and two thin membrane layers. The three channel layers contain two electrode layers and one fluid layer. The fluid layer lies in the middle of two electrode layers. Between the fluid layer and both electrode layers there are two thin membrane layers. These two thin membrane layers make the electrode not in direct contact with working fluid.

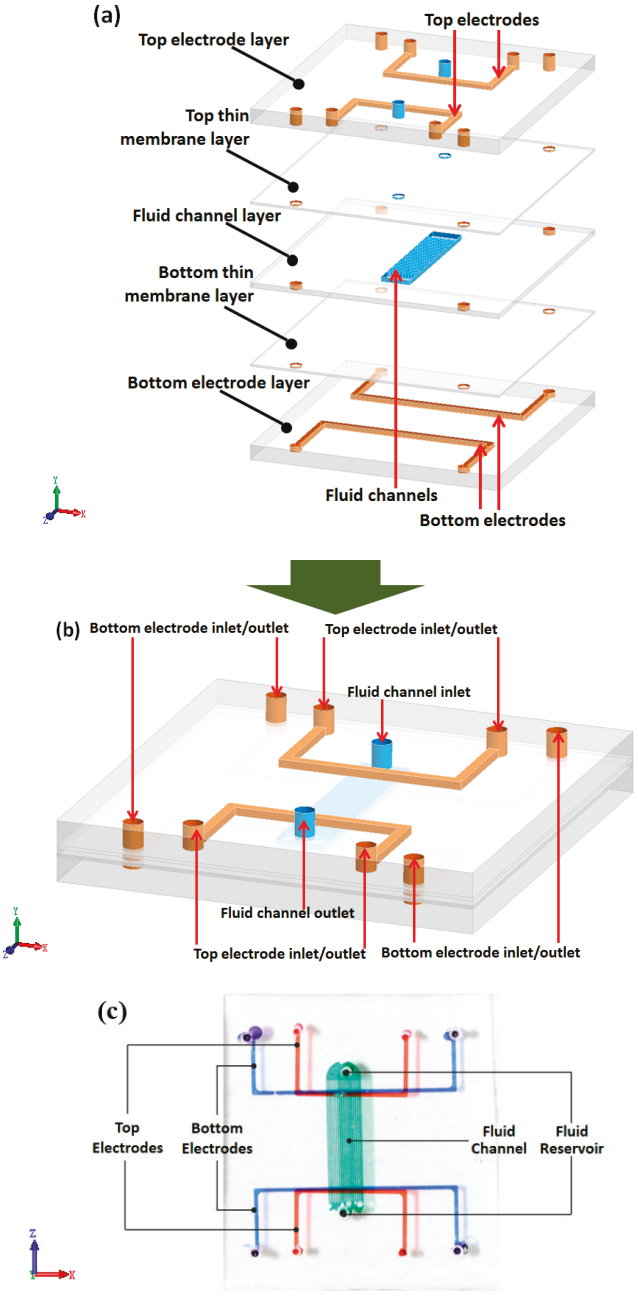

Figure 1. Schematic of the electroosmotic flow (EOF) pump. (**a**) Layer view; (**b**) combination view; (**c**) optical photograph of 3-demintional EOF pumps.

All three channel layers were designed separately. Each of the two electrode layers contains two symmetric electrode channels. For the convenience of injecting liquid metal, electrode channels

were designed in a U shape, with one injection inlet and outlet. The width of those channels is 400 µm, consistently. The distance between electrodes on the same layer is 8000 µm. Fluid channels are set perpendicular to the electrodes. In this work, we use 20 parallel channels as fluid channels. All 20 channels share the same inlet and outlet. The width of these fluid channels is 116 µm each, and the gap between the adjacent channels is 50 µm. The length of fluid channel is 10,500 µm. Moreover, in order to reduce the driving voltage of the pump, the membrane layers are made as thin as possible. Due to different fabrication process, the bottom thin membrane is 16µm thick, and top membrane is 43 µm thick. The dimension schematic of this pump is shown in Figure 2.

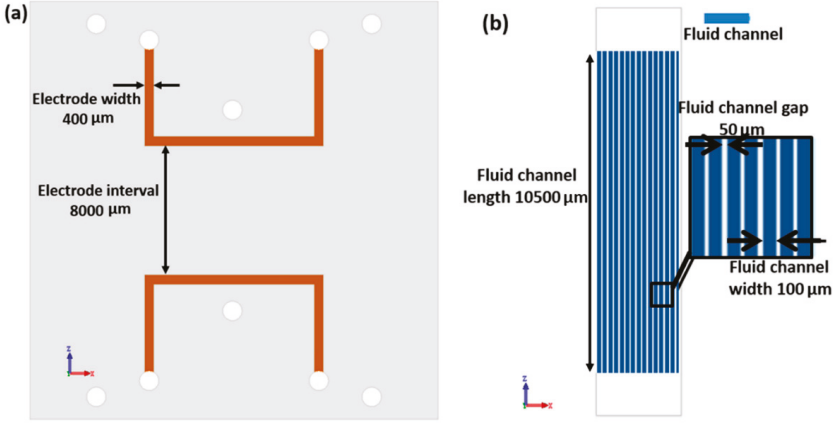

Figure 2. Schematic of the dimensions of EOF pump. (**a**) Electrode channel (top view) (**b**) fluid channel (top view).

While working, a voltage is applied between two electrodes on both top and bottom electrode layers, as shown in Figure 3. Because the U shapes of the electrode, there are two long parallel electrodes on both sides of fluid channels. Thus, there is a uniform electronic field along the fluid channels. Electroosmotic flow would then be generated in response to the electrode field.

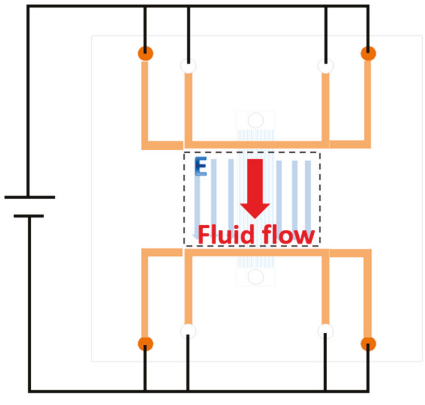

Figure 3. Working principle.

With the design including parallel fluid channels that are not in the same layer as the electrode channels, the number of fluid channels could be easily expanded if needed. Flow rate can be increased by making more parallel fluid channels. The distance between fluid channels and electrode

channels is controlled to be under 45 μm, and this lowers the driving voltage applied to the pump. Non-contact electrode design would prevent the bubble generation due to the electrode corrosion, and increase the stability and lifetime for this pump. Also, sample contamination would be prevented for biological applications.

2.2. Fabrication Process

The material of the chip is PDMS, and the electrode material is gallium-based alloy ($Ga_{66}In_{20.5}Sn_{13.5}$). The first step of making this pump is to prepare patterned or empty PDMS. All the channels are made by standard soft photolithography. Both top and bottom electrode layers are made by directly pouring PDMS on patterned silicon wafers. In the real fabrication process we found it difficult to make the PDMS membrane exactly as thin as the channel height. So, we combined the top thin membrane layer with fluid channel layer in fabrication process. This combined layer is made by spinning PDMS on a silicon wafer with fluid channel pattern at 1000 RPM, to form a 74 μm thick membrane. With 31 μm high channels, the membrane above fluid channel is 43 μm thick. The bottom thin membrane layer is made in the same way, except an empty silicon wafer is used and the speed is 3000 RPM, resulting in a 16 μm thick membrane. The four layers are then baked on the hot plate to solidify PDMS.

The second step is to remove PDMS and to bond each layer. In this step, we found it hard to remove a thin PDMS membrane from a silicon wafer without damaging it. Our solution is to bond a thick PDMS block on a thin membrane and remove the two layers together. In this case, we first bond the thick top electrode layer to fluid channel layer and remove the two layers together. Then, first two layers are bonded to the bottom thin membrane layer, and finally to the bottom electrode layer. The bonding process used oxygen plasma treatment. It is worth mentioning that the electrode channels of the top and bottom layers should be aligned preciously to guarantee the homogeneity of electric fields in the fluid channel. An align machine (Wenhao, Suzhou, China) was used to do the alignment. There are two aligning platforms in the machine. Two PDMS layers were stuck on these two platforms respectively and made the alignment under a microscope. Then these two platforms were taken off from the machine together with the PDMS layers and put into the plasma cleaner (Yanzhao Technology, Tangshan, China) to make the plasma treatment. Finally, the platforms were taken out quickly and put back to the align machine to make the final bonding of the two PDMS layers.

After finishing the four-layer structure, gallium-based alloy is injected into the electrode channels to form electrodes. Copper lines are used to connect electrode with power source. Package adhesive sealant is used to seal the copper wire and liquid metal, to fasten the connection. Figure 1c shows an optical photograph of the EOF pump. The fabrication process of this pump is simple and low-cost.

2.3. Experiment

The performance of this high flow rate 3-D EOF pump was tested in experiments. The working fluid was deionized (DI) water. Fluorescent particles with 0.52 μm diameter were added into the DI water by 1:10000 to test the flow rate. The fluorescent particles were 1% solid Red Fluorescent Polymer Microspheres from Fluoro-Max^{TM} (Thermo Scientific, Waltham, MA, USA). The excitation maxima of this particle is 542 nm, and the emission maxima is 612 nm. Zeiss Observer.Z1 microscope (Oberkochen, Germany) and X-cite Series 120Q (Excelitas Technologies, Waltham, MA, USA) laser source were used to observe particle movement. In the experiment, we used a large droplet to cover both the inlet and the outlet of the fluid channel. After putting a large droplet on the inlet and the outlet, the pressure-driven flow was balanced quickly in just several seconds. In each experiment, before applying voltage we made sure all the fluorescent particles were stagnant in the microchannel. Thus, pressure-driven flow can be neglected, and the fluid flow we observed was only EOF.

3. Results and Discussion

While measuring electroosmotic flow (EOF) velocity with fluorescent particles, electrophoresis (EPH) velocity needs to be considered. According to Ref. [22], measured velocity can be calculated by following equation:

$$u_{\text{meaure}} = u_{\text{eof}} + u_{\text{eph}} + u_{\text{pressure}} \quad (1)$$

$$u_{\text{eph}} = M_{\text{eph}} \times E \quad (2)$$

where u_{eof} is the flow velocity of EOF, u_{eph} is the flow velocity of EPH, u_{pressure} is velocity of pressure-driven flow, M_{eph} is EPH mobility, and E is electric field strength. In this experiment, pressure-driven flow can be neglected. In order to estimate M_{eph}, an EPH experiment was performed. The same particles with same concentration was used in this electrophoresis experiment. DI water with particles filled a large, round PDMS reservoir (r = 0.8 cm, h = 0.5 cm). Two platinum electrodes were put respectively at each end of the diameter of the reservoir. The diameter of the Pt electrode was 0.5 mm, so the distance between two electrodes was 0.7 cm. A 10 V voltage was added between the two electrodes. Particles moved towards and finally gathered at the positive electrode, proving that the particles are negatively charged. During the experiments, 10 particles moving directly from cathode to anode were chosen to estimate M_{eph}. Experimental results showed that $M_{\text{eph}} = -5.49$ μm cm/V s according to Equation (2).

In order to get the electric field strength in the experiment, an electric field simulation of this pump was performed with commercial software Comsol 5.2 (COMSOL Inc., Stockholm, Sweden). One fluid channel, two pairs of electrodes and a PDMS block are set in the model. All geometric parameters used in the simulation model are the parameters we measured in the real pump, as shown in Figure 4. The dielectric constant of PDMS we used (SYLGARD 184 Silicone Elastomer Kit, Dow Corning, MI, USA) was found on Dow Corning's official website (https://consumer.dow.com/) with a value of 2.72. The dielectric constant of water and liquid metal are set according to well-known values. Thus, the electric field strength in the fluid channel is simulated. For the driving voltage of 10 V, the simulated electric field strength was 0.205 V/cm at the point where we measured flow rate and velocity with fluorescent particles. Then, at 10 V, u_{eph} is calculated to be -6.753×10^{-2} mm/min based on Equation (2). According to the experiment results, u_{meaure} at 10 V is 3.60×10^{-1} mm/min. So, u_{eof} is 4.28×10^{-1} mm/min based on Equation (1). The ratio of EOF velocity and measured velocity is 1.188. This result will be used in the following experiment result calculation.

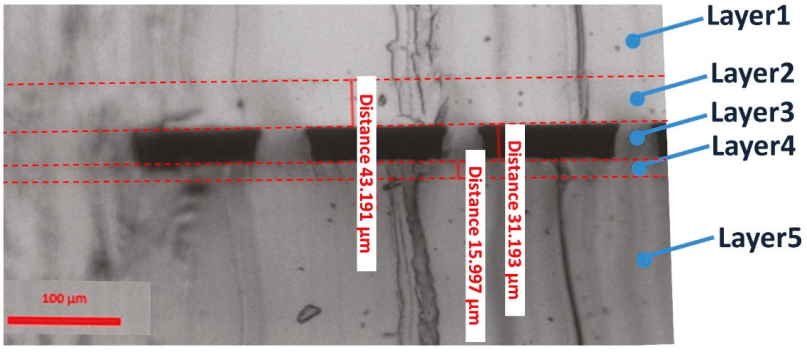

Figure 4. Side view of real pump chip dimensions. Layer 1: top electrode layer (electrode channel not shown here); layer 2: top membrane layer; layer 3: fluid channel layer; layer 4: bottom thin membrane layer; layer 5: bottom electrode layer (electrode channel not shown).

Figure 5 shows the sequential images of fluorescent particle movements of EOF. The applied voltage between electrodes is 10 V in this figure. Figure 5b–d show particle status at different time.

Those particles with the same letters A~E marked in each figure are the same particles at different times. The times in Figure 5b–d are 0 s, 5 s and 10 s, respectively. In the real calculation process, we calculated 15 particles at different voltages with each 5 channels (60 particles in all, 3 particles in every channel), and the average velocity of all these particles are used as the fluid velocity.

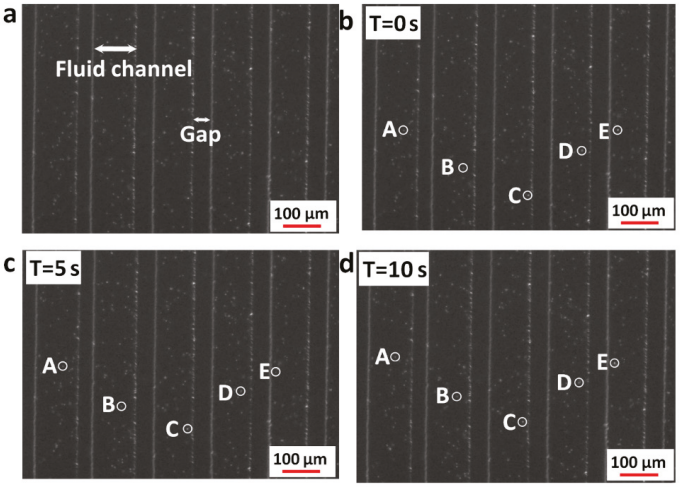

Figure 5. Sequential images of fluorescent particle movements of EOF. (**a**) Image instruction; (**b**) particle status at 0 s; (**c**) particle status at 5 s; (**d**) particle status at 10 s.

Flow rate was then calculated with fluid channel width 116 μm, height 31 μm and channel number 20. Results are shown in Figure 6, and actual channel dimensions are shown in Figure 6. In Figure 6a, the flow rate of 2 V to 80 V is shown, and flow rate from 2 V to 10 V is magnified and shown in Figure 6b. The flow rate is 5.69 nL/min at 2 V, and 248.18 nL/min at 80 V. The lowest driving voltage is 2 V.

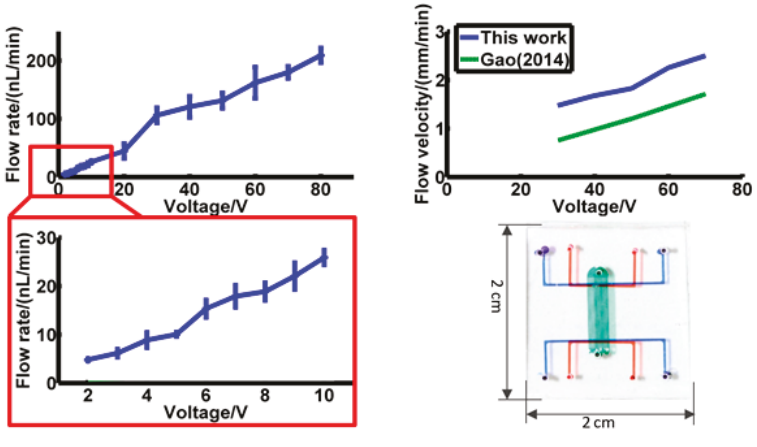

Figure 6. Flow rate at different voltage. (**a**) flow rate from 2 V to 80 V; (**b**) flow rate from 2 V to 10 V; (**c**) comparison of this work with Gao's work [1] with similar dimensions; (**d**) size of this pump.

The results show a linear trend between the flow rate and voltage. The error source might be the choice of particles during calculation. In electroosmotic flow, fluid velocity is higher near the solid

edge, and lower in the middle of the channel. We tried to choose these 3 fluorescent particles in every channel as evenly as possible, however errors might exist.

During the early stage of this experiment, a 30 μm-thick top membrane was tested, and the membrane was too easy to tear while removing the pattern from its base, because of the existence of the fluid channel. So, we chose a 43 μm-thick top membrane instead. Thinner top and bottom membranes might make a higher electric field in the fluid channel with the same voltage, but are hard to make into a successful pump. Also, even two membranes are with different thickness, the homogeneity of the electric field in fluid channels would stay the same.

Placing electrodes on both sides of the fluid channels can increase the electric field strength and uniformity. To verify the merit of this structure, another experiment was performed with only one electrode layer, with the same design parameters and the same data calculation process. Results show that at 10 V, one electrode structure has a fluid velocity of 0.053 mm/min, which is only 1/8 of the velocity of the two electrode-layer structures. Thus, two-layer design makes the pumping more efficient.

Compared with 2-dimentional single channel EOF pumps [1], the flow rate of this pump has apparently increased. Gao previously designed a 2-D structure in 2014 [1]. With similar design parameters and material, the flow velocity of Gao's pump is 1.32 mm/min at 50 V. In this work, this result is 2.18 mm/min. It is certain that, even though the flow velocity of these two pumps are similar, the flow rate of this pump is more than 100 times higher than in Gao's design [1], due to fluid channel dimension and number. What's more, in Gao's design, the pump volume is 0.9 cm^3 (1.5 cm × 3 cm × 2 mm). To get a similar flow rate by parallel connection 100 of that pump, the volume would be 90 cm^3. The size of pump in this work is only 2 cm^3 (2 cm × 2 cm × 0.5 cm), about 1/50 of that size.

The largest advantages of this pump are its high flow rate and low pumping voltage. By making a thin membrane between fluid channels and electrodes, the pumping voltage can be as low as 2 V, pretty low in noncontact electrode EOF pumps. By using parallel fluid channel design, flow rate is significantly increased. Also, this is an expandable structure. For some former EOF pumps [10,13,18], to increase flow rate by doubling fluid channel number, the whole pump volume is also doubled. For this pump, all fluid channels share the same pairs of electrodes, and to expand the fluid channel number from 20 to 40, only a 15% volume increase is needed. In the contact electrode structure, the fabrication process is always complicated, and expensive electrode material, like platinum, is used. In this noncontact design, room temperature liquid metal is cheap, and can be injected into channels to form electrodes, greatly simplifying the fabrication process. Noncontact electrodes also prevent sample contamination problems, joule heat problems, and strong electrophoresis, and prolong the pump's lifespan.

There are still limitations to this pump. Even though the flow rate has been increased over 100 times, it is still not enough. To get a 5 mL/min flow rate, 2000 V voltage is needed. To increase the flow rate, a shorter distance between electrodes on the same layer could be used.

4. Conclusions

In this study, we proposed and tested a new 3-dimentioanl low voltage EOF pump. A five-layer structure is fabricated in this pump, including one fluid channel layer, two electrode channel layers and two thin membranes between them. The fluid channel layer contains 20 parallel fluid channels, lying in the middle of the two electrode layers. The distance between fluid channels and both electrode channels is under 45 μm (43 μm and 16 μm). Room temperature liquid gallium-based allay was used as the electrodes. A fluid flow rate of 248.18 nL/min was achieved at 80 V, and the lowest driving voltage is 2 V. In the future, more work would be done to lower the driving voltage and apply it in biological analysis and drug delivery systems.

Author Contributions: Z.Y. and L.G. conceived, designed the experiments, and contributed reagents/materials; Z.Y. and R.Z. performed the experiments; M.G. and R.Z. helped Z.Y. to fabricate the microfluidic chips. Z.Y., R.Z., M.G., Z.D. and L.G. analyzed the data and wrote the paper.

Funding: This work is financially supported by the National Natural Science Foundation of China (Grant No. 31427801) and Science and Technology Program from State Grid Corporation of China: "Principle, Structural Design and Functional Verification of Multi-parameter Parallel Sensing with Liquid Metals".

Conflicts of Interest: The authors declare no conflict of interest.

References

1. Gao, M.; Gui, L. A handy liquid metal based electroosmotic flow pump. *Lab Chip* **2014**, *11*, 1866–1872. [CrossRef] [PubMed]
2. Mohammad, A.Z.; Shafishuhaza, S. Micromachined shape-memory-alloy microactuators and their application in biomedical devices. *Micromachines* **2015**, *6*, 879–901.
3. Veronica, B.; Jianbo, S. Integrated lateral flow device for flow control with blood separation and biosensing. *Micromachines* **2017**, *8*, 367.
4. Yaxiaer, Y.; Yasunari, K. A method of three-dimensional micro-rotational flow generation for biological applications. *Micromachines* **2016**, *7*, 140.
5. Florian, T.; Frank, G. A new concept of a drug delivery system with improved precision and patient safety features. *Micromachines* **2015**, *6*, 80–95.
6. Du, K.; Liu, W.Y.; Ren, Y.K.; Jiang, T.Y.; Song, J.N.; Wu, Q.; Tao, Y. A high-throughput electrokinetic micromixer via AC field-effect nonlinear electroosmosis control in 3D electrode configurations. *Micromachines* **2018**, *9*, 432. [CrossRef]
7. Wang, X.; Chang, C. Electroosmotic pumps and their applications in microfluidic systems. *Microfluid. Nanofluid.* **2009**, *6*, 145–162.
8. Zeng, S.; Chen, C.H. Fabrication and characterization of electroosmotic micropumps. *Sens. Actuators B Chem.* **2001**, *79*, 107–114.
9. Tripp, J.A.; Svec, F. High-pressure electroosmotic pumps based on porous polymer monoliths. *Sens. Actuators B Chem.* **2004**, *99*, 66–73.
10. Miao, J.Y.; Xu, Z.L. Micropumps based on the enhanced electroosmotic effect of aluminum oxide membranes. *Adv. Mater.* **2007**, *19*, 4234–4237. [CrossRef]
11. Chen, L.; Ma, J. An electroosmotic pump for packed capillary liquid chromatography. *Microchem. J.* **2003**, *75*, 15–21. [CrossRef]
12. Mcknight, T.E.; Culbertson, C.T. Electroosmotically induced hydraulic pumping with integrated electrodes on microfluidic devices. *Anal. Chem.* **2001**, *73*, 4045–4049. [CrossRef] [PubMed]
13. Takamura, Y.; Onoda, H. Low-voltage electroosmosis pump for stand-alone microfluidics devices. *Electrophoresis* **2003**, *24*, 185–192. [CrossRef] [PubMed]
14. Chen, C.H.; Santiago, J.G. A planar electroosmotic micropump. *J. Microelectromech. Syst.* **2003**, *11*, 672–683.
15. Green, N.G.; Ramos, A. Fluid flow induced by nonuniform AC electric fields in electrolytes on microelectrodes. I. Experimental measurements. *Phys. Rev. E* **2000**, *61*, 4011–4018. [CrossRef]
16. Wu, X.; Rajasekaran, P.R.; Martin, C.R. An alternating current electroosmotic pump based on conical nanopore membranes. *Acs Nano* **2016**, *10*, 4637–4643. [CrossRef] [PubMed]
17. Gu, C.; Jia, Z. Miniaturized electroosmotic pump capable of generating pressures of more than 1200 bar. *Anal. Chem.* **2012**, *84*, 9609–9614. [CrossRef] [PubMed]
18. Fu, X.; Mavrogiannis, N. Microfluidic pumping, routing and metering by contactless metal-based electro-osmosis. *Lab Chip* **2015**, *15*, 3600–3608. [CrossRef] [PubMed]
19. Yu, Y.; Wang, Q.; Wang, X.L.; Wu, Y.H.; Liu, J. Liquid metal soft electrode triggered discharge plasma in aqueous solution. *RSC Adv.* **2016**, *6*, 114773–114778. [CrossRef]
20. Yi, L.; Liu, J. Liquid metal biomaterials: A newly emerging area to tackle modern biomedical challenges. *Int. Mater. Rev.* **2017**, *62*, 415–440. [CrossRef]

21. Yu, Y.Z.; Lu, J.R. 3D printing for functional electronics by injection and package of liquid metals into channels of mechanical structures. *Mater. Des.* **2017**, *122*, 80–89.
22. Devasenathipathy, S.; Santiago, J.G. Particle tracing techniques for electrokinetic microchannel flows. *Anal. Chem.* **2002**, *74*, 3704–3713. [CrossRef] [PubMed]

micromachines

MDPI

Article

Direct Numerical Simulation of Seawater Desalination Based on Ion Concentration Polarization

Jie Li [1,*], Dilin Chen [1], Jian Ye [1], Lai Zhang [1], Teng Zhou [2,*] and Yi Zhou [1,*]

[1] School of Energy and Power Engineering, Wuhan University of Technology, Wuhan 430070, China
[2] Mechanical and Electrical Engineering College, Hainan University, Haikou 570228, China
* Correspondence: jieli@whut.edu.cn (J.L.); zhouteng@hainanu.edu.cn (T.Z.); zhouyi@whut.edu.cn (Y.Z.)

Received: 9 August 2019; Accepted: 23 August 2019; Published: 25 August 2019

Abstract: The problem of water shortage needs to be solved urgently. The membrane-embedded microchannel structure based on the ion concentration polarization (ICP) desalination effect is a potential portable desalination device with low energy consumption and high efficiency. The electroosmotic flow in the microchannel of the cation exchange membrane and the desalination effect of the system are numerically analyzed. The results show that when the horizontal electric field intensity is 2 kV/m and the transmembrane voltage is 400 mV, the desalting efficiency reaches 97.3%. When the electric field strength increases to 20 kV/m, the desalination efficiency is reduced by 2%. In terms of fluid motion, under the action of the transmembrane voltage, two reverse eddy currents are formed on the surface of the membrane due to the opposite electric field and pressure difference on both sides of the membrane, forming a pumping effect. The electromotive force in the channel exhibits significant pressure-flow characteristics with a slip boundary at a speed approximately six times that of a non-membrane microchannel.

Keywords: cross-membrane voltage; ion concentration polarization; desalination effect; pump effect; eddy current

1. Introduction

In 1809, Reuss [1] first discovered the electroosmotic flow (EOF) phenomenon in an experiment. In the late 19th century, Helmholt [2] first introduced the concept of the electrical double layer (EDL), which links the electric field, fluid flow, and ion concentration to describe the formation mechanism of the EOF in detail. When the ion concentration in the Debye layer is constant, the fluid velocity of the EOF is linearly related to the applied horizontal electric field. When the applied electric field destroys the equilibrium condition inside the Debye layer, the ion concentration in the layer changes to cause an uneven zeta potential, causing a nonlinear electroosmotic slip near the interface of the micro-nano channel [3]. These complex unbalanced electrokinetic phenomena are important in the field of biomolecules or charged particle separation and enrichment [4–6]. In particular, the development of new micro-nanofluid systems capable of changing the electrolyte concentration in the EDL has once again caused researchers' scientific interest in unbalanced EOF.

When an ion exchange membrane (IEM) can only absorb or pass a specific polar ion, these polar ions (such as cations) are subjected to a tangential electric field to reach the nanochannel (or membrane) and be absorbed. Due to the electric field force and the electrostatic repulsion of the ions themselves, the ions of the opposite polarity are far away from the nanochannel, resulting in a lower concentration of the ion depletion region, which greatly reduces the conductivity. On the other side of the nanochannel, a very high concentration of ions is formed. Therefore, ions diffuse from a high concentration region to a low concentration region near nanochannels, forming an ion concentration polarization (ICP) effect [7,8]. When the vertical electric field is strong, an extended space charge layer (ESC) is produced

between the solid surface and the diffusion layer [9,10]. Under the action of the horizontal electric field, the net charge in the ESC will drive the liquid to flow along the wall, and this flow is similar to the electroosmosis of the first kind (EOF1), formed by the action of a horizontal electric field on the double layer. Therefore, it is called the second kind (EOF2) [11]. However, for the charge of these two electroosmotic flows, the charge of the ESC is at least 10 times that in the electric double layer [12,13]. In recent years, researchers have developed EOF2 on ion exchange membranes or electrode surfaces and developed unstable nonlinear eddy currents in theories [14,15], experiments [16,17], and numerical simulations [18–23]. The phenomena of ICP and the formation mechanism of EOF2 are discussed in detail [24]. EOF2 has also been successfully applied to fluid or particle drives. Mishchuk et al. [25] placed ion exchange microspheres in microchannels and successfully designed the second type of the electroosmotic micropump, which greatly increased the flow rate. Kivanc et al. [26] realized the second kind of the electroosmotic micropump using a porous silicon skeleton structure as a substrate and analyzed the influence of the substrate area and thickness on the flow rate. At the same time, using ICP and EOF2 phenomena, Han's research team [27] used the nanochannels in microchannels to achieve efficient desalination of seawater. Several studies involving space charge models and related applications in ion-exchanged porous membranes have also attracted much attention. Sherwood et al. [28] analyzed a theoretical model of electroosmotic flow considering end effects. Yang et al. [29] developed a multi-component space charge transport model for an IEM using cylindrical pores of variable radius/charge density. Szymczyk et al. [30] also studied the pressure-driven ion transport of nanochannels with an inhomogenrous charge distribution. Moya [31] analyzed the electrochemical impedance of an IEM in two counterion ternary electrolyte solutions. Ahualli et al. [32] studied the equilibrium kinetics of the energy production of ion exchange membranes and battery capacitors. Deng et al. [33] experimentally confirmed that impact electrodialysis as a new method for water desalination and that other electrochemical separation is feasible.

At present, the research on the embedded microchannel system is mainly based on the experimental observation of the tracer particles. However, direct experimental monitoring of critical parameters (such as ion concentration) is still unrealistic, which hampers an accurate understanding of the microchannel system, and the accurate description must rely on numerical simulation. However, the impact that transmembrane voltage and horizontal voltage exert on desalination characteristics and pump efficiency has also not been studied. Based on the ideal ion exchange hypothesis (that is, only one ion is allowed to pass through the membrane surface), this study numerically simulated the dynamic characteristics of the micro-channel electric system embedded with a cation exchange membrane (CEM), and the influence of the horizontal electric field on the desalination effect and pump effect are analyzed. Below, Section 2 gives the system description, governing equations, and boundary conditions. The numerical results are given in Section 3.

2. Methods

2.1. System Setup

Figure 1 shows a schematic of a two-dimensional (2D) model, which is a microchannel embedded with an IEM in the middle of both top and bottom walls. The left boundary was connected to the reservoir, which was filled with NaCl solution. The microchannel walls were negatively charged and the surface charge density was set as σ_-, so the channel wall would adsorb cations and induce an EDL, resulting in more cations than anions in the channel. An externally axial electric field was imposed, inducing an EOF because of the Coulomb force and fluid drag. If the potential (V_L) at the left boundary is higher than that at the right boundary (V_R), the EOF flows from left to right. Therefore, the left and right boundaries were set as the inlet and outlet of the fluid, respectively. The lengths L_m of the IEM ($L_m << L$, the thickness was neglected) were assumed to permit passage of Na^+ only, and the surface potential of the membrane was set as V_m. For convenience of analysis, cross-membrane voltage $V_{cm} = (V_L + V_R)/2 - V_m$ was defined, representing the difference between the potential at

the middle of the channel without the membrane and the potential actually applied on the membrane. Larger V_{cm} generated a more obvious ICP phenomenon.

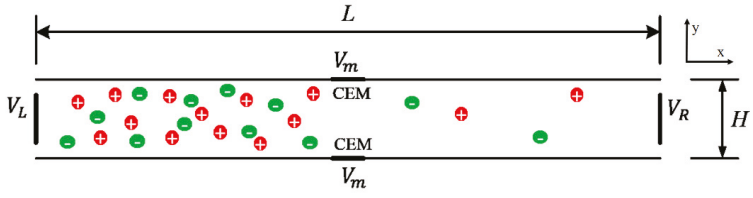

Figure 1. Schematic diagram of the microchannel model embedded with an ion exchange membrane (IEM).

2.2. Governing Equations and Boundary Conditions

In this study, the symmetric electrolyte NaCl solution was chosen. The governing equations of the EOF multi-physics coupling field included the Poisson–Nernst–Planck (PNP) equation and the improved Stokes equation. According to electrodynamics, in the diffusion layer the potential generated by the net charge satisfied the classical electrostatic Poisson equation:

$$-\varepsilon_0\varepsilon_f\nabla^2\phi = \rho_e = F\sum_{i=1}^{n} z_i c_i \tag{1}$$

where ε_0 and ε_f are the absolute permittivity constant of the vacuum and the relative dielectric constant of the fluid, respectively; ϕ is the electric potential within the solution; F is the Faraday constant; c_i and z_i are the ionic concentration and the valence of ions, respectively; and n is the number of ion species. $\sum_{i=1}^{n} Fz_i c_i$ is the net charge density ρ_e, which is the sum of all ions in the fluid.

According to ion transfer theory, ions in solution are affected by an electric field, flow field, and concentration field to form ion migration. Ion flux $\boldsymbol{N_i}$ includes the ion convective flux, diffusion flux, and electromigration flux.

$$\boldsymbol{N_i} = \boldsymbol{u}c_i - D_i\nabla c_i - z_i\frac{D_i}{RT}Fc_i\nabla\phi \tag{2}$$

where $\boldsymbol{u}$ is the fluid velocity, D_i is the diffusivity of the ith ionic species, and R and T are the general gas constant and the absolute temperature of the solution, respectively. In the steady state and lack of fluid flow, no chemical reaction occurs in the solution and the ion flux obeys the simplified Nernst–Planck (NP) equation:

$$\nabla\cdot\boldsymbol{N_i} = \nabla\cdot\left(-D_i\nabla c_i - z_i\frac{D_i}{RT}Fc_i\nabla\phi\right) = 0 \tag{3}$$

The electrical force under an external horizontal electric field

$$\boldsymbol{F} = -\nabla\phi \tag{4}$$

Therefore, according to the principle of conservation of momentum, the movement of fluid is governed by the improved Navier–Stokes (N–S) equation and continuous equation.

$$-\nabla p + \mu\nabla^2\boldsymbol{u} + \boldsymbol{F} = 0 \tag{5}$$

$$\nabla\cdot\boldsymbol{u} = 0 \tag{6}$$

where ρ is the fluid density; p is the pressure; and μ is the fluid dynamic viscosity. The inertial term in the N–S equation is ignored due to a small Reynolds number.

Select the microchannel width H as the feature length, $\mu U_0/H$ as the characteristic pressure, $U_0 = \varepsilon_0\varepsilon_f R^2T^2/(\mu HF^2)$ as the characteristic velocity, the bulk concentration C_0 as the characteristic concentration of the ion, and RT/F as the characteristic potential, and define

$\kappa^{-1} = \lambda_D = \sqrt{\varepsilon_0 \varepsilon_f RT / \sum_{i=1}^{2} F^2 z_i^2 C_{i0}}$ as the Debye length; the surface charge density σ corresponding to $\varepsilon_0 \varepsilon_f RT/(FH)$ is dimensionless, the diffusion coefficient is dimensionless according to $\varepsilon_0 \varepsilon_f R^2 T^2/(\mu F^2)$, and they are used to control the governing equation of the EOF coupling field without simplification. It should be noted that notations with an asterisk are used for the dimensionless parameters.

$$-\nabla^{*2}\phi^* = \frac{(kH)^2}{2}\left(c_1^* z_1 + c_2^* z_2\right) \tag{7}$$

$$\nabla^* \cdot \left(-D_i^* \nabla^* c_i^* - z_i D_i^* c_i^* \nabla^* \phi^* + \boldsymbol{u}^* c_i^*\right) = 0, i = 1, 2 \tag{8}$$

$$-\nabla^* p^* + \nabla^{*2} \boldsymbol{u}^* - \frac{(kH)^2}{2}\left(c_1^* z_1 + c_2^* z_2\right)\nabla^* \phi^* = 0 \tag{9}$$

$$\nabla^* \cdot \boldsymbol{u}^* = 0 \tag{10}$$

The boundary conditions are given as the following.
On the CEM surface:

$$\boldsymbol{u}^* = 0, n \cdot \nabla^* p^* = 0, \Phi^* = V_m \cdot \frac{F}{RT}, c_1^* = 2, n \cdot \nabla^* c_2^* = -z_2 c_2^* \cdot n \cdot \nabla^* \Phi^* \tag{11}$$

On the microchannel wall (non-membrane area):

$$\boldsymbol{u}^* = 0, n \cdot \nabla^* p^* = 0, n \cdot \nabla^* \Phi^* = \sigma_- \cdot \frac{HF}{RT}, n \cdot \nabla^* c_i^* = -z_i c_i^* \cdot n \cdot \nabla^* \Phi^* \tag{12}$$

At the inlet of the microchannel:

$$n \cdot \nabla^* \boldsymbol{u}^* = 0, p^* = 0, \Phi^* = V_L \cdot \frac{F}{RT}, c_i^* = 1 \tag{13}$$

At the outlet of the microchannel:

$$n \cdot \nabla^* \boldsymbol{u}^* = 0, p^* = 0, \Phi^* = 0, n \cdot \nabla^* c_i^* = 0 \tag{14}$$

2.3. Numerical Method and Code Validation

To ensure the accuracy and feasibility of the simulation results, we first compared the numerical prediction with the results of White et al. [34]. In the current simulation, the geometry of the non-membrane channel was set as length L = 1000 nm and height H = 100 nm. The surface charge density of microchannel walls was set as $\sigma_- = -0.001$ C/m^2. The channel was filled with NaCl solution ($z_1 = 1; z_2 = -1$), the initial concentration was set as C_0 = 10 mM, and the externally imposed axial electric field was set at 50 KV/m. Other parameters used in this study were set as μ = 0.001 N·s/m^2, $D_1 = 1.333 \times 10^{-9}$ m^2/s, $D_2 = 2.032 \times 10^{-9}$ m^2/s, $F = 9.649 \times 10^4$ C/mol, R = 8.31 J/(mol·K), T = 300 K, ε_f = 80, $\varepsilon_0 = 8.854 \times 10^{-12}$ F/m. The pressure and normal viscous stress at both ends of the channel were 0, and the wall of the channel was the no-slip boundary condition.

In this calculation, COMSOL v5.3a (COMSOL Inc., Stockholm, Sweden) was used to solve the governing equations with specified boundary conditions. Considering the geometric and physical settings, symmetric boundary conditions were used at the upper boundary of the computing domain, so only the lower half of the channel was modeled. The inaccuracy of the boundary flow field was due to the difference between the zeta potential of the channel wall and the boundary condition of the fixed potential at the junction of the inlet and outlet with the wall. Therefore, in order to reduce the sharp change of the potential at this position, no charge was applied on the two walls 1 μm away from the entrance and outlet, respectively. The calculation domain was divided into quadrilateral meshes, and a finer mesh was adopted near the charged wall, membrane surface, channel inlet, and outlet boundary,

and the total number of grids was 38,500. For steady-state analysis, a multi-frontal massively parallel sparse direct solver (MUMPS) was used to solve the fully coupled PNP-NS equation.

In order to verify the accuracy of the simulation results, we compared the calculated fluid velocity in the microchannel with the analytical solution of White et al. [34]. As shown in Figure 2, it is obvious that the simulation results are in good agreement with the analytical solutions. The abscissa was dimensionless $y^* = y/\lambda_D$ and the vertical axis was dimensionless $u^* = u/U_0$.

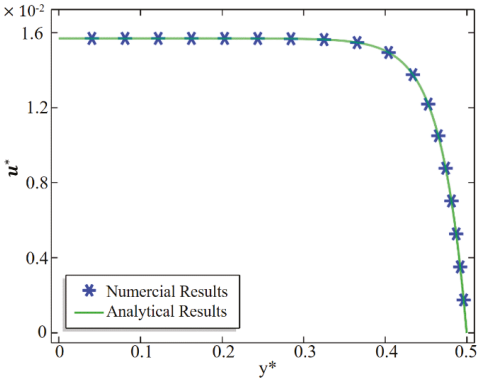

Figure 2. Comparison between the numerical (symbol) and analytical (solid line) results of the axial electroosmotic flow (EOF) velocity in a microchannel.

3. Results and Discussion

3.1. Desalting Effect

Referring to Figure 1, a microchannel of the length L = 100 μm and height H = 10 μm, embedded with membranes of length L_m = 2 μm was considered. The initial concentration of NaCl solution was 1 mM in the channel. In order to study the effect of the applied horizontal electric field strength on the ion transport and fluid flow in the channel, the inlet potential V_L was set as a variable parameter. Due to the strong nonlinearity of the system and the inconsistency of the initial conditions of the concentration and potential near the channel or membrane surface, the inlet potential needs to be slowly increased, with a range of 0.1 V–2 V, which can be assisted by the auxiliary parameter scanning in the solver.

As shown in Figure 3, the concentration distribution of Cl^- in the channel is given when the cross-membrane voltage, V_{cm} = 400 mV, and the potential at the inlet of the channel is 0.1 V, 0.5 V, 1 V and 2 V, respectively. It is observed that the inlet potential increases and the concentration of Cl^- at the upstream of the channel correspondingly increases. When the inlet potential is low (such as V_L = 0.1 V), the average electric field strength applied to the channel level is 1 kV/m, and the velocity of the formed EOF1 is small, so the fluid drives Cl^- to the right. The drag of the motion is small, and the strong electric field formed on the surface of the film due to the ICP phenomenon acts on the electric field force of Cl^- (to the left) to be greater than the drag force for the reverse motion, so Cl^- is concentrated upstream of the channel. However, when the inlet potential is high (such as V_L = 1 V), the average electric field of the channel is significantly enhanced, the fluid drag is greater than the electric field force, and the Cl^- aggregation zone migrates to the right. When V_L = 2 V, the Cl^- aggregation zone is very near the membrane surface area.

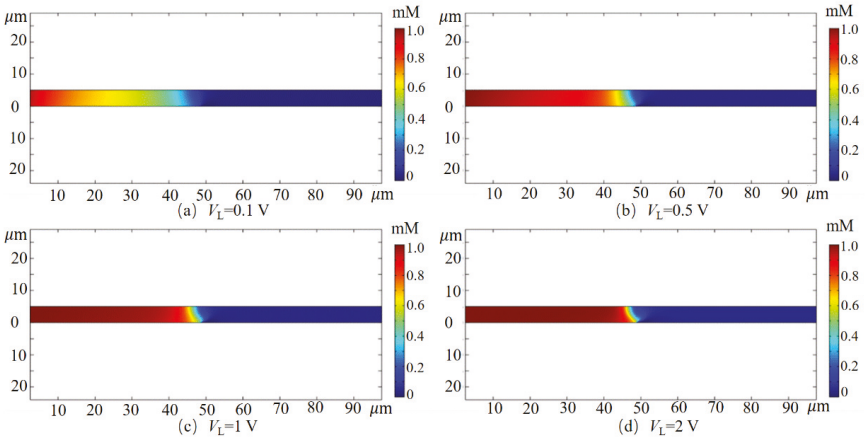

Figure 3. The concentration distribution of Cl^- in the channel at different inlet potentials at V_{cm} = 400 mV.

When the transmembrane voltage is V_{cm} = 0 (corresponding to no membrane in the channel), the cation is adsorbed on the channel wall surface and the membrane surface to form an EDL. Under the action of a horizontal electric field, a typical EOF1 appears in the channel. The concentration of cations in the EDL is greater than the concentration of the anions, while the concentration of ions outside the EDL is substantially constant. Applying a transmembrane voltage across the membrane encourages more cations to be expelled out of the system quickly through the CEM, while the anion remains in the upstream of the channel due to the repulsion of the strong electric field in front of the membrane, forming an ion depletion zone near the membrane. As the solution flows, the ion depletion zone expands downstream, eventually forming a very low concentration of fresh water zone downstream of the channel, and then fresh water flows out of the outlet to achieve desalination.

In order to better calculate the desalination efficiency of the system, Figure 4a shows the variation curve of the Cl^- concentration along the channel symmetry line when the inlet potential is 0.1 V, 0.5 V, 1 V, and 2 V, respectively. As can be seen, with the increase of entrance potential, the Cl^- concentration downstream of the channel does not change much. In order to obtain a specific data change, as shown in Figure 4b, when V_L = 0.1 V, the Cl^- concentration is the smallest (C_2 = 0.02 mM), and the desalting efficiency is as high as 98%. As the inlet potential increases, the Cl^- concentration gradually increases. When V_L = 2 V, the Cl^- concentration is increased to 0.047 mM, and the desalination efficiency is reduced by 2.7 percent.

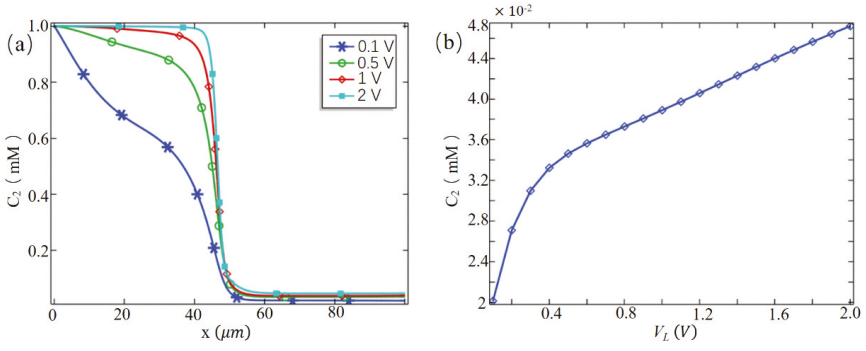

Figure 4. (**a**) The concentration curve of Cl^- along the channel symmetry line at different inlet potentials; (**b**) at the outlet, the average concentration of Cl^- with the inlet potential.

3.2. Pump Effect

Figure 5 shows the velocity streamlines around the channel intima position ($49 \leq x \leq 51$ μm) at V_{cm} = 400 mV with potentials at the channel inlet of 0.2 V, 1 V and 2 V, respectively. When V_L = 0.2 V, the maximum velocity of the fluid in the channel is 5.88×10^{-3} m/s, which is 294 times the EOF1 velocity in the non-membrane microchannel. Nonlinear vortices near the surface of the IEM or at the junction of the microchannel and the nanochannel are unique phenomena of such systems. Kim et al. [35] observed this in the experiment.

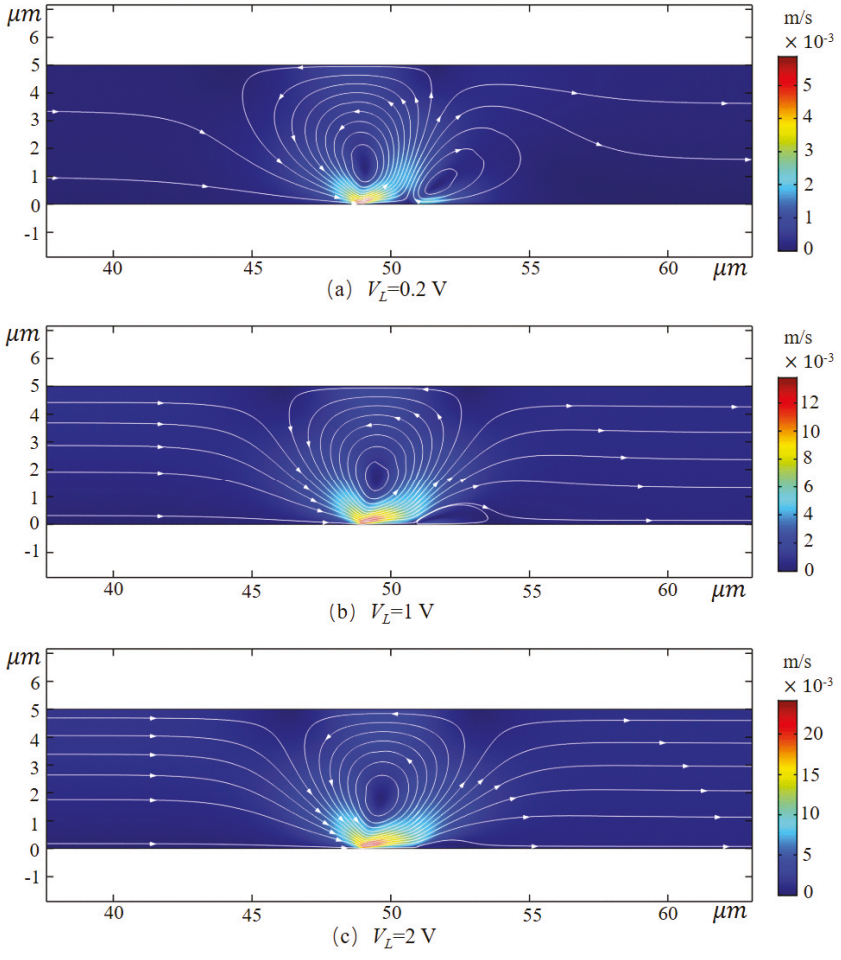

Figure 5. Velocity diagram of the velocity near the endometrial position ($49 \leq x \leq 51$ μm) at different inlet potentials at V_{cm} = 400 mV.

It is worth noting that there are two distinct nonlinear eddy currents near the ion exchange membrane. In order to study the formation mechanism of the eddy current, the variation law of electric field force and pressure difference in the channel was analyzed. Figure 6a shows the horizontal electric field force of the fluid at different positions on the wall along the y-axis when V_{cm} = 400 mV. The fluid at the membrane side and wall junction (x = 48.5 μm, x = 51.5 μm) is subjected to the maximum electric field force, and the range of action is much larger than that of the channel inlet and outlet

(x = 5 μm, x = 95 μm) and the membrane center (x = 50 μm). The direction of the electric field force on the upstream side (x = 48.5 μm) is positive, while that on the downstream side (x = 51.5 μm) is the opposite. The electric field force gradually decreases as it goes further from the wall surface and decreases to the same size as the channel inlet and outlet area at 10 λd from the wall surface. Under the combined action of forces, the pressure in the center of the channel has changed greatly. As shown in Figure 6b, at V_{cm} = 400 mV the pressure tends to change along the direction of the symmetry line of the microchannel. Due to the electrodynamic force, the pressure on the upstream side of the membrane decreased significantly, while on the downstream side of the membrane, the pressure difference on both sides of the membrane reached about 2.4 Pa, which produced a certain pumping effect.

Therefore, the fluid on the upstream side of the membrane moves rapidly to the right due to the electric field force, while the fluid on the downstream side of the membrane moves to the left, while the large pressure difference on both sides of the membrane forces the fluid upstream in the central region of the membrane (x = 50 μm). The direction flows back, thereby creating a vortex that rotates in a counterclockwise direction. Since the reverse electric field near the downstream side wall surface if the membrane is strong, a small eddy current rotating clockwise is formed there. As the horizontal electric field strength increases, the small eddy current gradually decreases or even disappears.

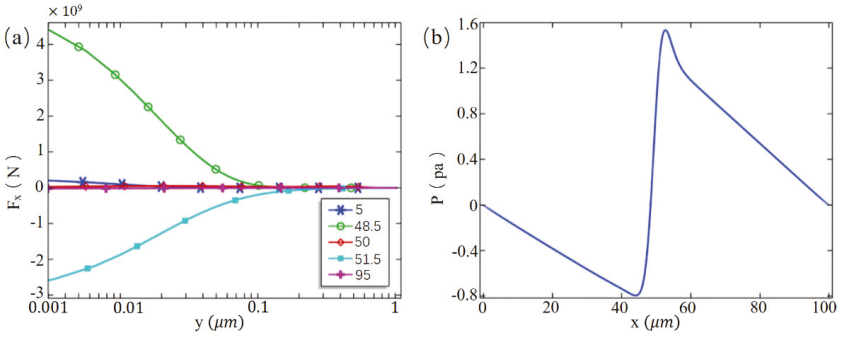

Figure 6. (**a**) Horizontal electric field force in the y direction at different coordinate values of the x-axis (V_{cm} = 400 mV); (**b**) The curve of the pressure along the line of symmetry of the channel.

In order to investigate the flow characteristics of fluids in the embedded microchannel at the different horizontal electric field, Figure 7 shows the tangential velocity distribution of the channel near the outlet (x = 90 μm) at V_{cm} = 0 mV and V_{cm} = 400 mV, respectively. When the cross-membrane voltage is 0, a plunger-like distribution of typical EOF1 is formed downstream of the channel, and when V_{cm} = 400 mV, it shows a significant parabolic distribution with the slip boundary, that is, the downstream of the channel is dominated by the pressure flow. When V_L = 0.1 V, the average velocity of the fluid at the outlet is about 6.38 × 10^{-5} m/s, which is about six times that of the EOF1 in the non-membrane microchannel with the same parameters (about 1 × 10^{-5} m/s). Therefore, the embedded microchannel has a stronger fluid drive capability than the conventional microchannel. When V_L = 2 V, the difference of the average velocity is almost constant, which means that the increase of the applied horizontal electric field has little effect on the pump effect.

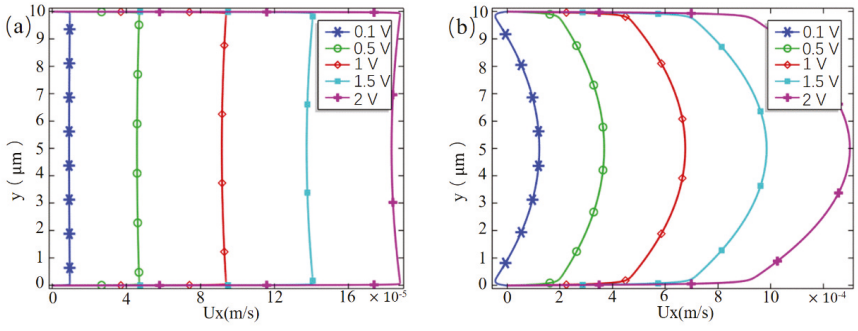

Figure 7. (**a**) Tangential velocity distribution of the cross section of the channel at x = 90 μm when V_{cm} = 0 mV; (**b**) tangential velocity distribution of the cross section of the channel at x = 90 μm when V_{cm} = 400 mV.

4. Conclusions

The fully coupled PNP-NS equation is solved numerically. A microchannel simulation model with a cation exchange membrane embedded on the wall was constructed, and the response characteristics of the embedded microfluidic system under different horizontal electric fields were analyzed. In summary, increasing the horizontal electric field will reduce the desalination effect of the system. At the horizontal electric and transmembrane voltages, the fluid flow in the channel exhibits the dual characteristics of electroosmotic flow and pressure flow. The flow rate is about six times higher than the conventional electroosmotic flow, and the embedded microchannels exhibit a significant pumping effect. The mechanism of the nonlinear eddy current on the surface of the ion exchange membrane is expounded, which provides a theoretical basis for the design of a new electroosmotic pump and desalination device.

Author Contributions: J.L., T.Z., and Y.Z. guided the work and revision of the paper; D.C. and J.Y. realized numerical simulation and paper writing; L.Z. collated the literature and revised the paper.

Funding: This work was funded by the National Natural Science Foundation of China (Grant No. 51806157). This work was calculated by the Supercomputing Center of the Dalian University of Technology.

Conflicts of Interest: The authors declare no conflict of interest.

References

1. Reuss, F.F. Notice sur un nouvel effet de l'electricité galvanique, Mémoire Soc. *Sup. Imp. de Moscou* **1809**, *2*, 327–337.
2. Helmholtz, H. Ueber einige Gesetze der Vertheilung elektrischer Ströme in körperlichen Leitern, mit Anwendung auf die thierisch-elektrischen Versuche. *Annalen der Physik* **1853**, *165*, 353–377. [CrossRef]
3. Stroock, A.D.; Weck, M.; Chiu, D.T.; Huck, W.T.; Kenis, P.J.; Ismagilov, R.F.; Whitesides, G.M. Patterning electro-osmotic flow with patterned surface charge. *Phys. Rev. Lett.* **2000**, *84*, 3314–3317. [CrossRef] [PubMed]
4. Li, Z.R.; Liu, G.R.; Chen, Y.Z.; Wang, J.S.; Bow, H.; Cheng, Y.; Han, J. Continuum transport model of Ogston sieving in patterned nanofilter arrays for separation of rod-like biomolecules. *Electrophoresis* **2008**, *29*, 329–339. [CrossRef] [PubMed]
5. Gascoyne, P.R.; Vykoukal, J. Particle separation by dielectrophoresis. *Electrophoresis* **2002**, *23*, 1973–1983. [CrossRef]
6. Li, Z.R.; Liu, W.; Zhu, Y.D.; Lu, X.H.; Gu, Y.T.; Han, J. Accurate multi-physics numerical analysis of particle preconcentration based on ion concentration polarization. *Int. J. Appl. Mech.* **2017**, *9*, 1750107. [CrossRef]
7. Mishchuk, N.A. Concentration polarization of interface and non-linear electrokinetic phenomena. *Adv. Colloid Interface Sci.* **2010**, *160*, 16–39. [CrossRef]

8. Smyrl, W.H.; Newman, J. Double layer structure at the limiting current. *Trans Faraday Soc.* **1967**, *63*, 207–216. [CrossRef]
9. Krol, J.J.; Wessling, M.; Strathmann, H. Concentration polarization with monopolar ion exchange membranes: current–voltage curves and water dissociation. *J. Membr. Sci.* **1999**, *162*, 145–154. [CrossRef]
10. Rubinstein, I.; Shtilman, L. Voltage against current curves of cation exchange membranes. *J. Chem. Soc. Faraday Trans. Molecul. Chem. Phys.* **1979**, *75*, 231–246. [CrossRef]
11. Dukhin, S.S. Electrokinetic phenomena of the second kind and their applications. *Adv. Colloid. Interface Sci.* **1991**, *35*, 173–196. [CrossRef]
12. Baran, A.A.; Babich, Y.A.; Tarovsky, A.A.; Mischuk, N.A. Superfast electrophoresis of ion-exchanger particles. *ColloidsSurfs* **1992**, *68*, 141–151. [CrossRef]
13. Kim, S.J.; Wang, Y.C.; Lee, J.H.; Jang, H.; Han, J. Concentration polarization and nonlinear electrokinetic flow near a nanofluidic channel. *Phys. Rev. Lett.* **2007**, *99*, 044501. [CrossRef] [PubMed]
14. Kwak, R.; Pham, V.S.; Lim, K.M.; Han, J. Shear flow of an electrically charged fluid by ion concentration polarization: Scaling laws for electroconvective vortices. *Phys. Rev. Lett.* **2013**, *110*, 114501. [CrossRef] [PubMed]
15. Khair, A.S.; Squires, T.M. Fundamental aspects of concentration polarization arising from nonuniform electrokinetic transport. *PhysFluids* **2008**, *20*, 087102. [CrossRef]
16. Yossifon, G.; Chang, H.C. Selection of nonequilibrium overlimiting currents: Universal depletion layer formation dynamics and vortex instability. *Phys. Rev. Lett.* **2008**, *101*, 254501. [CrossRef] [PubMed]
17. Rubinstein, S.M.; Manukyan, G.; Staicu, A.; Rubinstein, I.; Zaltzman, B.; Lammertink, R.G.; Mugele, F.; Wessling, M. Direct observation of a nonequilibrium electro-osmotic instability. *Phys. Rev. Lett.* **2008**, *101*, 236101. [CrossRef] [PubMed]
18. Rubinstein, I.; Maletzki, F. Electroconvection at an electrically inhomogeneous permselective membrane surface. *Faraday Trans.* **1991**, *87*, 2079–2087. [CrossRef]
19. Rubinstein, I.; Zaltzman, B.; Kedem, O. Electric fields in and around ion-exchange membranes1. *J. Membr. Sci.* **1997**, *125*, 17–21. [CrossRef]
20. Druzgalski, C.L.; Andersen, M.B.; Mani, A. Direct numerical simulation of electroconvective instability and hydrodynamic chaos near an ionselective surface. *Phys. Fluids* **2013**, *25*, 110804. [CrossRef]
21. Demekhin, E.A.; Nikitin, N.V.; Shelistov, V.S. Direct numerical simulation of electrokinetic in stability and transition to chaotic motion. *Phys. Fluids* **2013**, *25*, 122001. [CrossRef]
22. Pham, V.S.; Li, Z.; Lim, K.M.; White, J.K.; Han, J. Direct numerical simulation of electroconvective instability and hysteretic current-voltage response of a permselective membrane. *Phys. Rev. E* **2012**, *86*, 046310. [CrossRef] [PubMed]
23. Karatay, E.; Druzgalski, C.L.; Mani, A. Simulation of chaotic electrokinetic transport: Performance of commercial software versus custom-built direct numerical simulation codes. *J. Colloid Interface Sci.* **2015**, *446*, 67–76. [CrossRef] [PubMed]
24. Chang, H.C.; Yossifon, G.; Demekhin, E.A. Nanoscale electrokinetics and microvortices: How microhydrodynamics affects nanofluidic ion flux. *Annu. Rev. Fluid Mech.* **2012**, *44*, 401–426. [CrossRef]
25. Mishchuk, N.A.; Heldal, T.; Volden, T.; Auerswald, J.; Knapp, H. Micropump based on electroosmosis of the second kind. *Electrophoresis* **2009**, *30*, 3499–3506. [CrossRef]
26. Kivanc, F.C.; Litster, S. Pumping with electroosmosis of the second kind in mesoporous skeletons. *Sens. Actuators B-Chem.* **2011**, *151*, 394–401. [CrossRef]
27. Kim, S.J.; Li, L.D.; Han, J. Amplified electrokinetic response by concentration polarization near nanofluidic channel. *Langmuir* **2009**, *25*, 7759–7765. [CrossRef] [PubMed]
28. Sherwood, J.D.; Mao, M.; Ghosal, S. Electroosmosis in a finite cylindrical pore: simple models of end effects. *Langmuir* **2014**, *30*, 9261–9272. [CrossRef]
29. Yang, Y.; Pintauro P, N. Multicomponent space-charge transport model for ion-exchange membranes with variable pore properties. *Ind. Eng. Chem. Res.* **2004**, *43*, 2957–2965. [CrossRef]
30. Szymczyk, A.; Zhu, H.; Balannec, B. Pressure-driven ionic transport through nanochannels with inhomogenous charge distributions. *Langmuir* **2009**, *26*, 1214–1220. [CrossRef]
31. Moya A, A. Electrochemical impedance of ion-exchange membranes in ternary solutions with two counterions. *J. Phys. Chem. C* **2014**, *118*, 2539–2553. [CrossRef]

32. Ahualli, S.; Fernandez, M.M.; Iglesias, G.; Jiménez, M.L.; Liu, F.; Wagterveld, M.; Delgado, A.V. Effect of solution composition on the energy production by capacitive mixing in membrane-electrode assembly. *J. Phys. Chem. C* **2014**, *118*, 15590–15599. [CrossRef] [PubMed]
33. Deng, D.; Dydek, E.V.; Han, J.-H.; Schlumpberger, S.; Mani, A.; Zaltzman, B.; Bazant, M.Z. Overlimiting current and shock electrodialysis in porous media. *Langmuir* **2013**, *29*, 16167–16177. [CrossRef] [PubMed]
34. White, H.S.; Bund, A. Ion current rectification at nanopores in glass membranes. *Langmuir* **2008**, *24*, 2212–2218. [CrossRef] [PubMed]
35. Kim, S.J.; Ko, S.H.; Kang, K.H.; Han, J. Direct seawater desalination by ion concentration polarization. *Nat. Nanotech.* **2010**, *5*, 297–301. [CrossRef] [PubMed]

micromachines

MDPI

Article

An Exact Solution for Power-Law Fluids in a Slit Microchannel with Different Zeta Potentials under Electroosmotic Forces

Du-Soon Choi, Sungchan Yun * and WooSeok Choi *

Department of Mechanical Engineering, Korea National University of Transportation, Chungju, 27469, Korea; dschoi@ut.ac.kr

* Correspondence: syun@ut.ac.kr (S.Y.); w.choi@ut.ac.kr (W.C.); Tel.: +82-043-841-5127 (S.Y.); +82-043-841-5132 (W.C)

Received: 18 September 2018; Accepted: 3 October 2018; Published: 5 October 2018

Abstract: Electroosmotic flow (EOF) is one of the most important techniques in a microfluidic system. Many microfluidic devices are made from a combination of different materials, and thus asymmetric electrochemical boundary conditions should be applied for the reasonable analysis of the EOF. In this study, the EOF of power-law fluids in a slit microchannel with different zeta potentials at the top and bottom walls are studied analytically. The flow is assumed to be steady, fully developed, and unidirectional with no applied pressure. The continuity equation, the Cauchy momentum equation, and the linearized Poisson-Boltzmann equation are solved for the velocity field. The exact solutions of the velocity distribution are obtained in terms of the Appell's first hypergeometric functions. The velocity distributions are investigated and discussed as a function of the fluid behavior index, Debye length, and the difference in the zeta potential between the top and bottom.

Keywords: Electroosmosis; Power-law fluid; Non-Newtonian fluid; Asymmetric zeta potential

1. Introduction

Recently, microfluidic device applications are increasing in the fields of chemical analysis, medical diagnostics, material synthesis, and others [1–3]. In the field of microfluidics, flow control in a microchannel is one of the most important issues. The problem with conventional pressure-driven flow is that as the channel size decreases, the hydraulic area becomes extremely small, resulting in a significant increase in the corresponding hydraulic resistance [4]. Electroosmotic flow (EOF) does not suffer from this problem because it is the motion of fluid that depends on the electric field across a microchannel [5–7].

Many efforts have been made to study electroosmotic flow (EOF) using Newtonian fluids. However, a few microfluidic devices are used more frequently for processing biological fluids such as blood, saliva, DNA, and polymer solutions, which cannot be treated as Newtonian fluids. To analyze the EOF of such fluids, an approach to non-Newtonian constitutive relations should be considered [8–15].

Among the various constitutive laws for non-Newtonian fluids, the power law model is the most popular because of its simplicity and suitability for analyzing a wide range of fluids. Thus, many researchers have conducted EOF studies using the power law model [16–25]. Zhao et al. analyzed the EOF of power-law fluids and obtained the approximate solution of the velocity field in a slit microchannel [16]. In addition, they studied a general Smoluchowski slip velocity over a surface [17] and provided an exact solution of the velocity distribution in a slit microchannel [18]. They also analyzed the EOF of power-law fluids in cylindrical [19] and rectangular [20] microchannels.

Tang et al. conducted a numerical study of the EOF in microchannels of a power-law fluid using the lattice Boltzmann method [21]. Vasu and De analyzed a mathematical model of the EOF of power-law fluids in a rectangular microchannel at high zeta potential [22]. Babaie et al. and Hadigol et al. numerically analyzed the EOF of power-law fluids in a slit microchannel with pressure gradient [23,24]. Ng and Qi developed a simplified analytical model to describe the electrokinetic flow of a power-law fluid for varying wall potentials and channel heights in a slit channel [25].

Most previous studies have been performed on microchannels with the same zeta potential at the top and bottom walls. To our knowledge, however, many microfluidic devices are made with a combination of different materials, such as silicon dioxide (glass) as the base and polydimethylsiloxane as the top and side-walls. In these cases, asymmetric electrochemical boundary conditions should be applied for reasonable analysis of the EOF. Afonso et al. [26] and Choi et al. [27] analyzed the EOF of viscoelastic fluids in a microchannel with asymmetric zeta potential using the simplified Phan–Thien–Tannar model. Qi and Ng investigated the EOF of a power-law fluid through a slit channel where the walls were asymmetrically patterned with periodic variations in shape and zeta potential [28]. Hadigol et al. numerically investigated the characteristics of electroosmotic micromixing of power-law fluid in a slit microchannel with nonuniform zeta potential distributions along the walls of the channel [29]. Jiménez et al. investigated the start-up from rest of the EOF of Maxwell fluids in a rectangular microchannel with asymmetric high zeta potentials at the walls [30]. Peralta et al. conducted theoretical analysis of the start-up of oscillatory EOF in a parallel-plate microchannel under asymmetric zeta potentials [31]. Recently, Choi et al. presented the EOF in a rectangular microchannel using numerical analysis [32] and suggested an approximate solution for the EOF of power-law fluid with asymmetric zeta potential of a planar channel [33].

Obtaining the exact solution not only provides physical insight into the phenomena but can also serve as a benchmark for experimental, numerical, and asymptotic analyses. Zhao and Yang [18] have reported the exact solution for the EOF of a power-law fluid with a symmetric zeta potential. However, it remains a challenge to obtain the exact solution of the EOF in microchannels with asymmetric electrochemical boundary conditions.

In the present study, exact solutions for EOFs of power-law fluids in a slit microchannel with different zeta potentials at the top and bottom walls are presented. In addition, the key parameters affecting the velocity distribution of EOF, including the fluid behavior index, Debye length, and different zeta potentials at the top and bottom walls are analyzed.

2. Mathematical Formulation

Figure 1 shows a two-dimensional EOF in a slit microchannel of height $2H$. The top and bottom walls were charged with zeta potential ψ_t and ψ_b, respectively. An external electric field E_0 was applied to a power-law fluid with a constant density ρ and electric permittivity ϵ.

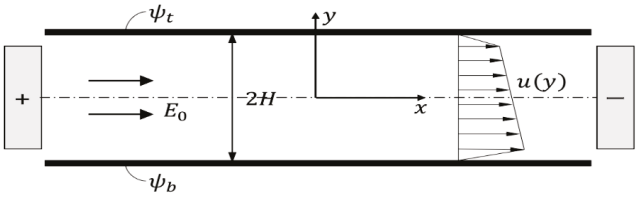

Figure 1. Schematic diagram of electroosmotic flow in a slit microchannel.

The velocity field in the microchannel is governed by the continuity and Cauchy momentum equations given as:

$$\nabla \cdot \mathbf{v} = 0, \tag{1}$$

$$\rho \frac{D\mathbf{v}}{Dt} = -\nabla p + \nabla \cdot \tau + \mathbf{F}, \tag{2}$$

where $\mathbf{v} = (u, v)$ is the velocity vector, p is the pressure, $\boldsymbol{\tau}$ is the stress tensor, and $\mathbf{F} = (F_x, F_y)$ is the body force. The stress tensor can be given by

$$\tau = \mu\left(\nabla\mathbf{v} + \nabla\mathbf{v}^T\right), \tag{3}$$

where μ is the effective viscosity.

For a steady, fully developed, unidirectional flow with no applied pressure and negligible gravitational force, the body force acts only along the x-direction and the Cauchy momentum equation in Equation (2) can be simplified as:

$$\frac{\mathrm{d}}{\mathrm{d}y}\left(\mu\frac{\mathrm{d}u}{\mathrm{d}y}\right) + F_x = 0. \tag{4}$$

The effective viscosity of the power-law fluid can be expressed as:

$$\mu = m\left|\frac{\mathrm{d}u}{\mathrm{d}y}\right|^{n-1}, \tag{5}$$

where m is the flow consistency index, and n is the flow behavior index.

The body force along the x-direction is given by:

$$F_x = \rho_e E_0. \tag{6}$$

The net charge density ρ_e can be obtained by the Poisson equation, which takes the form of:

$$\varepsilon\frac{\mathrm{d}^2\psi}{\mathrm{d}y^2} = -\rho_e. \tag{7}$$

With the assumption of Boltzmann distribution and small zeta potentials, the electrical potential profile in the electrical double layer (EDL) is governed by the linearized Poisson–Boltzmann equation expressed by:

$$\frac{\mathrm{d}^2\psi}{\mathrm{d}y^2} = \kappa^2\psi, \tag{8}$$

which is subject to the following boundary conditions:

$$\psi\big|_{y=H} = \psi_t, \psi\big|_{y=-H} = \psi_b. \tag{9}$$

κ^{-1} is called the Debye length and is defined as $\kappa^{-1} = (\varepsilon k_\mathrm{B} T/2e^2z^2n_\infty)^{1/2}$, where n_∞ and z are the bulk number concentration and the valence of ions, respectively, e is the fundamental charge, k_B is the Boltzmann constant, and T is the absolute temperature.

The solution for the electrical potential distribution is of the form:

$$\psi(y) = \frac{\psi_t + \psi_b}{2}\cdot\frac{\cosh(\kappa y)}{\cosh(\kappa H)} + \frac{\psi_t - \psi_b}{2}\cdot\frac{\sinh(\kappa y)}{\sinh(\kappa H)}. \tag{10}$$

Then, the net charge density ρ_e can be expressed as a function of the EDL potential

$$\rho_e(y) = -\kappa^2\varepsilon\psi(y). \tag{11}$$

With all the aforementioned considerations, the Cauchy momentum equation in Equation (4) is expressed as:

$$\frac{\mathrm{d}}{\mathrm{d}y}\left[m\left|\frac{\mathrm{d}u}{\mathrm{d}y}\right|^{n-1}\frac{\mathrm{d}u}{\mathrm{d}y}\right] - \kappa^2\varepsilon E_0\psi(y) = 0. \tag{12}$$

This equation is constrained by the following boundary conditions (no-slip conditions)

$$u\big|_{y=-H} = 0, u\big|_{y=H} = 0. \tag{13}$$

Substituting Equation (10) into Equation (12) yields:

$$\begin{cases} \dfrac{\mathrm{d}}{\mathrm{d}y}\left[\left(\dfrac{\mathrm{d}u}{\mathrm{d}y}\right)^n\right] = \dfrac{\kappa^2\varepsilon E_0}{m}\left(\dfrac{\psi_t+\psi_b}{2}\cdot\dfrac{\cosh(\kappa y)}{\cosh(\kappa H)} + \dfrac{\psi_t-\psi_b}{2}\cdot\dfrac{\sinh(\kappa y)}{\sinh(\kappa H)}\right), if\ \dfrac{\mathrm{d}u}{\mathrm{d}y} \geq 0, & \text{(14a)} \\ \dfrac{\mathrm{d}}{\mathrm{d}y}\left[\left(-\dfrac{\mathrm{d}u}{\mathrm{d}y}\right)^n\right] = -\dfrac{\kappa^2\varepsilon E_0}{m}\left(\dfrac{\psi_t+\psi_b}{2}\cdot\dfrac{\cosh(\kappa y)}{\cosh(\kappa H)} + \dfrac{\psi_t-\psi_b}{2}\cdot\dfrac{\sinh(\kappa y)}{\sinh(\kappa H)}\right), if\ \dfrac{\mathrm{d}u}{\mathrm{d}y} < 0. & \text{(14b)} \end{cases}$$

Since most of the materials that make up the microchannels have negative zeta potential [34,35], the wall zeta potentials are assumed to be negative in the present study; thus, the flow occurs in the $+x$-direction (if $E_0 > 0$). Let y_c be the point where $\left.\frac{\mathrm{d}u}{\mathrm{d}y}\right|_{y=y_c} = 0$, $(-H \leq y_c \leq H)$, then the velocity gradient is positive $\left(\frac{\mathrm{d}u}{\mathrm{d}y} \geq 0\right)$ in the interval $-H \leq y \leq y_c$, and negative $\left(\frac{\mathrm{d}u}{\mathrm{d}y} < 0\right)$ in the interval $y_c \leq y \leq H$.

Integrating Equation (14) with y leads to:

$$\frac{\mathrm{d}u}{\mathrm{d}y} = \begin{cases} \left(-\dfrac{\kappa\varepsilon E_0\psi_m}{m}\right)^{\frac{1}{n}}\left\{-\dfrac{\sinh(\kappa y)}{\cosh(\kappa H)} - R\cdot\dfrac{\cosh(\kappa y)}{\sinh(\kappa H)} + C^+\right\}^{\frac{1}{n}}, \text{ if } -H \leq y \leq y_c, & \text{(15a)} \\ -\left(-\dfrac{\kappa\varepsilon E_0\psi_m}{m}\right)^{\frac{1}{n}}\left\{-\left(-\dfrac{\sinh(\kappa y)}{\cosh(\kappa H)} - R\cdot\dfrac{\cosh(\kappa y)}{\sinh(\kappa H)} + C^-\right)\right\}^{\frac{1}{n}}, \text{ if } y_c < y \leq H, & \text{(15b)} \end{cases}$$

where ψ_m and R are the average zeta potential and the dimensionless zeta potential difference between the top and bottom walls, respectively, which are defined by:

$$\psi_m \equiv \frac{\psi_t+\psi_b}{2}, \tag{16}$$

$$R \equiv \frac{\psi_t-\psi_b}{\psi_t+\psi_b}, \tag{17}$$

and C^+ and C^- are integral constants.

Both Equations (15a) and (15b) should be zero at $y = y_c$. Therefore,

$$C^+ = C^- = \frac{\sinh(\kappa y_c)}{\cosh(\kappa H)} + R\cdot\frac{\cosh(\kappa y_c)}{\sinh(\kappa H)} \equiv C. \tag{18}$$

Integrating Equation (15) with the corresponding boundary condition in Equation (13) leads to the velocity distribution:

$$u(y) = \begin{cases} \left(-\dfrac{\kappa\varepsilon E_0\psi_m}{m}\right)^{\frac{1}{n}}\displaystyle\int_{-H}^{y}\left\{I(y')+C\right\}^{\frac{1}{n}}\mathrm{d}y', \text{ if } -H \leq y \leq y_c, & \text{(19a)} \\ -\left(-\dfrac{\kappa\varepsilon E_0\psi_m}{m}\right)^{\frac{1}{n}}\displaystyle\int_{H}^{y}\left\{-I(y')-C\right\}^{\frac{1}{n}}\mathrm{d}y', \text{ if } y_c < y \leq H, & \text{(19b)} \end{cases}$$

where

$$I(y) \equiv -\frac{\sinh(\kappa y)}{\cosh(\kappa H)} - R\cdot\frac{\cosh(\kappa y)}{\sinh(\kappa H)}, \tag{20}$$

By integrating Equation (19), the velocity distribution can be obtained as:

$$u(y) = \begin{cases} u_s\left[V^+(y) - V^+(-H)\right], \text{ if } -H \le y \le y_c, & \text{(21a)} \\ u_s\left[-V^-(y) + V^-(H)\right], \text{ if } y_c < y \le H, & \text{(21b)} \end{cases}$$

where u_s denotes the generalized Smoluchowski velocity for power-law fluids by employing the average zeta potential ψ_m at the top and bottom walls on the basis of the work of Zhao et al. [16], which is expressed as:

$$u_s = n\kappa^{\frac{1}{n}-1}\left(-\frac{\varepsilon E_0 \psi_m}{m}\right)^{\frac{1}{n}}, \tag{22}$$

and

$$V^+(y) \equiv -\frac{1}{(n+1)\sqrt{C^2+w^2}}\left[I(y)+C\right]^{\frac{n+1}{n}} F_1\left(1+\tfrac{1}{n};\ \tfrac{1}{2},\ \tfrac{1}{2};\ 2+\tfrac{1}{n};\ \tfrac{I(y)+C}{C+iw}, \tfrac{I(y)+C}{C-iw}\right), \tag{23a}$$

$$V^-(y) \equiv \frac{1}{(n+1)\sqrt{C^2+w^2}}\left[-I(y)-C\right]^{\frac{n+1}{n}} F_1\left(1+\tfrac{1}{n};\ \tfrac{1}{2},\ \tfrac{1}{2};\ 2+\tfrac{1}{n};\ \tfrac{I(y)+C}{C+iw}, \tfrac{I(y)+C}{C-iw}\right). \tag{23b}$$

$$y_c = \frac{1}{\kappa}\ln\left(\frac{C+\sqrt{C^2+w^2}}{\frac{R}{\sinh(\kappa H)}+\frac{1}{\cosh(\kappa H)}}\right). \tag{24}$$

$$w = \sqrt{\frac{1}{\cosh^2(\kappa H)} - \frac{R^2}{\sinh^2(\kappa H)}}. \tag{25}$$

The integral constant C can be obtained from the following equation:

$$J(C) = 0, \tag{26}$$

where $J(x)$ are defined by:

$$\begin{aligned} J(x) = &\left[I(-H)+x\right]^{\frac{n+1}{n}} F_1\left(1+\tfrac{1}{n};\ \tfrac{1}{2},\ \tfrac{1}{2};\ 2+\tfrac{1}{n};\ \tfrac{I(-H)+x}{x+iw}, \tfrac{I(-H)+x}{x-iw}\right) \\ &-\left[-I(H)-x\right]^{\frac{n+1}{n}} F_1\left(1+\tfrac{1}{n};\ \tfrac{1}{2},\ \tfrac{1}{2};\ 2+\tfrac{1}{n};\ \tfrac{I(H)+x}{x+iw}, \tfrac{I(H)+x}{x-iw}\right). \end{aligned} \tag{27}$$

The details of the mathematical derivations are described in Appendix A. It is a challenge to obtain the explicit form for the integral constant C. Thus, in this study, a numerical method was used for evaluating C.

$F_1(a; b_1, b_2; c; x, y)$ in Equation (23) is the Appell's first hypergeometric function [36], which can be represented as a one-dimensional integral form [37]:

$$\begin{aligned} F_1\left(1+\tfrac{1}{n};\ \tfrac{1}{2},\ \tfrac{1}{2};\ 2+\tfrac{1}{n};\ \tfrac{\gamma}{\alpha+i\beta}, \tfrac{\gamma}{\alpha-i\beta}\right) &= \frac{\Gamma\left(2+\frac{1}{n}\right)}{\Gamma\left(1+\frac{1}{n}\right)}\int_0^1 \frac{t^{\frac{1}{n}}}{\sqrt{1-\frac{\gamma t}{\alpha-i\beta}}\sqrt{1-\frac{\gamma t}{\alpha+i\beta}}}\mathrm{d}t \\ &= \frac{n+1}{n}\int_0^1 \frac{t^{\frac{1}{n}}}{\sqrt{\frac{\gamma^2 t^2 - 2\alpha\gamma t + (\alpha^2+\beta^2)}{\alpha^2+\beta^2}}}\mathrm{d}t, \end{aligned} \tag{28}$$

where α, β, and γ are real values, and $\Gamma(z)$ is a gamma function. It is evident from Equation (28) that, although the Appell's first hypergeometric function in Equation (23) has complex arguments, it always has a real value.

Alternatively, Equation (21) can be expressed in the single form using Equation (15) as follows:

$$u(y) = V(y) - V(-H), \tag{29}$$

where

$$V(y) \equiv -\frac{1}{\kappa}\frac{n}{n+1}\frac{1}{\sqrt{C^2+w^2}}\left(\frac{\mathrm{d}u}{\mathrm{d}y}\right)\left[I(y)+C\right]F_1\left(1+\tfrac{1}{n};\ \tfrac{1}{2},\ \tfrac{1}{2};\ 2+\tfrac{1}{n};\ \tfrac{I(y)+C}{C+iw}, \tfrac{I(y)+C}{C-iw}\right). \tag{30}$$

Equation (21) is applicable to the EOF of power-law fluids with arbitrary zeta potentials at the top and bottom walls. If the top and bottom walls have the same zeta potential, then the velocity distribution is expressed as follows:

$$u(y) = u_s\left[V_{symm}(H) - V_{symm}(y)\right], \tag{31}$$

where

$$V_{symm}(y) \equiv \frac{(-1)^{\frac{n-1}{2n}}}{n}\frac{\cosh(\kappa y)}{\cosh^{\frac{1}{n}}(\kappa H)}\,{}_2F_1\left(\frac{1}{2},\ \frac{n-1}{2n};\ \frac{3}{2};\ \cosh^2(\kappa y)\right) \tag{32}$$

which is identical to the result of Zhao and Yang [18] on the EOF of power-law fluid with a symmetrical zeta potential. The detailed derivations are described in Appendix B.

3. Results and Discussions

The key parameters that affect velocity distribution are the fluid behavior index n, electrokinetic parameter κH, and dimensionless zeta potential difference $R = (\psi_t - \psi_b)/(\psi_t + \psi_b)$ between ψ_t and ψ_b. In this section, the effects of these parameters on velocity distribution are investigated.

Figure 2 shows the dimensionless velocity (u/u_s) distributions from Equation (21) for different values of fluid behavior index n at a fixed κH of 15. Figure 2a represents the velocity distributions with same zeta potentials ($R = 0$) at the bottom and top, while Figure 2b indicates those of asymmetric zeta potentials with R of 0.2 ($\psi_t/\psi_b = 1.5$). In both cases of symmetric and asymmetric zeta potentials, as the fluid behavior index n decreases, the velocity gradient near the wall increases, and the plug-like characteristics of velocity distribution are enhanced. This is because the fluid with smaller fluid behavior index is less viscous, and the velocity can easily change from zero at the wall to the Smoluchowski velocity at the core region.

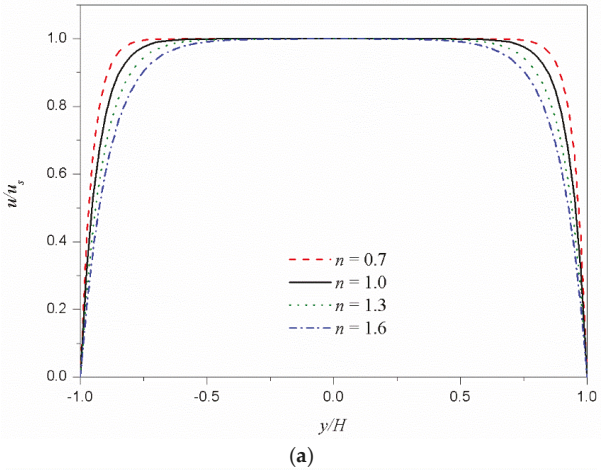

(**a**)

Figure 2. *Cont.*

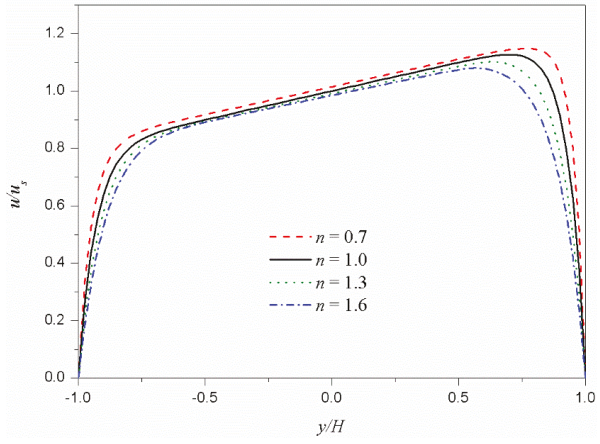

(**b**)

Figure 2. Dimensionless velocity distributions u/u_s for different values of the fluid behavior index n under $\kappa H = 15$. (**a**) Symmetric zeta potentials ($\psi_t/\psi_b = 1$). (**b**) Asymmetric zeta potentials ($\psi_t/\psi_b = 1.5$).

Figure 3 shows the dimensionless velocity (u/u_s) distributions for different values of κH. Figure 3a shows the velocity distributions of the shear thinning fluid ($n = 0.8$) and Figure 3b shows those of the shear thickening fluid ($n = 1.2$). In both cases, as κH increases, the velocity distribution changes from parabolic type to plug-like type. The increase of κH means a decrease in Debye length. In other words, the EDL thickness, on which the electrostatic body force is applied, decreases and the velocity distribution changes to a plug-like type.

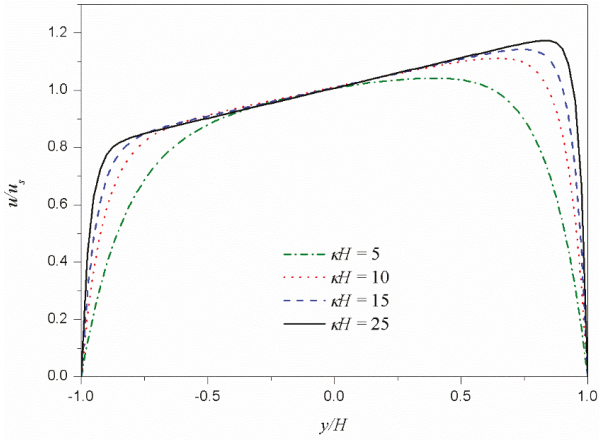

(**a**)

Figure 3. *Cont.*

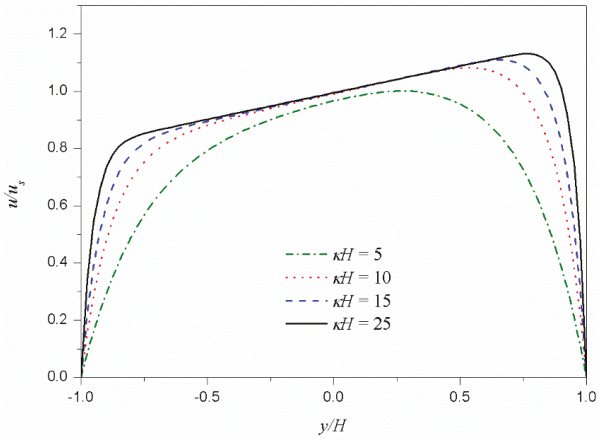

(**b**)

Figure 3. Dimensionless velocity distributions u/u_s for different values of κH under $\psi_t/\psi_b = 1.5$. (**a**) Shear thinning fluid ($n = 0.8$). (**b**) Shear thickening fluid ($n = 1.2$).

Figure 4 shows the dimensionless velocity (u/u_s) distributions according to the dimensionless zeta potential difference R at the bottom and top for the shear thinning fluid (Figure 4a) and shear thickening fluid (Figure 4b). For comparison, the symmetric case ($R = 0$) is also included in the figure. The velocity distributions near the top and bottom walls develop from zero (on the wall) to close to the generalized Smoluchowski velocity determined by the corresponding zeta potentials; in the core region, these two velocity distributions near the walls are almost linearly connected. Therefore, as the difference in zeta potential between the top and bottom walls increases, the velocity gradient in the core region increases. The velocity gradient in the core region decreases and increases the viscosity of the shear thinning fluid and shear thickening fluid, respectively. As a result, as the dimensionless zeta potential difference R increases, the velocity at the center ($y/H = 0$) increases for shear thinning fluids and decreases for shear thickening fluids.

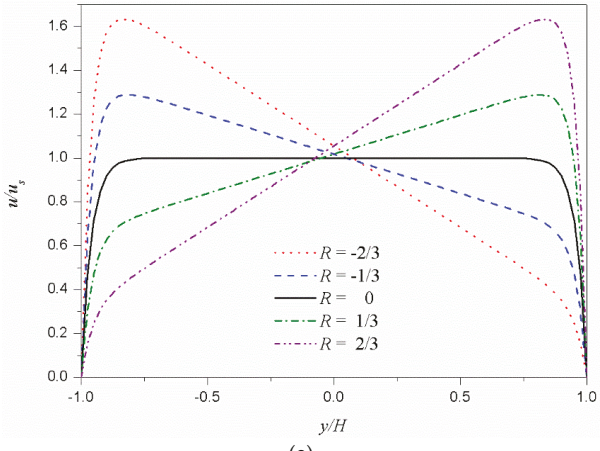

(**a**)

Figure 4. *Cont.*

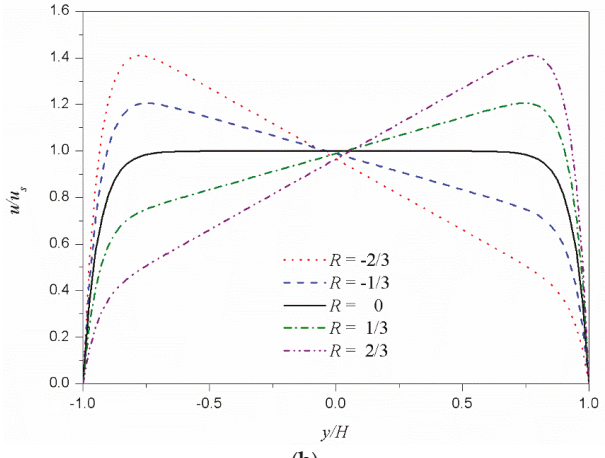

(**b**)

Figure 4. Dimensionless velocity distributions u/u_s as a function of the dimensionless zeta potential difference R. The values $-2/3$, $-1/3$, 0, 1/3, and 2/3 of R, correspond to 0.2, 0.5, 1.0, 2.0, and 5.0 of the zeta potential ratio (ψ_t/ψ_b), respectively. (**a**) Shear thinning fluid (n = 0.8). (**b**) Shear thickening fluid (n = 1.2).

4. Conclusions

In this study, the exact solutions are proposed for fully developed two-dimensional steady unidirectional EOFs of power-law fluids with different zeta potentials at the top and bottom walls. The exact solutions are expressed in terms of Appell's first hypergeometric functions. The effects of parameters such as the fluid behavior index n, electrokinetic parameter κH, and zeta potential ψ_t and ψ_b on the velocity distribution are investigated.

Author Contributions: All authors formulated the mathematical solution and discussed the results. D.-S.C. wrote the original manuscript. S.Y. and W.S.C. reviewed and edited the manuscript. All authors read and approved the final manuscript.

Acknowledgments: This work was supported by the National Research Foundation of Korea (NRF) grant funded by the Korea government (MSIP; Ministry of Science, ICT & Future Planning) (NRF-2017R1C1B5017472 and NRF-2017R1C1B5017734).

Conflicts of Interest: The authors declare no conflict of interest.

Appendix A

The general integral formula for Equation (19) is

$$\int (a\sinh(x)+b\cosh(x)+c)^n \mathrm{d}x = \frac{1}{a(n+1)\sqrt{1-\frac{b^2}{a^2}}}\operatorname{sech}\left(\tanh^{-1}\left(\frac{b}{a}\right)+x\right)\cdot$$
$$\sqrt{\frac{a\sqrt{1-\frac{b^2}{a^2}}-i\,a\sinh(x)-i\,b\cosh(x)}{a\sqrt{1-\frac{b^2}{a^2}}+i\,c}}\sqrt{\frac{a\sqrt{1-\frac{b^2}{a^2}}+i\,a\sinh(x)-i\,b\cosh(x)}{a\sqrt{1-\frac{b^2}{a^2}}-i\,c}}\cdot(a\sinh(x)+b\cosh(x)+c)^{n+1}\cdot \quad \text{(A1)}$$
$$F_1\left(1+n;\ \tfrac{1}{2},\ \tfrac{1}{2};\ 2+n;\ \frac{i(a\sinh(x)+b\cosh(x)+c)}{a\sqrt{1-\frac{b^2}{a^2}}-i\,c},\ \frac{i(a\sinh(x)+b\cosh(x)+c)}{a\sqrt{1-\frac{b^2}{a^2}}+i\,c}\right)+const.$$

Using Equation (A1), the primitive function of $\{I(y)+C\}^{\frac{1}{n}}$ in Equation (19) can be evaluated as

$$\int\{I(y)+C\}^{\frac{1}{n}}\mathrm{d}y = \frac{1}{\kappa}\frac{n}{n+1}\frac{1}{\sqrt{C^2+w^2}}\frac{|\psi(y)|}{\psi(y)}[I(y)+C]^{\frac{n+1}{n}}\cdot F_1\left(1+\frac{1}{n};\ \frac{1}{2},\ \frac{1}{2};\ 2+\frac{1}{n};\ \frac{I(y)+C}{C+iw},\frac{I(y)+C}{C-iw}\right)+const. \quad \text{(A2)}$$

where $\psi(y)$, $I(y)$ and w are defined in Equations (10), (20), and (25), respectively. The term $\frac{|\psi(y)|}{\psi(y)}$ means the sign of the electrical potential. Since the wall zeta potentials are assumed to be negative (ψ_t, ψ_b < 0), $\psi(y)$ always has a negative value; therefore, the term $\frac{|\psi(y)|}{\psi(y)}$ is -1. With all the aforementioned considerations, the velocity distribution is obtained as Equation (21).

At point $y = y_c$, the two equations according to the interval in Equation (21) should have the same value.

$$u_s\left[V^+(y_c)-V^+(-H)\right] = u_s\left[-V^-(y_c)+V^-(H)\right]. \quad \text{(A3)}$$

Since $I(y_c)+C=0$ by Equation (18), $V^+(y_c)=V^-(y_c)=0$.

Therefore, the integral constant C can be obtained from the following equation

$$V^+(-H)+V^-(H)=0 \quad \text{(A4)}$$

which is simplified as Equation (27).

Appendix B

For a symmetrical zeta potential, the R in Equation (17) is zero and the integral constant C is also zero because $\frac{\mathrm{d}u}{\mathrm{d}y}\Big|_{y=0}=0$. Owing to the symmetry, the velocity distribution can be considered only in the interval $0\le y\le H$. Then, Equation (23b) becomes

$$\begin{aligned} V^-(y) &= \frac{1}{n+1}cosh(\kappa H)\left[\frac{\sinh(\kappa y)}{\cosh(\kappa H)}\right]^{\frac{n+1}{n}}F_1\left(1+\frac{1}{n};\ \frac{1}{2},\ \frac{1}{2};\ 2+\frac{1}{n};\ i\sinh(\kappa y),-i\sinh(\kappa y)\right) \\ &= \frac{1}{n+1}sinh(\kappa y)\left[\frac{\sinh(\kappa y)}{\cosh(\kappa H)}\right]^{\frac{1}{n}}{}_2F_1\left(\frac{1}{2},\frac{1}{2n}+\frac{1}{2};\ ,\ \frac{1}{2n}+\frac{3}{2};\ -\sin\mathrm{h}^2(\kappa y)\right) \end{aligned}, \quad \text{(A5)}$$

where Appell's first hypergeometric function is reduced to the hypergeometric function ${}_2F_1(a_1, a_2; b; y)$.

Applying Euler's hypergeometric transformations [38,39] to the hypergeometric function in Equation (B1) gives

$$V^-(y)=\frac{(-1)^{\frac{n-1}{2n}}}{n}\frac{\cosh(\kappa y)}{\cosh^{\frac{1}{n}}(\kappa H)}{}_2F_1\left(\frac{1}{2},\frac{n-1}{2n};\frac{3}{2};\cosh^2(\kappa y)\right)+\frac{\sqrt{\pi}}{2n}\frac{\Gamma\left(\frac{n+1}{2n}\right)}{\Gamma\left(\frac{2n+1}{2n}\right)}\frac{(-1)^{\frac{n-1}{2n}}}{\cos\mathrm{h}^{\frac{1}{n}}(\kappa H)}. \quad \text{(A6)}$$

Then the velocity distribution can be obtained as

$$u(y)=u_s\left[-V^-(y)+V^-(H)\right]=u_s\left[V_{symm}(H)-V_{symm}(y)\right]. \quad \text{(A7)}$$

where $V_{symm}(y)$ is expressed in Equation (32).

References

1. Squires, T.M.; Quake, S.R. Microfluidics: Fluid physics at the nanoliter scale. *Rev. Mod. Phys.* **2005**, *77*, 977–1026. [CrossRef]
2. Sackmann, E.K.; Fulton, A.L.; Beebe, D.J. The present and future role of microfluidics in biomedical research. *Nature* **2014**, *507*, 181–189. [CrossRef] [PubMed]
3. Gravesen, P.; Branebjerg, J.; Jensen, O.S. Microfluidics-a review. *J. Micromech. Microeng.* **1993**, *3*, 168. [CrossRef]
4. Akers, A.; Gassman, M.; Smith, R. *Hydraulic Power System Analysis*; CRC Press: Boca Raton, FL, USA, 2006; ISBN 978-0-8247-9956-4.

5. Lyklema, J. *Fundamentals of Interface and Colloid Science: Solid-Liquid Interfaces*, 1st ed.; Academic Press: London, UK, 1995; ISBN 978-0-12-460524-4.
6. Hunter, R.J. *Introduction to Modern Colloid Science*, 1st ed.; Oxford University Press: Oxford, NY, USA, 1994; ISBN 978-0-19-855386-1.
7. Li, D. *Electrokinetics in Microfluidics*; Academic Press: Cambridge, MA, USA, 2004; ISBN 978-0-08-053074-1.
8. Das, S.; Chakraborty, S. Analytical solutions for velocity, temperature and concentration distribution in electroosmotic microchannel flows of a non-Newtonian bio-fluid. *Anal. Chim. Acta* **2006**, *559*, 15–24. [CrossRef]
9. Devarakonda, S.B.; Han, J.; Ahn, C.H.; Banerjee, R.K. Bioparticle separation in non-Newtonian fluid using pulsed flow in micro-channels. *Microfluid. Nanofluid.* **2007**, *3*, 391–401. [CrossRef]
10. Kolodner, P. Oscillatory convection in viscoelastic DNA suspensions. *J. Non-Newton. Fluid Mech.* **1998**, *75*, 167–192. [CrossRef]
11. Owens, R.G. A new microstructure-based constitutive model for human blood. *J. Non-Newton. Fluid Mech.* **2006**, *140*, 57–70. [CrossRef]
12. Yilmaz, F.; Gundogdu, M.Y. A critical review on blood flow in large arteries; relevance to blood rheology, viscosity models, and physiologic conditions. *Korea-Aust. Rheol. J.* **2008**, *20*, 197–211.
13. Park, H.M.; Lee, W.M. Helmholtz–Smoluchowski velocity for viscoelastic electroosmotic flows. *J. Colloid Int. Sci.* **2008**, *317*, 631–636. [CrossRef] [PubMed]
14. Olivares, M.L.; Vera-Candioti, L.; Berli, C.L.A. The EOF of polymer solutions. *Electrophoresis* **2009**, *30*, 921–928. [CrossRef] [PubMed]
15. Zhao, C.; Yang, C. Electrokinetics of non-Newtonian fluids: A review. *Adv. Colloid Interface Sci.* **2013**, *201–202*, 94–108. [CrossRef] [PubMed]
16. Zhao, C.; Zholkovskij, E.; Masliyah, J.H.; Yang, C. Analysis of electroosmotic flow of power-law fluids in a slit microchannel. *J. Colloid Interface Sci.* **2008**, *326*, 503–510. [CrossRef] [PubMed]
17. Zhao, C.; Yang, C. Nonlinear Smoluchowski velocity for electroosmosis of power-law fluids over a surface with arbitrary zeta potentials. *Electrophoresis* **2010**, *31*, 973–979. [CrossRef] [PubMed]
18. Zhao, C.; Yang, C. An exact solution for electroosmosis of non-Newtonian fluids in microchannels. *J. Non-Newton. Fluid Mech.* **2011**, *166*, 1076–1079. [CrossRef]
19. Zhao, C.; Yang, C. Electroosmotic flows of non-Newtonian power-law fluids in a cylindrical microchannel. *Electrophoresis* **2013**, *34*, 662–667. [CrossRef] [PubMed]
20. Zhao, C.; Zhang, W.; Yang, C. Dynamic Electroosmotic Flows of Power-Law Fluids in Rectangular Microchannels. *Micromachines* **2017**, *8*, 34. [CrossRef]
21. Tang, G.H.; Li, X.F.; He, Y.L.; Tao, W.Q. Electroosmotic flow of non-Newtonian fluid in microchannels. *J. Non-Newton. Fluid Mech.* **2009**, *157*, 133–137. [CrossRef]
22. Vasu, N.; De, S. Electroosmotic flow of power-law fluids at high zeta potentials. *Colloids Surf. A Physicochem. Eng. Asp.* **2010**, *368*, 44–52. [CrossRef]
23. Babaie, A.; Sadeghi, A.; Saidi, M.H. Combined electroosmotically and pressure driven flow of power-law fluids in a slit microchannel. *J. Non-Newton. Fluid Mech.* **2011**, *166*, 792–798. [CrossRef]
24. Hadigol, M.; Nosrati, R.; Raisee, M. Numerical analysis of mixed electroosmotic/pressure driven flow of power-law fluids in microchannels and micropumps. *Colloids Surf. A Physicochem. Eng. Asp.* **2011**, *374*, 142–153. [CrossRef]
25. Ng, C.-O.; Qi, C. Electroosmotic flow of a power-law fluid in a non-uniform microchannel. *J. Non-Newton. Fluid Mech.* **2014**, *208–209*, 118–125. [CrossRef]
26. Afonso, A.M.; Alves, M.A.; Pinho, F.T. Electroosmotic flow of viscoelastic fluids in microchannels under asymmetric zeta potentials. *J. Eng. Math.* **2011**, *71*, 15–30. [CrossRef]
27. Choi, W.; Joo, S.W.; Lim, G. Electroosmotic flows of viscoelastic fluids with asymmetric electrochemical boundary conditions. *J. Non-Newton. Fluid Mech.* **2012**, *187–188*, 1–7. [CrossRef]
28. Qi, C.; Ng, C.-O. Electroosmotic flow of a power-law fluid through an asymmetrical slit microchannel with gradually varying wall shape and wall potential. *Colloids Surf. A Physicochem. Eng. Asp.* **2015**, *472*, 26–37. [CrossRef]
29. Hadigol, M.; Nosrati, R.; Nourbakhsh, A.; Raisee, M. Numerical study of electroosmotic micromixing of non-Newtonian fluids. *J. Non-Newton. Fluid Mech.* **2011**, *166*, 965–971. [CrossRef]

30. Jiménez, E.; Escandón, J.; Bautista, O.; Méndez, F. Start-up electroosmotic flow of Maxwell fluids in a rectangular microchannel with high zeta potentials. *J. Non-Newton. Fluid Mech.* **2016**, *227*, 17–29. [CrossRef]
31. Peralta, M.; Arcos, J.; Méndez, F.; Bautista, O. Oscillatory electroosmotic flow in a parallel-plate microchannel under asymmetric zeta potentials. *Fluid Dyn. Res.* **2017**, *49*, 035514. [CrossRef]
32. Choi, W.; Yun, S.; Choi, D.-S. Electroosmotic flows of power-law fluids with asymmetric electrochemical boundary conditions in a rectangular microchannel. *Micromachines* **2017**, *8*, 165. [CrossRef]
33. Choi, W.; Yun, S.; Choi, D.-S. Approximate solution for electroosmotic flow of power-law fluids in a planar microchannel with asymmetric electrochemical boundary conditions. *Micromachines* **2018**, *9*, 265. [CrossRef]
34. Kirby, B.J.; Hasselbrink, E.F. Zeta potential of microfluidic substrates: 1. Theory, experimental techniques, and effects on separations. *Electrophoresis* **2004**, *25*, 187–202. [CrossRef] [PubMed]
35. Gallardo-Moreno, A.M.; Vadillo-Rodríguez, V.; Perera-Núñez, J.; Bruque, J.M.; González-Martín, M.L. The zeta potential of extended dielectrics and conductors in terms of streaming potential and streaming current measurements. *Phys. Chem. Chem. Phys.* **2012**, *14*, 9758–9767. [CrossRef] [PubMed]
36. Appell, P. Sur les séries hypergéométriques de deux variables et sur des équations différentielles linéaires aux dérivées partielles. *C. R. Hebd. Seances Acad. Sci.* **1880**, *90*, 296–298, 731–735.
37. Picard, É. Sur une extension aux fonctions de deux variables du problème de Riemann relativ aux fonctions hypergéométriques. *Annales Scientifiques de l'École Normale Supérieure Série 2* **1881**, *10*, 305–322. (In French) [CrossRef]
38. Barnes, E.W. A New Development in the Theory of the Hypergeometric Functions. *Proc. Lond. Math. Soc.* **1908**, *6*, 141–177. [CrossRef]
39. Bailey, W.N. *Generalised Hypergeometric Series*; Cambridge University Press: Cambridge, UK, 1935; pp. 3–4.

micromachines

MDPI

Article

Electroosmotic Flow Behavior of Viscoelastic LPTT Fluid in a Microchannel

Dilin Chen [1], Jie Li [1,*], Haiwen Chen [1], Lai Zhang [1], Hongna Zhang [2,*] and Yu Ma [2,*]

[1] School of Energy and Power Engineering, Wuhan University of Technology, Wuhan 430070, China; 132979767518@163.com (D.C.); chw168920@163.com (H.C.); lai_zhang_123@163.com (L.Z.)
[2] Institut Franco-Chinois de l'Energie Nucléaire, Sun Yat-sen University, Zhuhai 519000, China
* Correspondence: jieli@whut.edu.cn (J.L.); zhanghn26@mail.sysu.edu.cn (H.Z.); mayu9@mail.sysu.edu.cn (Y.M.); Tel.: +86-150-0712-5296 (J.L.); +86-131-2592-5951 (H.Z. & Y.M.)

Received: 28 October 2019; Accepted: 10 December 2019; Published: 15 December 2019

Abstract: In many research works, the fluid medium in electroosmosis is considered to be a Newtonian fluid, while the polymer solutions and biological fluids used in biomedical fields mostly belong to the non-Newtonian category. Based on the finite volume method (FVM), the electroosmotic flow (EOF) of viscoelastic fluids in near-neutral (pH = 7.5) solution considering four ions (K^+, Cl^-, H^+, OH^-) is numerically studied, as well as the viscoelastic fluids' flow characteristics in a microchannel described by the Linear Phan-Thien–Tanner (LPTT) constitutive model under different conditions, including the electrical double layer (EDL) thickness, the Weissenberg number (*Wi*), the viscosity ratio and the polymer extensibility parameters. When the EDL does not overlap, the velocity profiles for both Newtonian and viscoelastic fluids are plug-like and increase sharply near the charged wall. Compared with Newtonian fluid at *Wi* = 3, the viscoelastic fluid velocity increases by 5 times and 9 times, respectively, under the EDL conditions of kH = 15 and kH = 250, indicating the shear thinning behavior of LPTT fluid. Shear stress obviously depends on the viscosity ratio and different *Wi* number conditions. The EOF is also enhanced by the increase (decrease) in polymer extensibility parameters (viscosity ratio). When the extensibility parameters are large, the contribution to velocity is gradually weakened.

Keywords: electroosmotic flow; viscoelastic fluid; Linear Phan-Thien–Tanner (LPTT); pH; electrical double layer

1. Introduction

In recent years, with the development of multi-disciplines and mutual integration, microfluidic chips have become more widespread. In the shipping industry, broad application prospects can be foreseen in the Point-of-Care Testing (PoCT) of seafarers' diseases [1,2] and the desalination [3,4] of automatic signal transmission. In addition, microfluidic chips have many applications in the sensing and detection of nanoparticles [5–7], operations and reactions in analytical chemistry [8,9], encryption and decryption of information, future military communication, etc. The electrodynamic transport characteristics of micro- and nanofluidic devices have important basic and practical significance. Reuss [10] first discovered the electroosmotic flow (EOF) phenomenon in the laboratory. Helmholtz [11] considered the liquid and electric flow phenomena comprehensively for the first time, connecting the electric phenomenon, fluid flow and ion concentration, and proposing a complete electrical double layer (EDL) model theory. When direct current (DC) or alternating current (*AC*) voltage is applied along the horizontal direction of the microchannel, the direction of the external electric field is tangent to the charged surface, and the liquid ions in the EDL will be directionally displaced by the electric

field force, thus driving the fluid microclusters to move along the direction of the electric field force to form EOF.

Medical diagnostics include testing biological fluids such as saliva, blood and mucus, which exhibit viscoelastic behavior [12–14]. A growing number of PoCT methods involve the study of biological samples on laboratory microfluidic devices [15,16]. From the view of the chip-based microfluidic device laboratory, electroosmotic flow activity has been well studied and analyzed [17,18]. The use of simplified Possion–Boltzmann (PB) and Debye–Hückel (DH) models [19–22] for the analysis of EOF has made great progress, and the different solutions are extensive [23]. Yossifon et al. [24] analyzed the nonlinear current-voltage characteristics of nanochannels. Ma et al. [25] and Yeh et al. [26] proposed an analytical solution for the EOF of Newtonian fluids with multiple ion and pH characteristics. Huang et al. [27] first deduced a model to study the zeta potential and ionic conductivity of cylindrical nanopores with overlapping EDL. However, most biological fluids exhibit viscoelastic behavior [12–14]. Their non-Newtonian fluid characteristics are quite different from Newtonian fluids, including their shear rate-dependent viscosity, memory effect, and principal stress difference [28,29]. Therefore, the EOF of this kind of fluid should be distinguished from the traditional Newtonian fluid. Recently, more EOF theoretical studies on micro/nanofluidics have considered non-Newtonian properties. Das et al. [30] used the power law model to derive the analytical solution of the EOF in a rectangular microchannel. Zimmerman et al. [31] numerically simulated the electric flow behavior in a microchannel with a T-junction using the Carreau–Yasuda model. Berli and Olivares [32] used a multi-parameter non-Newtonian model to analyze the EOF in straight and cylindrical pipes. Zhao et al. [33] derived the analytical solution of power-law fluids' EOF and analyzed the effects of generic flow behavior index (n). Li et al. [34] studied the transient flow of Maxwell fluid in a long, straight microchannel and the effect of relaxation time. Mei et al. [35] analyzed the EOF characteristics of Linear Phan-Thien–Tanner (LPTT) fluids in a nanoslit with EDL overlap.

Most of the previous viscoelastic fluid EOF studies neglected the introduction of pH and H^+ and OH^- ions [17–24,36–41], or made an inaccurate characterization of biological fluid parameters [25–27] by a Newtonian fluid constitutive model (under pH conditions). Nowadays, a large number of biological experimental operations and chemical detection processes consider near-neutral conditions (pH = 7.5), such as specific drug release [42–44], biological fluid separation operation and amplification detection [45,46], sensor performance improvement [47–50], maintaining good activity of a microbial solution [51], and so on. Therefore, studying the EOF of viscoelastic fluid under near-neutral pH conditions may be far-reaching. Based on the finite volume method (FVM), the non-simplified Poisson–Nernst–Planck (PNP) model is used to describe the ion transport behavior. The LPTT constitutive model is considered to describe the viscoelastic properties, and a solution of pH 7.5 with H^+ and OH^- ions is mainly considered. The Weissenberg number (Wi), EDL thickness, viscosity ratio, extensibility parameters and net charge density are numerically studied. The mathematical model and boundary conditions are given in Section 2, and the numerical method is verified in Section 3. Finally, the parameter research and conclusions are presented.

2. Mathematical Model and Boundary Conditions

The motion of incompressible viscoelastic fluid with near-neutral solution (pH = 7.5) is considered in a long channel with length L, height H and width W, including K^+, Cl^-, H^+ and OH^- ions under the applied potential V_0 across the channel. Assuming that the channel height is much less than the length and the width ($H << L$, $H << W$), the problem can be simplified to a 2D problem, shown in Figure 1. Cartesian coordinates are used, the y-axis is the direction of channel height H, the x-axis is the direction of length, and the origin is fixed on the symmetrical line (y = H).

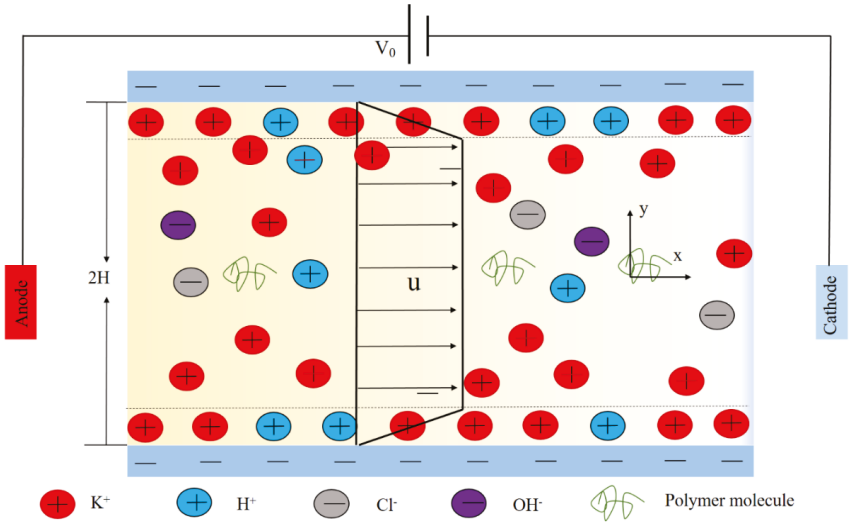

Figure 1. Schematic diagram of viscoelastic fluid electroosmotic flow (EOF).

The continuity equation and the momentum equation are as follows:

$$\nabla \cdot \boldsymbol{u} = 0 \tag{1}$$

$$-\nabla p + 2\eta_s \nabla \cdot \boldsymbol{D} + \nabla \cdot \tau + \rho_e \boldsymbol{E} = 0 \tag{2}$$

In the above, $\boldsymbol{u}$ and p are velocity and pressure, respectively; η_s is the dynamic viscosity of the solvent; $\boldsymbol{D} = \frac{1}{2}\left[\nabla \boldsymbol{u} + (\nabla \boldsymbol{u})^T\right]$ is a deformation tensor; ρ_e is the charge density of the electrolyte solution; $\boldsymbol{E} = -\nabla\psi$ represents electric field, where ψ is the potential in solution; $\boldsymbol{\tau}$ is an extra stress tensor and can be described by different constitutive models, such as Oldryod-B, FENE-P and PPT. $\boldsymbol{\tau}$ can usually be written as a function of the conformation tensor $\boldsymbol{c}$, and $\boldsymbol{c}$ is the tensor variable of the macromolecular structure of the polymer; the LPPT model is used to describe the viscoelastic fluid in this section.

$$\boldsymbol{\tau} = \frac{\eta_p}{\lambda}(\boldsymbol{c} - \boldsymbol{I}) \tag{3}$$

where η_p is the polymer stress tensor and λ is the relaxation time.

The conformation tensor ($\boldsymbol{c}$) for the LPTT model is governed by

$$\boldsymbol{u}\nabla \cdot \boldsymbol{c} - (c \cdot \nabla \boldsymbol{u}^T + \nabla \boldsymbol{u} \cdot \boldsymbol{c}) = -\frac{1}{\lambda}(1 + \varepsilon(tr(\boldsymbol{c}) - 3))(\boldsymbol{c} - \boldsymbol{I}) \tag{4}$$

where ε is the extensibility parameter and $tr(\boldsymbol{c})$ is the trace of the conformation tensor $\boldsymbol{c}$.

The potential ψ in the electrolyte solution is controlled by the Poisson equation:

$$-\varepsilon_f \nabla^2 \psi = F \sum_{i=1}^{i=4} z_i c_i \tag{5}$$

where ε_f is fluid permittivity; F is the Faraday constant; c_i and z_i (i = 1, 2, 3, 4) are the concentration and charge valence, respectively. The transport of ion concentrations is controlled by the Nernst–Planck equation:

$$\nabla \cdot N_j = \nabla \cdot \left(\boldsymbol{u}c_i - D_i \nabla c_i - z_i \frac{D_i}{RT} F c_i \nabla \psi\right) = 0 \tag{6}$$

where R is the general gas constant; T is the absolute temperature; Di is the diffuse rate of the i-th ion, and $N_j = \boldsymbol{u}c_i - D_i\nabla c_i - z_i\frac{D_i}{RT}Fc_i\nabla\psi$, $(j = 1, ...4)$ indicates each ion flux.

The KCl solution bulk concentration C_0 was selected as the ion concentration scale, RT/F as the potential scale, channel height H as the length scale, $u_0 = \varepsilon_f R^2T^2/(2\eta_0 HF^2)$ as the velocity scale, $\eta_0 = \eta_s + \eta_p$ as zero-shear rate total viscosity, and $\rho {u_0}^2$ as the pressure scale. The normalized governing Equations (1), (2) and (4)–(6) can be written:

$$\nabla' \cdot \boldsymbol{u}' = 0 \tag{7}$$

$$\boldsymbol{u}' \cdot \nabla' \boldsymbol{u}' = -\nabla' p' + \frac{\beta}{Re}\nabla'^2 \boldsymbol{u}' + \frac{(1-\beta)}{Re \cdot Wi}\nabla' \cdot \boldsymbol{c} - \frac{(kH)^2}{2Re}\left(\sum_{i=1}^{i=4} z_i {c'}_i\right)\nabla'\psi' \tag{8}$$

$$\boldsymbol{u}' \cdot \nabla' \boldsymbol{c} - \left(\boldsymbol{c} \cdot \nabla' {\boldsymbol{u}'}^T + \nabla' \boldsymbol{u}' \cdot \boldsymbol{c}\right) = -\frac{1}{Wi}(1 + \varepsilon(tr(\boldsymbol{c}) - 3))(\boldsymbol{c} - \boldsymbol{I}) \tag{9}$$

$$\nabla'^2\psi' = \frac{(kH)^2}{2}(z_1 {c'}_1 + z_2 {c'}_2 + z_3 {c'}_3 + z_4 \, c \, \prime_4) \tag{10}$$

$$\nabla' \cdot \left(\boldsymbol{u}' {c'}_i - D'_i \nabla' {c'}_i - z_i D'_i \nabla'_i \psi'\right) = 0, i = 1.., 4 \tag{11}$$

In the above, $\boldsymbol{u}'$, p', ψ', and ${c'}_i$ are dimensionless velocity, pressure, electric potential, and ion concentration, respectively. The Debye length is $k^{-1} = \sqrt{\varepsilon_f RT / \sum_{i=1}^{4} F^2 z_i^2 C_0}$. The viscosity ratio $\beta = \eta_s/\eta_0$ is the ratio of the solvent viscosity to the total viscosity. The dimensionless Reynolds number is $Re = 2\rho u_0 H/\eta_0$, and the Weissenberg number is $Wi = \lambda u_0/2H$.

The boundary conditions are given below.

(1) On the charged wall: the boundary is nonslip and ion-impenetrable and bears a surface charge density σ_0, and others are zero gradient.

$$\boldsymbol{u}' = 0, n \cdot \nabla'\psi' = \sigma_0 \cdot \frac{HF}{RT}, n \cdot \nabla' \, c \, \prime_i = -z_i {c'}_i n \cdot \nabla'\psi', n \cdot \nabla' \boldsymbol{c} = 0 \tag{12}$$

(2) At the anode (or cathode): the potential difference is V_0, the pressure is 0, and each ionic concentration maintains its bulk value.

$$n \cdot \nabla' \boldsymbol{u}' = 0, \psi' = V_0 \cdot \frac{F}{RT}(or \quad 0), p' = 0, {c'}_i = 1, n \cdot \nabla' \boldsymbol{c} = 0 \tag{13}$$

As the problem is symmetric, at the centerline of channel $x = H$, zero gradient is imposed on all variables.

3. Numerical Method and Code Validation

The high Weissenberg number problem (HWNP) loses numerical accuracy and stability under relatively high Wi [35,52]. The Log Conformation Reformulation (LCR) method [52,53] has proven to be one of the most effective strategies for overcoming this problem, and the procedure is presented as follows.

As the conformation tensor $\boldsymbol{c}$ is a symmetric positive definite (SPD) matrix, its matrix logarithm exists as

$$\boldsymbol{\Psi} = \log(\boldsymbol{c}) = \boldsymbol{R}^T \log(\Lambda)\boldsymbol{R} \tag{14}$$

where Λ is a diagonal matrix whose diagonal elements are the eigenvalues of $\boldsymbol{c}$; and $\boldsymbol{R}$ is an orthogonal matrix composed of eigenvectors of $\boldsymbol{c}$.

Then, the evolution Equation (9) for the conformation tensor $\boldsymbol{c}$ can be reformulated in terms of this new variable $\boldsymbol{\Psi}$ as

$$\boldsymbol{u}^{'} \cdot \nabla' \boldsymbol{\psi} - (\boldsymbol{\Omega} \cdot \boldsymbol{\Psi} - \boldsymbol{\Psi} \cdot \boldsymbol{\Omega}) - 2\boldsymbol{B} = -\frac{1}{Wi} e^{-\boldsymbol{\Psi}} \left(1 + \varepsilon \left(tr\left(e^{\boldsymbol{\Psi}}\right) - 3\right)\right)\left(e^{\boldsymbol{\Psi}} - \boldsymbol{I}\right) \tag{15}$$

where $\boldsymbol{\Omega}$ and $\boldsymbol{B}$ are the anti-symmetric matrix and the symmetric traceless matrix of the decomposition of the velocity gradient tensor $\nabla' \boldsymbol{u}^{'}$, as derived by Fattal and Kupferman [53] and Zhang et al. [54]. After $\boldsymbol{\Psi}$ is solved, the conformation tensor $\boldsymbol{c}$ can be recovered from the matrix-exponential of $\boldsymbol{\Psi}$ as

$$\boldsymbol{c} = \exp(\boldsymbol{\Psi}) \tag{16}$$

A new solver which solves the above equations (Equations (7)–(16)) was created based on the open source computational fluid dynamics (CFD) software OpenFOAM (version 6.0, The OpenFOAM Foundation Ltd, London, UK). Quick, Gauss Linear, and MINMOD schemes are used to discretize the convection terms in Equations (8), (11) and (15), respectively. The coupling of velocity and pressure fields is solved by splitting of operators (PISO) in Equation (8). Orthogonal mesh is used with much denser mesh distributed near the charged wall.

In addition, in order to verify the accuracy of the new solver for the viscoelastic EOF, we compare the numerical results with those of Afonso et al. [37], who simplified the analytical solution of EOF. The simplified PTT (sPTT) model in the two-dimensional microchannel assumes a low zeta potential and a thin EDL, so a simplified Poisson–Boltzmann equation can be used. The geometry of the channel is set to height H = 100 nm and length L = 300 nm. The solvent viscosity is set to zero and can be compared to the sPTT model in the reference. The other parameters are set as follows: $D_1 = 1.96 \times 10^{-9}$ m^2·s^{-1}, $D_2 = 2.03 \times 10^{-9}$ m^2·s^{-1}, T = 300 K, F = 96485 C·mol^{-1}, $\varepsilon_f = 7.08 \times 10^{-10}$ CV^{-1}·m^{-1}. The potential at the inlet is set to 0.05 V, and the outlet is grounded. The zeta potential on the wall is set to −4.36 mV. We define the dimensionless parameter $kH = \frac{H}{\lambda_D} = \sqrt{\frac{H^2 \sum_{i=1}^{2} F^2 z_i^2 C_0}{\varepsilon_f RT}}$, which represents the ratio of the height of the channel to EDL thickness.

Figure 2 shows the predicted dimensionless x-component velocity distribution in the middle of the channel at kH = 15. The corresponding values are analytical solutions for Newtonian fluids (Wi = 0) and viscoelastic fluids at ε = 1 and various Wi. It can be seen that the velocity distribution is plug-like in kH = 15, and it increases with higher Wi. The numerical results are in good agreement with the analytical solutions of Afonso et al. [31] for Newtonian and viscoelastic fluids under different Wi.

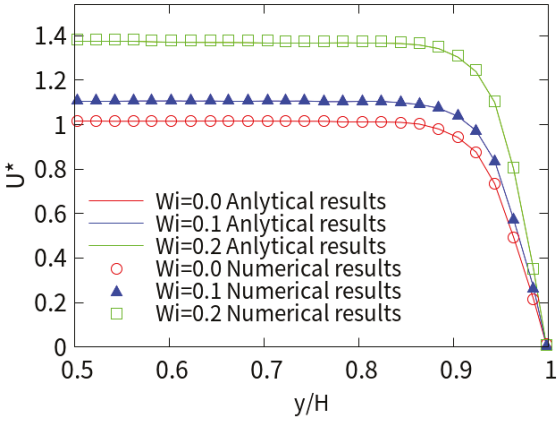

Figure 2. Comparison between the numerical (symbol) and analytical (solid line) results of the axial EOF velocity at different Weissenberg numbers (Wi).

4. Results and Discussion

The validated solver is then used to solve the (long enough) microchannel electrodynamic behavior of four ions for different *Wi* numbers, extensibility parameters, and viscosity ratios. The non-simplified PNP model is used to describe the ionic transport and potential distribution, and the LPTT constitutive model characterizes the fluid properties. The channel height is $2H = 30$ μm and the length is $L = 200$ μm. A finer mesh is created around the charged wall to capture its EDL. Typically, the total number of elements is around 88,500 to achieve convergence and grid-independent results. Considering the fully developed EOF under different *Wi*, the diffusion rates of K^+ and Cl^- ions are $D_1 = D_2 = 1 \times 10^{-9}$ $m^2 \cdot s^{-1}$, at different KCl bulk concentrations, $C_0 = 0.01$, 0.1 and 1 mM. We consider the near-neutral solution (pH = 7.5), H^+ concentration $C_3 = 10^{-pH+3}$ mM, OH^- concentration $C_4 = 10^{-(14-pH)+3}$ mM, and the diffusion rates [25,26] are $D_3 = 9.31 \times 10^{-9}$ $m^2 \cdot s^{-1}$, and $D_4 = 5.30 \times 10^{-9}$ $m^2 \cdot s^{-1}$, surface charge density $\sigma_0 = 0.03$ mC/m^2, and the applied potential $V_0 = 1$ V. Other parameters: extensibility parameter $\varepsilon = 0.25$, viscosity ratio $\beta = 0.1$. We maintain the above settings in the study unless otherwise stated.

4.1. The Influence of Wi Numbers

Figure 3 shows the dimensionless velocity considering $kH = 15$. It can be seen that the velocity increases sharply and reaches its magnitude near the charged wall, showing a plunger-like profile. The larger the *Wi* number, the more pronounced the plunger profile. This is because the thickness of EDL is much smaller than the height of the channel, so the charge is neutral outside the EDL region, and the velocity of the ion in the EDL is very slow when it is attracted by the Coulomb force. The maximum velocity for $Wi = 3$ at the centerline of viscoelastic fluid is 5 times that of Newtonian fluid. With the increase in *Wi*, the velocity increases monotonously in the whole range of *Wi*.

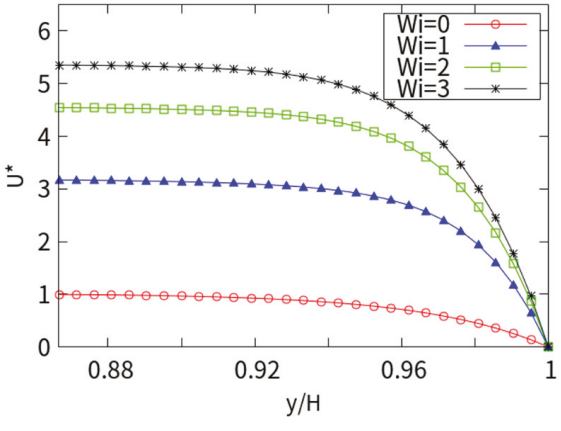

Figure 3. Cross-section velocity in the x direction with $kH = 15$.

Figure 4 shows the dimensionless velocity considering $kH = 250$, with *Wi* values of 0, 1, 2, and 3, respectively. A sudden change was observed near the charge wall, and the plunger flow was more pronounced. The reason is that the thickness of the EDL is extremely small, the internal counter ions are tightly bound in the EDL, and the flow rate in the EDL is sufficiently negligible to be approximately zero. The amplitude increases with the increase in the Weissenberg number. The influence on the velocity is obvious with a low number, but the influence is gradually reduced with a higher *Wi*. As the *Wi* increases, the flow rate shows a monotonous increase over the entire *Wi* range studied. The small EDL thickness ($kH = 250$) is reflected in the suddenly changed U^*. It can be seen that the influence of the *Wi* number on the flow rate is huge, and the viscoelastic fluid velocity ($Wi = 3$) is more than 9 times that of the Newtonian fluid.

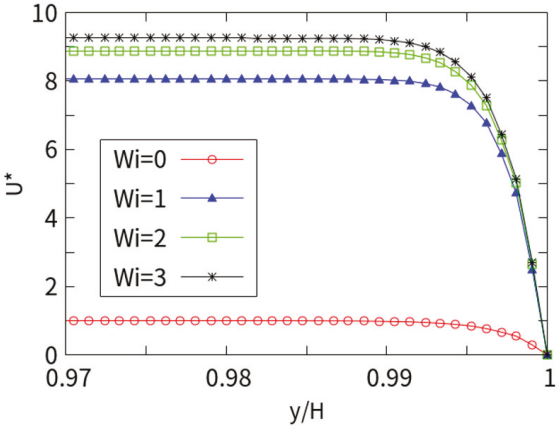

Figure 4. Cross-section velocity in the x direction with kH = 250.

Figure 5 shows the shear stress (τ_{xy}) values under different *Wi*. It can be seen that the shear stress is zero at the center of the channel away from the charged wall and sharply increases in the near-wall EDL (y-axis from 0.86 to 1.0 y/H). Obviously, the shear stress is also related to the *Wi*. As the *Wi* number increases, the viscoelasticity of the fluid increases. When the *Wi* is 0, it approximates Newtonian fluid and exhibits the maximum near-wall stress. With the increase in the *Wi*, the flow velocity increases near the charged wall, the shear rate (velocity gradient) increases, and the local viscous force decreases. Therefore, the shearing effect is weakened near the charged wall with the increasing *Wi*. This is due to the behavior of shear-thinning fluids (LPTT).

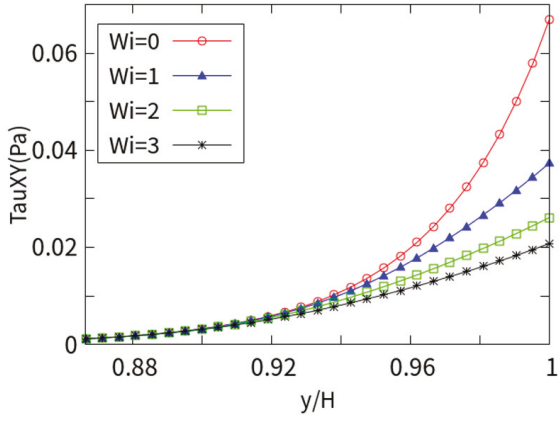

Figure 5. Shear stress at different *Wi* numbers with kH = 15.

4.2. Analysis of Different EDL Thicknesses

Figure 6 shows the dimensionless velocity of the near wall (0.13 H) at different kH with *Wi* = 1. As kH increases, the EDL thickness decreases monotonously. It can be seen that when the EDL thickness is gradually increased, a similar plunger-like velocity distribution gradually transitions to the parabolic velocity. At low concentrations, the EDL overlap trend is more obvious. Therefore, the velocity distribution shows a large unevenness toward the centerline. The flow rate is higher due to the increase in counter ions throughout the channel compared with the results for thin EDL thickness.

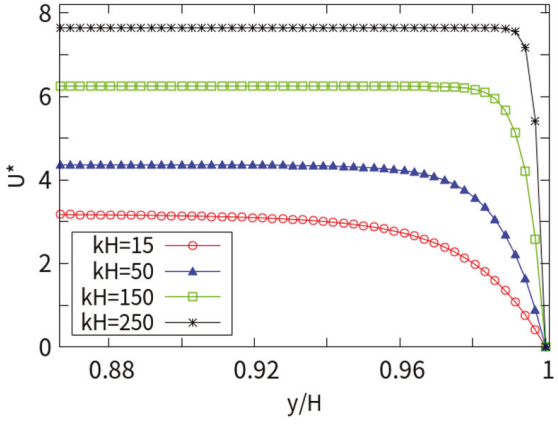

Figure 6. Velocity distribution of different electrical double layer (EDL) thicknesses.

Figure 7 shows the near-wall concentrations of K^+, H^+, Cl^-, and OH^- at different EDL thicknesses, dimensionless concentration $c_i^* = c_i/c_{i0}$. In general, the cations near the charged wall are greater than the bulk concentration, and the anions are less than the bulk concentration. With the increase in kH in the steady state, the cations are attracted to the charged wall, while the anions are repelled. The concentration of cations increases rapidly, nearly 1.5 times the bulk concentration near the wall surface, while the anions are repelled, decreasing along the center to the wall surface, until the near-wall concentration is close to 0.68 times the bulk concentration. In addition, the concentration ($kH = 250$) indicates that the EDL is extremely thin, and the stern layer is closely arranged.

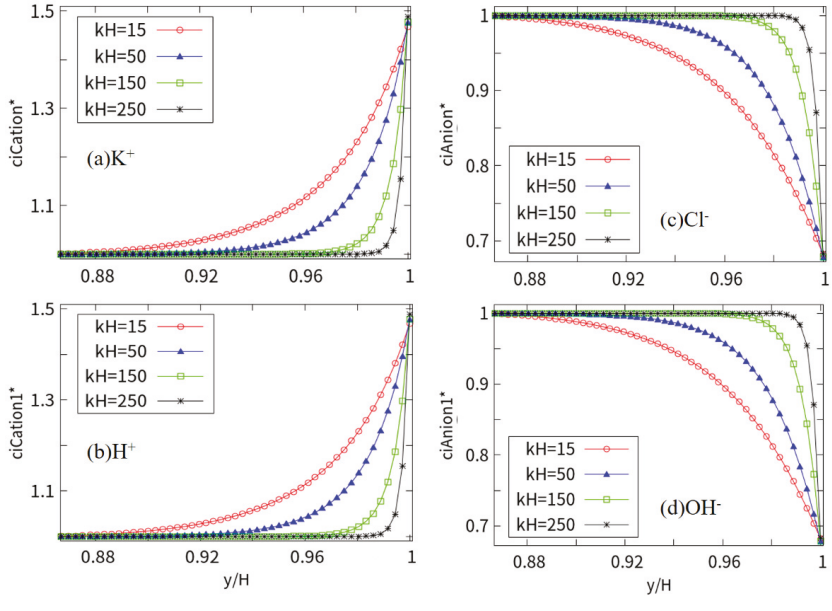

Figure 7. Wall distribution of anions and cations at different kH (the vertical axis indicates the dimensionless concentration $c_i^* = c_i/c_{i0}$).

Figure 8 shows the net charge density index $rhoD = \left|\frac{\rho_e}{\rho_{e\max}}\right|$ near the wall. When it is smaller, there are many regions with a charge density index >0.5, indicating that the anions and cations are relatively dispersed near the wall and ion aggregation is low. With the increase in kH, the region with charge density >0.5 decreases, indicating that the degree of aggregation of anions and cations is high, and most of the regions approximate their bulk concentration. When kH = 250, the charge density is very small, and the anions and cations are assembled in a layer of two to three ions. The trend is very consistent with the ion distribution characteristics shown in Figure 7.

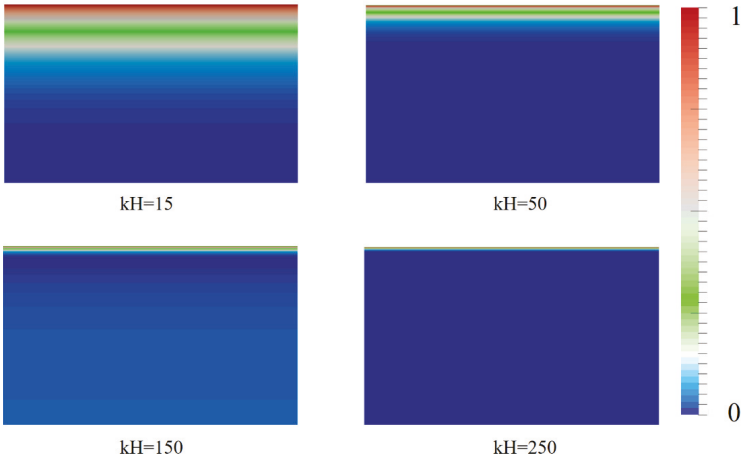

Figure 8. Net charge density index at different kH.

Figure 9 is a plot of the net mobile ions ($Cnet = \sum_{i=1}^{4} z_i c_i$) trend in cross-section for various background salt concentrations (or EDL thicknesses). Since the wall is negatively charged, more cations are attracted to the wall due to static electricity, while the anions are repelled. This phenomenon increases as kH increases. In this case, as the concentration of the KCl solution increases, the ion density of the surface increases greatly, causing a more considerable amount of cations to collect near the wall, thereby repelling a large amount of co-ions (anions). When kH = 250, the ions drop abruptly and the cations gather densely near the wall surface, similar to that shown in Figure 8. The curve of kH = 50 and kH = 150 is between high and low EDL thicknesses, and the trend is in accordance with the concentration curve near the charged wall.

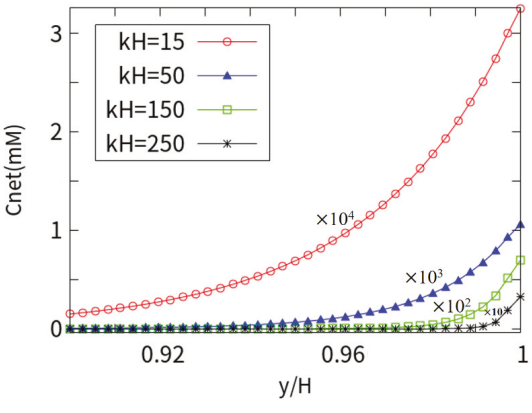

Figure 9. Net mobile ions trend in cross-section.

4.3. Rheological Parameter Effects of LPTT Model on Flow Velocity

The EOF of a viscoelastic fluid depends on the rheological parameters. Figure 10 shows the dimensionless velocity profiles for different viscosity ratios (β), with $Wi = 1$ and $kH = 50$. As the viscosity ratio increases, the magnitude of the velocity decreases correspondingly, and the velocity for $\beta = 0.05$ is about 3 times higher than that at $\beta = 0.50$. The flow mainly depends on the solvent viscosity, and the lower the solvent viscosity (proportion), the higher the velocity. This can be explained by the effect of macromolecular agglomeration on viscoelastic fluids.

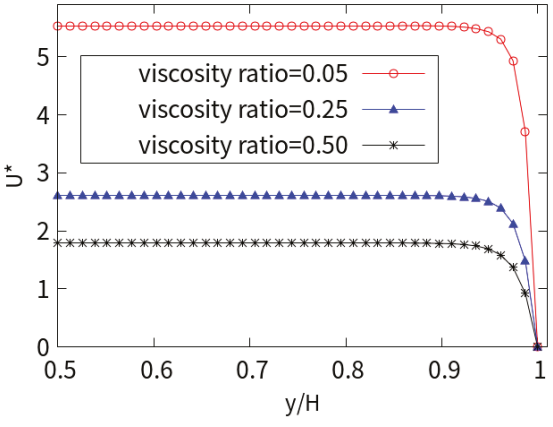

Figure 10. Near-wall velocity for different viscosity ratios.

Figure 11 shows the shear stress values of the xy plane under different viscosity ratios (β). It can be seen that the shear stress is almost zero in the central area of the entire channel and increases sharply in the vicinity of the charged wall. The numerical results show that as the viscosity ratio (β) increases, the amplitude of the shear stress decreases. This is due to the shear thinning characteristics of the LPTT fluid, which affect the increase in the shear rate at the wall surface, resulting in an increase in velocity. As the viscosity ratio decreases, the shear stress $\tau_{xy} = \eta_0 \frac{\partial u}{\partial y}$ near the wall increases due to the increase in the ratio of solute viscosity, high gradients of velocity, molecular agglomeration, and macromolecular elasticity.

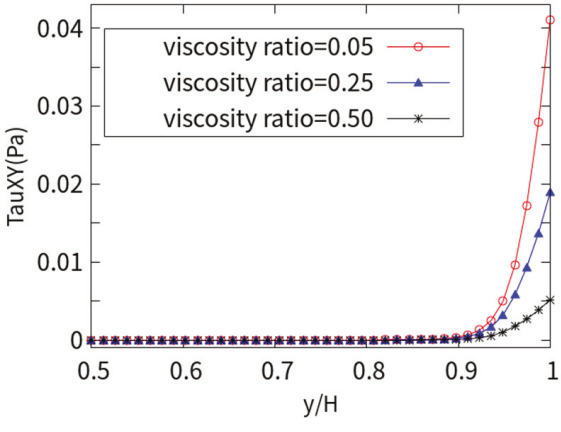

Figure 11. Shear stress for different viscosity ratios.

Figure 12 shows the cross-section EOF under different extensibility parameters (ε). The velocity at $\varepsilon = 1$ is twice the value at $\varepsilon = 0.05$. The smaller extensibility parameters, the greater the contribution to the velocity. However, with the increase in the stretching parameters, the contribution is gradually weakened.

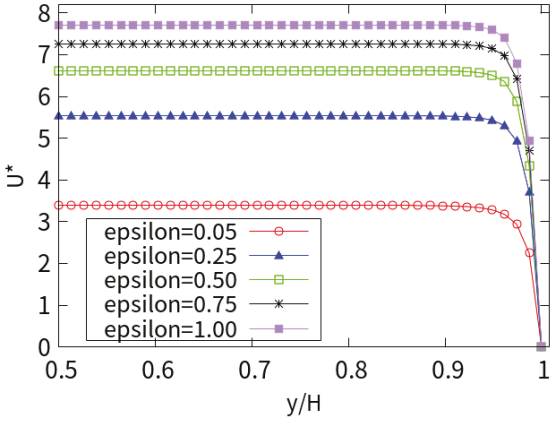

Figure 12. Near-wall velocity for different extensibility parameters.

5. Conclusions

The EOF of viscoelastic fluids in long microchannels was numerically studied, and the effect of the rheological properties of LPTT fluids was considered on fully developed EOF with near-neutral condition (pH = 7.5 and four ions). The nonlinear PNP equation is used to describe the potential and ion concentration distribution without using the simplified PB or DH model assumptions. The overall conclusions are as follows:

(1) When the EDLs do not overlap, the velocity distributions of different Weissenberg numbers are all plunger-like, and the influence of the *Wi* number on the flow velocity is significant. The velocity of the viscoelastic fluid was observed to increase significantly compared with Newtonian fluid. For thick electric double layers ($kH = 15$), the maximum velocity at $Wi = 3$ at the centerline of the viscoelastic fluid is 5 times that of Newtonian fluid. As the *Wi* increased, the flow rate showed a monotonous increase over the entire *Wi* range studied. For the thin double layer ($kH = 250$), the viscoelastic fluid with a *Wi* value of 3 has a maximum velocity that is 9 times that of Newtonian fluid.

(2) Newtonian fluid ($Wi = 0$) has the largest shear-stress at the surface charged wall, and as the *Wi* number increases, the local viscous force decreases, which weakens the shear-thinning behavior. As the velocity increases with the increase in kH, the concentration of cations is close to 1.5 times that of the bulk concentration, and the concentration of anions is close to 0.68 times that of the bulk concentration. When the $kH = 250$, the anions and cations are concentrated in a layer of two to three ions.

(3) As the viscosity ratio (β) increases, the magnitude of the dimensionless U^* decreases correspondingly, and the velocity at $\beta = 0.05$ is about 3 times that at $\beta = 0.50$. With the viscosity ratio dropping, the shear-stress near the wall increases. This is due to the large solute viscosity, the effects of molecular agglomeration and macromolecular elasticity. The velocity at $\varepsilon = 1$ is twice that at $\varepsilon = 0.05$. When the extensibility parameter is large, the contribution is gradually weakened.

The research results may contribute to experimental research on the latest PoCT devices. These devices can be used in biological fluid detection and new generation microchip applications, from the development of medical devices with artificial flow driving to portable diagnostic kits.

Author Contributions: J.L., H.Z., and Y.M. guided the work and revision of the paper; D.C. and H.C. realized numerical simulation and paper writing; D.C. and L.Z. collated the literature and revised the paper.

Funding: This work was funded by the National Natural Science Foundation of China (Grant No. 51606054), and this work was supported by NSAF (Grant No. U1830118).

Conflicts of Interest: The authors declare no conflict of interest.

References

1. Gutierrez, M.A.; Moreno, R.A.; Rebelo, M.S. Information and communication technologies and global health challenges. In *Global Health Informatics*; Academic Press: Cambridge, MA, USA, 2017; pp. 50–93.
2. Luppa, P.B.; Müller, C.; Schlichtiger, A.; Schlebusch, H. Point-of-care testing (POCT): Current techniques and future perspectives. *Trac Trends Anal. Chem.* **2011**, *30*, 887–898. [CrossRef]
3. Li, Z.R.; Liu, G.R.; Chen, Y.Z.; Wang, J.S.; Bow, H.; Cheng, Y.; Han, J. Continuum transport model of Ogston sieving in patterned nanofilter arrays for separation of rod-like biomolecules. *Electrophoresis* **2008**, *29*, 329–339. [CrossRef] [PubMed]
4. Li, J.; Chen, D.; Ye, J.; Zhang, L.; Zhou, T.; Zhou, Y. Direct numerical simulation of seawater desalination based on ion concentration polarization. *Micromachines* **2019**, *10*, 562. [CrossRef] [PubMed]
5. Ouyang, W.; Ye, X.; Li, Z.; Han, J. Deciphering ion concentration polarization-based electrokinetic molecular concentration at the micro-nanofluidic interface: Theoretical limits and scaling laws. *Nanoscale* **2018**, *10*, 15187–15194. [CrossRef] [PubMed]
6. Li, Z.; Liu, W.; Gong, L.; Zhu, Y.; Gu, Y.; Han, J. Accurate multi-physics numerical analysis of particle preconcentration based on ion concentration polarization. *Int. J. Appl. Mech.* **2017**, *9*, 1750107. [CrossRef]
7. Gong, L.; Ouyang, W.; Li, Z.; Han, J. Force fields of charged particles in micro-nanofluidic preconcentration systems. *AIP Adv.* **2017**, *7*, 125020. [CrossRef] [PubMed]
8. Gervais, T.; Jensen, K.F. Mass transport and surface reactions in microfluidic systems. *Chem. Eng. Sci.* **2006**, *61*, 1102–1121. [CrossRef]
9. Gong, L.; Ouyang, W.; Li, Z.; Han, J. Direct numerical simulation of continuous lithium extraction from high Mg2+/Li+ ratio brines using microfluidic channels with ion concentration polarization. *J. Membr. Sci.* **2018**, *556*, 34–41. [CrossRef]
10. Reuss, F.F. Notice sur un nouvel effet de l'electricité galvanique, Mémoire Soc. *Sup. Imp. Moscou* **1809**, *2*, 327–337.
11. Helmholtz, H.V. Ueber einige gesetze der vertheilung elektrischer ströme in körperlichen leitern, mit anwendung auf die thierisch-elektrischen versuche (schluss.). *Ann. Phys.* **1853**, *165*, 353–377. [CrossRef]
12. Braga, P.C.; Moretti, M.; Piacenza, A.; Montoli, C.C.; Guffanti, E.E. Effects of seaprose on the rheology of bronchial mucus in patients with chronic bronchitis. A double-blind study vs placebo. *Int. J. Clin. Pharmacol. Res.* **1993**, *13*, 179–185. [PubMed]
13. Stokes, J.R.; Davies, G.A. Viscoelasticity of human whole saliva collected after acid and mechanical stimulation. *Biorheology* **2007**, *44*, 141–160. [PubMed]
14. Jun Kang, Y.; Lee, S.J. Blood viscoelasticity measurement using steady and transient flow controls of blood in a microfluidic analogue of Wheastone-bridge channel. *Biomicrofluidics* **2013**, *7*, 054122. [CrossRef] [PubMed]
15. Nguyen, N.T.; Shaegh, S.A.M.; Kashaninejad, N.; Phan, D.T. Design, fabrication and characterization of drug delivery systems based on lab-on-a-chip technology. *Adv. Drug Deliv. Rev.* **2013**, *65*, 1403–1419. [CrossRef] [PubMed]
16. Ríos, Á.; Zougagh, M.; Avila, M. Miniaturization through lab-on-a-chip: Utopia or reality for routine laboratories? A review. *Anal. Chim. Acta* **2012**, *740*, 1–11. [CrossRef]
17. Zeng, S.; Chen, C.H.; Mikkelsen, J.C., Jr.; Santiago, J.G. Fabrication and characterization of electroosmotic micropumps. *Sens. Actuators B Chem.* **2001**, *79*, 107–114. [CrossRef]
18. Kaushik, P.; Abhimanyu, P.; Mondal, P.K.; Chakraborty, S. Confinement effects on the rotational microflows of a viscoelastic fluid under electrical double layer phenomenon. *J. Non-Newton. Fluid Mech.* **2017**, *244*, 123–137. [CrossRef]
19. Burgreen, D.; Nakache, F.R. Electrokinetic flow in ultrafine capillary slits1. *J. Phys. Chem.* **1964**, *68*, 1084–1091. [CrossRef]
20. Dutta, P.; Beskok, A. Analytical solution of combined electroosmotic/pressure driven flows in two-dimensional straight channels: Finite Debye layer effects. *Anal. Chem.* **2001**, *73*, 1979–1986. [CrossRef]

21. Dutta, P.; Beskok, A.; Warburton, T.C. Electroosmotic flow control in complex microgeometries. *J. Microelectromechanical Syst.* **2002**, *11*, 36–44. [CrossRef]
22. Kang, Y.; Yang, C.; Huang, X. AC electroosmosis in microchannels packed with a porous medium. *J. Micromechanics Microengineering* **2004**, *14*, 1249. [CrossRef]
23. Petsev, D.N.; Lopez, G.P. Electrostatic potential and electroosmotic flow in a cylindrical capillary filled with symmetric electrolyte: Analytic solutions in thin double layer approximation. *J. Colloid Interface Sci.* **2006**, *294*, 492–498. [CrossRef] [PubMed]
24. Yossifon, G.; Mushenheim, P.; Chang, Y.C.; Chang, H.C. Nonlinear current-voltage characteristics of nanochannels. *Phys. Rev. E* **2009**, *79*, 046305. [CrossRef] [PubMed]
25. Ma, Y.; Xue, S.; Hsu, S.C.; Yeh, L.H.; Qian, S.; Tan, H. Programmable ionic conductance in a pH-regulated gated nanochannel. *Phys. Chem. Chem. Phys.* **2014**, *16*, 20138–20146. [CrossRef]
26. Yeh, L.H.; Zhang, M.; Qian, S. Ion transport in a pH-regulated nanopore. *Anal. Chem.* **2013**, *85*, 7527–7534. [CrossRef]
27. Huang, M.J.; Mei, L.; Yeh, L.H.; Qian, S. pH-Regulated nanopore conductance with overlapped electric double layers. *Electrochem. Commun.* **2015**, *55*, 60–63. [CrossRef]
28. Huppler, J.D.; Ashare, E.; Holmes, J.A. Rheological properties of three solutions. Part I. Non-newtonian viscosity, normal stresses, and complex viscosity. *Trans. Soc. Rheol.* **1967**, *11*, 159–179. [CrossRef]
29. Ortiz, S.L.; Lee, J.S.; Figueroa-Espinoza, B.; Mena, B. An experimental note on the deformation and breakup of viscoelastic droplets rising in non-Newtonian fluids. *Rheol. Acta* **2016**, *55*, 879–887. [CrossRef]
30. Das, S.; Chakraborty, S. Analytical solutions for velocity, temperature and concentration distribution in electroosmotic microchannel flows of a non-Newtonian bio-fluid. *Anal. Chim. Acta* **2006**, *559*, 15–24. [CrossRef]
31. Zimmerman, W.B.; Rees, J.M.; Craven, T.J. Rheometry of non-Newtonian electrokinetic flow in a microchannel T-junction. *Microfluid. Nanofluidics* **2006**, *2*, 481–492. [CrossRef]
32. Berli, C.L.; Olivares, M.L. Electrokinetic flow of non-Newtonian fluids in microchannels. *J. Colloid Interface Sci.* **2008**, *320*, 582–589. [CrossRef] [PubMed]
33. Zhao, C.; Yang, C. An exact solution for electroosmosis of non-Newtonian fluids in microchannels. *J. Non-Newton. Fluid Mech.* **2011**, *166*, 1076–1079. [CrossRef]
34. Li, X.X.; Yin, Z.; Jian, Y.J.; Chang, L.; Su, J.; Liu, Q.S. Transient electro-osmotic flow of generalized Maxwell fluids through a microchannel. *J. Non-Newton. Fluid Mech.* **2012**, *187*, 43–47. [CrossRef]
35. Mei, L.; Zhang, H.; Meng, H.; Qian, S. Electroosmotic flow of viscoelastic fluid in a nanoslit. *Micromachines* **2018**, *9*, 155. [CrossRef] [PubMed]
36. Park, H.M.; Lee, W.M. Effect of viscoelasticity on the flow pattern and the volumetric flow rate in electroosmotic flows through a microchannel. *Lab A Chip* **2008**, *8*, 1163–1170. [CrossRef] [PubMed]
37. Afonso, A.M.; Alves, M.A.; Pinho, F.T. Analytical solution of mixed electro-osmotic/pressure driven flows of viscoelastic fluids in microchannels. *J. Non-Newton. Fluid Mech.* **2009**, *159*, 50–63. [CrossRef]
38. Sousa, J.J.; Afonso, A.M.; Pinho, F.T.; Alves, M.A. Effect of the skimming layer on electro-osmotic—Poiseuille flows of viscoelastic fluids. *Microfluid. Nanofluidics* **2011**, *10*, 107–122. [CrossRef]
39. Dhinakaran, S.; Afonso, A.M.; Alves, M.A.; Pinho, F.T. Steady viscoelastic fluid flow between parallel plates under electro-osmotic forces: Phan-Thien–Tanner model. *J. Colloid Interface Sci.* **2010**, *344*, 513–520. [CrossRef]
40. Choi, W.; Joo, S.W.; Lim, G. Electroosmotic flows of viscoelastic fluids with asymmetric electrochemical boundary conditions. *J. Non-Newton. Fluid Mech.* **2012**, *187*, 1–7. [CrossRef]
41. Sarma, R.; Deka, N.; Sarma, K.; Mondal, P.K. Electroosmotic flow of Phan-Thien–Tanner fluids at high zeta potentials: An exact analytical solution. *Phys. Fluids* **2018**, *30*, 062001. [CrossRef]
42. Yatvin, M.B.; Kreutz, W.; Horwitz, B.A.; Shinitzky, M. pH-sensitive liposomes: Possible clinical implications. *Science* **1980**, *210*, 1253–1255. [CrossRef] [PubMed]
43. Horswill, A.R.; Stoodley, P.; Stewart, P.S.; Parsek, M.R. The effect of the chemical, biological, and physical environment on quorum sensing in structured microbial communities. *Anal. Bioanal. Chem.* **2007**, *387*, 371–380. [CrossRef] [PubMed]
44. El-Ghaffar, M.A.; Hashem, M.S.; El-Awady, M.K.; Rabie, A.M. pH-sensitive sodium alginate hydrogels for riboflavin controlled release. *Carbohydr. Polym.* **2012**, *89*, 667–675. [CrossRef] [PubMed]
45. Higa, S.; Suzuki, T.; Hayashi, A.; Tsuge, I.; Yamamura, Y. Isolation of catecholamines in biological fluids by boric acid gel. *Anal. Biochem.* **1977**, *77*, 18–24. [CrossRef]

46. Zaporozhchenko, I.A.; Morozkin, E.S.; Skvortsova, T.E.; Bryzgunova, O.E.; Bondar, A.A.; Loseva, E.M.; Laktionov, P.P. A phenol-free method for isolation of microRNA from biological fluids. *Anal. Biochem.* **2015**, *479*, 43–47. [CrossRef]
47. Wang, M.Q.; Ye, C.; Bao, S.J.; Zhang, Y.; Yu, Y.N.; Xu, M.W. Carbon nanotubes implanted manganese-based MOFs for simultaneous detection of biomolecules in body fluids. *Analyst* **2016**, *141*, 1279–1285. [CrossRef]
48. Brahman, P.K.; Pandey, N.; Topkaya, S.N.; Singhai, R. Fullerene–C60–MWCNT composite film based ultrasensitive electrochemical sensing platform for the trace analysis of pyruvic acid in biological fluids. *Talanta* **2015**, *134*, 554–559. [CrossRef]
49. Bollella, P.; Sharma, S.; Cass, A.E.; Tasca, F.; Antiochia, R. Minimally invasive glucose monitoring using a highly porous gold microneedles-based biosensor: Characterization and application in artificial interstitial fluid. *Catalysts* **2019**, *9*, 580. [CrossRef]
50. Nandakumar, V.; Dolan, C.; Baumann, N.A.; Block, D.R. Effect of pH on the quantification of body fluid analytes for clinical diagnostic testing. *Am. J. Clin. Pathol.* **2019**, *152* (Suppl. 1), S10–S11. [CrossRef]
51. Lin, D.Q.; Fernández-Lahore, H.M.; Kula, M.R.; Thömmes, J. Minimising biomass/adsorbent interactions in expanded bed adsorption processes: A methodological design approach. *Bioseparation* **2001**, *10*, 7–19. [CrossRef]
52. Hulsen, M.A.; Fattal, R.; Kupferman, R. Flow of viscoelastic fluids past a cylinder at high Weissenberg number: Stabilized simulations using matrix logarithms. *J. Non-Newton. Fluid Mech.* **2005**, *127*, 27–39. [CrossRef]
53. Fattal, R.; Kupferman, R. Constitutive laws for the matrix-logarithm of the conformation tensor. *J. Non-Newton. Fluid Mech.* **2004**, *123*, 281–285. [CrossRef]
54. Zhang, H.N.; Li, D.Y.; Li, X.B.; Cai, W.H.; Li, F.C. Numerical simulation of heat transfer process of viscoelastic fluid flow at high Weissenberg number by log-conformation reformulation. *J. Fluids Eng.* **2017**, *139*, 091402. [CrossRef]

micromachines

MDPI

Article

Electroosmotic Flow of Viscoelastic Fluid in a Nanochannel Connecting Two Reservoirs

Lanju Mei [1] and Shizhi Qian [2,*]

[1] Department of Engineering and Aviation Sciences, University of Maryland Eastern Shore, Princess Anne, MD 21853, USA; lmei@umes.edu
[2] Department of Mechanical and Aerospace Engineering, Old Dominion University, Norfolk, VA 23529, USA
* Correspondence: sqian@odu.edu; Tel.: +1-757-683-3304

Received: 18 October 2019; Accepted: 30 October 2019; Published: 31 October 2019

Abstract: Electroosmotic flow (EOF) of viscoelastic fluid with Linear Phan-Thien–Tanner (LPTT) constitutive model in a nanochannel connecting two reservoirs is numerically studied. For the first time, the influence of viscoelasticity on the EOF and the ionic conductance in the micro-nanofluidic interconnect system, with consideration of the electrical double layers (EDLs), is investigated. Regardless of the bulk salt concentration, significant enhancement of the flow rate is observed for viscoelastic fluid compared to the Newtonian fluid, due to the shear thinning effect. An increase in the ionic conductance of the nanochannel occurs for the viscoelastic fluid. The enhancement of the ionic conductance is significant under the overlapping EDLs condition.

Keywords: electroosmotic flow; viscoelastic fluid; nanofluidics; ionic conductance; electrical double layer

1. Introduction

In recent decades, micro/nanofluidics has received significant interest due to its promising applications in bioengineering and chemical engineering [1–5]. Electroosmosis, first reported by Reuss [6], has been widely studied both experimentally and theoretically due to its unique feature of easily manipulating flow at micro/nanoscale [7–11]. At nanoscale, the electric double layer (EDL) may become overlapped under the condition of low bulk salt concentration [12,13], resulting in the ionic selective property of the nanochannel [14].

As is common in chemical and biomedical applications, solutions are often made from large molecules, such as polymer or DNA. These solutions exhibit non-linear rheological behavior that is distinctively different from the Newtonian fluid [15,16], such as the variable viscosity and normal stress difference [17]. Understanding the EOF of these non-Newtonian fluids is of practical importance for the experimental design as well as the operation of various micro/nanofluidic devices. Bello et al. [18] firstly experimentally showed that the electroosmotic flow velocity of a polymer solution in a capillary is much higher than the predicted Helmholtz–Smoluchowski velocity. Chang et al. [19] experimentally investigated the EOF of polymer solutions and observed the drag reduction and reduced effective viscosity. Huang et al. [20] conducted the experimental and theoretical study on the non-Newtonian EOF, and showed the enhancement of the EOF velocity due to the shear thinning effect. Recently, more researches on the EOF of non-Newtonian fluids have been conducted from the theoretical aspect. For example, Zhao et al. [21,22] derived closed-form solutions for the electroosmotic flow of power-law fluids over a planar surface and a parallel-plate microchannel. Tang et al. [23] numerically studied the EOF of power-law non-Newtonian fluid in microchannel, and showed the influence of fluid rheology on the EOF pattern. Choi et al. [24] analytically studied the EOF of viscoelastic fluid with Phan-Thien–Tanner (PTT) model in a two-dimensional microchannel, and analyzed the effects of

relaxation time, extensibility parameter, and slip parameter of the PTT model on the velocity and flow rate. Mukherjee et al. [25] developed the closed-form EOF velocity distribution for viscoelastic fluid of the simplified PTT (sPTT) model in microchannel confined between two parallel plates. Martínez et al. [26] asymptotically analyzed the EOF of a viscoelastic fluid with sPTT model in a wavy-wall microchannel, and examined the effects of the wave number and viscoelastic character of the fluid. Park et al. [27] derived the Helmholtz–Smoluchowski velocity and analytically calculated the volumetric flow rate in a microchannel for the EOF of PTT fluid. Afonso et al. [28] developed the analytical solution for the EOF of viscoelastic fluid in a microchannel by using both PTT model and Finitely Extensible Nonlinear Elastic with Peterlin closure (FENE–P) model. Dhinakaran et al. [29] analytically investigated the steady EOF of viscoelastic fluid between parallel plates using the PTT model.

Most of the theoretical studies on EOF of viscoelastic fluid are in microscale, where the assumptions of small charge density and relatively thin EDL are reasonable. When the characteristic length of the channel is on nanoscale, the EDL thickness becomes comparable to the nanochannel height [30,31], the nonlinear Poisson–Nernst–Planck equations have to be used to solve for the electric potential and ionic concentration. Mei et al. [32] numerically studied the EOF of viscoelastic fluid in a nanoslit and reported the effect of the rheological property of Linear Phan-Thien–Tanner (LPTT) fluid on the fully developed EOF. In this study, the work of Mei et al. [32] is extended to investigate the EOF of the LPTT viscoelastic fluid in a nanochannel connecting two large reservoirs, which is closer to the actual experimental devices. The influence of the rheological property of the viscoelastic fluid on the ionic conductance across the nanochannel is examined with consideration of the EDLs overlapping condition.

2. Mathematical Model

Consider a nanochannel of height H_c, length L_c, and width W connecting two reservoirs of height H_r and length L_r. A binary KCl electrolyte solution of bulk concentration C_0 is filled in the nanochannel and is electrically driven by an external potential bias V_0 applied between the inlet (Anode) and outlet (Cathode). Assume that the nanochannel height is much smaller than its width and length (i.e., $H_c \ll L_c$, $H_c \ll W$), so the problem can be simplified to a 2D problem schematically shown in Figure 1. Cartesian coordinate system O–xy is adopted with x-axis in the height direction, y-axis in the length direction, and origin fixed on the center of the upper channel surface. As the problem is symmetric about the central axis *GI*, only half of the geometry is considered, with symmetric boundary conditions applied for all fields on the symmetry axis.

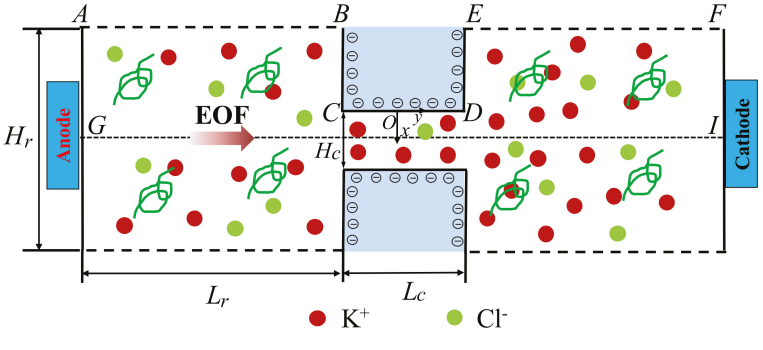

Figure 1. Schematic diagram of a nanochannel connecting two reservoirs at both ends. Uniform negative surface charges are distributed on the nanochannel wall and the adjacent walls of reservoirs. An external electric field is applied by a potential bias between the inlet (Anode) and outlet (Cathode).

The mass and momentum conservation equations governing the incompressible viscoelastic fluid are

$$\nabla \cdot \boldsymbol{u} = 0 \tag{1}$$

$$\rho\left(\frac{\partial \boldsymbol{u}}{\partial t} + \boldsymbol{u}\cdot\nabla\boldsymbol{u}\right) = -\nabla p + 2\eta_s\nabla\cdot\left[\nabla\boldsymbol{u} + (\nabla\boldsymbol{u})^T\right] + \nabla\cdot\boldsymbol{\tau} - \rho_e\nabla\phi \tag{2}$$

where $\boldsymbol{u}$ and p denote the velocity field and pressure, respectively; ϕ is the electric potential and ρ_e is the volume charge density within the electrolyte solution; ρ and η_s represent the fluid density and the solvent dynamic viscosity, respectively; and the polymeric stress tensor $\boldsymbol{\tau}$ accounts for the memory of the viscoelastic fluid. Depending on the type of viscoelastic fluid, different constitutive models have been developed to describe the relation of $\boldsymbol{\tau}$ and the deformation rate of the fluid, such as Oldryod–B model, Giesekus model, LPTT model, and so forth. For the LPPT model adopted in this study, $\boldsymbol{\tau}$ is given by

$$\boldsymbol{\tau} = \frac{\eta_p}{\lambda}(\boldsymbol{c} - \boldsymbol{I}) \tag{3}$$

where $\boldsymbol{c}$ is the symmetric conformation tensor representing the configuration of the polymer molecules, η_p is the polymeric viscosity, and λ is the relaxation time of the polymer.

For the LPTT model, the equation governing the conformation tensor $\mathbf{c}$ is

$$\frac{\partial \boldsymbol{c}}{\partial t} + \boldsymbol{u}\nabla\cdot\boldsymbol{c} - \left(\boldsymbol{c}\cdot\nabla\boldsymbol{u}^T + \nabla\boldsymbol{u}\cdot\boldsymbol{c}\right) = -\frac{1}{\lambda}(1 + \varepsilon(\mathrm{tr}(\boldsymbol{c}) - 3))(\boldsymbol{c} - \boldsymbol{I}) \tag{4}$$

where the non-linear parameter ε is the extensibility parameter.

The channel surface in contact with the electrolyte solution of permittivity ε_f will become charged and an electric double layer enriched with counterions will develop in the vicinity of the charged surface. The electric potential and ionic concentration within the electrolyte solution are governed by the Poisson equation and the Nernst–Planck equation as

$$-\varepsilon_f\nabla^2\varnothing = F\left(z_1c_1' + z_2c_2'\right) \tag{5}$$

$$\frac{\partial c_i}{\partial t} + \nabla\cdot\left(uc_i - D_i\nabla c_i - z_i\frac{D_i}{RT}Fc_i\nabla\varnothing\right) = 0, \quad i = 1, 2 \tag{6}$$

In the above, z_i, D_i and c_i are the valence, diffusivity, and ionic concentration of ith ionic species (i = 1 for K^+, 2 for Cl^-), respectively; F, R, and T are the Faraday constant, gas constant, and the absolute temperature, respectively.

Select the channel height H_c as length scale, $U_0 = \varepsilon_f R^2T^2/\left(\eta_0 H_c F^2\right)$ as velocity scale with $\eta_0 = \eta_s + \eta_p$ being the total viscosity, $\rho {U_0}^2$ as the pressure scale, RT/F as electric potential scale, the bulk concentration C_0 as the ionic concentration scale, and the set of governing Equations (1)–(2) and (4)–(6) can be normalized as

$$\nabla'\cdot\boldsymbol{u}' = 0 \tag{7}$$

$$\frac{\partial \boldsymbol{u}'}{\partial t'} + \boldsymbol{u}'\cdot\nabla'\boldsymbol{u}' = -\nabla'p' + \frac{\beta}{Re}\nabla'^2\boldsymbol{u}' + \frac{(1-\beta)}{Re\cdot Wi}\nabla'\cdot\boldsymbol{c} - \frac{(H_c/\lambda_D)^2}{2Re}\left(z_1c_1' + z_2c_2'\right)\nabla'\varnothing' \tag{8}$$

$$\frac{\partial \boldsymbol{c}}{\partial t'} + \boldsymbol{u}'\cdot\nabla'\boldsymbol{c} - \left(\boldsymbol{c}\cdot\nabla'\boldsymbol{u}'^T + \nabla'\boldsymbol{u}'\cdot\boldsymbol{c}\right) = -\frac{1}{Wi}(1 + \varepsilon(\mathrm{tr}(\boldsymbol{c}) - 3))(\boldsymbol{c} - \boldsymbol{I}) \tag{9}$$

$$\nabla'^2\varnothing' = \frac{1}{2}\left(\frac{H_c}{\lambda_D}\right)^2\left(z_1c_1' + z_2c_2'\right) \tag{10}$$

$$\frac{\partial c_i'}{\partial t'} + \nabla'\cdot\left(\boldsymbol{u}'c_i' - \frac{D_i}{H_cU_0}\nabla'c_i' - \frac{z_iD_i}{H_cU_0}c_i'\nabla'\varnothing'\right) = 0, i = 1, 2 \tag{11}$$

In the above, all the variables with prime indicate their dimensionless form; the Debye length is $\lambda_D = \sqrt{\varepsilon_f RT/\sum_{i=1}^{2} F^2z_i^2C_0}$; β is the ratio of the solvent viscosity to the total viscosity, i.e., $\beta = \frac{\eta_s}{\eta_0}$; the dimensionless Reynolds number is $Re = \rho U_0H_c/\eta_0$, and Weissenberg number is $Wi = \lambda U_0/H_c$. The boundary conditions are given as follows.

At the symmetric axis, zero normal gradient is applied for all variables.

At the Anode (or Cathode),

$$\mathbf{n}\cdot\nabla'\boldsymbol{u}' = 0,\ p' = 0,\ \varnothing' = V_0\cdot\frac{F}{RT}\ (\text{or } 0), c_i' = 1,\ \mathbf{n}\cdot\nabla'\boldsymbol{c} = 0 \tag{12}$$

where **n** represents the normal unit vector on the surface.

On the nanochannel wall with a uniform surface charge density σ_s,

$$\boldsymbol{u}' = 0,\ \mathbf{n}\cdot\nabla'\varnothing' = \sigma_s\cdot\frac{H_cF}{RT}, -\mathbf{n}\cdot\nabla' c_i' - z_i c_i'\mathbf{n}\cdot\nabla'\varnothing' = 0,\ \mathbf{n}\cdot\nabla'\boldsymbol{c} = 0 \tag{13}$$

On the surfaces of reservoir (i.e., AB and EF), a symmetric boundary condition is imposed to account for the large size reservoirs.

The initial conditions are set as

$$\boldsymbol{u}' = 0, \boldsymbol{c} = \boldsymbol{I},\ c_1' = 1,\ c_2' = 1,\ \varnothing' = 0, \text{at } t' = 0 \tag{14}$$

3. Numerical Method and Code Validation

One of the most challenging problems for the numerical simulation of viscoelastic fluid flow is the high Weissenberg Number Problem (HWNP), i.e., the loss of numerical accuracy and stability at a relatively high *Wi* [33–35]. Log conformation reformulation (LCR) method [34] has been shown as one of the most effective strategy to overcome this issue, and is adopted in this study. The procedure is presented as follows.

Due to the symmetric positive definite (SPD) property of conformation tensor **c**, its matrix logarithm exists as

$$\boldsymbol{\Psi} = \log(\boldsymbol{c}) = \mathbf{R}^T\log(\boldsymbol{\Lambda})\mathbf{R} \tag{15}$$

where $\boldsymbol{\Lambda}$ is a diagonal matrix whose diagonal elements are the eigenvalues of $\boldsymbol{c}$; and $\boldsymbol{R}$ is an orthogonal matrix composed of the eigenvectors of $\boldsymbol{c}$.

The equation for the conformation tensor can be rewritten in terms of $\boldsymbol{\Psi}$ as

$$\boldsymbol{u}'\cdot\nabla'\boldsymbol{\Psi} - (\boldsymbol{\Omega}\cdot\boldsymbol{\Psi} - \boldsymbol{\Psi}\cdot\boldsymbol{\Omega}) - 2\boldsymbol{B} = -\frac{1}{Wi}e^{-\boldsymbol{\Psi}}\left(1+\varepsilon\left(\mathrm{tr}\left(e^{\boldsymbol{\Psi}}\right)-3\right)\right)\left(e^{\boldsymbol{\Psi}}-\boldsymbol{I}\right) \tag{16}$$

where $\boldsymbol{\Omega}$ and $\boldsymbol{B}$ are the anti-symmetric matrix and the symmetric traceless matrix of the decomposition of the velocity gradient tensor $\nabla'\mathbf{u}'$, as derived by Fattal and Kupferman [35].

Then, the conformation tensor **c** can be obtained from $\boldsymbol{\Psi}$ as

$$\boldsymbol{c} = \exp(\boldsymbol{\Psi}) \tag{17}$$

To numerically solve the coupled set of Equations (7)–(8), (10)–(11), and (16) along with the boundary and initial conditions, a new solver is implemented in an open source software for CFD–OpenFOAM. QUICK, Gauss Linear, and MINMOD schemes are used to discretize the convection terms in Equations (8), (11), and (16), respectively. Pressure Implicit with Splitting of Operators (PISO) algorithm is used to solve Equation (8). Finer mesh is distributed near the charged wall and a mesh convergence study is conducted to ensure the accuracy of the following simulations.

The developed solver has been shown to accurately simulate the viscoelastic fluid of EOF in a nanoslit [32]. To further check the accuracy and the validity of the developed solver, we simulate a Newtonian EOF in a nanochannel with reservoirs, the geometry of which is used for the following study, and compare the results with that obtained from finite element software Comsol (version 5.1, Comsol, Stockholm, Sweden). The geometric parameters are given as $H_c = 20$ nm, $L_c = 100$ nm, $H_r = 200$ nm, $L_r = 200$ nm, W $= 1$ μm. Other parameters are set as $V_0 = 0.05$ V, $\sigma_s = -0.005\ c/\mathrm{m}^2$, $D_1(D_2) = 1.96\ (2.03)\times10^{-9}\mathrm{m}^2\mathrm{s}^{-1}$, $\varepsilon_f = 7.08\times10^{-10}\mathrm{CV}^{-1}\mathrm{m}^{-1}$.

For the simulations in this study, the time is set long enough that all flows reach steady state, and the steady results are shown below.

Figure 2 shows the comparison of the simulated dimensionless velocity in the channel length direction at the middle cross section of the nanochannel with the results obtained in commercial software Comsol (www.comsol.com) for different bulk salt concentrations, C_0 = 0.5, 5, and 50 mM, corresponding to $\frac{H_c}{2\lambda_D}$ = 0.74, 2.33, and 7.35. Under low salt concentration C_0 = 0.5 mM, as the thickness of EDL is larger than half of the channel height, i.e., the EDLs are overlapping, the velocity gradually increases from the wall and reaches maximum velocity at the center of the nanochannel. For high bulk salt concentration C_0 = 50 mM with thin EDL, the velocity increases to its maximum value within a distance from the charged surface and remains at its maximum value. It is obvious that good agreement between our numerical results and the Comsol simulation is achieved for both cases of thin EDL and overlapping EDLs.

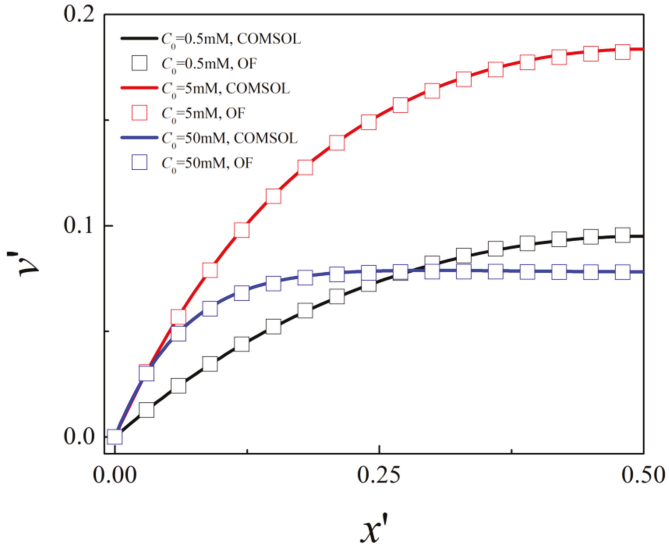

Figure 2. Distribution of the dimensionless axial velocity at the center of the nanochannel for bulk salt concentrations C_0 = 0.5 mM, 5 mM, and 50 mM: symbols (OpenFOAM) and lines (Comsol).

The EOF of viscoelastic fluid in the same geometry is then solved by the validated solver to investigate the effects of Weissenberg number *Wi* on the flow rate and ionic conductance. The viscosity ratio and the extensibility parameter for the LPTT viscoelastic fluid are set to $\beta = 0.1$ and $\varepsilon = 0.25$.

4. Results and Discussion

First of all, the volume flow rate across the channel is calculated at the middle of the channel ($y' = 0$) as $Q = 2WH_cU_0\int_0^{1/2} v'dx'$ for bulk salt concentration C_0 = 0.5 mM, 5 mM, and 50 mM under different Weissenberg *Wi*, as shown in Figure 3. With the same Weissenberg number, the volume flow rate is lowest at C_0 = 0.5 mM, while it is the highest at C_0 = 5 mM. The former is because for low bulk salt concentration C_0 = 0.5 mM, the overall net charge density and thus the electric body force within the nanochannel is low. The highest flow rate at moderate bulk salt concentration C_0 = 5 mM is due to the fact that the EDLs are slightly overlapped, so the net ionic concentration within the nanochannel is higher compared to those for both C_0 = 0.5 mM and C_0 = 50 mM. Under the same bulk salt concentrations, *Q* monotonously increases with *Wi* within the investigated range, which is due to the shear thinning effect of viscoelastic fluid of the LPTT model. Besides this, the increase of flow

rate is more obvious for $Wi < 50$ and becomes less apparent as Wi further increases. This indicates that the effect of Wi on the shear viscosity becomes less apparent with increasing Wi. At Wi =200, the flow rates are 4.95, 7.89, and 9.74 times of that for Newtonian fluid at C_0 = 0.5 mM, 5 mM, and 50 mM, respectively. This indicates that the shear thinning effect is more obvious for the case with smaller EDL thickness.

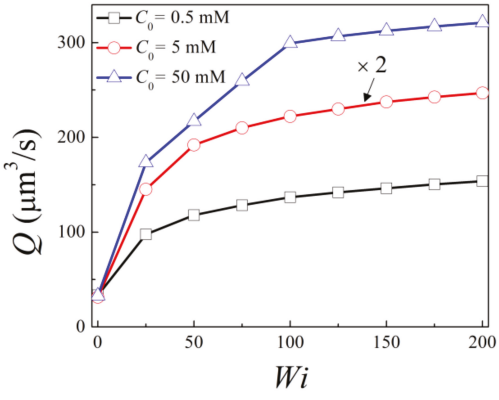

Figure 3. Variation of volume flow rate with the Weissenberg number for bulk concentration C_0 = 0.5 mM, 5 mM, and 50 mM.

The ionic conductance within the nanochannel is calculated as

$$G = \frac{I}{V_0} = \frac{2W}{V_0}\int_0^{H_r/2}\sum_{i=1}^{2} Fz_i\left(vc_i - D_i\frac{\partial c_i}{\partial y} - z_i\frac{D_i}{RT}Fc_i\frac{\partial \varnothing}{\partial y}\right)dx \tag{18}$$

In terms of dimensionless variables, the ionic conductance can be written as

$$\begin{aligned} G &= \frac{2C_0\varepsilon_f R^2T^2W}{V_0\eta_0 \mathrm{F}}\int_0^{\frac{H_r}{2H_c}}\sum_{i=1}^{2} z_i\left(vc_i' - \frac{D_i}{H_cU_0}\frac{\partial c_i'}{\partial y'} - \frac{z_iD_i}{H_cU_0}c_i'\frac{\partial \varnothing'}{\partial y'}\right)dx' \\ &= \frac{2C_0\varepsilon_f R^2T^2W}{V_0\eta_0 \mathrm{F}}\int_0^{\frac{H_r}{2H_c}}\left(v'c_1' - \frac{D_1}{H_cU_0}\frac{\partial c_1'}{\partial y'} - \frac{D_1}{H_cU_0}c_1'\frac{\partial \varnothing'}{\partial y'}\right) \\ &\quad -\left(v'c_2' - \frac{D_2}{H_cU_0}\frac{\partial c_2'}{\partial y'} + \frac{D_2}{H_cU_0}c_2'\frac{\partial \varnothing'}{\partial y'}\right)dx' \end{aligned} \tag{19}$$

It is obvious that the ionic conductance consists of convective, diffusive, and migrative components, which can be written as

$$G_c = \frac{2C_0\varepsilon_f R^2T^2W}{V_0\eta_0 \mathrm{F}}\int_0^{\frac{H_r}{2H_c}} v'\left(c_1' - c_2'\right)dx' \tag{20a}$$

$$G_d = \frac{2C_0\varepsilon_f R^2T^2W}{V_0\eta_0 \mathrm{F}}\int_0^{\frac{H_r}{2H_c}} \frac{1}{H_cU_0}\left(-D_1\frac{\partial c_1'}{\partial y'} + D_2\frac{\partial c_2'}{\partial y'}\right)dx' \tag{20b}$$

$$G_m = \frac{2C_0\varepsilon_f R^2T^2W}{V_0\eta_0 \mathrm{F}}\int_0^{\frac{H_r}{2H_c}} \frac{1}{H_cU_0}\frac{\partial \varnothing'}{\partial y'}\left(-D_1c_1' - D_2c_2'\right)dx' \tag{20c}$$

Figure 4 shows the variation of the ionic conductance with the Weissenberg number for bulk salt concentrations of C_0 = 0.5 mM, 5 mM, and 50 mM, respectively. For C_0 = 0.5 mM and 5 mM, apparent increase of ionic conductance is seen for viscoelastic fluid compared to that of the Newtonian fluid, and the ionic conductance monotonously increase with Wi. Similar to the trend of the flow rate, the increase becomes less obvious for higher Wi. For 50 mM, ionic conductance slightly increases for viscoelastic fluid at Wi = 50 compared to the Newtonian fluid, and remains almost constant as Wi further increases.

At *Wi* = 200, the ionic conductance is 1.27, 1.20, and 1.03 times that for Newtonian fluid under bulk salt concentrations of C_0 = 0.5 mM, 5 mM, and 50 mM, respectively. Thus, the enhancement of ionic conductance is more obvious for low salt concentration, under which the EDLs are highly overlapped, and becomes less apparent as C_0 increases. When the bulk salt concentration is relatively high, the effect of viscoelasticity on the ionic conductance is negligible.

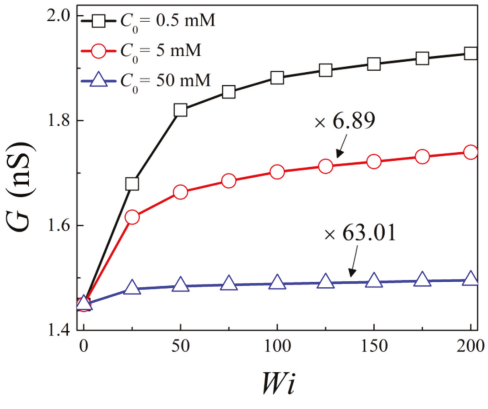

Figure 4. Variation of ionic conductance with Weissenberg number for C_0 = 0.5 mM, 5 mM, and 50 mM.

The variation of ionic conductance with *Wi* for different bulk concentrations can be analyzed by the contributions of the convective, diffusive, and migrative components in Equation (20). Figure 5 presents the percentage of the convective and migrative components for Newtonian fluid and viscoelastic fluid of *Wi* = 200 at C_0 = 0.5 mM, 5 mM and 50 mM, respectively. The diffusive component is not shown due to the fact that for all cases, the percentage of diffusive conductance is less than 0.5%, and thus its contribution is negligible. Besides this, to better compare the results of the Newtonian fluid and the viscoelastic fluid, the percentage of viscoelastic is shown with respect to the Newtonian fluid under the same C_0. For viscoelastic of *Wi* = 200, an apparent increase in the convective ionic conductance is observed compared to that of the Newtonian fluid, while an obvious decrease of migrative component is seen for viscoelastic fluid. The increase of the convective ionic conductance is due to shear thinning effect, as it is proportional to the mainstream velocity. The decrease of migrative ionic conductance stems from the change in the distributions of the electric potential and the ionic concentration under the presence of viscoelasticity. The increase of the convective component exceeds the decrease of the migrative component, resulting in an overall increase of the ionic conductance. Besides this, at low bulk salt concentration, the ratio of the convective component to the migrative component is relatively large, thus the increase of convective component for viscoelastic fluid contributes significantly to the increase of the total ionic conductance. As the bulk salt concentration increases, the contribution of the convective component becomes smaller, thus the increase of the total ionic conductance for viscoelastic fluid becomes less significant. In Newtonian fluid, the migrative component dominates for all three salt concentrations, while in viscoelastic fluid the convective component dominates when the EDLs are overlapped.

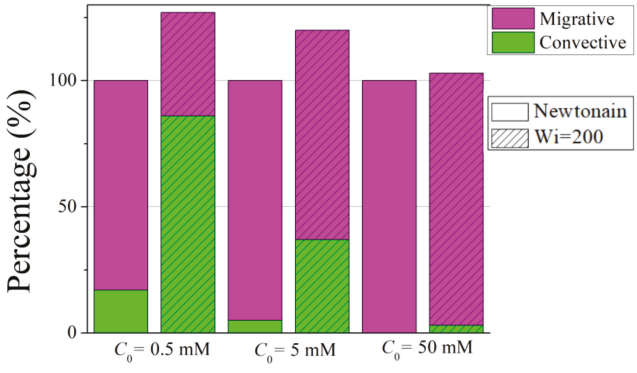

Figure 5. Percentage of the convective and migrative ionic conductance components for Newtonian and viscoelastic fluids of Wi = 200 for C_0 = 0.5 mM, 5 mM, and 50 mM, respectively. For clarity, the percentage of the components for viscoelastic fluid is shown with respect to the Newtonian fluid under the same bulk salt concentration. Thus, the total height for viscoelastic fluid becomes 127%, 120%, and 103% for C_0 = 0.5 mM, 5 mM, and 50 mM, respectively.

Figure 6 depicts the distribution of the dimensionless $\frac{\partial \varnothing'}{\partial y'}$ along the centerline of the nanochannel for Newtonian fluid and viscoelastic fluid of Wi = 200 for the case of overlapped EDLs (i.e., C_0 = 0.5 mM). Within the confined nanochannel, the value of $\frac{\partial \varnothing'}{\partial y'}$ remains almost constant, while a sharp increase (decrease) occurs near the opening at the Cathode (Anode) side. This variation arises from the large change of net charge density within the solution in both reservoirs compared to the region near the nanochannel, due to the highly overlapped EDLs. Besides this, it is noticed that within the confined nanochannel, a decrease in the magnitude of $\frac{\partial \varnothing'}{\partial y'}$ occurs for viscoelastic fluid compared to the Newtonian fluid. This decrease explains the decrease in the migrative ionic conductance, which is proportional to $\frac{\partial \varnothing'}{\partial y'}$. However, the effect of viscoelasticity on the electric potential distribution is not significant. This can be explained as following. As the surface charge density is assumed to be uniformly distributed at the nanochannel wall, the induced EOF velocity is almost parallel to the nanochannel surface. Under this condition, the ionic distribution and thus the electric potential is mainly determined by the surface charge density, and the increase of EOF velocity has negligible effect on the electric potential [36].

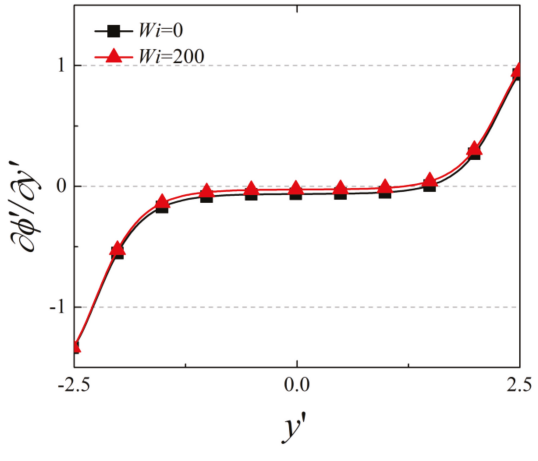

Figure 6. The variation of $\frac{\partial \varnothing'}{\partial y'}$ along the symmetry axis of the nanochannel for C_0 = 0.5 mM.

5. Conclusions

Numerical simulation on the EOF of viscoelastic fluid with an LPTT model in a nanochannel connecting two reservoirs is carried out with a new finite volume solver implemented in OpenFOAM. The implemented solver is validated by comparing the result of the current simulation with that from commercial finite element software Comsol for Newtonian fluid with the same geometry. For the first time, the condition of highly overlapped EDLs is taken into consideration for the EOF of viscoelastic fluid. Besides this, the surface charge density is much larger than the typical value used for the theoretical study in microscale, where the linearization is used to solve for the electric potential. Obvious increase in the volume flow rate is obtained for the viscoelastic fluid compared to Newtonian fluid due to the shear thinning effect of LPTT fluid. The enhancement is more significant under high bulk salt concentration where EDL is not overlapped. An enhancement in ionic conductance also occurs for viscoelastic fluid, and the enhancement becomes less significant as the bulk salt concentration increases. The increase of the ionic conductance arises from the increase of its convective component, which is directly proportional to the enhanced EOF velocity. In contrast to Newtonian fluid, where migrative ionic conductance always dominates over the convective and diffusive components, the convective current becomes dominant when the EDLs are overlapped for viscoelastic fluid. As the bulk salt concentration increases, the contribution of the convective ionic conductance decreases and the enhancement in the ionic conductance for the viscoelastic fluid becomes less significant.

Author Contributions: Numerical Simulation, L.M.; Writing—original draft, L.M.; Revision and Supervision, S.Q.

Conflicts of Interest: The authors declare no conflict of interest.

References

1. Hsu, W.-L.; Daiguji, H. Manipulation of protein translocation through nanopores by flow field control and application to nanopore sensors. *Anal. Chem.* **2016**, *88*, 9251–9258. [CrossRef] [PubMed]
2. Park, M.C.; Kim, M.; Lim, G.T.; Kang, S.M.; An, S.S.A.; Kim, T.S.; Kang, J.Y. Droplet-based magnetic bead immunoassay using microchannel-connected multiwell plates (μCHAMPs) for the detection of amyloid beta oligomers. *Lab Chip* **2016**, *16*, 2245–2253. [CrossRef] [PubMed]
3. Chen, X.; Zhang, S.; Zhang, L.; Yao, Z.; Chen, X.; Zheng, Y.; Liu, Y. Applications and theory of electrokinetic enrichment in micro-nanofluidic chips. *Biomed. Microdevices* **2017**, *19*, 19. [CrossRef] [PubMed]
4. Plecis, A.; Nanteuil, C.M.; Haghiri-Gosnet, A.-M.; Chen, Y. Electropreconcentration with charge-selective nanochannels. *Anal. Chem.* **2008**, *80*, 9542–9550. [CrossRef]
5. Karniadakis, G.; Beskok, A.; Aluru, N. *Microflows and Nanoflows: Fundamentals and Simulation*; Springer: Berlin, Germany, 2006.
6. Reuss, F. Charge-induced flow. *Proc. Imp. Soc. Nat. Mosc.* **1809**, *3*, 327–344.
7. Li, L.; Wang, X.; Pu, Q.; Liu, S. Advancement of electroosmotic pump in microflow analysis: A review. *Anal. Chimica Acta* **2019**, *1060*, 1–16. [CrossRef]
8. Di Fraia, S.; Massarotti, N.; Nithiarasu, P. Modelling electro-osmotic flow in porous media: A review. *Int. J. Numer. Method. Heat Fluid Flow* **2018**, *28*, 472–497. [CrossRef]
9. Shehzad, N.; Zeeshan, A.; Ellahi, R. Electroosmotic flow of MHD power law Al2O3-PVC nanouid in a horizontal channel: Couette-Poiseuille flow model. *Commun. Theor. Phys.* **2018**, *69*, 655. [CrossRef]
10. Ma, Y.; Yeh, L.-H.; Lin, C.-Y.; Mei, L.; Qian, S. pH-regulated ionic conductance in a nanochannel with overlapped electric double layers. *Anal. Chem.* **2015**, *87*, 4508–4514. [CrossRef]
11. Rashidi, S.; Bafekr, H.; Valipour, M.S.; Esfahani, J.A. A review on the application, simulation, and experiment of the electrokinetic mixers. *Chem. Eng. Proc. Process Intensif.* **2018**, *126*, 108–122. [CrossRef]
12. Huang, M.-J.; Mei, L.; Yeh, L.-H.; Qian, S. pH-Regulated nanopore conductance with overlapped electric double layers. *Electrochem. Commun.* **2015**, *55*, 60–63. [CrossRef]
13. Baldessari, F. Electrokinetics in nanochannels: Part I. Electric double layer overlap and channel-to-well equilibrium. *J. Colloid Interface Sci.* **2008**, *325*, 526–538. [CrossRef] [PubMed]
14. Kim, S.J.; Wang, Y.-C.; Lee, J.H.; Jang, H.; Han, J. Concentration polarization and nonlinear electrokinetic flow near a nanofluidic channel. *Phys. Rev. Lett.* **2007**, *99*, 044501. [CrossRef] [PubMed]

15. Zimmerman, W.; Rees, J.; Craven, T. Rheometry of non-Newtonian electrokinetic flow in a microchannel T-junction. *Microfluid. Nanofluid.* **2006**, *2*, 481–492. [CrossRef]
16. Nam, J.; Lim, H.; Kim, D.; Jung, H.; Shin, S. Continuous separation of microparticles in a microfluidic channel via the elasto-inertial effect of non-Newtonian fluid. *Lab Chip* **2012**, *12*, 1347–1354. [CrossRef] [PubMed]
17. Zhao, C.; Yang, C. Electro-osmotic mobility of non-Newtonian fluids. *Biomicrofluidics* **2011**, *5*, 014110. [CrossRef] [PubMed]
18. Bello, M.S.; De Besi, P.; Rezzonico, R.; Righetti, P.G.; Casiraghi, E. Electroosmosis of polymer solutions in fused silica capillaries. *Electrophoresis* **1994**, *15*, 623–626. [CrossRef]
19. Chang, F.-M.; Tsao, H.-K. Drag reduction in electro-osmosis of polymer solutions. *Appl. Phys. Lett.* **2007**, *90*, 194105. [CrossRef]
20. Huang, Y.; Chen, J.; Wong, T.; Liow, J.-L. Experimental and theoretical investigations of non-Newtonian electro-osmotic driven flow in rectangular microchannels. *Soft Matter* **2016**, *12*, 6206–6213. [CrossRef]
21. Zhao, C.; Yang, C. An exact solution for electroosmosis of non-Newtonian fluids in microchannels. *J. Non-Newton. Fluid Mech.* **2011**, *166*, 1076–1079. [CrossRef]
22. Zhao, C.; Yang, C. Nonlinear Smoluchowski velocity for electroosmosis of Power-law fluids over a surface with arbitrary zeta potentials. *Electrophoresis* **2010**, *31*, 973–979. [CrossRef] [PubMed]
23. Tang, G.; Li, X.; He, Y.; Tao, W. Electroosmotic flow of non-Newtonian fluid in microchannels. *J. Non-Newton. Fluid Mech.* **2009**, *157*, 133–137. [CrossRef]
24. Choi, W.; Joo, S.W.; Lim, G. Electroosmotic flows of viscoelastic fluids with asymmetric electrochemical boundary conditions. *J. Non-Newton. Fluid Mech.* **2012**, *187*, 1–7. [CrossRef]
25. Mukherjee, S.; Das, S.S.; Dhar, J.; Chakraborty, S.; DasGupta, S. Electroosmosis of viscoelastic fluids: Role of wall depletion layer. *Langmuir* **2017**, *33*, 12046–12055. [CrossRef]
26. Martínez, L.; Bautista, O.; Escandón, J.; Méndez, F. Electroosmotic flow of a Phan-Thien–Tanner fluid in a wavy-wall microchannel. *Colloid. Surf. A Physicochem. Eng. Asp.* **2016**, *498*, 7–19. [CrossRef]
27. Park, H.; Lee, W. Helmholtz–Smoluchowski velocity for viscoelastic electroosmotic flows. *J. Colloid Interface Sci.* **2008**, *317*, 631–636. [CrossRef]
28. Afonso, A.; Alves, M.; Pinho, F. Analytical solution of mixed electro-osmotic/pressure driven flows of viscoelastic fluids in microchannels. *J. Non-Newton. Fluid Mech.* **2009**, *159*, 50–63. [CrossRef]
29. Dhinakaran, S.; Afonso, A.; Alves, M.; Pinho, F. Steady viscoelastic fluid flow between parallel plates under electro-osmotic forces: Phan-Thien–Tanner model. *J. Colloid Interface Sci.* **2010**, *344*, 513–520. [CrossRef]
30. Mei, L.; Yeh, L.-H.; Qian, S. Gate modulation of proton transport in a nanopore. *Phys. Chem. Chem. Phys.* **2016**, *18*, 7449–7458. [CrossRef]
31. Haywood, D.G.; Harms, Z.D.; Jacobson, S.C. Electroosmotic flow in nanofluidic channels. *Anal. Chem.* **2014**, *86*, 11174–11180. [CrossRef]
32. Mei, L.; Zhang, H.; Meng, H.; Qian, S. Electroosmotic flow of viscoelastic fluid in a nanoslit. *Micromachines* **2018**, *9*, 155. [CrossRef] [PubMed]
33. Comminal, R.; Spangenberg, J.; Hattel, J.H. Robust simulations of viscoelastic flows at high Weissenberg numbers with the streamfunction/log-conformation formulation. *J. Non-Newton. Fluid Mech.* **2015**, *223*, 37–61. [CrossRef]
34. Fattal, R.; Kupferman, R. Time-dependent simulation of viscoelastic flows at high Weissenberg number using the log-conformation representation. *J. Non-Newton. Fluid Mech.* **2005**, *126*, 23–37. [CrossRef]
35. Fattal, R.; Kupferman, R. Constitutive laws for the matrix-logarithm of the conformation tensor. *J. Non-Newton. Fluid Mech.* **2004**, *123*, 281–285. [CrossRef]
36. Grigoriev, R.; Schuster, H.-G. *Transport and Mixing in Laminar Flows: From Microfluidics to Oceanic Currents*; Wiley-VCH: Hoboken, NJ, USA, 2012.

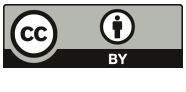

micromachines

MDPI

Article

Multifrequency Induced-Charge Electroosmosis

Kai Du [1], Jingni Song [1], Weiyu Liu [1,*], Ye Tao [2,*] and Yukun Ren [2,*]

[1] School of Electronics and Control Engineering, and School of Highway, Chang'an University, Middle-Section of Nan'er Huan Road, Xi'an 710064, China

[2] State Key Laboratory of Robotics and System, Harbin Institute of Technology, West Da-Zhi Street 92, Harbin 150001, China

* Correspondence: liuweiyu@chd.edu.cn (W.L.); tarahit@gmail.com (Y.T.); rykhit@hit.edu.cn (Y.R.); Tel.: +86-029-82334543 (W.L.); +86-0451-86418028 (Y.R.); Fax: +86-029-82334555 (W.L.); +86-0451-86402658 (Y.R.)

Received: 5 June 2019; Accepted: 1 July 2019; Published: 3 July 2019

Abstract: We present herein a unique concept of multifrequency induced-charge electroosmosis (MICEO) actuated directly on driving electrode arrays, for highly-efficient simultaneous transport and convective mixing of fluidic samples in microscale ducts. MICEO delicately combines transversal AC electroosmotic vortex flow, and axial traveling-wave electroosmotic pump motion under external dual-Fourier-mode AC electric fields. The synthetic flow field associated with MICEO is mathematically analyzed under thin layer limit, and the particle tracing experiment with a special powering technique validates the effectiveness of this physical phenomenon. Meanwhile, the simulation results with a full-scale 3D computation model demonstrate its robust dual-functionality in inducing fully-automated analyte transport and chaotic stirring in a straight fluidic channel embedding double-sided quarter-phase discrete electrode arrays. Our physical demonstration with multifrequency signal control on nonlinear electroosmosis provides invaluable references for innovative designs of multifunctional on-chip analytical platforms in modern microfluidic systems.

Keywords: multifrequency induced-charge electroosmosis; simultaneous pumping and convective mixing; dual-Fourier-mode AC forcing; traveling-wave/standing-wave AC electroosmosis; microfluidics

1. Introduction

Mixing two or multiple sample streams within a confined fluidic channel is important and challenging in the fields of chemical engineering, biomedical diagnostics, electronic cooling, and drug discovery [1]. A number of methods have been proposed over the past decade to enhance sample blending at the nanoliter scale, and can be chiefly classified into either passive or active mixer decided by the underlying fluid physics [2,3]. Since passive mixing extends the contact phase interface, increases the diffusion time, and destabilizes the laminar flow mode between co-flowing liquid media driven by an external pressure gradient, by inserting complex curved geometry or solid barriers into the internal channel, it depends entirely on molecular diffusion or hydrodynamic chaotic advection. [4]. On the other hand, active microfluidic mixers exploit external energy input to initiate fluid motion for improving the device mixing efficiency—e.g., acoustic/ultrasonic, magnetic, electrochemical, laser, and electrokinetic approaches [5]. In particular, electrohydrodynamic (EHD) fluid flow has been broadly applied in microsystems to realize ample mixing of fluidic samples [6–9]. The recent development of microelectronic processing technology has allowed for an ease at which closely packed microscale electrode arrays can be patterned and integrated into microfluidic channels. This opens up a new opportunity for imparting dynamic electrokinetic forces to the liquid medium by employing an external AC electric field [10–15]. In contrast with linear electroosmotic streaming on insulating charged channel sidewalls, EHD fluid motion appears as a series of flow vortex above an array of ideally polarizable

metal-strip electrodes, and the voltage required is commonly no more than dozens of volts [16,17]. In this way, AC nonlinear electrokinetics is able to achieve a higher degree of freedom control on localized flow behavior, and finds interesting applications in pumping, mixing, and separation of target analyte in the context of microfluidics, in virtue of its superior flexibility by adjusting the amplitude, phase gradient, and field frequencies of the voltage wave, namely, AC electrothermal (ACET) [18–38] and AC electroosmosis (ACEO) [39–53].

ACET is originated by Maxwell-Wagner smeared structural polarization [54]. In order for the Gauss law and current continuity condition to be satisfied at the same time, charged ionic clouds are induced across a thermal gradient inside the bulk fluid submitted to external AC excitations. These induced sinusoidal charges are in turn acted by the same-frequency harmonic electric field to exert a time-averaged DEP force on the liquid body, which is proportional to the voltage squared (external heating) or fourth-power value (internal heating), and therefore steady convection of aqueous solution can be expected even in oscillating fields [55]. In the latter, since the electrothermal body force increases linearly with the liquid ionic strength to the leading order, ACET is effective in driving high-conductivity biofluids within the range of 0.05–5 S/m. However, for dilute electrolyte with conductivity no more than 0.01 S/m, ACET will lose effect, unless artificial heating elements are delicately embedded into the insulating substrate, while doing this would need intricate micromachining steps.

Unlike ACET that causes electroconvection in the bulk phase of concentrated solutions, ACEO is a kind of surface streaming flow, in which the electrostatic interaction of the external AC voltage wave with its own induced charge cloud within an induced double layer (IDL) drives a net electrokinetic slipping flow right outside the Debye layer [56–58]. Since it relies mainly on electrochemical polarization at the electrode/electrolyte interface, ACEO serves as a method of choice for actuating fluid flows of dilute electrolyte, wherein ion overscreening rather than overcrowding dominates for low ion-conductivity environment [59,60]. It has been reported that both standing-wave (SW) and traveling-wave (TW) AC voltage signals can be utilized for producing ACEO streaming flows in microchannel embedding metal-strip electrode arrays. SW-induced ACEO usually generates vortex fluid motion adjacent to the oppositely-polarized electrode pair, with great potential in causing analyte mixing [61]. On the other hand, TW-induced ACEO (TWEO) can induce parallel streamlines above a linear electrode track of continuous phase transition in sinusoidal voltage at the double-layer dispersion frequency [62–67]. To the best of our knowledge, however, ACEO and TWEO have never been applied together in the same fluidic device before, and the scientific information of their combined effect on the resultant microflow behavior is still missing as well.

To address the above issue, we present herein a unique concept of multifrequency nonlinear induced-charge electroosmotic (MICEO) streaming, in terms of a brand-new manipulation tool of particle and liquid contents in microfluidic systems. As shown in Figure 1, two types of AC signals of distinct field frequencies—i.e., one standing and one traveling potential wave—are first added together and then imposed to double-sided discrete electrode array arranged on either side of the channel sidewalls. A mathematical analysis considering dual Fourier-mode actuation indicates that, the global feature of the electrokinetic flow streamlines can be flexibly adjusted by making a change in the voltage amplitudes and exciting frequencies of the hybrid SW/TW signals. The synthetic flow field pertinent to MICEO can be made to either have greater vorticity or produce faster unidirectional pump flow rate, as ACEO or TWEO of distinct actuating frequencies dominates the resultant fluid physics, respectively. Then, the effectiveness of this physical phenomenon is validated by particle tracing experiment above a confocal spiral microelectrode array using a special powering technique. Finally, by conducting direct numerical simulation, we visually clarified that MICEO in the presence of both in-phase and out-of-phase electrode polarizations can spawn a series of EHD micro-vortices in the lateral direction and ICEO fluid transport along the axial direction, which is in favor of realizing simultaneous unidirectional delivery and convective mixing of nanoparticles even without the need of the application of an external pressure gradient. These results offer precious physical insight into developing flexible microfluidic platforms for fully-automated sample treatment with MICEO.

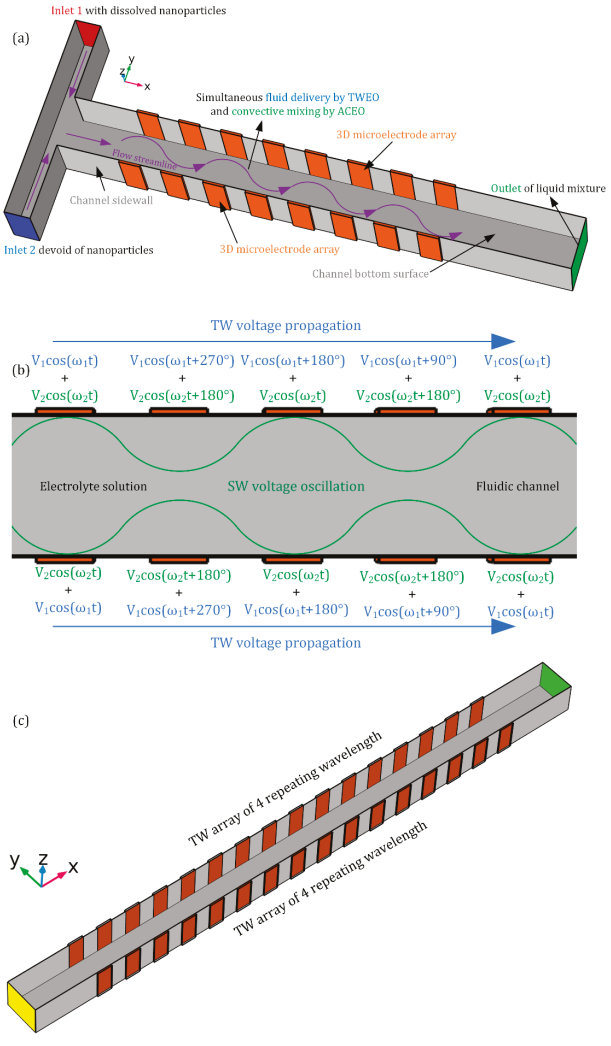

Figure 1. 3D schematic diagram of MICEO-enabled pump-free liquid transport and mixing in a microfluidic device embedding double-sided 3D metal-strip electrode arrays. For a proof of concept study, a discrete quarter-phase *TW* voltage signal of amplitude V_1 (V_{TW}) and field frequency f_1(f_{TW}), as well as a *SW* potential gradient of amplitude V_2 (V_{SW}) and oscillating frequency f_2 (f_{SW}) are first superimposed and then applied to the sidewall discrete electrode arrangement. During exposure to the dual-frequency phase-shifted electric fields, any micro/nano-scale solid entities within the working fluid can be delivered unidirectionally by TWEO and stirred by transverse ACEO vortex flow field at the same time. (**a**) In this way, we can realize simultaneous pumping and convective mixing of chemical analytes in a straight microchannel by introducing the fluid physics of MICEO. (**b**) Detailed information on the voltage signals imposed on the sidewall electrode arrays. A progressively phase-shifted traveling potential wave of four discrete phases oscillates at frequency ω_1 and propagates toward the downstream outlet port, which is then effectively added to a standing-wave voltage gradient at frequency ω_2. The synthetic electrical signal is ultimately imposed to the consecutively-distributed 3D sidewall electrode strips for inducing helical streamlines that enable the device dual role in pumping and mixing at the same time. (**c**) The full-scale 3D computational domain applied in the FEM-based commercial software package (Comsol Multiphysics 5.3a).

2. Methods

2.1. Geometry Configuration of the MICEO-Enabled Microfluidic Device for Simulations Study

In this work, we first conducted a theoretical and simulation analysis on the flow pattern of MICEO adjacent to two parallel traveling-wave electrode arrays of four discrete phases, which are arranged on the opposite sides of the fluidic channel having a vertical height of H_c, as shown in Figure 1. The basic device geometry for enabling MICEO streaming next to the ideally polarizable phase-shifted metal strips is displayed in Figure 1a, wherein the central canal of width W_c and length L_c is sandwiched by two linear *TW* electrode tracks of $n = 4$ repeating wavelength on both sides.

Two AC potential waves of distinct oscillating frequencies are applied to the multiphase discrete electrode arrangement at the same time. Firstly, a progressively phase-shifted *TW* voltage signal with four discrete phases is imposed to the two electrode strip layers of nanometer thickness in sequence, which are mounted on both channel sidewalls along the channel length direction. A discrete traveling-voltage wave of an explicit form, $\phi_1^i = V_1 \cos(\omega_1 t - 2\pi(i-1)/4)$, where $i = 1, 2, 3, 4$ denotes the i-th electrode, moves along the level of linear electrode track towards the channel exit. Since both electrode width and separation have an identical size W_E, the *TW* voltage has a wavelength of $\lambda = 8W_E$ that reflects the spatial periodicity of the Fourier mode causing out-of-phase electrochemical polarization. Secondly, we apply an in-phase *SW* potential gradient to the adjacent oppositely-polarized electrodes, i.e., $\phi_2^i = V_2 \cos(\omega_2 t - 2\pi(i-1)/2)$, where $i = 1, 2$ stands for the i-th electrode in every repeating wavelength. It is noteworthy that *TW* and *SW* electric fields have distinct driving frequencies (ω_1 and ω_2, respectively), so that the hybrid sinusoidal voltage signal has a dual Fourier-mode nature, as shown in Figure 1b.

While ACEO fluid motion produced by the *SW* electric field gives rise to series of chaotic micro-vortices along the channel width direction, TWEO due to the traveling potential wave applied along the level of the discrete electrode arrangement produces a quite constant pump flow component along the length direction. Consequently, these two kinds of nonlinear electroosmotic flow fields, both of which intersect perpendicularly with one another, may coact and produce helical streamlines that are able to continuously transport and stir the incoming fluidic samples, even without an external pressure difference, as shown in Figure 1a.

2.2. Theory and Mathematical Model of Multi-Frequency ICEO

In ACEO, the normal potential gradient is responsible for charging IDL capacitance, which is subsequently driven by the tangential counterpart into electroconvection. So, ICEO fluid motion has a quadratic dependence on the imposed voltage, and therefore it is still valid under low-frequency AC forcing. In the scientific history, Ramos and co-workers [56] conducted the most pioneering investigations of induced double layer (IDL) charging on coplanar electrodes subjected to a low-frequency harmonic actuation, wherein the initial normal field component is provided by the free surface charge induced on conducting surfaces, and unveiled that the electric field right outside the diffuse screening cloud supplied by the metal strips can act on its own induced counterionic charge layer at the ideally polarizable surfaces of block electrodes, so as to generate ACEO under field frequencies on the order of the inverse *RC* time constant for electrochemical ion relaxation. Since the Debye screening charge appears as a consequence of the externally-imposed voltage gradient, both the induced surface charge and tangential AC forcing are sinusoidal functions of the observation time, resulting in net electrokinetic streaming, even in low-frequency alternating fields.

Following the pioneering work of Ramos and co-workers [57,58] on ACEO in microchannels embedding coplanar electrode strips, Bazant and Squires [43,44] argued that an externally-applied background electric field can push forward its own induced counterion charge within the diffuse double layer on a polarizable solid surface immersed in electrolytes. In this way, a nonlinear Coulomb force is exerted inside the thin Debye layer, and they make use of the academic term 'induced-charge electroosmosis (ICEO)' to vividly illustrate the interesting phenomenon of nonlinear electroosmotic

streaming on solid surfaces of finite electrical properties. ICEO conceptually includes ACEO/TWEO on electrode arrays subjected to external wiring, and ICEO on floating leaky dielectric solid surfaces, as well as electroconvective instability (EI) near a ion-selective medium [44].

In current analysis, since each individual metal strip in the double-sided electrode array has an explicit AC potential pre-set by a multiphase sinewave generator, we choose to use the term ACEO or TWEO to indicate that the nonlinear electroosmosis is directly originated from the surface of driving electrodes and there are no floating electrodes in the device channel.

The hybrid TW/SW electrical signal contains two Fourier modes of distinct field frequencies, i.e., $f_1 = f_{\mathrm{tw}}$ and $f_2 = f_{\mathrm{sw}}$. In fact, it is reasonable to solve for the *TW* and *SW* fields separately, in analogy to the mathematical treatment of multifrequency DEP [68]. A commercial software package, COMSOL Multiphysics (version 5.3a) is used to numerically obtain the flow field of TWEO, ACEO, as well as their combined effect on sample treatment.

Our theoretical analysis hires the linear *RC* circuit theory which is valid under the Debye-Hückel limit. Therefore, we can safely divide the microsystem into two contiguous regions, including the IDL on the electrode surface and bulk phase of the liquid solution. Within the latter, to the leading order, the ion concentration is homogenous, so the electric current conservation is safely reduced to the Laplace equation for both the *TW* and *SW* fields [6]

$$\nabla^2 \widetilde{\phi}_1 = 0 \text{ (for } TW \text{ field component)} \tag{1a}$$

$$\nabla^2 \widetilde{\phi}_2 = 0 \text{ (for } SW \text{ field component)} \tag{1b}$$

In above equations, we have invoked complex variable analysis under sinusoidal excitations, that is, $\phi_1(\mathrm{t}) = \mathrm{Re}(\widetilde{\phi}_1 e^{j\omega_1 t})$ and $\phi_2(\mathrm{t}) = \mathrm{Re}(\widetilde{\phi}_2 e^{j\omega_2 t})$. The IDL at the ideally polarizable interface is in effect a series capacitance of a Stern layer C_S, and a diffuse layer $C_D = \varepsilon/\lambda_D$. Here, λ_D denotes Debye length, and ε the solution permittivity. The combined capacity has a value of $C_0 = C_D C_S/(C_D + C_S) = C_D/(1+\delta)$, in terms of the surface impedance ratio $\delta = C_D/C_s$. Counterion screening inside the liquid phase enters into consideration, so to account for the Coulomb force within the IDL. Accordingly, the Ohm current from the bulk has to relay the displacement current flowing across the thin boundary layer, in terms of a current continuity on the surface of those metal strips [69–72]

$$\sigma \boldsymbol{n} \cdot \nabla \widetilde{\phi}_1 = j\omega_1 \frac{C_D}{1+\delta}(\widetilde{\phi}_1 - \widetilde{\phi}_1^i) \text{ for the } i\text{th terminal in the } TW \text{ field} \tag{2a}$$

$$\sigma \boldsymbol{n} \cdot \nabla \widetilde{\phi}_2 = j\omega_2 \frac{C_D}{1+\delta}(\widetilde{\phi}_2 - \widetilde{\phi}_2^i) \text{ for the } i\text{th terminal in the } SW \text{ field} \tag{2b}$$

where σ is the liquid conductivity, $\widetilde{\phi}_1/\widetilde{\phi}_2$ the TW/SW potential at the IDL's outer rim. $\widetilde{\phi}_1^i/\widetilde{\phi}_2^i$ denotes the TW/SW body potential of the i-th sidewall electrode in each repeating wavelength, and $\boldsymbol{n}$ the unit vector normal to the conducting surface. We can get a characteristic *RC* dispersion frequency $f_{RC} = (1+\delta)\sigma\lambda_D/2\pi\varepsilon \mathrm{W_E} = \mathrm{O}(10^{2\sim3})$ Hz in the context of dilute electrolyte according to Equation (2).

The zeta potential phasor induced by the TW/SW signals, as well as the natural counterpart across the diffuse screening cloud are respectively given by

$$\widetilde{\zeta}_1 = \frac{1}{1+\delta}(\widetilde{\phi}_i^i - \widetilde{\phi}_1) \text{ (zeta potential for } TW \text{ field)} \tag{3a}$$

$$\widetilde{\zeta}_2 = \frac{1}{1+\delta}(\widetilde{\phi}_2^i - \widetilde{\phi}_2) \text{ (zeta potential for } SW \text{ field)} \tag{3b}$$

$$\zeta_{\mathrm{fixed}} = \frac{\sigma_{\mathrm{free}}\lambda_D}{\varepsilon} \text{ (natural zeta potential)} \tag{3c}$$

where σ_{free} denotes the fixed charge density on insulating charged surfaces due to chemical adsorption. Since the discrete electrode array is physically embedded on channel sidewalls, Coulomb force within

the electrical double layer overwhelms any other electrokinetics, resulting in a hybrid ICEO slip flow at the solid/electrolyte interface

$$\begin{aligned} \boldsymbol{u}_{slip}(\mathrm{t}) &= \tfrac{-\varepsilon}{\eta}(\zeta_{\mathrm{fixed}} + \mathrm{Re}(\widetilde{\zeta}_1 e^{j\omega_1 t}) + \mathrm{Re}(\widetilde{\zeta}_2 e^{j\omega_2 t}))(\mathrm{Re}(\widetilde{\boldsymbol{E}}_1^t e^{j\omega_1 t}) + \mathrm{Re}(\widetilde{\boldsymbol{E}}_2^t e^{j\omega_2 t})) \\ &= \tfrac{-\varepsilon}{\eta}\left[\begin{array}{l} \zeta_{\mathrm{fixed}}(\mathrm{Re}(\widetilde{\boldsymbol{E}}_1^t e^{j\omega_1 t}) + \mathrm{Re}(\widetilde{\boldsymbol{E}}_2^t e^{j\omega_2 t})) + \mathrm{Re}(\widetilde{\zeta}_1 e^{j\omega_1 t})\mathrm{Re}(\widetilde{\boldsymbol{E}}_1^t e^{j\omega_1 t}) + \mathrm{Re}(\widetilde{\zeta}_1 e^{j\omega_1 t})\mathrm{Re}(\widetilde{\boldsymbol{E}}_2^t e^{j\omega_2 t}) \\ +\mathrm{Re}(\widetilde{\zeta}_2 e^{j\omega_2 t})\mathrm{Re}(\widetilde{\boldsymbol{E}}_1^t e^{j\omega_1 t}) + \mathrm{Re}(\widetilde{\zeta}_2 e^{j\omega_2 t})\mathrm{Re}(\widetilde{\boldsymbol{E}}_2^t e^{j\omega_2 t}) \end{array}\right] \end{aligned} \quad (4)$$

With unequal driving frequencies ($f_1 \neq f_2$), the time-averaged slipping velocity resulted from the hybrid TW/SW voltage signal is given by

$$\left\langle \boldsymbol{u}_{\mathrm{slip}} \right\rangle = \frac{-\varepsilon}{2\eta}\mathrm{Re}(\widetilde{\zeta}_1 \widetilde{\boldsymbol{E}}_1^{t\,*}) + \frac{-\varepsilon}{2\eta}\mathrm{Re}(\widetilde{\zeta}_2 \widetilde{\boldsymbol{E}}_2^{t\,*}) \quad (5)$$

where the asterisk * denotes the complex conjugate, $< \ldots >$ the time-average operator, the superscript t the tangential electric field component. From preceding equation, we have made it clear that the combined MICEO liquid motion is in effect a direct linear superposition of the TWEO and ACEO flow field, as long as the Reynolds number is negligibly small.

As for incompressible Newtonian fluid, the fully-developed velocity field abides by the Stokes equation [73]

$$-\nabla p + \eta \nabla^2 \boldsymbol{u} = 0 \quad (6a)$$

$$\nabla \cdot \boldsymbol{u} = 0 \quad (6b)$$

where η represents the dynamic viscosity, and p the static pressure of the liquid medium. Equation (6) is subjected to MICEO slipping $\langle \boldsymbol{u}_S \rangle$ on the double-sided multiphase electrode arrays.

A standard convection–diffusion equation is utilized to calculate the concentration distribution of incoming analytes in the fluidic channel, which arises from a combined action of molecular diffusion effect and electroconvection due to MICEO slipping [74–76]

$$\nabla \cdot (\boldsymbol{u}c - D_{\mathrm{solute}} \nabla c) = 0 \quad (7)$$

where c is the concentration field of nanoparticles dispersed in the liquid medium, and $D_{\mathrm{solute}} = 10^{-11}$ m^2/s their diffusivity in a concentration gradient, which is determined from Einstein equation for solid nanospheres with 40 nm in diameter.

2.3. Numerical Simulation

We employ a FEM-based commertial software package, Comsol Multiphysics 5.3a, to make analysis of the induced charge electrokinetic flow next to the metal electrode arrays and its practical application in fully-autmomated sample treatment in microfluidics, with the full-scale 3D computational domain shown in Figure 1c. Considering an actual operation in realistic conditions, a double-sided electrode strip array with a finite number $n = 4$ of the repeating wavelength is used in the simulation work (Figure 1c).

The calculation procedure of MICEO and electroconvection-enabled multidirectional mass transfer in the fluidic channel is as follows. At first, we calculate the Laplace equation Equations (1a) and (1b) for the complex amplitude of *TW* and *SW* voltage, with the electrode surface subjected to the *RC* charging boundary condition Equations (2a) and (2b), respectively. In terms of potential phasor, the *TW* and *SW* body potential of the driving electrodes are $\widetilde{\phi}_1^i = V_1 \mathrm{e}^{-j2\pi(i-1)/4}$ (i = 1,2,3,4) and $\widetilde{\phi}_2^i = V_2 \mathrm{e}^{-j2\pi(i-1)/2}$ (i = 1,2) respectively for Equations (2a) and (2b). Normal component of total electric current density $\boldsymbol{n} \cdot \nabla\widetilde{\phi} = 0$ vanishes at other insulating surfaces to close the electrical boundary-value issue. Then, once both the *TW* and *SW* electric field components are known, they are substituted into Equation (5) to calculate the time-averaged MICEO slipping flow. Subsequently, the EHD fluid motion in the bulk Equation (6) is computed by imparting Equation (5) to these ideally polarizable surfaces embedded

on both channel sidewalls. Both inlet and outlet are set as open boundarys. Besides, non-slip and no penetration $\boldsymbol{n}\cdot\boldsymbol{u} = \boldsymbol{t}\cdot\boldsymbol{u} = 0$ are imposed on all the other insulating channel sidewalls as well as the chamber top and bottom surface. Finally, transportation equation Equation (7) is computed for obtaining the analyte concentration distribution inside the fluidic channel under the combined action of diffusive and electroconvective mass transfer. Any normal flux is forbidden on the electrode and channel inner surfaces. Fluorescent particles of r = 20 nm in radius with a thermal diffusivity of $D = 10^{-11}$ m^2·s^{-1} are employed in the simulation analysis [77–79], the concentration of which is set to c = 1 mol·m^{-3} at the left side and 0 mol·m^{-3} at the right side of the upstream entrance, respectively. In addition, the normal diffusion flux disappears at the outlet plane, so as to reconstruct the actual situation for sample treatment in microfluidics.

We make use of stationary solvers for the set of control equations submitted to boundary conditions from physical constraints. The complex SW/TW potential phasor, MICEO fluid motion and sample delivery are separately solved in sequence. Free tetrahedral meshes are employed for discretization of the full-scale 3D computational geometry used in the numerical simulation (Figure 1c), and the maximum grid size near the electrode edges is assigned to be no more than 1/10 (2 μm) of the span of an individual metal strip, with a grid growth factor of 1.05 as the meshes extend from the conducting surface to the leaky dielectric bulk suspension. During the numerical computation, we preferentially apply the PARDISO solver because of its quicker iteration speed. The Reynolds number in current situation is no more than one, i.e., Rey = ρfuWe/η~O(0.02) < 1 for u = 1 mm/s and W_e = 20 μm, so that MICEO slipping flow is laminar, not turbulent in essence. Even so, under externally-imposed dual-Fourier-mode AC forcing, MICEO slip can still engender time-averaged axial pump flow and transverse vortex streaming in the bulk phase, due to its quadratic voltage dependence no matter how many actuating frequencies are engaged, which results in its dual functionality in simultaneous sample delivery and convective mixing in microscale ducts.

3. Results and Discussion

3.1. Characterization of the ACEO Flow Component

For analytical convenience, geometry size of the device design keeps unchanged during the most preliminary study: $W_e = W_{ee}$ = 20 μm, n = 4, Lc = 0.8 mm, Wc = 50 μm and Hc = 40 μm, i.e., with an appropriate cross-sectional aspect ratio of 1.25. The PDMS channel walls on both sides sandwich a central straight duct full of conducting electrolyte solution. The test values for various physicochemical properties are as follows: σ = 0.001 S/m, ε = 80 ε_0, C_s = 0.8F/m^2, λD = 37.6 nm, δ = 0.0235, η = 0.001 Pa·s, c_0 = 1 mM, $f_{RC} = (1+\delta)\sigma\lambda_D/2\pi\varepsilon W_E$ = 432.8 Hz, and λ = 8W_e = 160 μm. Since $\lambda D/\lambda = 2.35\times10^{-4} <$ 0.001, it is reasonable to arouse the thin layer approximation in this situation.

Due to a dynamic force balance between Coulomb attraction and thermal diffusion at a solid/saline-solution interface, a Debye screening layer, inside which counterion charge cloud overwhelms the coion counterpart, would develop naturally due to the fixed free charge density chemically adsorbed on the surface of a solid object immersed in electrolytes, or compulsively under externally-imposed electric fields. In this work, since there is no DC voltage applied to the driving electrode array, electrostatic force within the native EDL always time-averages to zero under multifrequency AC forcing. For this reason, we mainly concentrate on the latter effect of field-induced diffuse charge dynamics, that is, capacitive charging of the IDL on ideally polarizable surfaces of the blocking electrodes caused by the hybrid sinusoidal SW/TW signals imposed sequentially on the consecutively-distributed metal strips.

At the very start, we pay attention to the flow pattern due to the separate action of ACEO and TWEO above the phase-shifted 3D sidewall electrodes. First and foremost, when only *SW* signals are supplied to the microsystem ($V_1 \neq 0$ and $V_2 = 0$), although TWEO is absent, a series of chaotic EHD micro-vortices are induced throughout the channel by ACEO (Figure 2).

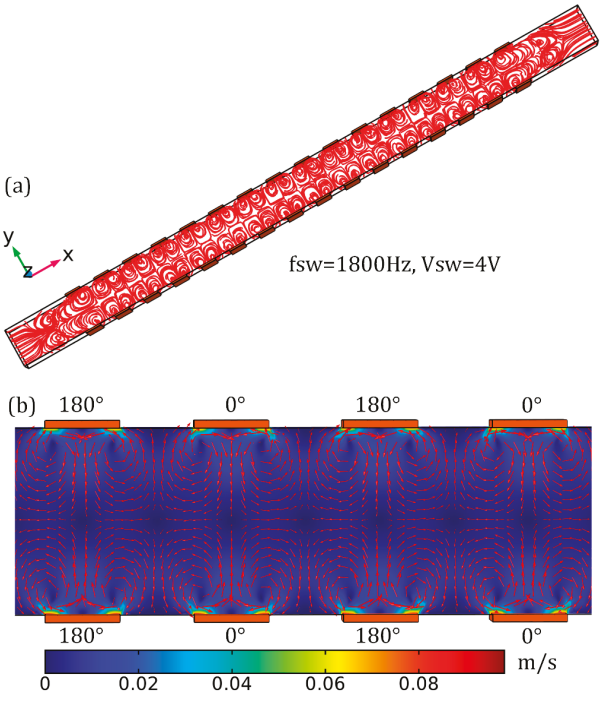

Figure 2. Computational visualization of the ACEO fluid motion due to the individual application of the *SW* signal voltage, namely, V_{TW} = 0 V. (**a**) ACEO streamline distribution in the 3D microfluidic device embedding double-sided four-phase discrete electrode array of n = 4 repeating wavelength, and (**b**) A surface and arrow plot of ACEO vortex flow field at V_{SW} = 4 V, f_{SW} = 1800 Hz in the horizontal central plane of the fluidic chamber with z = 20 μm.

In DC limit, considering rather complete Debye screening effect, most of the applied *SW* voltage drops across the diffuse screening cloud formed at the electrode/suspension interface, resulting in negligibly small electric field strength in the bulk phase. As the actuating frequency of the *SW* voltage grows and exceeds the reciprocal *RC* time scale f_{RC} for the equivalent circuit of the double-layer impedance in series connection with the bulk resistance, incomplete charge screening occurs on the electrode surface when considering electrochemical relaxation within the thin boundary layer, resulting in evident leakage of electric field lines into the liquid suspension.

In this way, the potential drop between the metal surface and electrolyte bulk drops rapidly for frequencies beyond $f \approx 700$ Hz (the black line in Figure 3a), and the enhanced electric field intensity caused by this factor (Figure 3b) helps push forward the counterions accumulated within the IDL more fiercely, giving rise to a single relaxation peak of out-of-phase Debye screening charge on each electrode surface around f = 700 Hz (the red line in Figure 3a). As the field frequency further increases and even exceeds the reciprocal *RC* time scale $f \approx 700$ Hz, however, electrochemical ion relaxation takes place on those metal surfaces, so that both the real and imaginary components of the induced zeta potential from ACEO would decay at the electrode/electrolyte interface.

Accordingly, as we raise the electric field frequency of the *SW* voltage signal from DC limit to 1 MHz, the in-phase double-layer voltage drop decreases monotonously due to a relaxation process. On the contrary, however, the out-of-phase counterpart is maximized within an intermediate frequency range around f = 700 Hz and manifests as a bell-shaped curve (the red line in Figure 3a), implying ACEO flow velocity would be appreciably suppressed once the signal frequency further keeps away

from the key frequency. At low signal frequencies, all of the applied *SW* voltage drops across the IDL above the double-sided electrode array, leaving no electric field in the bulk (the red line in Figure 3b). Under the high frequency limit, relaxation dynamics starts to become apparent, namely, there is insufficient time for the induced space charge to accumulate within the diffuse double layer on the surface of blocking electrode in each half cycle of the AC voltage wave, giving rise to negligibly small tangential field component (the black line in Figure 3b). Therefore, double-layer charging is most evident around the critical frequency for ACEO, and any aberration of imposed field frequency from this key point would attenuate the ACEO phenomenon.

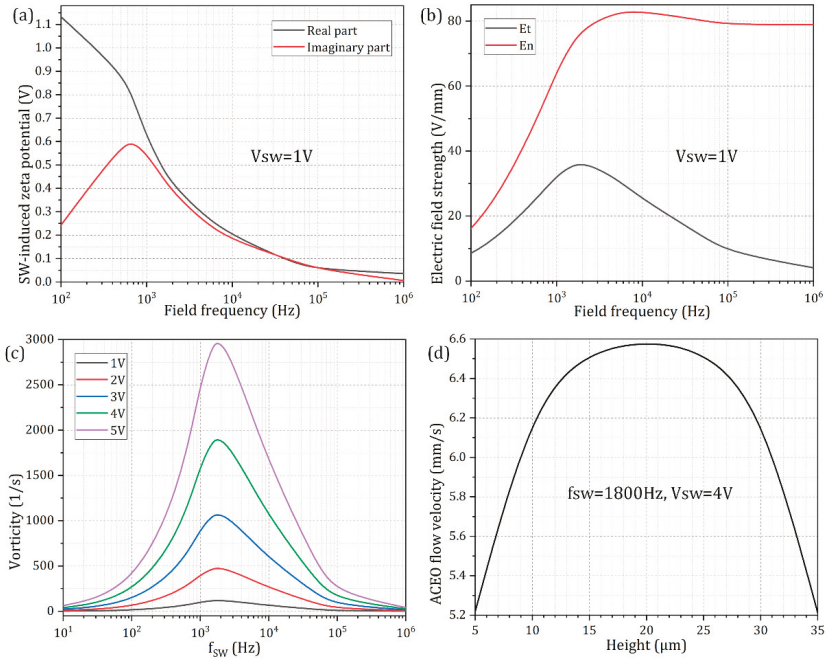

Figure 3. Quantitative calculation results of the electric field (**a**,**b**) and flow field (**c**,**d**) information in the situation of ACEO. (a,b), for a given voltage amplitude V_{SW} = 1 V, (a) real and imaginary parts of the zeta potential induced by the applied *SW* voltage signals as a function of the imposed frequency, (b) Frequency dependence of the tangential and normal components of the electric field vector right outside the IDL on those conducting surfaces. (c) Frequency dependence of hydrodynamic vorticity magnitude from ACEO for a series of *SW* voltage amplitude, wherein the ideal driving frequency that holds potential for convective mixing has always an identical value around f = 1800 Hz; (d) ACEO flow velocity as a function of vertical distance from the channel bottom surface at *fsw* = 1800 Hz and *Vsw* = 4 V.

As the frequency rises, the normal electric field component right outside the IDL would increases gradually as well (the red line in Figure 3b), while its tangential counterpart varies non-monotonically and reaches a single peak value at an intermediate frequency (the black line in Figure 3b). Since the electrode bars would recover from an insulator in low-frequency limit to its intrinsic role of an ideal conductor (Figure 3b) within high-frequency range with a characteristic microscopic distance scale O(λD) off these ideally polarizable surfaces, it behaves more as a typical leaky dielectric around the *RC* dispersion frequency where the tangential part of the electric field lines maximizes.

Besides the effect of induced double-layer charging, another indirect consequence of electrochemical polarization is the induction of fluid motion due to ICEO slipping at low signal

frequencies. When employing a *SW* voltage wave, ICEO manifests as a series of counter-rotating micro-eddies near the electrode array, namely, ACEO. As shown in Figure 2a,b, for the full-scale 3D computational space where a double-sided discrete electrode array of four repeating wavelengths is integrated into both sidewalls of a straight fluidic channel, since ACEO is originated by nonlinear Coulomb force inside the thin IDL, the time-averaged ACEO flow velocity is quickest right outside the Debye layer (in coincidence with the electrode surface in the simulation), and vanishes in the midchannel located in between the opposing electrode array due to viscous diffusion of liquid momentum (Figure 2b). From the linear asymptotic analysis by Gonzalez et al. In [57], ACEO is only significant around *RC* relaxation frequency, and vanishes in both low (due to complete Debye screening) and high (due to electrochemical ion relaxation) frequency limit. This can be well validated by Figure 3c, in which the vorticity magnitude due to ACEO attains a single relaxation peak at the inverse *RC* time constant for capacitive charging of electrical double layer f_{RC}^{SW} = 1.8 kHz, which is about two orders of magnitude smaller than the Debye relaxation frequency $f_{MW} = \sigma_f/2\pi\varepsilon_f$= 225 kHz of the bulk fluid. In the analytical model of linear *RC* circuit theory, the characteristic inverse *RC* time scale for charging of the induced double layer on ideally polarizable surfaces is given by $f_{RC} = (1+\delta)\sigma\lambda_D/2\pi\varepsilon$R, which should be in accordance with the simulation result 1.8 KHz from the bi-layer mathematical model used in current work. Here, δ denotes the surface capacitance ratio, σ the liquid conductivity, λD the Debye screening length, R the characteristic microscopic length scale for ACEO. In this sense and in order for the theoretical prediction to match the simulation results, *R* ought to equal approximately one-fourth of the electrode width, i.e., $R = W_e/4 = 5$ μm.

Since a full-scale 3D numerical model has been adopted in our simulation analysis, the ACEO flow velocity also makes a change with a variation in the suspension height of the particle sample (Figure 3d). As shown in Figure 3d, the surface-averaged electrokinetic flow rate attains a peak value at the middle horizonal section of the fluidic chamber, while it decays sharply once the place of interest further approaches the channel top and/or bottom surface, as caused by an adverse influence of the presence of viscous boundary layer at the boundary of the simulation domain.

3.2. TWEO Pump Behavior Driven by A Single Phase-Shifted Harmonic Field

We then arbitrarily remove ACEO by constraining V_{SW} = 0 and focus on the effect that an externally-imposed traveling potential wave may have on the resultant ICEO flow field, that is, TWEO. Pumping of electrolytes by TWEO arises from the action of an applied *TW* electric field on its own induced Debye screening charge within the thin IDL, which is formed on top of the ideally polarizable surface immersed in saline solution. In this study, we realize such a traveling field via the same double-sided discrete electrode array as used in previous simulation analysis for ACEO convection (Figure 4a), upon which the corresponding sinusoidal voltages of correct phase sequence are imposed.

Unidirectional movement of liquid element is observable on application of a traveling wave potential to the double-sided electrode structure at frequencies on the order of the inverse *RC* time constant of the saline solution. On imposing a *TW* signal propagating downstream, the fluid motion is directed straightly to the right electrolytic port, as shown in Figure 4a,b. On inversing the travel direction of the sinewave, the parallel laminar streamlines reverse direction and move from the right to the left side (not shown). Thereby, it is definite that the traveling wave potential is responsible for the phenomenon of directed liquid transport.

As shown in Figure 4c, at very low frequencies, the double-layer charge and tangential field component have a 90° phase difference and are completely out of phase, so no net flow can be produced. At the same time, the electric field in the bulk phase is weakened to great extent due to the formation of dynamic IDL in quasi-equilibrium state. As the signal frequency of the traveling potential wave approaches an intermediate characteristic relaxation frequency f_{RC}^{TW} = 400 Hz, the phase lag between the Debye screening charge and tangential AC forcing decreases so that a time-averaged fluid motion in the direction of the travel of the *TW* takes place (the peak point in Figure 4c). Although the density of the induced charge cloud may decrease, the electric field right outside the Debye layer increases in

strength. Since we have employed herein the linearization theory, the ideal operating frequency of the electroosmotic pump is independent of the *TW* voltage amplitude (Figure 4c), while this would not hold true when nonlinear effects such as surface conduction and anisotropic IDL capacity have to be taken into account. With further increase of the signal frequency, the pump flow rate decays monotonously because of the occurrence of incomplete Debye screening. As a consequence, similar to ACEO, TWEO always exhibits a single relaxation peak arising from double-layer dispersion.

Even so, ACEO and TWEO have distinct ideal manipulation frequency, which is 1800 Hz and 400 Hz in current device design, respectively. According to Equation (4), a large deviation of the two characteristic peak-flow frequencies greatly facilitates the independent control on electrokinetic fluid transport and convective mixing via separately adjusting the *TW* and *SW* voltage signals.

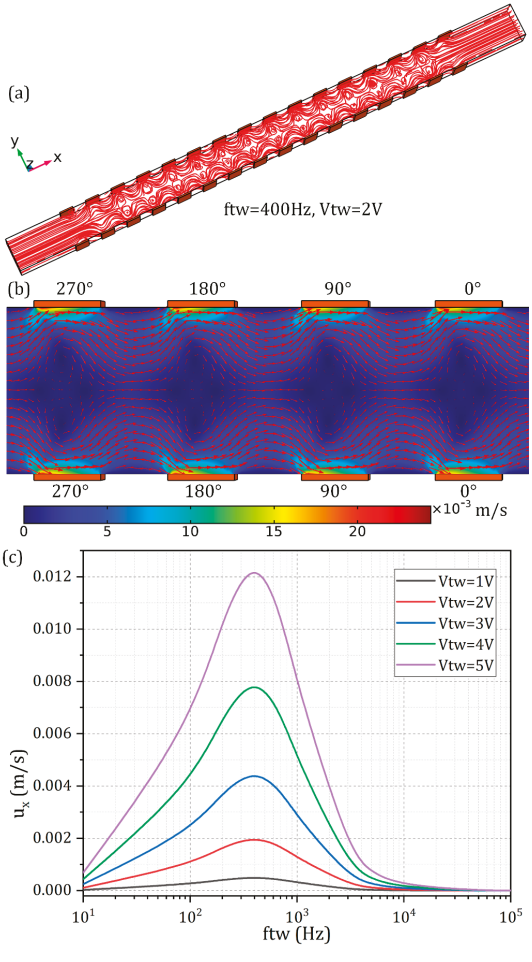

Figure 4. Numerical investigation of TWEO fluid motion caused by a pair of progressively phase-shifted *TW* potential signals synchronously moving along the top and bottom rows of the double-sided electrode arrays. (**a**) TWEO pumping streamline distribution in the 3D microfluidic device with a channel height of Hc = 40 μm, and (**b**) a surface and arrow plot of TWEO pump flow field at V_{TW} = 2 V and f_{TW} = 400 Hz in the horizontal central plane of the fluidic chamber, with the most salient feature of TW-induced co-field unidirectional fluid transport; (**c**) frequency dependence of the averaged pump flow rate in the direction of the traveling wave within the range of *TW* voltage amplitude from V_{TW} = 1 V to 5 V.

3.3. Multi-Frequency ICEO from Combined ACEO and TWEO

In previous sections, we have demonstrated the respective role of *SW* and *TW* excitation in correspondingly producing transversal ACEO chaotic vortex and axial TWEO pump behavior. Accordingly, it is then of paramount significance to unite both ICEO phenomena and test their combined contribution to the synthetic electroosmotic flow field. For realizing MICEO, a hybrid sinewave of dual oscillating frequencies is applied to the double-sided discrete electrode array, with the specific voltage-phase sequence matching that shown in Figure 1b.

For analytical convenience, the *TW* voltage amplitude is fixed at V_{TW} = 2 V, and the two voltage modes oscillate at their optimum driving frequency for enabling the most effective ACEO vortex and TWEO liquid transport in light of the flow speed, i.e., f_{SW} = 1800 Hz and f_{TW} = 400 Hz. As shown in Figure 5, with an increase in the *SW* voltage amplitude from 1 V (Figure 5a), 3 V (Figure 5b) to 5 V (Figure 5c), the resultant ICEO fluid motion transits from almost a pure pump mode moving in the direction of the travel of the *TW* signal to a more complicated EHD flow pattern affected simultaneously by a series of local ACEO vortices and global TWEO medium delivery towards downstream. That is, at a given *TW* field strength, increasing the *SW* signal is able to enhance the electrokinetic flow vorticity, while it plays a negligibly small effect on the pump behavior.

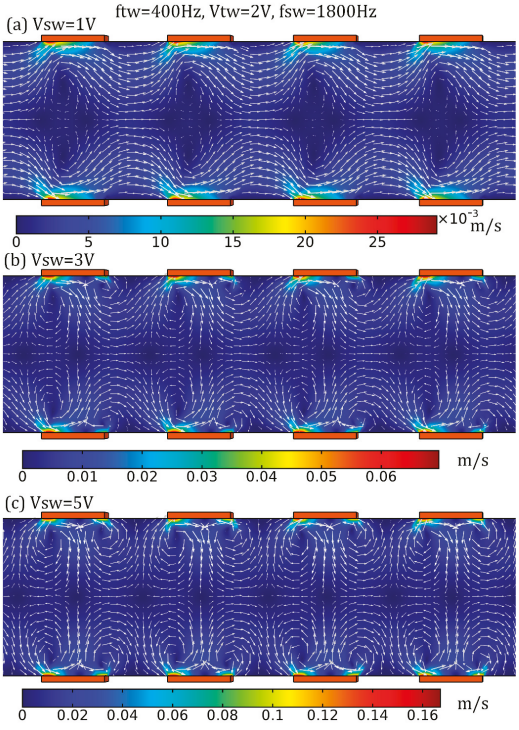

Figure 5. Simulation analysis of the MICEO flow behavior from combined ACEO and TWEO actuated by AC forcing of two distinct oscillating frequencies, 1800 Hz and 400 Hz, respectively, in the horizontal central plane of the 3D device design. (**a–c**) Impact of V_{SW} on the resultant electroosmotic flow field, as the amplitude of *TW* voltage is fixed at V_{TW} = 2 V (unit: m/s), (a) V_{SW} = 1 V, (b) V_{SW} = 3 V, (c) V_{SW} = 5 V. Accordingly, the vorticity grows sharply with the amplitude of SW signal, while the pump motion remains almost unchanged.

Besides these qualitative pictures, flow vorticity and pump performance due to MICEO are further mathematically quantified in Figure 6. According to Figure 6a, the pump flow rate can be merely controlled by tuning the *TW* signal, and the *SW* electric field has indeed no contribution to the unidirectional fluid transport whatever the *TW* field strength is. The pump flow rate grows quadratically with the *TW* voltage, since TWEO is a nonlinear electrokinetic effect where the electric field propels its own induced charge within the IDL at the electrode/electrolyte interface. On the other hand, from Figure 6b, although it is possible for both TWEO and ACEO to adjust the magnitude of the vorticity field, *SW* signal input serves as a better method of choice for achieving separate control on device dual functionality since its variation does not exert an impact on the ultimate MICEO pump performance (Figure 6b). In this sense, the comprehensive fluid physics of MICEO can be arbitrarily reconfigured by delicately recombining a hybrid *SW*/*TW* sinewave, whose functionality can be oriented towards either convective mixing when ACEO vortex flow field dominates or fully-automated external-pump-free liquid delivery when horizontal TWEO streaming is more efficient.

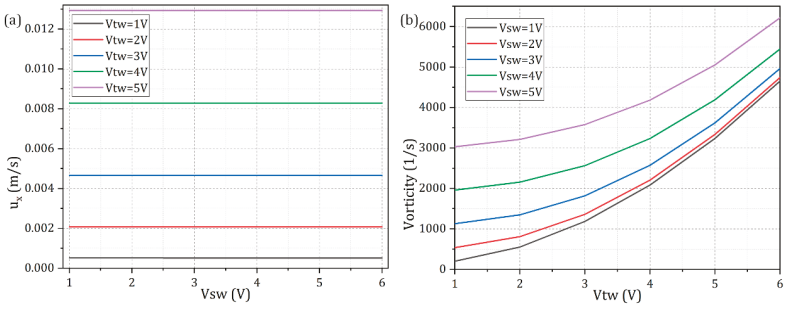

Figure 6. Analysis of the interplay of ACEO and TWEO with respect to the MICEO device performance in terms of simultaneous on-chip fluid delivery and electroconvective mixing. (**a**) V_{SW}-dependence of the electroosmotic pump behavior (the flow speed along the channel length direction) for different *TW* voltage amplitude; (**b**) V_{TW}-dependence of the resultant hydrodynamic vorticity for different *SW* potential amplitude.

3.4. Experimental Observation of MICEO Flow Field Above a Confocal Spiral Microelectrode Array

3.4.1. Device Configuration and Experimental Method

To demonstrate the availability of current MICEO flow theory, a multiphase electrokinetic microfluidic device is fabricated and then we conduct the particle tracing experiment. Multilayer fabrication process has to be applied if the configuration of a linear electrode track of different voltage phases is adopted. To avoid complicated wiring, we come up with a special device design of a confocal spiral quarter-terminal electrode array of $n = 5$ repeating wavelength, as has been used in our previous work (Figure 1 in [80]), so it is not shown here. These conducting rings are deposited on a thick glass substrate and covered by a PDMS microchannel with two opening cylindrical electrolytic ports of 2 mm in radius. The four circulating metal strips share an equal width of $L_E = 100$ μm, and the nearest gap size between adjacent electrode phases equals $L_G = 30$ μm. Consequently, the wavelength of single repeating spatial period is $L = 4(L_E + L_G) = 520$ μm, and the diameter of the whole helix is about 6 mm. One great benefit of this circulating design is that, inter-phase insulation and external wiring of the four sequential terminals can be accomplished at the periphery of the circular electrode system at a time, with much more convenience of device operation compared to that for a linear multi-phase array [67].

We choose aqueous saline solution as the potential candidate of the working fluid, its ionic conductivity is carefully controlled by modulating KCl salt and supervised via a conductivity meter. The solution conductivity for flow tracing experiment is $\sigma = 0.001$ S/m, which is in the dilute limit for actuating MICEO in the absence of ion overcrowding effect [81–83]. Considering the much lower ionic

strength of the bulk fluid, the ITO metal strips can be treated as ideally polarizable solid conductors in current device design. The sample particles used here were polystyrene nanospheres (Molecular Probes Co.) with diameter of r = 250 nm. To prepare the fluorescent nanocolloids, a 10 μL liquid solution containing 10% particle samples was diluted with the 10 μS/cm KCl solution into 2 mL, so as to keep track of the dynamic motion behavior of latex beads caused by MICEO streaming flow. The working fluid with tracer particles is then injected into the fluidic channel and eventually stuffs it.

We employ a commercial multichannel function generator (TGA12104, TTi, Cambs, UK) to generate dual-frequency sinusoidal voltage signals with controllable spatial-temporal phase transition trait. The specific transient waveform of the applied voltage is monitored using a commercial digital oscilloscope (TDS2024, Tektronix, Beaverton, OR, USA). Besides, the experimental observation window is selected preferentially at the lower left side of the ring-shaped electrode array.

3.4.2. Experimental Results and Discussion

In essence, a hybrid phase-shifted dual-Fourier-mode sinewave is required for actuating MICEO along the electrode track in the annular device design. We introduce here a special transient powering technique, however, in order to differentiate ACEO and MICEO merely using a single experimental video (see Supplementary Video and Figure 7). At the very beginning, with the function generator switched off, the nanoparticle samples are distributed homogeneously in the electrolyte solution, and no obvious concentrating phenomenon is observable due to the domination of stochastic Brownian motion of nanoscale entities (not shown).

On application of a *SW* voltage signal of Vsw = 2 V, fsw = 50 Hz, and 180° phase lag to the adjacently-arranged electrode strips, vortex flow field due to ACEO slipping transports the nanoparticles from the surrounding bulk medium to the centerline of the surface of the blocking electrodes, resulting in the formation of 10 particle assembly lines, as shown in Figure 7a, and it takes about 20–30 s for the dynamic trapping process to reach the steady state, when the number of particles around the flow stagnation region becomes almost saturated and cannot increase any longer. Once the *SW* signal has been maintained for 30 s and the 10 circular assembly lines have been well developed (Figure 7a), a traveling field with V_{TW} = 2 V, f_{TW} = 70 Hz and 90° phase difference between consecutively distributed metal strips is superimposed with the preexisted *SW* signal (Figure 7b). In this scenario, according to the theory of MICEO streaming established in preceding sections, a unidirectional pump flow component of TWEO is induced by the additional *TW* voltage signal, and it can effectively superimpose with the series of lateral ACEO micro-vortices along the channel length direction. In this sense, MICEO fluid motion from combined ACEO and TWEO is much stronger than ACEO or TWEO works alone, so more latex beads are transported and then adhered onto the ideally polarizable surfaces of the phase-shifted metal strips by the synthetic flow field of MICEO, which gives rise to an increase in the number of assembly line from 10 to 20 (Figure 7b). Very interestingly, the newly formed 10 circular trapping lines by TWEO are much thinner than that due to ACEO, so that the complete sample distribution pattern under the influence of MICEO is now characterized by the repeating spatial periodicity of one thin line from TWEO and one neighboring thick counterpart from ACEO (Figure 7b), which also takes about 20–30 s to achieve the stable state.

As long as the MICEO-induced fluorescent lines with alternatively-placed thick and thin counterparts have been completely assembled, we switch off the *TW* voltage component immediately. With time goes on, the 10 thin trapping lines by TWEO vanish, and the sample distribution pattern recovers to the original 10 thick lines due to the action of ACEO (Figure 7b′). However, the fluorescence intensity in Figure 7b′ is made much higher than that before the application of MICEO (Figure 7a). It is our speculation that although the TWEO pumping effect no longer exists once the *TW* signal is withdrawn, the samples originally captured by TWEO would enter the actuating range of ACEO whirlpool in the bulk fluid and then be attracted onto the flow stagnation region defined by ACEO. That is, with the *TW* signal powered off while the *SW* voltage invariably maintained, the particles originally occupying these thin lines would move to their adjacent thick lines (Figure 7b,b′), resulting

in further thickening of the particle trapping lines formed by ACEO, which indicates a better device performance in sample collection (Figure 7b′).

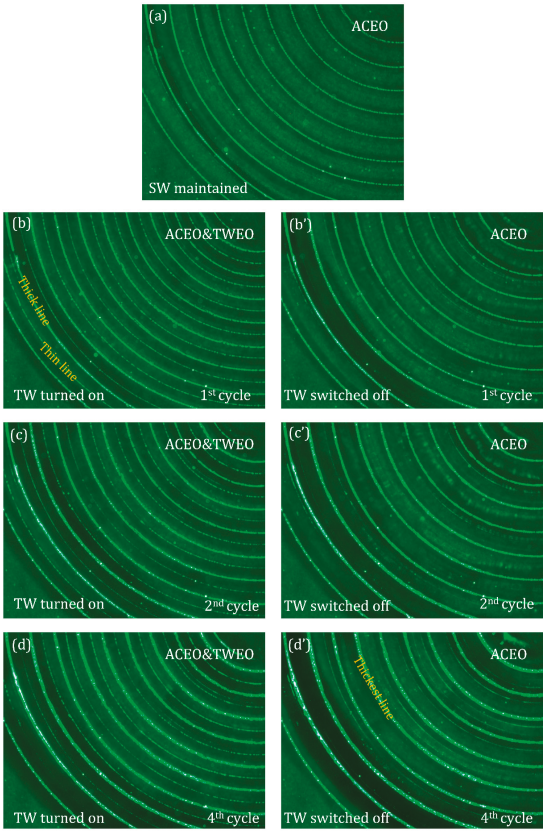

Figure 7. Top view of the flow tracing experiment of MICEO, which takes advantage of the confocal spiral four-phase electrokinetic microchip introduced in [80], and the observation window is chosen at the lower left side of the annular array. (**a**) At the most initial time, only a *SW* voltage signal with Vsw = 2 V, fsw = 50 Hz and 180° phase difference between every adjacent electrode is imposed to the annular array with 4 (number of discrete voltage phase) × 5 (number of repeating wavelength) metal strips, 10 particle trapping lines are formed on the annular electrode strips by ACEO vortex streaming; (**b**) after 30 s, another *TW* voltage sequence with V_{TW} = 2 V, f_{TW} = 70 Hz and 90° phase difference between consecutively distributed metal strips is superimposed with the already-existed *SW* signal, which generates stronger vortex flow field and an additional outward pump flow component, resulting in doubling in the number of particle assembly line, as characterized by the repeating spatial periodicity of one thin line and one neighboring thick counterpart. (**b′**) 30 s later, the traveling sinewave is withdrawn with the *SW* signal being invariably maintained, although the number of collection lines is reduced from 20 to 10, the fluorescent intensity becomes stronger indicating a better particle trapping performance. (**c**,**c′**) The second cycle of adding and removing the TWEO flow component with respect to the ACEO fluid motion that has always been maintained for a same time period of 1 min (30 s + 30 s). (**d**,**d′**) The fourth cycle of adding and deleting the TWEO pump flow component relative to the maintained ACEO for an identical time period of 1 min (30 s + 30 s). It is noteworthy that, by using the particular technique of MICEO, the particle trapping performance of ICEO is enhanced to great extent, as can be evidenced from (a,b′,c′) to (d′). Please refer to the Supplementary Video.

The above experimental procedure—namely, actuating MICEO for 30 s and then remove TWEO leaving only ACEO for 30 s—is repeated four times in total, as sequentially shown in Figure 7(c,c′,d,d′). The sample assembly pattern remains identical as that in Figure 7b,b′, respectively, while the trapping performance becomes more appreciable as the repetition cycle increases, as can be clearly evidenced by a stark contrast in the fluorescent intensity between Figure 7a,d′. In this way, the existence of the physical phenomenon of MICEO streaming flow is preliminarily demonstrated by conducting particle tracing experiments, which holds great potential for flexible sample handling in modern microfluidic systems.

3.5. Influence of Electrolyte Conductivity and Channel Height on MICEO Streaming

All the preceding simulations have assumed the working fluid has a quite low electric conductivity of 0.001 S/m. For the sake of biological applications, however, the buffer solution and cell culture medium usually require the liquid conductivity to be no less than 0.1 S/m, so it is necessary to test the feasibility of the actuation of an effective MICEO fluid motion at higher ion concentrations.

For high-conductivity environment, the linear *RC* polarization model may not be so accurate as the dilute electrolyte condition, but it can still capture the most salient feature of MICEO beyond the Debye-Huckel limit. In this sense, we calculated the frequency dependence of MICEO fluid motion at four distinct level of ionic strength (Figure 8). As shown in Figure 8a, whatever the specific solution conductivity is, the flow vorticity caused by ACEO always exhibits a single double layer dispersion process at the characteristic inverse *RC* time constant of electrochemical polarization on the blocking electrodes. While the ideal flow frequency rises with the ionic strength, the peak electrokinetic flow vorticity decreases as the liquid conduction increases. Similar variation trends also hold true for the TWEO pump flow velocity (Figure 8b). That is, the optimal pump frequency enhances at higher ion concentrations, but the peak flow rate decreases sharply once the solution conductivity increases by three orders of magnitude from 0.001 S/m to 1 S/m. The reason behind is quite clear: on one hand, the rise in solution ionic strength shrinks the double-layer thickness, so that the Stern layer becomes more dominant over the diffuse screening cloud at a larger solution conductivity, which suppresses the induction process of the counterions and thereafter lowers the ICEO flow velocity and vorticity; on the other hand, a higher liquid conduction implies a smaller impedance of the bulk fluid, and accordingly, a higher characteristic relaxation frequency is needed to short-circuit the double-layer voltage drop by half and provide sufficient electric field leakage for enabling appreciable EHD fluid motion.

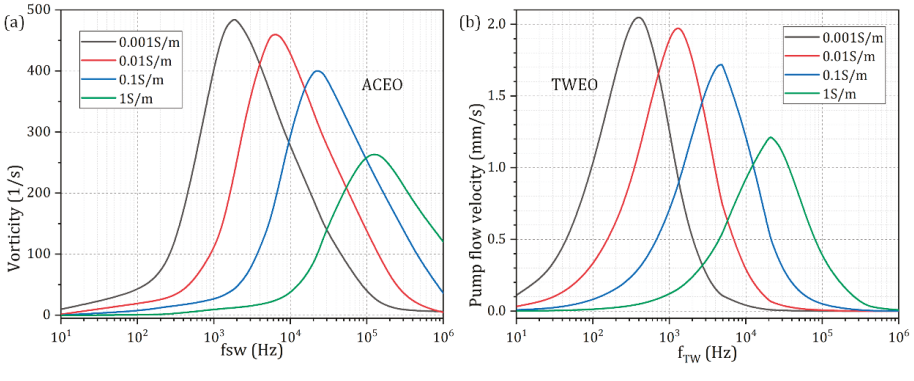

Figure 8. Effect of liquid electric conductivity on the resultant MICEO flow field under a finite channel height of Hc = 40 μm. (**a**) For V_{TW} = 0 and V_{SW} = 2 V, the frequency dependence of vorticity due to ACEO at varying medium conductivities. (**b**) For V_{TW} = 2 V and V_{SW} = 0 V, the frequency dependence of electrokinetic pump flow rate due to TWEO for different level of solution ionic strength.

A finite channel height, which is usually encountered in practical experiment, may also exert a negative influence on MICEO fluid flows. As shown in Figure 9, although a moderate cross-sectional aspect ratio of 1.25 has been applied in preceding analysis (Hc = 40 μm), both ACEO fluid motion and TWEO pump behavior are very susceptible to changes in the channel vertical dimension. On one hand, as Hc increases from 10 μm to 160 μm, the global electroosmotic flow velocity enhances monotonously (Figure 9a,b), due to, in part, the less negative influence from the viscous boundary layers formed at the channel top and bottom wall. On the other hand, although an increase in the height of the fluidic chamber helps improve the electrokinetic flow status, the ideal operating frequency is not affected in any way (Figure 9a,b), in that it is the electrode width and separation in the horizontal plane rather than the vertical dimension that determine the characteristic polarization length scale for the actuation of ICEO. As a consequence, considering a practical application in sample manipulation with MICEO in microfluidics, it is quite feasible to raise the channel height for engendering stronger electroosmotic fluid motion and better device performance.

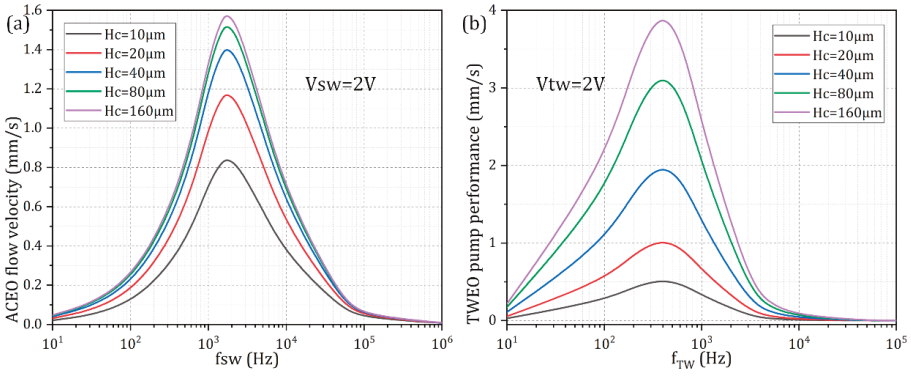

Figure 9. Effect of the finite channel height on the resulted MICEO fluid motion for a given liquid conductivity 0.001 S/m. (**a**) For V_{TW} = 0 and V_{SW} = 2 V, the frequency dependence of ACEO flow velocity for varying channel vertical dimension. (**b**) For V_{TW} = 2 V and V_{SW} = 0 V, the frequency dependence of TWEO pump flow rate for different channel height.

3.6. Simulation Study of Simultaneous Pumping and Convective Mixing by MICEO

From the above analysis, MICEO is capable of achieving a high degree of freedom control on the resultant ICEO flow pattern, this excellent feature makes it convenient to use the fluid physics of MICEO for developing multifunctional fluidic devices at the micrometer dimension. As an illustrative example, we still employ the device design with n = 4 repeating wavelength of linear TW electrode track embedded along both sidewalls of a straight microchannel, as shown in Figure 1a,c.

For the sake of analyte mixing, a T-shape junction is arranged at the upstream section, where there are a pair of face-to-face inlets for injection of two co-flowing liquid solution of identical properties. The solution passing through inlet 1 is an aqueous electrolyte containing target nanoparticles, while that entering inlet 2 is a pure saline solution of same electric conductivity and does not have any solid-state solutes. An eligible liquid mixture in high-throughput is obtainable at the channel outlet (the green plane in Figure 1a) right downstream the double-sided quarter-phase metal strip array, as long as appropriate AC voltage waves are imposed to the set of electrode pads. From the preceding analysis, however, it is appropriate for us to arbitrarily increase the height of the channel from 40 μm to 500 μm for achieving an ideal MICEO-enabled sample treatment, which is able to evidently diminish the adverse vertical channel confinement effect.

In the simulation analysis of the device dual-functionality, the actuating frequencies are still set as these ideal ones, that is, f_{SW} = 1800 Hz and f_{TW} = 400 Hz, and we fix the TW voltage amplitude at

V_{TW} = 1.5 V, so as to focus on the effect that the *SW* signal has on the pump and mixing performance. As shown in Figure 10a, in the absence of ACEO whirlpools with the supply of the *SW* voltage source turned off (V_{SW} = 0 V), the electrolyte solution is indeed solely pumped by TWEO from the T-junction to the downstream outlet port, and the average transportation speed u_x = 2.89 mm/s is totally determined by the *TW* signal. However, under this situation, the two-coflowing side-by-side laminar streams move parallelly along the channel length direction, and there is no apparent advective perturbation to the two-phase contact interface. Therefore, sample stirring, if there is any, is merely caused by molecular diffusion effect across the concentration gradient perpendicular to the phase boundary, giving rise to a humble mixing performance no more than 20% at the exit plane (Figure 10a).

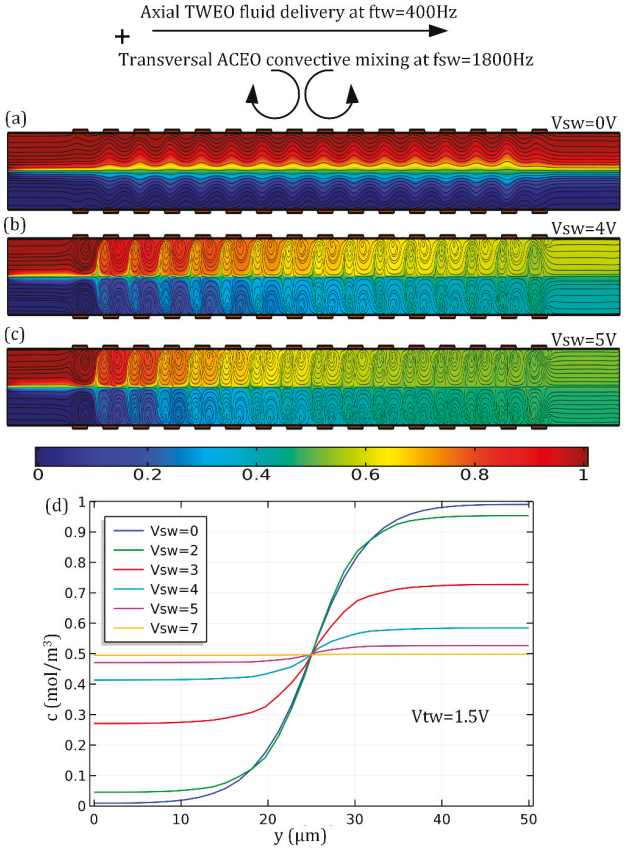

Figure 10. Simultaneous external-pump-free sample delivery and convective stirring completely driven by multifrequency induced-charge electroosmosis with a sufficient channel height of Hc = 500 μm compared to the lateral dimension Wc = 50 μm. (**a**–**c**) Sample treatment with MICEO under given f_{TW} = 400 Hz, f_{SW} = 1800 Hz and V_{TW} = 1.5 V, a surface plot of analyte concentration and a streamline plot of MICEO flow field as a function of V_{SW} in the horizontal central plane of the fluidic channel; (a) V_{SW} = 0 V where the interface between the two co-flowing laminar streams is mainly expanded by Brownian diffusion mechanism; (b) V_{SW} = 4 V where both diffusion and lateral ACEO chaotic advection contribute to perturb the contact-interface; (c) V_{SW} = 5 V where the strong EHD shear stress is main mechanism responsible for splitting and recombination of the central phase boundary. (**d**) Analyte concentration distribution along the channel centerline of the exit plane. In ((a–c), it is noteworthy that the length scale in the *y*-direction is arbitrarily extended twofold for enabling better visual clarification of MICEO-induced dual-functionality in simultaneous analyte pumping and mixing.

On the contrary, on switching the *SW* signal on with voltage amplitude V_{SW} = 4 V, a series of turbulent ACEO micro-vortices in opposite rotating directions takes place in the vicinity of the double-sided electrode array, being symmetric with respect to the horizontal centerline of the fluidic channel (Figure 10b). The lateral ACEO electrokinetic eddies distributed along the flow path intersect orthogonally with the laminar pump streamlines in the longitudinal direction induced by TWEO, resulting in the formation of double helical streamlines that move along the channel length direction until reaching the downstream outlet, where a liquid mixture of moderate mixing efficiency γ = 85.31% can be collected manually (Figure 10b). On increasing the *SW* voltage amplitude from 4 V to 5 V, although the TWEO pump flow rate keeps the same, the lateral electro-convective perturbation acting on the phase boundary becomes larger in strength, giving rise to a more helical flow profile and a better device mixing performance γ = 95.11% with an identical sample throughput (Figure 10c).

As shown in Figure 10d, this can be reflected by the distribution of sample concentration gradient inside the outlet plane as well. To be specific, the lateral concentration profile varies from 0 mol/m^3 to 1 mol/m^3 quite sharply at V_{SW} = 0 V (the blue line in Figure 10d), with the particle number density gradient similar to that at the channel inlet (not shown). As the *SW* voltage grows up gradually, the concentration profile has a propensity to become much flatter (from the green to the purple line in Figure 10d). What is more, as V_{SW} further increases and approaches 7 V (the yellow line in Figure 10d), the concentration profile becomes almost a straight line oriented along the channel width direction and is of a constant value c = 0.5 mol/m^3, that is, the surface-averaged analyte concentration in the inlet plane.

In this sense, as the incoming liquid solution is continuously delivered by horizontal TWEO pump streamlines towards the channel exit, ACEO vortex flow field of sufficient actuating range exerts an effective hydrodynamic stress on the concentration gradient, which alternatively splits and recombines (SAR) the diffusing interfaces along the channel axial direction, that is, it serves as a category of field-induced chaotic advection mechanism similar to the previous passive SAR micromixer exploiting more complicated 3D channel structures [84]. Although the turbulent MICEO streaming induced by the hybrid AC signals promotes the molecule exchange rate across the diffusing phase interface by accelerating convective mass transfer along the channel width direction, the most prominent improvement of the proposed microdevice over those active micromixers reported in previous literatures is that there is no need for an external mechanical syringe to enable sample delivery in current fluidic mixer, since the liquid medium can be automatically pumped by TWEO originated by phase-shifted component of the applied voltage gradient.

At last, it is essential to present some quantitative calculation data about the device dual-functionality and make a pertinent analysis. As shown in Figure 11a, within the framework of ideal working frequencies (*ftw* = 400 Hz, *fsw* = 1800 Hz), whatever the traveling wave signal is, the device mixing performance always enhances with the rise of the magnitude of the standing wave voltage, since the TWEO pump flow rate remains unchanged at a fixed *TW* signal while the lateral ACEO electroconvective perturbation reinforces by raising the *SW* voltage in this scenario. Besides, as displayed in Figure 11b, whatever the *SW* signal is, the mixing index at the outlet plane always decreases as voltage amplitude of the *TW* electric field increases. As for the second case, the vertical EHD shear stress on the interface keeps the same at a given *SW* voltage, while the horizontal pumping body force is made more potent by increasing the *TW* signal, and thereby, though the mixing index drops, the axial flow flux increases resulting in a higher sample throughput. To this end, it is quite convenient to regulate the ratio of mixing efficiency to the device throughput by adjusting the relative magnitude of the *SW* and *TW* voltage signal, implying a high degree of freedom control on the dual-functionality of the microfluidic chip in simultaneous analyte transport and convective mixing at the nanoliter scale.

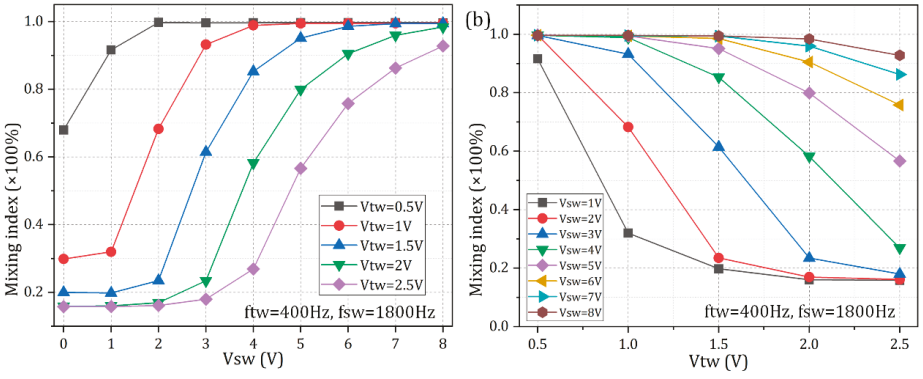

Figure 11. Quantitative characterization of the mixing efficiency of the dual-functionality MICEO microfluidic device, which makes use of pure nonlinear electrodynamic effect in double Fourier-mode AC fields. (**a**) V_{SW}-dependence of the mixing index for different *TW* voltage amplitude; (**b**) V_{TW}-dependence of the sample mixing performance under different *SW* voltage magnitude.

3.7. Advantages and Limitations of the Method of MICEO

One distinguished trait of MICEO is that the electrokinetic flow profile is easily controllable by coordinating the voltage ratio between the *SW* and *TW* signal, as long as the ideal frequencies for ACEO and TWEO to operate separately have been confirmed by theoretical prediction. The convection mode can be made either more chaotic as ACEO predominates or more parallelly streaming when TWEO pumping of electrolytes is dominant. In addition, with appropriate voltage combinations, it is quite feasible to realize simultaneous delivery and convective mixing by exploiting a general device design into which a double-sided quarter-phase linear electrode array is embedded. What is more, induced-charge electroosmotic trapping performance of nanoparticles can be enhanced to great extent via utilizing the unique technique of MICEO introduced herein.

Frankly speaking, in spite of these aforementioned advantages, there are still two limitations that potentially affect the actual performance of current method for practical on-chip applications: on one hand, since it has been reported that the physics of ICEO is mainly apt for driving fluid motion in the limit of dilute electrolyte, MICEO may malfunction in highly concentrated buffer solutions where ion overcrowding overwhelms ion overscreening inside the IDL on the ideally polarizable surface; on the other hand, since there is a 90° voltage phase shift between consecutively distributed metal strips in each repeating wavelength, it is inevitable to apply multilayer fabrication process if the configuration of a linear *TW* electrode track is to be utilized.

3.8. Guidelines on the Usage of MICEO for Improving Real Microfluidic Systems

According to the discussions in Section 3.7, if researchers want to make use of MICEO to improve their own microfluidic systems, they should at first make a judgement on whether their fluidic sample can survive in low-conductivity buffer solutions. As previously reported, ICEO is effective for liquid electric conductivity being no more than 0.02 S/m. Moreover, no ICEO fluid motion is observable on top of the electrode array in high-conductivity liquid buffers, when considering a shrinkage in IDL thickness and an enhancement in the steric effect with growing ionic strength. So, biological materials, it they require low conductivity buffers, can still be utilized in ICEO experiments. In this sense, ICEO is merely apt for handling low-conductivity solutions where the induced double layer can be fully developed. Even so, there are still many kinds of samples needing electrokinetic manipulation in dilute electrolytes, e.g., bacteria particles dispersed in tap water, whose content is of great importance for human's physical health. Indeed, it is counterintuitive to deal with biological samples suspended in highly conductive fluids by electroosmotic streaming. By taking suitable pre-processing steps, however,

this drawback can be alleviated to some extent. For example, resuspending the samples of bioparticles in low-conductivity sucrose media not only can maintain their viability, but solution conductivity is lowered to the level of DI water enabling an effective actuation of ICEO on polarizable surfaces as well.

Once the issue of medium conductivity is addressed, it is then necessary to make use of the simulation model outlined in Sections 2.2 and 2.3 to test the feasibility of the device design with distinct electrode patterns in practical on-chip sample handling. In the simulation study, researchers ought to take advantage of multifrequency phase-shifted AC sinewaves exerting on the discrete electrode array for inducing the phenomenon of MICEO, under the synergy of both in-phase and out-of-phase electrochemical polarizations and explore the effect that different voltage parameters would have on the resultant electroosmotic flow pattern. The optimized experimental parametric space at a given channel structure can be discovered as well for producing the anticipated helical streamlines with a prescribed axial-pump/transversal-mixing flow velocity ratio. In this sense, numerical prediction in advance with Equations (1)–(7) has the potential to help improve the success rate of realistic experiment in which MICEO is employed for a series of particle manipulation process.

4. Conclusions

To summarize, we have presented results from both simulation analysis and experimental observation, to introduce a brand-new physical concept of multifrequency induced-charge electroosmotic (MICEO) slipping on ideally polarizable surfaces of a series of parallelly-placed metal strips. In MICEO, a phase-shifted hybrid AC voltage signal is imposed to a double-sided discrete electrode array arranged along channel sidewalls, and the time-averaged nonlinear Coulomb force within the induced-double layer, wherein the Debye screening charge has two components oscillating at distinct frequencies and spatial phase gradients, gives rise to simultaneous directed transport and convective mixing of the working fluid under a subtle combination of lateral ACEO turbulent perturbation and axial TWEO pumping motion. Our theoretical analysis and experimental validation demonstrate, for the first time, that induced-charge electroosmosis can be actuated by multi-frequency AC electric fields of different phase-transition characteristics at the same time. This kind of multiple Fourier-mode ICEO streaming is directly related to several exciting applications, including particle preconcentration, simultaneous sample delivery and stirring, as well as any subsequent biochemical analysis in microfluidics. The horizontal TWEO streamlines (rotating ACEO micro-vortices) are either profitable for pumping (mixing) or harmful for mixing (pumping), and our physical descriptions on multi-frequency ICEO above driving electrode arrays can guide the elaborate design of flexible electrokinetic frameworks to either strengthen or suppress them. The most salient feature about MICEO is its robust dual-functionality in unidirectional delivery and chaotic mixing of chemical analytes in a synergistic mode, and it is quite feasible to reconcile their relative importance by adjusting the ratio of standing and traveling wave voltage amplitudes. It is highly anticipated that multifrequency ICEO would actively stimulate the interdisciplinary research on nonlinear electrokinetics, analytical chemistry, and condensed matter physics in the broad context of microfluidics, nanofluidics, and lab-on-a-chip in the near future.

Supplementary Materials: The following are available online at http://www.mdpi.com/2072-666X/10/7/447/s1, Video S1: Flow tracing experiment of MICEO.

Author Contributions: Writing—original draft preparation, K.D.; Supervision and project administration, Y.R.; Methodology, W.L.; Conceptualization, Y.T.; Software, J.S.

Funding: This project is financially supported by the National Natural Science Foundation of China (nos.11672095, 11702035, 11702075), Natural Science Foundation of Shaanxi Province (no. 2019JQ-073), the Chang'an University Fundamental Research Funds for the Central Universities (no. 310832171008), Shaanxi key industrial innovation chain (group)-industrial field (2019ZDLGY15-04-02, no. 2018ZDCXL-GY-05-04, no. 2018ZDCXL-GY-05-07-02), Self-Planned Task (SKLRS201803B) of State Key Laboratory of Robotics and System (HIT).

Conflicts of Interest: The authors declare no conflict of interest.

References

1. Dittrich, P.S.; Tachikawa, K.; Manz, A. Micro total analysis systems. Latest advancements and trends. *Anal. Chem.* **2006**, *78*, 3887–3908. [CrossRef] [PubMed]
2. Lee, C.Y.; Chang, C.L.; Wang, Y.N.; Fu, L.M. Microfluidic mixing: A review. *Int. J. Mol. Sci.* **2011**, *12*, 3263–3278. [CrossRef] [PubMed]
3. Squires, T.M.; Messinger, R.J.; Manalis, S.R. Making it stick: Convection, reaction and diffusion in surface-based biosensors. *Nat. Biotechnol.* **2008**, *26*, 417–426. [CrossRef] [PubMed]
4. Chen, L.; Wang, G.; Lim, C.; Seong, G.H.; Choo, J.; Lee, E.K.; Kang, S.H.; Song, J.M. Evaluation of passive mixing behaviors in a pillar obstruction poly(dimethylsiloxane) microfluidic mixer using fluorescence microscopy. *Microfluid. Nanofluid.* **2009**, *7*, 267–273. [CrossRef]
5. James, G.; Hold, A.E.; Arne, E.; Khan, A. A review of passive and active mixing systems in microfluidic devices. *Int. J. Multiphys.* **2009**, *1*, 1–32.
6. Ramos, A. *Electrokinetics and Electrohydrodynamics in Microsystems*; Springer Science & Business Media: Berlin, Germany, 2011; Volume 530.
7. Williams, S. Ac dielectrophoresis lab-on-chip devices. In *Encyclopedia of Microfluidics and Nanofluidics*; Springer: Berlin, Germany, 2008; pp. 1–8.
8. Morgan, H.; Green, N.G. *Ac Electrokinetics: Colloids and Nanoparticles*; Research Studies Press: Philadelphia, PA, USA, 2003.
9. Bazant, M.Z.; Thornton, K.; Ajdari, A. Diffuse-charge dynamics in electrochemical systems. *Phys. Rev. E* **2004**, *70*, 021506. [CrossRef]
10. Ramos, A.; Morgan, H.; Green, N.G.; Castellanos, A. Ac electrokinetics: A review of forces in microelectrode structures. *J. Phys. D Appl. Phys.* **1998**, *31*, 2338. [CrossRef]
11. Castellanos, A.; Ramos, A.; Gonzalez, A.; Green, N.G.; Morgan, H. Electrohydrodynamics and dielectrophoresis in microsystems: Scaling laws. *J. Phys. D Appl. Phys.* **2003**, *36*, 2584. [CrossRef]
12. Liu, W.; Ren, Y.; Tao, Y.; Chen, X.; Yao, B.; Hui, M.; Bai, L. Control of two-phase flow in microfluidics using out-of-phase electroconvective streaming. *Phys. Fluids* **2017**, *29*, 112002. [CrossRef]
13. Liu, W.; Ren, Y.; Tao, Y.; Li, Y.; Chen, X. Controllable rotating behavior of individual dielectric microrod in a rotating electric field. *Electrophoresis* **2017**, *38*, 1427–1433. [CrossRef]
14. Liu, W.; Ren, Y.; Tao, Y.; Yao, B.; Liu, N.; Wu, Q. A universal design of field-effect-tunable microfluidic ion diode based on a gating cation-exchange nanoporous membrane. *Phys. Fluids* **2017**, *29*, 112001. [CrossRef]
15. Boymelgreen, A.M.; Balli, T.; Miloh, T.; Yossifon, G. Active colloids as mobile microelectrodes for unified label-free selective cargo transport. *Nat. Commun.* **2018**, *9*, 760. [CrossRef] [PubMed]
16. Wu, J.J. Ac electro-osmotic micropump by asymmetric electrode polarization. *J. Appl. Phys.* **2008**, *103*, 024907. [CrossRef]
17. Ajdari, A. Pumping liquids using asymmetric electrode arrays. *Phys. Rev. E* **2000**, *61*, R45. [CrossRef]
18. Kunti, G.; Bhattacharya, A.; Chakraborty, S. Analysis of micromixing of non-newtonian fluids driven by alternating current electrothermal flow. *J. Non-Newton. Fluid Mech.* **2017**, *247*, 123–131. [CrossRef]
19. Kunti, G.; Bhattacharya, A.; Chakraborty, S. A scaling analysis for electrohydrodynamic convection with variable thermophysical and electrical properties. *Int. J. Heat Mass Transf.* **2017**, *109*, 215–222. [CrossRef]
20. Green, N.G.; Ramos, A.; Gonzalez, A.; Castellanos, A.; Morgan, H. Electrothermally induced fluid flow on microelectrodes. *J. Electrost.* **2001**, *53*, 71–87. [CrossRef]
21. Gimsa, J.; Stubbe, M.; Gimsa, U. A short tutorial contribution to impedance and ac-electrokinetic characterization and manipulation of cells and media: Are electric methods more versatile than acoustic and laser methods? *J. Electr. Bioimpedance* **2014**, *5*, 74–91. [CrossRef]
22. Liu, W.; Ren, Y.; Shao, J.; Jiang, H.; Ding, Y. A theoretical and numerical investigation of travelling wave induction microfluidic pumping in a temperature gradient. *J. Phys. D Appl. Phys.* **2014**, *47*, 075501. [CrossRef]
23. Liu, W.; Ren, Y.; Tao, Y.; Chen, X.; Wu, Q. Electrode cooling effect on out-of-phase electrothermal streaming in rotating electric fields. *Micromachines* **2017**, *8*, 327. [CrossRef]
24. Park, S.; Yossifon, G. Electrothermal based active control of ion transport in a microfluidic device with an ion-permselective membrane. *Nanoscale* **2018**, *10*, 11633–11641. [CrossRef] [PubMed]
25. Liu, X.; Yang, K.; Wadhwa, A.; Eda, S.; Li, S.; Wu, J. Development of an ac electrokinetics-based immunoassay system for on-site serodiagnosis of infectious diseases. *Sens. Actuators A Phys.* **2011**, *171*, 406–413. [CrossRef]

26. Park, S.; Koklu, M.; BeskoK, A. Particle trapping in high-conductivity media with electrothermally enhanced negative dielectrophoresis. *Anal. Chem.* **2009**, *81*, 2303–2310. [CrossRef] [PubMed]
27. Lian, M.; Islam, N.; Wu, J. Ac electrothermal manipulation of conductive fluids and particles for lab-chip applications. *IET Nanobiotechnol.* **2007**, *1*, 36–43. [CrossRef] [PubMed]
28. Green, N.G.; Ramos, A.; González, A.; Castellanos, A.; Morgan, H. Electric field induced fluid flow on microelectrodes: The effect of illumination. *J. Phys. D Appl. Phys.* **2000**, *33*, L13. [CrossRef]
29. Stubbe, M.; Gyurova, A.; Gimsa, J. Experimental verification of an equivalent circuit for the characterization of electrothermal micropumps: High pumping velocities induced by the external inductance at driving voltages below 5 v. *Electrophoresis* **2013**, *34*, 562–574. [CrossRef]
30. Williams, S.J. Enhanced electrothermal pumping with thin film resistive heaters. *Electrophoresis* **2013**, *34*, 1400–1408. [CrossRef]
31. Kale, A.; Song, L.; Lu, X.; Yu, L.; Hu, G.; Xuan, X. Electrothermal enrichment of submicron particles in an insulator-based dielectrophoretic microdevice. *Electrophoresis* **2017**, *39*, 887–896. [CrossRef]
32. Loire, S.; Kauffmann, P.; Mezić, I.; Meinhart, C. A theoretical and experimental study of ac electrothermal flows. *J. Phys. D Appl. Phys.* **2012**, *45*, 185301. [CrossRef]
33. Iverson, B.D.; Garimella, S.V. Experimental characterization of induction electrohydrodynamics for integrated microchannel pumping. *J. Micromech. Microeng.* **2009**, *19*, 055015. [CrossRef]
34. Felten, M.; Staroske, W.; Jaeger, M.S.; Schwille, P.; Duschl, C. Accumulation and filtering of nanoparticles in microchannels using electrohydrodynamically induced vortical flows. *Electrophoresis* **2008**, *29*, 2987–2996. [CrossRef] [PubMed]
35. Du, E.; Manoochehri, S. Enhanced ac electrothermal fluidic pumping in microgrooved channels. *J. Appl. Phys.* **2008**, *104*, 064902. [CrossRef]
36. Cao, J.; Cheng, P.; Hong, F. A numerical study of an electrothermal vortex enhanced micromixer. *Microfluid. Nanofluid.* **2008**, *5*, 13–21. [CrossRef]
37. Stubbe, M.; Holtappels, M.; Gimsa, J. A new working principle for ac electro-hydrodynamic on-chip micro-pumps. *J. Phys. D Appl. Phys.* **2007**, *40*, 6850. [CrossRef]
38. Singhal, V.; Garimella, S.V. Induction electrohydrodynamics micropump for high heat flux cooling. *Sens. Actuators A Phys.* **2007**, *134*, 650–659. [CrossRef]
39. Tao, Y.; Ren, Y.; Liu, W.; Wu, Y.; Jia, Y.; Lang, Q.; Jiang, H. Enhanced particle trapping performance of induced charge electroosmosis. *Electrophoresis* **2016**, *37*, 1326–1336. [CrossRef]
40. Ren, Y.; Liu, W.; Tao, Y.; Hui, M.; Wu, Q. On ac-field-induced nonlinear electroosmosis next to the sharp corner-field-singularity of leaky dielectric blocks and its application in on-chip micro-mixing. *Micromachines* **2018**, *9*, 102. [CrossRef]
41. Liu, W.; Wu, Q.; Ren, Y.; Cui, P.; Yao, B.; Li, Y.; Hui, M.; Jiang, T.; Bai, L. On the bipolar dc flow field-effect-transistor for multifunctional sample handing in microfluidics: A theoretical analysis under the debye–huckel limit. *Micromachines* **2018**, *9*, 82. [CrossRef]
42. Liu, W.; Ren, Y.; Tao, Y.; Li, Y.; Wu, Q. On traveling-wave field-effect flow control for simultaneous induced-charge electroosmotic pumping and mixing in microfluidics: Physical perspectives and theoretical analysis. *J. Micromech. Microeng.* **2018**, *28*, 055004. [CrossRef]
43. Squires, T.M.; Bazant, M.Z. Induced-charge electro-osmosis. *J. Fluid Mech.* **2004**, *509*, 217–252. [CrossRef]
44. Bazant, M.Z.; Squires, T.M. Induced-charge electrokinetic phenomena: Theory and microfluidic applications. *Phys. Rev. Lett.* **2004**, *92*, 066101. [CrossRef] [PubMed]
45. Yossifon, G.; Frankel, I.; Miloh, T. Symmetry breaking in induced-charge electro-osmosis over polarizable spheroids. *Phys. Fluids* **2007**, *19*, 217. [CrossRef]
46. Yossifon, G.; Frankel, I.; Miloh, T. On electro-osmotic flows through microchannel junctions. *Phys. Fluids* **2006**, *18*, 381. [CrossRef]
47. Leinweber, F.C.; Eijkel, J.C.T.; Bower, J.G.; van den Berg, A. Continuous flow microfluidic demixing of electrolytes by induced charge electrokinetics in structured electrode arrays. *Anal. Chem.* **2006**, *78*, 1425–1434. [CrossRef] [PubMed]
48. Squires, T.M. Induced-charge electrokinetics: Fundamental challenges and opportunities. *Lab Chip* **2009**, *9*, 2477–2483. [CrossRef] [PubMed]
49. Gregersen, M.M.; Andersen, M.B.; Soni, G.; Meinhart, C.; Bruus, H. Numerical analysis of finite debye-length effects in induced-charge electro-osmosis. *Phys. Rev. E* **2009**, *79*, 066316. [CrossRef] [PubMed]

50. Eckstein, Y.; Yossifon, G.; Seifert, A.; Miloh, T. Nonlinear electrokinetic phenomena around nearly insulated sharp tips in microflows. *J. Colloid Interface Sci.* **2009**, *338*, 243–249. [CrossRef]
51. García-Sánchez, P.; Ramos, A. Electrorotation of a metal sphere immersed in an electrolyte of finite debye length. *Phys. Rev. E* **2015**, *92*, 052313. [CrossRef]
52. Zehavi, M.; Yossifon, G. Particle dynamics and rapid trapping in electro-osmotic flow around a sharp microchannel corner. *Phys. Fluids* **2014**, *26*, 133–143. [CrossRef]
53. Zehavi, M.; Boymelgreen, A.; Yossifon, G. Competition between induced-charge electro-osmosis and electrothermal effects at low frequencies around a weakly polarizable microchannel corner. *Phys. Rev. Appl.* **2016**, *5*, 044013. [CrossRef]
54. Gimsa, J.; Eppmann, P.; Prüger, B. Introducing phase analysis light scattering for dielectric characterization: Measurement of traveling-wave pumping. *Biophys. J.* **1997**, *73*, 3309. [CrossRef]
55. González, A.; Ramos, A.; Morgan, H.; Green, N.G.; Castellanos, A. Electrothermal flows generated by alternating and rotating electric fields in microsystems. *J. Fluid Mech.* **2006**, *564*, 415–433. [CrossRef]
56. Green, N.G.; Ramos, A.; González, A.; Morgan, H.; Castellanos, A. Fluid flow induced by nonuniform ac electric fields in electrolytes on microelectrodes. I. Experimental measurements. *Phys. Rev. E* **2000**, *61*, 4011. [CrossRef]
57. González, A.; Ramos, A.; Green, N.G.; Castellanos, A.; Morgan, H. Fluid flow induced by nonuniform ac electric fields in electrolytes on microelectrodes. Ii. A linear double-layer analysis. *Phys. Rev. E* **2000**, *61*, 4019. [CrossRef]
58. Green, N.G.; Ramos, A.; Gonzalez, A.; Morgan, H.; Castellanos, A. Fluid flow induced by nonuniform ac electric fields in electrolytes on microelectrodes. Iii. Observation of streamlines and numerical simulation. *Phys. Rev. E* **2002**, *66*, 026305. [CrossRef] [PubMed]
59. Liu, W.; Shao, J.; Ren, Y.; Liu, J.; Tao, Y.; Jiang, H.; Ding, Y. On utilizing alternating current-flow field effect transistor for flexibly manipulating particles in microfluidics and nanofluidics. *Biomicrofluidics* **2016**, *10*, 034105. [CrossRef] [PubMed]
60. Ren, Y.; Liu, W.; Jia, Y.; Tao, Y.; Shao, J.; Ding, Y.; Jiang, H. Induced-charge electroosmotic trapping of particles. *Lab Chip* **2015**, *15*, 2181–2191. [CrossRef]
61. Wu, J.; Ben, Y.; Chang, H.-C. Particle detection by electrical impedance spectroscopy with asymmetric-polarization ac electroosmotic trapping. *Microfluid. Nanofluid.* **2005**, *1*, 161–167. [CrossRef]
62. Gonzalez, A.; Ramos, A.; García-Sánchez, P.; Castellanos, A. Effect of the combined action of faradaic currents and mobility differences in ac electro-osmosis. *Phys. Rev. E* **2010**, *81*, 016320. [CrossRef]
63. Liu, W.; Shao, J.; Ren, Y.; Wu, Y.; Wang, C.; Ding, H.; Jiang, H.; Ding, Y. Effects of discrete-electrode arrangement on traveling-wave electroosmotic pumping. *J. Micromech. Microeng.* **2016**, *26*, 095003. [CrossRef]
64. García-Sánchez, P.; Ramos, A.; Green, N.; Morgan, H. Traveling-wave electrokinetic micropumps: Velocity, electrical current, and impedance measurements. *Langmuir* **2008**, *24*, 9361–9369. [CrossRef] [PubMed]
65. Ramos, A.; González, A.; García-Sánchez, P.; Castellanos, A. A linear analysis of the effect of faradaic currents on traveling-wave electroosmosis. *J. Colloid Interface Sci.* **2007**, *309*, 323–331. [CrossRef] [PubMed]
66. Ramos, A.; Morgan, H.; Green, N.G.; González, A.; Castellanos, A. Pumping of liquids with traveling-wave electroosmosis. *J. Appl. Phys.* **2005**, *97*, 084906. [CrossRef]
67. Cahill, B.P.; Heyderman, L.J.; Gobrecht, J.; Stemmer, A. Electro-osmotic streaming on application of traveling-wave electric fields. *Phys. Rev. E* **2004**, *70*, 036305. [CrossRef] [PubMed]
68. Urdaneta, M.; Smela, E. Multiple frequency dielectrophoresis. *Electrophoresis* **2007**, *28*, 3145–3155. [CrossRef] [PubMed]
69. Zhang, K.; Ren, Y.; Tao, Y.; Liu, W.; Jiang, T.; Jiang, H. Efficient micro-nano particle concentration using direct current induced thermal buoyancy convection for multiple liquid media. *Anal. Chem.* **2019**, *91*, 4457–4465. [CrossRef] [PubMed]
70. Tao, Y.; Liu, W.; Ren, Y.; Hu, Y.; Li, G.; Ma, G.; Wu, Q. On developing field-effect-tunable nanofluidic ion diodes with bipolar, induced-charge electrokinetics. *Micromachines* **2018**, *9*, 179. [CrossRef] [PubMed]
71. Sun, H.; Ren, Y.; Liu, W.; Feng, X.; Hou, L.; Tao, Y.; Jiang, H. Flexible continuous particle beam switching via external-field-reconfigurable asymmetric induced-charge electroosmosis. *Anal. Chem.* **2018**, *90*, 11376–11384. [CrossRef]
72. Canpolat, C.; Qian, S.; Beskok, A. Micro-piv measurements of induced-charge electro-osmosis around a metal rod. *Microfluid. Nanofluid.* **2013**, *14*, 153–162. [CrossRef]

73. Squires, T.M.; Quake, S.R. Microfluidics: Fluid physics at the nanoliter scale. *Rev. Mod. Phys.* **2005**, *77*, 977. [CrossRef]
74. Jain, M.; Yeung, A.; Nandakumar, K.J. Efficient micromixing using induced-charge electroosmosis. *J. Microelectromech Syst.* **2009**, *18*, 376–384. [CrossRef]
75. Wu, Z.; Li, D. Micromixing using induced-charge electrokinetic flow. *Electrochim. Acta* **2008**, *53*, 5827–5835. [CrossRef]
76. Zhao, H.; Bau, H.H. Microfluidic chaotic stirrer utilizing induced-charge electro-osmosis. *Phys. Rev. E* **2007**, *75*, 066217. [CrossRef] [PubMed]
77. Wu, Z.; Li, D. Mixing and flow regulating by induced-charge electrokinetic flow in a microchannel with a pair of conducting triangle hurdles. *Microfluid. Nanofluid.* **2008**, *5*, 65–76. [CrossRef]
78. Zhang, F.; Daghighi, Y.; Li, D. Control of flow rate and concentration in microchannel branches by induced-charge electrokinetic flow. *J. Colloid Interface Sci.* **2011**, *364*, 588–593. [CrossRef] [PubMed]
79. Jain, M.; Yeung, A.; Nandakumar, K. Induced charge electro osmotic mixer: Obstacle shape optimization. *Biomicrofluidics* **2009**, *3*, 022413. [CrossRef] [PubMed]
80. Ren, Y.; Song, C.; Liu, W.; Jiang, T.; Song, J.; Wu, Q.; Jiang, H. On hybrid electroosmotic kinetics for field-effect-reconfigurable nanoparticle trapping in a four-terminal spiral microelectrode array. *Electrophoresis* **2019**, *40*, 979–992. [CrossRef]
81. Prabhakaran, R.A.; Zhou, Y.; Zhao, C.; Hu, G.; Song, Y.; Wang, J.; Yang, C.; Xuan, X. Induced charge effects on electrokinetic entry flow. *Phys. Fluids* **2017**, *29*, 42–48. [CrossRef]
82. Bazant, M.Z.; Kilic, M.S.; Storey, B.D.; Ajdari, A. Towards an understanding of induced-charge electrokinetics at large applied voltages in concentrated solutions. *Adv. Colloid Interface Sci.* **2009**, *152*, 48–88. [CrossRef] [PubMed]
83. Schnitzer, O.; Yariv, E. Induced-charge electro-osmosis beyond weak fields. *Phys. Rev. E* **2012**, *86*, 061506. [CrossRef]
84. Feng, X.; Ren, Y.; Jiang, H. An effective splitting-and-recombination micromixer with self-rotated contact surface for wide reynolds number range applications. *Biomicrofluidics* **2013**, *7*, 647. [CrossRef] [PubMed]

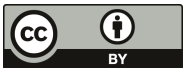

micromachines

MDPI

Article

An Experimental Study of 3D Electrode-Facilitated Particle Traffic Flow-Focusing Driven by Induced-Charge Electroosmosis

Tianyi Jiang [1], Ye Tao [1,*], Hongyuan Jiang [1], Weiyu Liu [2,*], Yansu Hu [2] and Dewei Tang [1]

[1] State Key Laboratory of Robotics and System, Harbin Institute of Technology, Harbin 150001, China; jty_hit@hit.edu.cn (T.J.); jhy_hit@hit.edu.cn (H.J.); dwtang@hit.edu.cn (D.T.)

[2] School of Electronics and Control Engineering, Chang'an University, Xi'an 710064, China; huyansu@chd.edu.cn

* Correspondence: tarahit@gmail.com (Y.T.); liuweiyu@chd.edu.cn (W.L.); Tel.: +86-0451-86-418-028 (Y.T.); +86-029-82-334-543 (W.L.)

Received: 30 January 2019; Accepted: 15 February 2019; Published: 18 February 2019

Abstract: In this paper we present a novel microfluidic approach for continuous, rapid and switchable particle concentration, using induced-charge electroosmosis (ICEO) in 3D electrode layouts. Field-effect control on non-linear electroosmosis in the transverse direction greatly facilitates a selective concentration of biological yeast cells from a straight main microchannel into one of the three downstream branch channels in our microfluidic device. For the geometry configuration of 3D driving electrode plates on sidewalls and a 2D planar gate electrode strip on the channel bottom surface, we briefly describe the underlying physics of an ICEO-based particle flow-focusing method, and provide relevant simulation results to show how gate voltage amplitude can be used to guide the motion trajectory of the concentrated particle stream. With a relatively simple geometrical configuration, the proposed microfluidic device provides new possibilities to controllably concentrate micro/nanoparticles in continuous flow by using ICEO, and is suitable for a high-throughput front-end cell concentrator interfacing with various downstream biosensors.

Keywords: microfluidic particle concentrator; continuous and switchable particle flow-focusing; composite electrode arrangement; induced-charge electroosmosis; field-effect flow control

1. Introduction

In a number of biomedical and analytical applications, it is a crucial step to purify or extract target micro- or nano- particles from various sample matrices. To process samples with a low number of particles, a concentration step is usually imperative to abate the sample volume to an effective range (nL to μL) that microfluidic devices can handle [1,2]. Numerous methods have been developed concerning microfluidic particle concentration and manipulation in lab-on-a-chip systems such as direct current (DC) electrokinetics [3,4], alternating current (AC) electrohydrodynamics [5–18], dielectrophoresis [19–25], hydrodynamics, ultrasonic wave [26–28] magnetism, and ion concentration polarization [29–31].

Induced-charge electrokinetic phenomenon occurs as an applied electric field E induces a bipolar diffuse screening cloud adjacent to a polarizable solid surface immersed in electrolyte, then forces that induced double-layer (IDL) into an induced-charge electroosmotic (ICEO) flow [32–45]. This promising technique has been utilized to realize many microfluidic applications, including liquid pumping [33,46–49], mixing [50–52], as well as induced-charge electrophoresis of polarizable particles [53–59]. However, the use of ICEO fluid motion to achieve flexible particle manipulation has rarely been exploited. Recently, we reported position-controllable trapping of microscale particles on a bipolar metal strip in static flow condition by exploiting a tunable ICEO technique, termed the

AC-flow field effect transistor (AC-FFET) [60]. To generate AC-FFET, a gate electrode (GE) is placed inside an externally-applied AC electric field for introducing biased ICEO slipping flow on its ideally polarizable surface, and can be flexibly addressed. By contrast with traditional methods, one important feature of AC-FFET is that a change in the gate voltage amplitude enables a variation in lateral ICEO flow profile above GE, greatly facilitating a flexible particle trapping technique [60].

Although AC-FFET is flexible in particle manipulation, in most situations, a microfluidic device that is able to focus incoming particle samples in a continuous pressure-driven fluid flow rather than a static condition is often of greater scientific significance [20,29,61]. Inspired by this, on the basis of AC-FFET, we present herein a novel microfluidic approach for continuous, rapid and switchable particle concentrating with 3D electrode layouts. The microfluidic device with composite electrode structure consists of a pair of face-to-face 3D silver-polydimethylsiloxane (Ag-PDMS) [62] driving electrodes fabricated on both sidewalls of the device channel and a planar indium tin oxide (ITO) metal strip acting as the gate electrode (GE), all of which are disposed along the longitudinal direction of the main channel bifurcating into three downstream branch channels (Figure 1).

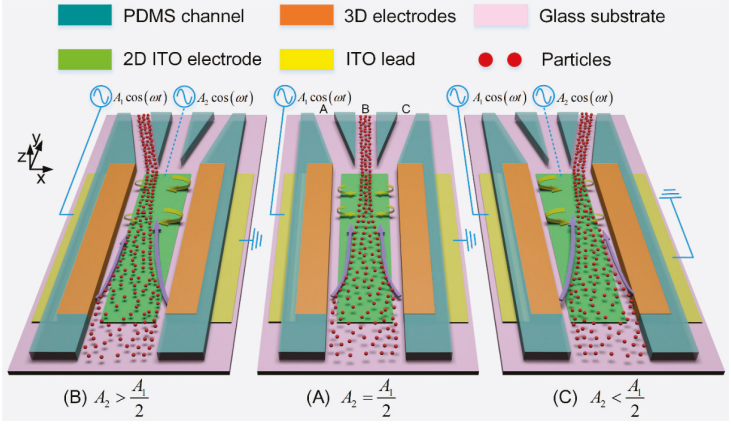

Figure 1. A 3D schematic of the presented microfluidic particle concentrator that is capable of continuously focusing the incoming particle samples into a switchable downstream branch channel by adjusting the voltage amplitude of the indium tin oxide (ITO) gate electrode (GE): (**A**) when the middle ITO electrode floats in potential, i.e., $A_2 = \frac{A_1}{2}$, the two opposite induced-charge electroosmotic (ICEO) eddies above the electrode surface divert the trajectories of the incoming particles to the middle branch B; (**B**) when the biased gate voltage of ITO GE is more than its floating potential, i.e., $A_2 > \frac{A_1}{2}$, the single dominating ICEO micro-vortex which is clockwise rotating above the electrode surface makes particles move into the left branch A; (**C**) when $A_2 < \frac{A_1}{2}$, particles move into the right branch C due to the action of the counterclockwise rotating ICEO vortex.

The performance of the concentration device is validated by flow-focusing yeast cells of 5 μm in diameter suspended in low-conductivity KCl aqueous solution. By controlling the gate voltage amplitude, transverse ICEO convective rolls of adjustable flow profiles are induced above the surface of the planar GE, so that the device can continuously concentrate the incoming yeast cells into a switchable downstream branch channel (Figure 1). The proposed approach of continuous label-free sample processing provides a robust front-end concentration interface for a variety of biosensors and detection systems, without major limitation in downstream integration.

2. Mechanism of Switchable Particle Concentration by Using Alternating Current-Flow Field Effect Transistor (AC-FFET)

A bi-layer asymptotic model of ICEO convective flow has been proposed in our previous work [60], where a non-linear slip profile above the reciprocal resistor-capacitor (RC) time scale explains the stable and position-controllable trapping of yeast cells on the surface of a bipolar metal strip. In this study, by combining this non-linear ICEO slip profile with an incoming laminar flowing stream from the inlet to the outlets, we develop a novel microfluidic device to focus particle samples continuously from the suspending medium into a selective downstream branch channel (Figure 1).

We first deal with the standard physical process of ICEO at the liquid/floating electrode interface. As Figure 2A shows, on switching the AC voltage wave on, initial normal component of electric field vector on the ITO electrode surface brings mobile counter-ions to the metal/electrolyte interface, where they pile up and form a dipolar IDL after a characteristic RC time scale $\tau_{RC} = aC_D/\sigma_f(1+\delta) = \varepsilon_f a/\sigma_f \lambda_D(1+\delta)$ ($a = 0.5\,L$) is the macroscopic length scale, L = 500 μm the width of ITO strip electrode, $C_D = \varepsilon_f/\lambda_D$ the diffuse layer capacitance, δ is the surface capacitance ratio) due to a force equilibrium between electrostatic attraction and thermal diffusion as shown in Figure 2B. The Debye length of IDL $\lambda_D = \sqrt{D\varepsilon_f/\sigma_f}$ lies in the range of 0.5–100 nm for aqueous solutions, where $D = 2 \times 10^{-9}$ m^2/s is the ionic diffusivity, while $\varepsilon_f = 7.08 \times 10^{-10}$ F/m and $\sigma_f = 0.001$ S/m are the dielectric permittivity and electrical conductivity of the bulk fluid, respectively.

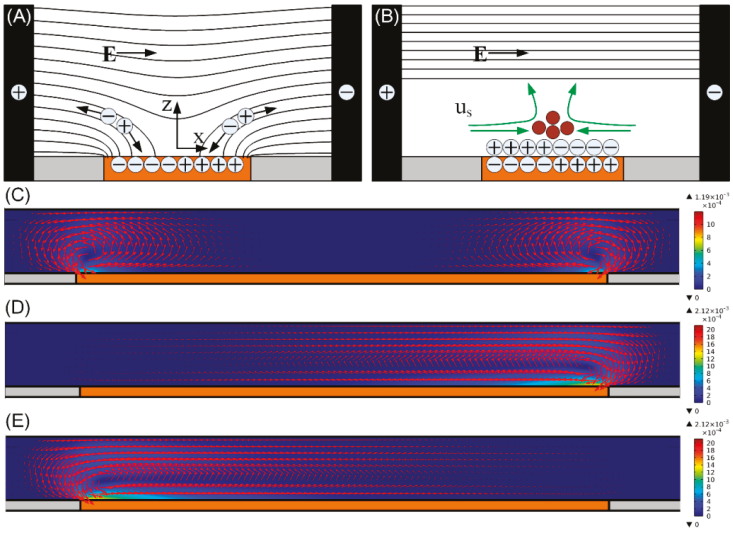

Figure 2. (**A**,**B**) Formation of ICEO around an ideally polarizable ITO metal strip, a floating ITO electrode (orange) is polarized by ionic current in a suddenly applied background electric field supplied by the sidewall 3D silver-polydimethylsiloxane (Ag-PDMS) driving electrodes (black), with the black lines and green arrows representing the electric field lines and ICEO flow velocity vectors, respectively. (**A**) Mobile counter-ions follow the electric field lines to the electrode surface; (**B**) at steady state, an induced double-layer (IDL) of dipolar nature and finite Debye length is formed at the metal/electrolyte interface, leaving only tangential bulk electric field forcing the IDL into ICEO convective flow. (**C**–**E**) A surface and arrow plot of ICEO flow field in the *x*-*z* plane for switchable particle concentrating (unit: m/s): (**C**) when the ITO electrode floats in potential, i.e., $A_2 = A_1/2$, at f = 300 Hz and A_1 = 30 V for concentrating particles into the middle branch; When different biased gate voltage A_2 is imposed on the ITO GE at f = 30 Hz and A_1 = 15 V; (**D**) A_2 = 14.875 V for concentrating particles into the left branch; and (**E**) A_2 = 0.125 V for concentrating particles into the right branch.

At steady state, an inhomogeneous distribution of the induced surface charge in the diffuse screening cloud fully repels the bulk field lines, so the ideally polarizable metal surface of the floating electrode behaves as an insulator from the perspective of an observer at very low frequencies (Figure 2B). The tangential field component acting on its own induced ionic charge in the IDL gives rise to two opposite ICEO eddies in the transverse *x*-*z* plane, resulting in a lateral flow stagnation line at the center of the electrode surface which can be exploited for particle concentration at proper conditions (Figure 2B). When the field frequency exceeds the surface-averaged reciprocal RC charging time $f_{RC-average} = \sigma_f(1+\delta)/2\pi C_d(0.5L) = 37$ Hz for the equivalent circuit of the interfacial double-layer capacitance coupled to the bulk resistance, incomplete double-layer charging takes place due to the relaxation process. As a consequence, the metal surface recovers to a perfect conductor for frequency beyond $f_{RC-average}$, and ICEO flow velocity decreases by half at $f_{RC-average} = 37$ Hz.

Long–range ICEO micro-vortices constantly transport particles from the bulk fluid to the transversal flow stagnation region at the electrode center (Figure 2), where they can be stably trapped if the upward ICEO fluidic drag can be balanced by the downward buoyancy force [60]. In our previous work, we report that for field frequency above the reciprocal RC charging time $f_{RC-average} = 37$ Hz, a spectrum of charging modes results in a nonlinear ICEO slip profile on the surface of the planar ITO electrode [60]. Since the nonlinear ICEO slip profile above $f_{RC-average}$ induces a negligibly small upward ICEO flow component, the downward buoyancy force is able to overcome the upward fluidic drag, which makes the cells entrained by bulk ICEO flow trapped at the center of the electrode surface.

Now we introduce the above idea of ICEO-based particle trapping into a continuous-flow microfluidic device, where an incoming Poiseuille stream of inlet flow velocity u_0 is stably flowing from the inlet to the three downstream outlet branches (Figure 1).

By energizing the sidewall 3D Ag-PDMS driving electrodes with an AC voltage signal $A_1\cos(\omega t)$ and keeping the potential of the planar ITO strip electrode $\frac{A_1}{2}\cos(\omega t)$ floating, ICEO flow is induced above the ITO electrode surface with a symmetrical flow profile perpendicular to that of the forward laminar stream carrying the particle sample to be concentrated. Here, $f = 2\pi/\omega$, ω and A_1 are the field frequency, angular frequency, and voltage amplitude of the AC voltage, respectively.

From Figure 1A, as transported by transverse ICEO flow in the *x*-*z* plane from the bulk fluid to the electrode center, particles are at the same time dragged forward by the incoming Poiseuille flow from the inlet to the downstream outlets. A combined action of the transverse ICEO flow and the forward laminar flow diverts the trajectories of most incoming particles to branch B.

By adopting the tunable ICEO technique, AC-FFET [60], and energizing the ITO GE with a biased AC gate voltage $A_2\cos(\omega t)$ different from its floating potential $\frac{A_1}{2}\cos(\omega t)$, ICEO flow with an asymmetric flow profile is produced in the transverse direction. As a result of one dominating ICEO micro-vortex above the surface of the ITO electrode, the incoming particles move into the left (or right) branch as $A_2 > \frac{A_1}{2}$ (or $A_2 < \frac{A_1}{2}$) (Figure 1B,C).

As a consequence, by controlling the gate voltage amplitude and, therefore, generating transverse ICEO convection of adjustable flow profiles above the ideally polarizable surface, continuously focusing the incoming particle samples into a preferential branch channel is achieved in this microfluidic device (Figure 1).

To demonstrate the feasibility of the particle concentrator, numerical simulation of ICEO flow using Comsol Multiphysics 5.3a is performed in the *x*-*z* plane, with the detailed simulation procedure provided in Section 3.5. ICEO flow indeed yields vortices over the ITO electrode for achieving particle concentration in the transverse direction (Figure 2C–E). By comparing the cases with different biased gate voltage A_2, broken symmetry of ICEO convective rolls occurs once the gate voltage A_2 deviates enough from the natural floating potential of GE $\frac{A_1}{2}$.

When $A_2 = \frac{A_1}{2}$, the two opposite eddies above the electrode surface (Figure 2C) can focus the incoming particles into the middle branch B. When $\frac{A_1}{2} < A_2 < A_1$, the only clockwise ICEO vortex over the ITO diverts the trajectories of the incoming particles to the left branch A (Figure 2D). When

$0 < A_2 < \frac{A_1}{2}$, particles move into the right branch C due to the action of the counterclockwise rotating ICEO vortex (Figure 2E).

3. Materials and Method

3.1. Device Geometry and Fabrication

The microfluidic chip was composed of a main microchannel branching into three downstream outlets, as shown in Figure 3A. The four branch channels were connected to 4 respective reservoirs—the inlet, outlet A, outlet B and outlet C. The inlet and outlets were all of 6 mm in height and 6 mm in diameter, giving rise to volumetric capacity of about 170 µL. Under such capacity, the liquid level difference was able to drive a steady flow for about 15 min in the main channel.

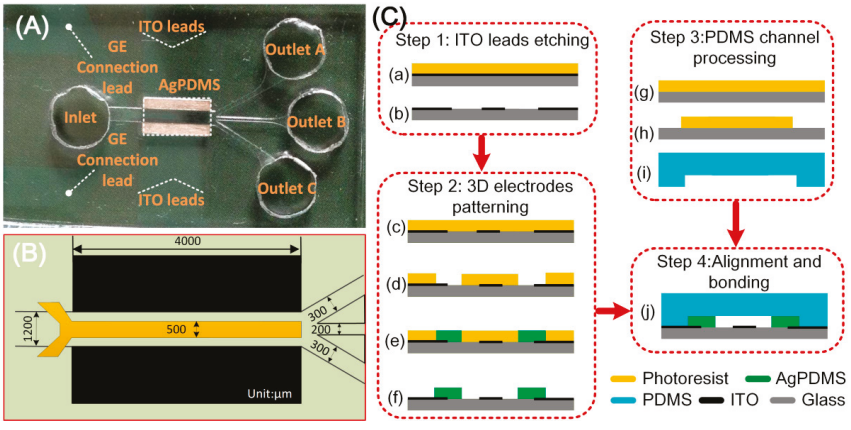

Figure 3. (**A**) A photograph of the microfluidic particle concentrator; (**B**) 2D illustration of the device geometry; (**C**) fabrication process of the experimental chip.

A pair of face-to-face 3D Ag-PDMS driving electrodes of 60 µm in thickness were fabricated on both sidewalls of the device channel, resulting in a 1.2 mm effective channel width (Figure 3B). The sidewall 3D electrodes were linked to the outer AC source through ITO leads. A planar ITO strip electrode of L = 500 µm in width and 200 nm in thickness was symmetrically disposed along the bottom centerline of the main channel and acted as GE. The length of Ag-PDMS electrodes was 4mm and equalled that of the ITO electrode. All the channels were 60 µm in height, while some other major dimensions of the configuration are shown in Figure 3B.

The device was fabricated following the similar procedures as presented in our previous work [63]. In brief, the fabrication procedure consists of four steps as shown in Figure 3C: ITO leads etching, 3D electrodes patterning, PDMS channel processing, and alignment and bonding.

First, a clean ITO glass slide was laminated by negative dry film resist (Riston SD238, DuPont, Wilmington, DE, USA), followed by a photolithography process. The slide with patterned dry film was submerged into an etching solution to obtain the ITO leads, and then the dry film was stripped off by $NaCO_3$ solution. After that, the slide was then laminated by two layers of dry film, followed by another photolithography process, hence generating the dry-film mold. Conductive Ag-PDMS gel [62] was then filled into the dry-film mold to form the sidewall 3D electrodes. After the fabrication of 3D Ag-PDMS electrodes, a PDMS microchannel was fabricated using conventional soft lithography method. Finally, the PDMS slab and the glass substrate with composite electrode structure were aligned under an optical microscope and bonded by oxygen plasma treatment.

3.2. Quantification of Particle Focusing Efficiency

Particle focusing efficiency η_X for branch X among A, B and C can be defined as:

$$\eta_X = \frac{N_X}{N_{total}} = \frac{N_X}{N_A + N_B + N_C} \times 100\% \quad (1)$$

Here $N_{total} = N_A + N_B + N_C$ is the total number of particles moving into the three branch channels as counted per half minute, and N_X the number of particles moving into branch X over the same time period.

3.3. Sample Preparation

The performance of the microfluidic particle concentrator was validated with yeast cells as the incoming particle samples, which were suspended in 0.001 S/m KCl aqueous solution. To prepare the sample solution of viable yeast cells, we suspended 50 mg of Baker's dry yeast in 20 mL DI water to make a mixture and put this mixture in an oven at 30 °C for 1 h. After reactivation, we transferred 1 mL of the yeast suspension to a centrifuge tube. The yeast suspension was then washed and centrifuged with DI water for three times. After removing the supernatant, we transferred the precipitation of yeast cells to 1 mL of a 1 mS/m KCl aqueous solution. Prior to every experiment, the yeast cell solution was diluted 20 times in KCl solution of identical electrical conductivity, and a 5% bovine serum albumin (BSA) solution was applied to coat the microchannel for ~1 h to prevent the particles from adhering to any solid walls.

3.4. Experimental Setup

A sample solution suspended with microparticles was first injected into the inlet. An AC signal, which was applied to the 3D electrodes through ITO leads, provided an AC electric field in the main channel. ICEO vortex flow was then formed on top of the ITO strip electrode, which dragged the particles from the surrounding medium to the ITO surface.

The AC voltage signals applied to all the electrodes were produced by a series combination of a function generator (TGA12104, TTi, Buckinghamshire, UK) and a signal amplifier (Model2350, TEGAM, Geneva, OH, USA), and their waveforms were monitored by a digital oscilloscope (TDS2024, Tektronix, Beaverton, OR, USA).

A sinusoidal voltage signal $A_1 \cos(\omega t)$ was applied to the left sidewall Ag-PDMS electrode, and the right one was grounded (Figure 1). The middle ITO GE was either floating in potential for concentrating particles into the middle branch B, or imposed with a biased voltage $A_2 \cos(\omega t)$ for selectively focusing particles into a desired side branch A or C.

The yeast cell solution was injected through the microchannel with an approximate inflow velocity u_0 = 200 μm/s at the channel inlet. Without a background AC electric field, the cells were distributed uniformly in the main channel and no obvious cell-concentrating phenomenon occurred (Figure 4A).

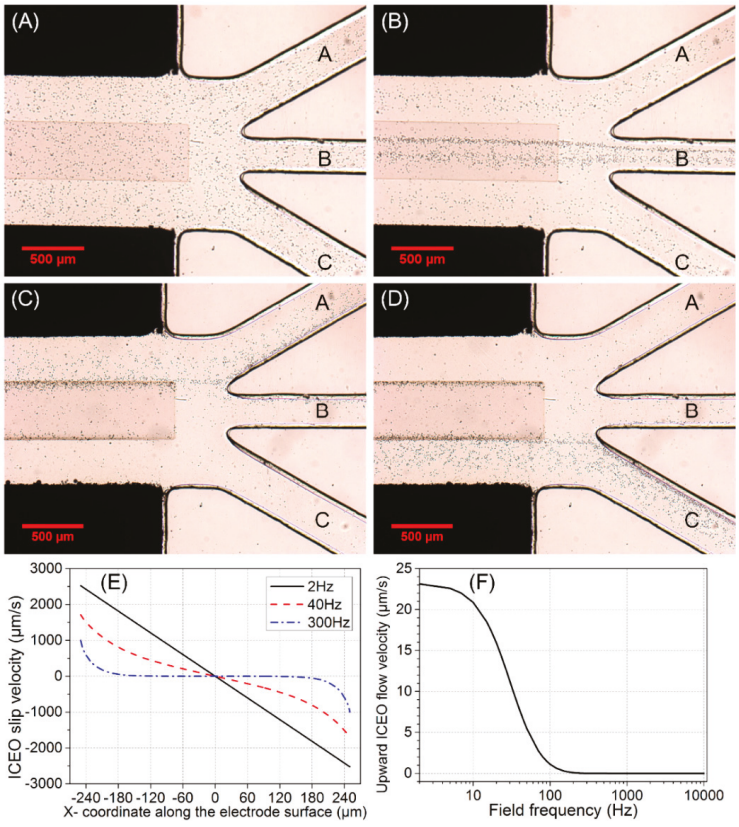

Figure 4. (**A**–**D**) Experimental observation of switchable particle concentrating at the main channel/branch channel junction for fixed inlet flow velocity u_0 = 200 μm/s and different gate voltage A_2: (**A**) initial distribution of yeast cells without AC power; (**B**) continuous-flow cell concentrating into the middle branch B by ICEO at f = 300 Hz and A_1 = 25 V when the ITO electrode floats in potential, i.e., $A_2 = \frac{A_1}{2}$; Continuous-flow cell concentrating into a desired side branch by AC-flow field effect transistor (AC-FFET) at f = 30 Hz and A_1 = 15 V for different biased gate voltage A_2, (**C**) for A_2 = 14.875 V, 78% cells move into the left branch A, and (**D**) for A_2 = 0.125 V, the trajectories of 78% cells are diverted to the right branch C. (**E**,**F**) Simulation results for A_1 = 30 V: (**E**) ICEO slip profiles on the surface of ITO electrode at different field frequencies; (**F**) frequency-dependent upward ICEO flow velocity at z = 2.5 μm (half of the cell diameter) above the center of ITO electrode surface.

The behavior of particles was observed under an optical microscope (BX53, Olympus, Tokyo, Japan) and video-taped by using a Charge-coupled Device (CCD) camera (RETIGA2000R, Qimaging, Surrey, BC, Canada). As we concerned particle focusing near the outlet branches, the experimental observation window was chosen at the main channel/branch channel junction.

3.5. Simulation Procedure

A standard bi-layer asymptotic model of the ICEO flow had been derived in our previous work, which made the electrokinetic problem readily decouple into one of electrochemical ion relaxation and another of viscous fluid flow originated by nonlinear electroosmotic slip at the polarizable surface. In this study, numerical simulation of the ICEO flow was acquired via Comsol Multiphysics 5.3a to

enable a better understanding on how the particle concentrator works, with the simulation procedure provided below.

(a) Electrochemical ion relaxation

In the bulk, potential phasor $\widetilde{\phi}$ satisfies the Laplace equation due to a constant conductivity throughout the entire channel:

$$\nabla^2\widetilde{\phi} = 0 \tag{2}$$

And $\widetilde{E} = -\nabla\widetilde{\phi}$ is the electric field phasor.

As for thin IDL approximation, the following RC boundary condition can be used to describe the double-layer charging process on the ideally polarizable metal surface of the floating electrode:

$$\sigma_f\left(\boldsymbol{n}\cdot\nabla\widetilde{\phi}\right) = j\omega\frac{C_{\mathrm{D}}}{1+\delta}\left(\widetilde{\phi} - \widetilde{V_0}\right) \tag{3}$$

Here $\delta = \frac{C_D}{C_S}$ is the surface capacitance ratio of the diffuse layer capacitance $C_D = \frac{\varepsilon_f}{\lambda_D}$ to the compact layer capacitance $C_S = 0.2\ \mathrm{F/m^2}$, $\omega = 2\pi f$ the angular frequency of the applied sinusoidal voltage, $\widetilde{V_0} = A_1/2$ the floating potential or $\widetilde{V_0} = A_2$ the fixed potential of the middle ITO GE, ϕ the potential in the fluid bulk just outside the diffuse double-layer, $C_0 = \frac{C_D}{1+\delta}$ the total area-specific capacitance at the metal/electrolyte interface, and $\boldsymbol{n}$ a unit normal vector on the surface of ITO electrode.

Double-layer polarization around the driving electrodes was neglected due to a much lower characteristic charging frequency, so we imposed a fixed-potential boundary condition there:

$$\widetilde{\phi} = A_1 \text{ (On the left electrode)} \tag{4a}$$

$$\widetilde{\phi} = 0 \text{ (On the right electrode)} \tag{4b}$$

The condition of zero normal electric current was imposed on insulating channel walls:

$$\boldsymbol{n}\cdot\nabla\widetilde{\phi} = 0 \tag{5}$$

(b) Induced-charge electroosmotic flow

After solving for the electrostatic potential, the next step was to solve for the ICEO fluid flow velocity $\boldsymbol{u}$ satisfying the Stokes equation for creeping flow:

$$\begin{cases} -\nabla p + \nabla\cdot\left(\eta\left(\nabla\boldsymbol{u} + (\nabla\boldsymbol{u})^T\right)\right) = 0 \\ \nabla\cdot\boldsymbol{u} = 0 \end{cases} \tag{6}$$

where p is the hydraulic pressure, and $\eta = 0.001\ \mathrm{Pa\cdot s}$ the viscosity of KCL aqueous solution.

The expression for time-averaged ICEO slip velocity on the polarizable surface of the floating electrode can be derived from the generalization of Helmholtz–Smoluchowski formula

$$\left\langle \boldsymbol{u}_{slip}\right\rangle = -\frac{\varepsilon}{\eta}\langle\zeta\boldsymbol{E_t}\rangle = -\frac{\varepsilon}{\eta}\frac{1}{2}\mathrm{Re}\left(\widetilde{\zeta}\widetilde{\boldsymbol{E}}_{\boldsymbol{t}}^{\ *}\right) = \frac{1}{2}\frac{\varepsilon_f}{\eta}\frac{1}{1+\delta}\mathrm{Re}\left(\left(\widetilde{\phi} - \widetilde{V_0}\right)\left(\widetilde{\boldsymbol{E}} - \widetilde{\boldsymbol{E}}\cdot\boldsymbol{n}\cdot\boldsymbol{n}\right)^*\right) \tag{7}$$

Here < > means the time-averaged value in a harmonic field, * the complex conjugate operator, and Re() the real part of a complex number. $\widetilde{\boldsymbol{E}}_t = \left(\widetilde{\boldsymbol{E}} - \widetilde{\boldsymbol{E}}\cdot\boldsymbol{n}\cdot\boldsymbol{n}\right)$ is the tangential component of electric field vector on the electrode surface, and $\widetilde{\zeta} = \frac{1}{1+\delta}\left(\widetilde{V_0} - \widetilde{\phi}\right)$ the induced zeta potential contributing to the ICEO fluid flow.

Besides, we applied no slip wall boundary condition on the surface of the driving electrodes and other insulating channel walls:

$$\boldsymbol{u} = 0 \tag{8}$$

(c) Modeling settings of the particle concentrator

To clarify the importance of ICEO flow effect on continuous and switchable particle concentrating, a numerical simulation employing COMSOL Multiphysics 5.3a was performed in the *x*-*z* plane.

The proposed 2D simulation model (Figure S1) was comprised of a microchamber with a pair of sidewall 3D Ag-PDMS driving electrodes. One planar indium tin oxid (ITO) electrode was deposited at the center of the channel bottom. The corresponding boundary conditions for electrostatics and hydrodynamics are summarized in Table S1, as shown in the Supplementary Information.

4. Results and Discussion

From Figure 4A,B, when ITO electrode floats in potential, yeast cells that stably move into middle branch B consist of two components: (1) incoming particles that are initially located above the surface of the ITO electrode; (2) particles that are not initially situated above the electrode surface but in close proximity to it can be transported by bulk ICEO vortical flows onto the electrode surface and subsequently enter branch B. However, incoming cell samples far away from the ITO electrode cannot be effectively influenced by ICEO flow, and hence move into the side branch A or C, which indicates the effective actuating range of ICEO convective flow is quite limited in this microfluidic device (Figure S2).

The simulated ICEO slip profile on the surface of ITO electrode transits gradually from a linear one in DC limit to a nonlinear one at 300 Hz beyond the RC relaxation frequency $f_{\text{RC-average}}$ = 37 Hz (Figure 4E), resulting in negligibly small upward ICEO fluidic drag acting on the cell samples beyond 200 Hz (Figure 4F).

We chose 300 Hz as an appropriate field frequency to concentrate cells into branch B by considering two aspects. On the one hand, below 200 Hz, the strong upward ICEO fluidic drag at the electrode center can overcome the downward buoyancy force, so cells make circulating motion with ICEO eddies. On another hand, at much higher frequencies, ICEO diminishes due to the mechanism of double-layer relaxation. Consequently, at 300 Hz, not only there is sufficient transverse ICEO driving force to push particles onto the electrode surface, but also the downward buoyancy force can overcome the upward ICEO fluidic drag to achieve stable cell trapping.

In contrast with the 25% particle-focusing efficiency in the absence of ICEO, η_B increases by 30% once AC background field of f = 300 Hz and A_1 = 25 V is provided. With a further increase in A_1 from 25 V to 30 V, however, η_B stays around 55%, partly due to the limited actuating range of ICEO eddies from vertical channel confinement (Figure S2A).

Besides the limited effective range of ICEO flow, another important characteristic of particle focusing is that cell samples cannot aggregate transversely to form a thin particle assembly line located at the center of the electrode surface, in stark contrast with our previous ICEO-based cell-trapping device [60]. What actually happens is that the incoming cells move along the longitudinal direction of the ITO electrode in the form of a wide particle stream instead of a thin assembly line (Figure 4B), due to the negative effect of vertical channel confinement on ICEO slip velocity along the ITO surface (Figure S3).

By employing the concept of AC-FFET and applying a second AC voltage signal $V_2(t) = A_2 \cos(\omega t)$ to the middle ITO GE different from its floating potential $V_{2\text{-}0}(t) = A_1/2 \cos(\omega t)$, we are able to continuously concentrate the incoming cells into the side branch at a low field frequency f = 30 Hz slightly below the double-layer relaxation frequency $f_{\text{RC-average}}$ = 37 Hz (Figure 4C,D). Since a much lower frequency 30 Hz is chosen this time, the voltage amplitude A_1 imposed on the sidewall Ag-PDMS electrode pair is lowered to 15 V for avoiding electrolysis and bubble formation. To induce effective AC-FFET phenomena, voltage amplitude A_2 = 14.875 V or 0.125 V is applied to the ITO GE.

When A_2 = 14.875 V is applied to GE, the trajectories of 78% cells are diverted to branch A (Figure 4C). Due to a voltage symmetry effect, when $A_2 = A_1 - 14.875$ V = 0.125 V is applied, 78% of cells move into branch C (Figure 4D).

From Figure 2D, when A_2 = 14.875 V > $A_1/2$, the field intensity in the right inter-electrode gap dominates over that in the left gap, which leads to a more intense double-layer charging effect on

the right side of the electrode surface and, therefore, makes the right ICEO eddy dominate over the left one. Moreover, under the circumstance that A_2 is sufficiently approaching A_1, there is only a single dominating ICEO micro-vortex above the electrode surface (Figure 2D). This ICEO vortex is clockwise-rotating, acting as the role of the original right ICEO eddy (Figure 2C). The ICEO flow tends to push the cells from the right side of the ITO electrode to the left side, and has negligibly small upward flow component at the left side due to the vertical channel confinement effect (analysis not shown). Once particles are transported to the left side of the ITO electrode by transverse ICEO convection, they are pushed forward by the incoming Poiseuille stream with almost the same height due to the weak upward fluidic drag. Since they can never circulate back to the right side of the ITO electrode due to the negligible upward flow component at the left side, the cells finally move into branch A, which is in good accordance with Figure 4C.

Vice versa, from Figure 2E, under the condition of A_2 = 0.125 V that is sufficiently approaching the grounding state, the counterclockwise ICEO eddy above the electrode surface diverts the trajectories of most cells to branch C, in qualitative agreement with Figure 4D.

Although we have made use of yeast cells of 5 μm in diameter suspended in low-conductivity KCl aqueous solution for confirming the actual device concentration performance in dynamic flow condition, our method is apt for dealing with any other micro/nanoscale sample as well. Particles having different mass density and geometric size may be collected at different height above the surface of GE, considering their positive effect on the gravitational force that acts downward. That is, particles of smaller radius or lower mass density would be arrested by the ICEO vortex at a larger vertical distance from the channel bottom surface, and thereby suffer from weakened lateral ICEO fluidic drag and enhanced forward transport compared to larger or heavier colloids. As a result, lighter or smaller incoming particle samples may form a wider colloid stream and transport more quickly along the channel length direction. As a consequence, a microfluidic separation device can be then developed by combining AC-FFET and distinct levels of ICEO arresting force in the lateral direction for continuously separating particle species maintained at different height away from the substrate surface, which serves potentially as an important topic of our future research.

5. Conclusions

In summary, we have demonstrated a microfluidic particle concentrator with composite 3D electrode structures, which utilizes AC-FFET to continuously focus the incoming particles into a switchable downstream branch channel at high throughput. When the ITO electrode floats in potential, transverse ICEO micro-vortexes with a symmetrical flow profile guide most of incoming yeast cells to move into the middle branch. By applying a second AC voltage to the ITO GE with amplitude deviating enough from its floating potential, the single ICEO eddy induced above the electrode surface successfully diverts the trajectories of incoming cells to the left or right branch at 30Hz, depending on whether the rotation direction of this dominating ICEO vortex is clockwise or counterclockwise. Such a continuous-flow and branch-switchable microfluidic particle concentrator presented here would be flexible for integration with various kinds of downstream devices, and is suited to front-end concentration interfaces for a variety of biosensors and detection systems.

Supplementary Materials: The following are available online at http://www.mdpi.com/2072-666X/10/2/135/s1, Figure S1: 2D simulation model of ICEO flow (not to scale), Table S1: Boundary conditions used in numerical simulation, Figure S2: Influence of vertical channel confinement on the actuating range of ICEO flow: a surface and arrow plot of ICEO flow field in the x-z plane at f = 300 Hz and A_1 = 30 V for different channel height H (unit: m/s), (A) H = 60 μm (experimental condition); (B) H = 500 μm (hypothetical); (C) H = 1000 μm (hypothetical), Figure S3: Simulation results at f = 300 Hz and A_1 = 30 V: (A) ICEO slip profiles on the electrode surface for different channel height H; (B) ICEO slip velocity at x = 50 μm as a function of channel height, Video S1: Video clip of 3D electrode-induced field-effect-resettable particle flow-focusing.

Author Contributions: Conceptualization, H.J.; methodology, W.L.; software, Y.T.; writing—original draft preparation, T.J.; writing—review and editing, Y.H.; supervision and project administration, D.T.

Funding: This project was funded by the National Natural Science Foundation of China (grant number 11702035, 11702075), Shaanxi kefa 2018 No. 9 key industrial innovation chain (group)-industrial field (grant number 2018ZDCXL-GY-05-04, 2018ZDCXL-GY-05-07-02), the Chang'an University Fundamental Research Funds for the Central Universities (grant number 310832171008, 300102328105, 300102328107, 300102328501), and the Youth Innovation Team of Shaanxi Universities.

Conflicts of Interest: The authors declare no conflict of interest.

References

1. Dittrich, P.S.; Tachikawa, K.; Manz, A. Micro total analysis systems. Latest advancements and trends. *Anal. Chem.* **2006**, *78*, 3887–3908. [CrossRef] [PubMed]
2. Wu, S.; Lin, Q.; Yuen, Y.; Tai, Y.-C. MEMS flow sensors for nano-fluidic applications. *Sens. Actuators A Phys.* **2001**, *89*, 152–158. [CrossRef]
3. Hu, G.; Li, D. Multiscale phenomena in microfluidics and nanofluidics. *Chem. Eng. Sci.* **2007**, *62*, 3443–3454. [CrossRef]
4. Wang, Y.; Lin, Q.; Mukherjee, T. System-oriented dispersion models of general-shaped electrophoresis microchannels. *Lab Chip* **2004**, *4*, 453–463. [CrossRef] [PubMed]
5. Wong, P.K.; Chen, C.-Y.; Wang, T.-H.; Ho, C.-M. Electrokinetic bioprocessor for concentrating cells and molecules. *Anal. Chem.* **2004**, *76*, 6908–6914. [CrossRef] [PubMed]
6. Gao, J.; Sin, M.L.; Liu, T.; Gau, V.; Liao, J.C.; Wong, P.K. Hybrid electrokinetic manipulation in high-conductivity media. *Lab Chip* **2011**, *11*, 1770–1775. [CrossRef]
7. Velasco, V.; Williams, S.J. Electrokinetic concentration, patterning, and sorting of colloids with thin film heaters. *J. Colloid. Interface Sci.* **2013**, *394*, 598–603. [CrossRef]
8. Park, S.; Koklu, M.; BeskoK, A. Particle trapping in high-conductivity media with electrothermally enhanced negative dielectrophoresis. *Anal. Chem.* **2009**, *81*, 2303–2310. [CrossRef]
9. Wu, J.; Ben, Y.; Battigelli, D.; Chang, H.-C. Long-range AC electroosmotic trapping and detection of bioparticles. *Ind. Eng. Chem. Res.* **2005**, *44*, 2815–2822. [CrossRef]
10. Bhatt, K.H.; Grego, S.; Velev, O.D. An AC electrokinetic technique for collection and concentration of particles and cells on patterned electrodes. *Langmuir* **2005**, *21*, 6603–6612. [CrossRef]
11. Kumar, A.; Kwon, J.-S.; Williams, S.J.; Green, N.G.; Yip, N.K.; Wereley, S.T. Optically modulated electrokinetic manipulation and concentration of colloidal particles near an electrode surface. *Langmuir* **2010**, *26*, 5262–5272. [CrossRef] [PubMed]
12. Liu, W.; Ren, Y.; Shao, J.; Jiang, H.; Ding, Y. A theoretical and numerical investigation of travelling wave induction microfluidic pumping in a temperature gradient. *J. Phys. D Appl. Phys.* **2014**, *47*, 075501. [CrossRef]
13. Ren, Y.; Jiang, H.; Yang, H.; Ramos, A.; García-Sánchez, P. Electrical manipulation of electrolytes with conductivity gradients in microsystems. *J. Electrost.* **2009**, *67*, 372–376. [CrossRef]
14. Ristenpart, W.; Aksay, I.; Saville, D. Electrically guided assembly of planar superlattices in binary colloidal suspensions. *Phys. Rev. Lett.* **2003**, *90*, 128303. [CrossRef] [PubMed]
15. Trau, M.; Saville, D.; Aksay, I. Field-induced layering of colloidal crystals. *Science* **1996**, *272*, 706–709. [CrossRef] [PubMed]
16. Trau, M.; Saville, D.; Aksay, I. Assembly of colloidal crystals at electrode interfaces. *Langmuir* **1997**, *13*, 6375–6381. [CrossRef]
17. Uppalapati, M.; Huang, Y.M.; Jackson, T.N.; Hancock, W.O. Microtubule alignment and manipulation using AC electrokinetics. *Small* **2008**, *4*, 1371–1381. [CrossRef] [PubMed]
18. Liu, X.; Yang, K.; Wadhwa, A.; Eda, S.; Li, S.; Wu, J. Development of an AC electrokinetics-based immunoassay system for on-site serodiagnosis of infectious diseases. *Sens. Actuators A Phys.* **2011**, *171*, 406–413. [CrossRef]
19. Park, S.; Zhang, Y.; Wang, T.H.; Yang, S. Continuous dielectrophoretic bacterial separation and concentration from physiological media of high conductivity. *Lab Chip* **2011**, *11*, 2893–2900. [CrossRef]
20. Chen, D.; Du, H. A microfluidic device for rapid concentration of particles in continuous flow by DC dielectrophoresis. *Microfluid. Nanofluid.* **2009**, *9*, 281–291. [CrossRef]
21. Velev, O.D.; Bhatt, K.H. On-chip micromanipulation and assembly of colloidal particles by electric fields. *Soft Matter* **2006**, *2*, 738–750. [CrossRef]
22. Velev, O.D.; Gangwal, S.; Petsev, D.N. Particle-localized AC and DC manipulation and electrokinetics. *Ann. Rep. Sect. C Phys. Chem.* **2009**, *105*, 213–246. [CrossRef]

23. Ranjan, N.; Vinzelberg, H.; Mertig, M. Growing One-Dimensional Metallic Nanowires by Dielectrophoresis. *Small* **2006**, *2*, 1490–1496. [CrossRef] [PubMed]
24. Barsotti, R.J.; Vahey, M.D.; Wartena, R.; Chiang, Y.M.; Voldman, J.; Stellacci, F. Assembly of metal nanoparticles into nanogaps. *Small* **2007**, *3*, 488–499. [CrossRef] [PubMed]
25. Palapati, N.; Pomerantseva, E.; Subramanian, A. Single nanowire manipulation within dielectrophoretic force fields in the sub-crossover frequency regime. *Nanoscale* **2015**, *7*, 3109–3116. [CrossRef] [PubMed]
26. Nilsson, A.; Petersson, F.; Jönsson, H.; Laurell, T. Acoustic control of suspended particles in micro fluidic chips. *Lab Chip* **2004**, *4*, 131–135. [CrossRef] [PubMed]
27. Shi, J.; Ahmed, D.; Mao, X.; Lin, S.-C.S.; Lawit, A.; Huang, T.J. Acoustic tweezers: Patterning cells and microparticles using standing surface acoustic waves (SSAW). *Lab Chip* **2009**, *9*, 2890–2895. [CrossRef] [PubMed]
28. Chen, Y.; Ding, X.; Lin, S.-C.S.; Yang, S.; Huang, P.-H.; Nama, N.; Zhao, Y.; Nawaz, A.A.; Guo, F.; Wang, W.; et al. Tunable nanowire patterning using standing surface acoustic waves. *ACS Nano* **2013**, *7*, 3306–3314. [CrossRef]
29. Kwak, R.; Kim, S.J.; Han, J. Continuous-flow biomolecule and cell concentrator by ion concentration polarization. *Anal. Chem.* **2011**, *83*, 7348–7355. [CrossRef]
30. Ko, S.H.; Song, Y.-A.; Kim, S.J.; Kim, M.; Han, J.; Kang, K.H. Nanofluidic preconcentration device in a straight microchannel using ion concentration polarization. *Lab Chip* **2012**, *12*, 4472–4482. [CrossRef]
31. Kim, P.; Kim, S.J.; Han, J.; Suh, K.Y. Stabilization of ion concentration polarization using a heterogeneous nanoporous junction. *Nano Lett.* **2009**, *10*, 16–23. [CrossRef] [PubMed]
32. Ramos, A.; Morgan, H.; Green, N.G.; Castellanos, A. AC electric-field-induced fluid flow in microelectrodes. *J. Colloid. Interface Sci.* **1999**, *217*, 420–422. [CrossRef] [PubMed]
33. Ajdari, A. Pumping liquids using asymmetric electrode arrays. *Phys. Rev. E* **2000**, *61*, R45. [CrossRef]
34. Squires, T.M.; Bazant, M.Z. Induced-charge electro-osmosis. *J. Fluid Mech.* **2004**, *509*, 217–252. [CrossRef]
35. Pascall, A.J.; Squires, T.M. Induced charge electro-osmosis over controllably contaminated electrodes. *Phys. Rev. Lett.* **2010**, *104*, 088301. [CrossRef] [PubMed]
36. Squires, T.M. Induced-charge electrokinetics: Fundamental challenges and opportunities. *Lab Chip* **2009**, *9*, 2477–2483. [CrossRef]
37. Bazant, M.Z.; Squires, T.M. Induced-charge electrokinetic phenomena. *Curr. Opin. Colloid Interface Sci.* **2010**, *15*, 203–213. [CrossRef]
38. Bazant, M.Z.; Squires, T.M. Induced-charge electrokinetic phenomena: Theory and microfluidic applications. *Phys. Rev. Lett.* **2004**, *92*, 066101. [CrossRef]
39. Leinweber, F.C.; Tallarek, U. Concentration polarization-based nonlinear electrokinetics in porous media: Induced-charge electroosmosis. *J. Phys. Chem. B* **2005**, *109*, 21481–21485. [CrossRef]
40. Ren, Y.K.; Morganti, D.; Jiang, H.Y.; Ramos, A.; Morgan, H. Electrorotation of metallic microspheres. *Langmuir* **2011**, *27*, 2128–2131. [CrossRef]
41. García-Sánchez, P.; Ren, Y.; Arcenegui, J.J.; Morgan, H.; Ramos, A. Alternating current electrokinetic properties of gold-coated microspheres. *Langmuir* **2012**, *28*, 13861–13870. [CrossRef] [PubMed]
42. Squires, T.M.; Quake, S.R. Microfluidics: Fluid physics at the nanoliter scale. *Rev. Mod. Phys.* **2005**, *77*, 977. [CrossRef]
43. Davidson, S.M.; Andersen, M.B.; Mani, A. Chaotic induced-charge electro-osmosis. *Phys. Rev. Lett.* **2014**, *112*, 128302. [CrossRef] [PubMed]
44. Leinweber, F.C.; Eijkel, J.C.T.; Bower, J.G.; van den Berg, A. Continuous flow microfluidic demixing of electrolytes by induced charge electrokinetics in structured electrode arrays. *Anal. Chem.* **2006**, *78*, 1425–1434. [CrossRef] [PubMed]
45. Eckstein, Y.; Yossifon, G.; Seifert, A.; Miloh, T. Nonlinear electrokinetic phenomena around nearly insulated sharp tips in microflows. *J. Colloid. Interface Sci.* **2009**, *338*, 243–249. [CrossRef] [PubMed]
46. Bazant, M.Z.; Ben, Y. Theoretical prediction of fast 3D AC electro-osmotic pumps. *Lab Chip* **2006**, *6*, 1455–1461. [CrossRef] [PubMed]
47. Brown, A.; Smith, C.; Rennie, A. Pumping of water with ac electric fields applied to asymmetric pairs of microelectrodes. *Phys. Rev. E* **2000**, *63*, 016305. [CrossRef] [PubMed]
48. Olesen, L.H.; Bruus, H.; Ajdari, A. ac electrokinetic micropumps: The effect of geometrical confinement, Faradaic current injection, and nonlinear surface capacitance. *Phys. Rev. E* **2006**, *73*, 056313. [CrossRef]

49. Studer, V.; Pépin, A.; Chen, Y.; Ajdari, A. An integrated AC electrokinetic pump in a microfluidic loop for fast and tunable flow control. *Analyst* **2004**, *129*, 944–949. [CrossRef]
50. Harnett, C.K.; Templeton, J.; Dunphy-Guzman, K.A.; Senousy, Y.M.; Kanouff, M.P. Model based design of a microfluidic mixer driven by induced charge electroosmosis. *Lab Chip* **2008**, *8*, 565–572. [CrossRef]
51. Wu, Z.; Li, D. Micromixing using induced-charge electrokinetic flow. *Electrochim. Acta* **2008**, *53*, 5827–5835. [CrossRef]
52. Jain, M.; Yeung, A.; Nandakumar, K. Induced charge electro osmotic mixer: Obstacle shape optimization. *Biomicrofluidics* **2009**, *3*, 022413. [CrossRef] [PubMed]
53. Gangwal, S.; Cayre, O.J.; Bazant, M.Z.; Velev, O.D. Induced-charge electrophoresis of metallodielectric particles. *Phys. Rev. Lett.* **2008**, *100*, 058302. [CrossRef] [PubMed]
54. Kilic, M.S.; Bazant, M.Z. Induced-charge electrophoresis near a wall. *Electrophoresis* **2011**, *32*, 614–628. [CrossRef] [PubMed]
55. Rose, K.A.; Hoffman, B.; Saintillan, D.; Shaqfeh, E.S.; Santiago, J.G. Hydrodynamic interactions in metal rodlike-particle suspensions due to induced charge electroosmosis. *Phys. Rev. E* **2009**, *79*, 011402. [CrossRef] [PubMed]
56. Saintillan, D.; Darve, E.; Shaqfeh, E.S. Hydrodynamic interactions in the induced-charge electrophoresis of colloidal rod dispersions. *J. Fluid Mech.* **2006**, *563*, 223–259. [CrossRef]
57. Zhao, H.; Bau, H.H. On the effect of induced electro-osmosis on a cylindrical particle next to a surface. *Langmuir* **2007**, *23*, 4053–4063. [CrossRef] [PubMed]
58. Yossifon, G.; Frankel, I.; Miloh, T. Symmetry breaking in induced-charge electro-osmosis over polarizable spheroids. *Phys. Fluids* **2007**, *19*, 068105. [CrossRef]
59. Arcenegui, J.J.; García-Sánchez, P.; Morgan, H.; Ramos, A. Electro-orientation and electrorotation of metal nanowires. *Phys. Rev. E* **2013**, *88*, 063018. [CrossRef] [PubMed]
60. Ren, Y.; Liu, W.; Jia, Y.; Tao, Y.; Shao, J.; Ding, Y.; Jiang, H. Induced-charge electroosmotic trapping of particles. *Lab Chip* **2015**, *15*, 2181–2191. [CrossRef] [PubMed]
61. Jia, Y.; Ren, Y.; Jiang, H. Continuous-flow focusing of microparticles using induced-charge electroosmosis in a microfluidic device with 3D AgPDMS electrodes. *RSC Adv.* **2015**, *5*, 66602–66610. [CrossRef]
62. Niu, X.; Peng, S.; Liu, L.; Wen, W.; Sheng, P. Characterizing and patterning of PDMS-based conducting composites. *Adv. Mater.* **2007**, *19*, 2682–2686. [CrossRef]
63. Jia, Y.; Ren, Y.; Jiang, H. Continuous dielectrophoretic particle separation using a microfluidic device with 3-D electrodes and vaulted obstacles. *Electrophoresis* **2015**, *36*, 1744–1753. [CrossRef] [PubMed]

micromachines

MDPI

Article

A High-Throughput Electrokinetic Micromixer via AC Field-Effect Nonlinear Electroosmosis Control in 3D Electrode Configurations

Kai Du [1,†], Weiyu Liu [1,†], Yukun Ren [2,*], Tianyi Jiang [2], Jingni Song [1], Qian Wu [3] and Ye Tao [2]

1 School of Electronics and Control Engineering, and School of Highway, Chang'an University, Middle-Section of Nan'er Huan Road, Xi'an 710064, China; dukai@chd.edu.cn (K.D.); liuweiyu@chd.edu.cn (W.L.); jn2012jenny@sina.com (J.S.)

2 State Key Laboratory of Robotics and System, Harbin Institute of Technology, West Da-zhi Street 92, Harbin 150001, China; jty_hit@sina.com (T.J.); tarahit@gmail.com (Y.T.)

3 Science and Technology on Reactor System Design Technology Laboratory, Nuclear Power Institute of China, Chengdu 610213, China; mercuryno.12@163.com

* Correspondence: rykhit@hit.edu.cn; Tel.: +86-0451-8641-8028; Fax: +86-0451-8640-2658

† Authors contributed equally to this work.

Received: 9 August 2018; Accepted: 24 August 2018; Published: 26 August 2018

Abstract: In this study, we make use of the AC field-effect flow control on induced-charge electroosmosis (ICEO), to develop an electrokinetic micromixer with 3D electrode layouts, greatly enhancing the device performance compared to its 2D counterpart of coplanar metal strips. A biased AC voltage wave applied to the central gate terminal, i.e., AC field-effect control, endows flow field-effect-transistor of ICEO the capability to produce arbitrary symmetry breaking in the transverse electrokinetic vortex flow pattern, which makes it fascinating for microfluidic mixing. Using the Debye-Huckel approximation, a mathematical model is established to test the feasibility of the new device design in stirring nanoparticle samples carried by co-flowing laminar streams. The effect of various experimental parameters on constructing a viable micromixer is investigated, and an integrated microdevice with a series of gate electrode bars disposed along the centerline of the channel bottom surface is proposed for realizing high-flux mixing. Our physical demonstration on field-effect nonlinear electroosmosis control in 3D electrode configurations provides useful guidelines for electroconvective manipulation of nanoscale objects in modern microfluidic systems.

Keywords: electrokinetic micromixer; induced-charge electroosmosis; field-induced Debye screening; AC field-effect flow control; electrochemical ion relaxation

1. Introduction

Stirring two or more sample streams is crucial and challenging for clinical diagnostics, thermal management and drug development in micrometer scale [1]. A myriad of approaches have been discovered since the last decade to enhance sample mixing in microfluidic channels, including either active or passive micromixer, considering the driving mechanism upon which they work [2]. Because passive mixing stretches the two-phase contact surface, increases the time of interfacial mass exchange and perturbs the laminar streamlines between co-flowing buffer media by embedding solid obstacles into the microchannel, it is completely dependent on the molecular diffusion effect or chaotic convection [3]. On the contrary, active micromixers employ external energy input for arousing dynamic fluid motion to improve the mixing efficiency, such as Rayleigh streaming [4], magnetic [5], and electrokinetic [6–8].

Among them, electrohydrodynamic has been extensively exploited in microsystems to achieve flexible sample manipulation. In particular, recent progress of microelectronic processing makes the integration of compact microelectrode arrays into microchannels much easier, offering precious opportunities for exerting active Coulomb/dielectric forces on the fluid bulk during exposure to AC electric fields [9,10]. In contrast with dc electroosmotic (DCEO) slipping on insulating charged channel sidewalls [11–13], electroconvection emerges as a series of vortex flow along a discrete electrode array with voltage of merely several volts, so AC electrokinetics is able to achieve more flexible control on the local flow pattern, and is appropriate for some interesting applications, such as fluid transport [14–16], sample mixing [17–19] and generation of concentration-gradient [20] in microdevices. Taking into account the high degree of freedom controllability by adjusting the magnitude, phase relation and field frequency of the imposed voltage signal, both AC electrothermal (ACET) flow [21–23] and induced-charge electroosmosis (ICEO) [24–26] have been gaining unprecedented attention from the microfluidic community.

The origin of ACET consists in smeared structural polarization [27–29]. Since electric properties are usually a function of local temperature elevation, Joule heating gives rise to inhomogeneous liquid conductivity and permittivity in applied AC fields. Both free and bound charges are induced by the interaction of the dielectric gradient with the AC fields, which also accounts for the dielectrophoretic force acting on each liquid element, so that ACET is a nonlinear electrokinetic phenomenon and can therefore survive in AC fields [30–32]. Since the electrothermal body force density increases with temperature gradient, it is efficient to make use of ACET to manipulate high-conductivity biological buffers that can even produce sufficient electric heat generation at small voltages [33–35]. Artificial heating elements have to be embedded into the device internal, however, in order for ACET to act effectively on dilute electrolyte, which requires intricated micro-processing techniques [36].

Different form ACET which appears as a kind of bulk electroconvection due to Maxwell-Wagner structural polarization, induced-charge electrokinetics (ICEK) originates from diffuse charge dynamics over ideally or even weakly polarizable surfaces driven by external DC/AC fields [37–39]. That is, ICEK occurs when a background electric field induces a Debye screening layer at a polarizable solid/liquid interface due to a balance between electrostatic attraction and thermal diffusion, and then forces the counterionic charge within the induced double layer (IDL) into ICEO streaming flow [40–42]. Since the Debye length containing mobile ions decays with increasing ionic strength [43–45], ICEO is particularly effective for manipulating low-conductivity liquid medium [46–51].

To our best knowledge, field-effect flow control is most initially proposed for accelerating traditional DCEO pump flow [52–54]. In this study, however, we innovatively introduce this concept to the field of nonlinear electrokinetics. Specifically, AC field-effect control through a gate terminal immersed in buffer solution enables ICEO to generate arbitrary symmetry breaking in flow pattern of induction whirlpools. This idea of field-effect control on nonlinear electroosmosis is vividly referred to as 'AC flow field-effect transistor' (AC-flow-FET) [55,56]. With appropriate device architecture, asymmetric ICEO micro-vortices resulted from biased gate voltages in AC-flow-FET would bring great benefits to sample mixing in dilute electrolyte, as is the major focus of subsequent analysis.

2. Materials and Methods

2.1. Device Design of Micromixers with AC Field-Effect Flow Control on ICEO

On the basis of field-effect nonlinear electroosmosis control, we then attempt to develop active electrokinetic micromixers of optimal performance for dilute fluids. The basic structure of the micromixer using AC-flow-FET is schematically exhibited in Figure 1a,b. The microdevice has three branch channels, including two inlets for flow injection and a single outlet for sample discharge, in correspondence to three reservoirs, respectively. The entrance of the microchannel is of a 'Y' structure (not shown).

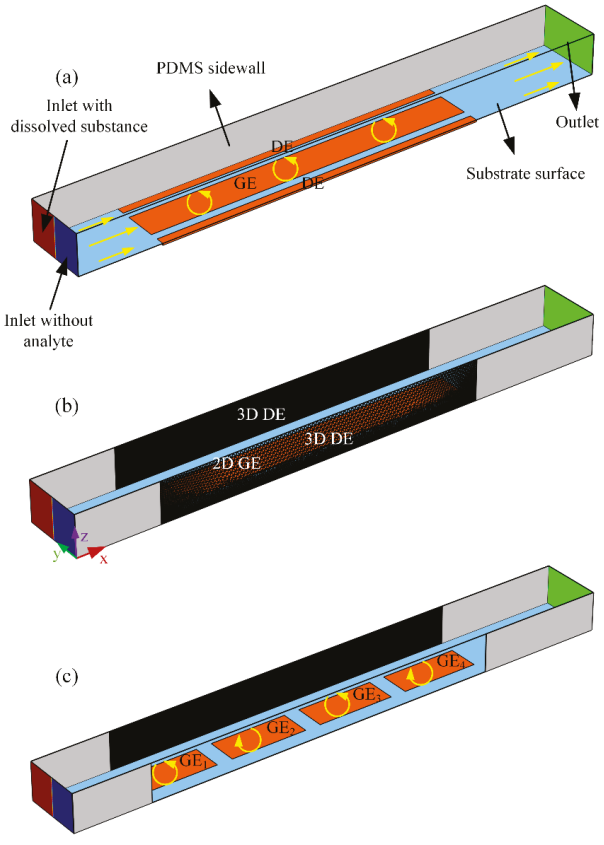

Figure 1. Device design of field-effect-reconfigurable ICEO micromixer with the configuration of three parallel metal strips. (**a**) An AC-flow-FET micromixer using 2D electrode structures, in which the co-flowing laminar streams intersect perpendicularly with the transversal asymmetric ICEO whirlpool, rending the two-phase contact interface rotate in counterclockwise direction on the surface of the central GE strip, helping mingle the analyte carried by the incoming pressure-driven flow to certain extent; (**b**) An ICEO micromixer in 3D electrode configurations, in which a pair of 3D sidewall DE is in perpendicular orientation to the flat GE metal strips placed along the centerline of channel bottom surface, this can greatly enhance the device performance compared with its 2D counterpart (**a**), taking into account the vanishing ACEO on DE and enhanced double-layer polarization on GE. (**c**) An integrated high-throughput ICEO micromixer with 3D electrode layouts, where four GE are disposed sequentially along the channel length direction, and controlled by two oppositely polarized gate terminals. It is noteworthy that the rotating direction of ICEO micro-eddy on each individual GE can be arbitrarily adjusted by applying different gate polarity, so as to spin and enlarge the diffusing phase boundary more efficiently and lead to better mixing performance than that of only having one gate terminal (**b**).

Two distinct designs of electrode structure are conceived here. The 2D and 3D electrode configurations are shown in Figure 1a,b, respectively. The 2D case employs three ideally polarizable metal strips, including a pair of driving electrode (DE) of same length L_D and a central gate electrode (GE) of length L_G arranged on the surface of glass substrate in parallel along the longitudinal channel of length L_C. In contrast, under 3D situation, a pair of Ag-PDMS conducting electrodes are embedded

into the channel sidewalls, in perpendicular orientation with the gate strip positioned on the channel bottom surface (Figure 1b). A proper application of 3D DE can enhance double-layer polarization at the solid/electrolyte interface and thereby accelerate the turbulent electroconvection on the GE surface, which improves substantially the device performance in comparison with the 2D layout using coplanar metal bars.

For the simulation analysis of both configurations, a straight PDMS microchannel of height H is tightly bonded with a glass base (not shown). The GE bar at the channel centerline has a width of W_G, and the 2D DE of W_D, respectively, with an interelectrode separation W_{DG} between DE and GE adjacently placed, resulting in a total span $W_C = 2W_{DG} + W_G + 2W_D$ of the microchannel (Figure 1a). With 3D electrodes (Figure 1b), however, the nearest distance between the central GE and sidewall DE equals $W_{DG3D} = W_D + W_{DG}$, such that the channel width W_C would keep the same for both geometry.

In the calculation, the fluidic channel is first flushed with a buffer solution of ionic conductivity $\sigma = 0.001$ S/m and dielectric permittivity $\varepsilon = 80\varepsilon_0$. The left inlet branch continuously injects fresh liquid of identical electrical properties, which carries the fluorescein nanoparticles for mixing, while the right entrance pumps aqueous electrolyte without colloidal particles. On account of the molecular diffusion effect, the phase boundary between the co-flowing laminar streams is slightly expanded, mingling the fluorescein to a minor degree, and a limited mixing performance lower than 20% is anticipated at the exit of the main channel.

For both device structures (Figure 1a,b), nevertheless, once we switch the multichannel function generator on, imposing a harmonic driving voltage of $V_D\cos(2\pi ft)$ to the pair of DE (either 2D or 3D), and an in-phase gate voltage wave $V_G\cos(2\pi ft)$ of identical exciting frequency to the central gate terminal. Here, V_D and V_G stand for the amplitude of driving and gate voltage signals, f and $\omega = 2\pi f$ the linear and angular frequency, respectively. With the help of AC field-effect flow control, a rotating ICEO vortex of adjustable flow profile would be produced on the surface of gate bars in the lateral direction, which perpendicularly intersects with the two side-by-side incoming laminar streams to result in helical particle-flow locus toward the channel exit, such that the phase interface stretches and rotates more rapidly than the situation merely exploiting molecular diffusion effect in a concentration gradient. For this reason, field-effect-reconfigurable ICEO whirlpools in the device structure of ac-flow-FET can flexibly direct the mixing behavior of incoming fluidic samples, especially with the 3D electrode layout (Figure 1b), as will be discussed in Section 3.1.

To further witness the viability of field-effect flow control on ICEO, a paradigm of high-flux 3D micromixer using ac-flow-FET is developed, where a series of gate electrode bars rather than a single one are placed sequentially along channel length direction, as shown in Figure 1c. In this highly-integrated microdevice, as asymmetric ICEO eddies with opposite streaming directions alternate along the path of Poiseuille flow, the rotating direction of the diffusing phase interface can be arbitrarily tuned by imposing distinct ac voltage phase to each individual gate terminal. Consequently, with a moderate distance cycle for bidirectional double-layer polarization of the lateral electroosmotic flow, we can obtain better device efficiency from this advanced mixer in terms of high-throughput and optimal mixing performance (Figure 1c) than the simplified case only taking advantage of unidirectional electrochemical polarization (Figure 1b).

2.2. Theoretical Basis

For mathematical simulation, we can partition the entire microsystem into two correlated regions, including the IDL at the surface of ideally polarizable metal electrodes and bulk of the buffer medium. Within the latter, the liquid electrical properties are homogeneous to the leading order. The charge conservation for the AC potential is therefore governed by the Laplace equation. For analytical convenience, we introduce the complex amplitude for harmonic electric field variables, e.g., the transient potential $\phi(t) = \mathrm{Re}\left(\tilde{\phi}e^{j\omega t}\right)$, in which $\tilde{\phi}$ with a tilde symbol denotes the voltage

phasor in frequency domain. In this way, current continuity condition in the bulk under sinusoidal steady state becomes:

$$\nabla^2\widetilde{\phi} = 0 \tag{1}$$

Under the Debye-Huckel limit, we set aside those non-ideal effects that may suppress ICEO fluid motion, including electrode reaction, concentration polarization, steric effect and so on. The IDL around the polarizable surfaces consists of a compact Stern layer of capacitance C_S, and a diffuse double-layer of capacitance $C_D = \varepsilon/\lambda_D$, and they are placed in series to sustain the entire overpotential at the electrode/medium interface. Here, λ_D is the Debye length, and ε the buffer permittivity. Accordingly, the total capacity of IDL comes from the combination of the above two layers $C_0 = C_D C_S/(C_D + C_S) = C_D/(1+\delta)$, with $\delta = C_D/C_s$ being the surface capacitance ratio. Since the electrode surface blocks any normal ion motion within a thin boundary layer, Ohmic current from the bulk has to relay the displacement current running across the IDL at the outer edge of Debye layer [57]:

$$\sigma\boldsymbol{n}\cdot\nabla\widetilde{\phi} = j\omega\frac{C_D}{1+\delta}(\widetilde{\phi} - \widetilde{\phi}_E) \tag{2}$$

where σ denotes the medium conductivity, $\widetilde{\phi}$ the complex potential in the bulk right outside the IDL, $\widetilde{\phi}_{\mathrm{E}}$ the voltage phasor of either the driving or gate electrode, and $\boldsymbol{n}$ the unit vector normal to the electrode surfaces. It is assumed the IDL can only be short circuited by polarization current in harmonic AC fields. We need not resolve the internal structure of Debye screening layer, and instead, surface impedance layer on the electrode surface is treated as a Robin-type boundary condition Equation (2). In this way, capacitive charging of IDL at the electrode/electrolyte interface can be numerically reconstructed. A scaling analysis of Equation (2) presents a characteristic RC relaxation frequency $f_{RC} = (1+\delta)\sigma\lambda_D/2\pi\varepsilon R = \mathrm{O}(100)$ Hz for dilute sample solution at micrometer dimension, with R denoting the macroscopic distance scale of electrochemical polarization, e.g., $R = W_G/2$ for ICEO on GE and $R = W_G + 2W_{DG} \approx W_C$ for ACEO on DE. After substitution, $f_{GE}^{RC} = (1+\delta)\sigma\lambda_{\mathrm{D}}/\pi\varepsilon W_G$ and $f_{DE}^{RC} = (1+\delta)\sigma\lambda_{\mathrm{D}}/2\pi\varepsilon W_C$, with f_{DE}^{RC} always no more than f_{GE}^{RC} in current device design.

A portion of the applied voltage difference drops across the diffuse double-layer, with its phasor amplitude given by [58]:

$$\widetilde{\zeta} = \frac{1}{1+\delta}(\widetilde{\phi}_E - \widetilde{\phi}) \tag{3}$$

Since all the electrodes are fixed in space, electrostatic force within the diffuse screening cloud gives rise to steady ICEO slip fluid motion on electrode surfaces in the presence of a tangential field component $\boldsymbol{E}_t = \mathrm{Re}\left(\widetilde{\boldsymbol{E}}_t e^{j\omega t}\right) = \mathrm{Re}\left(\left(\widetilde{\boldsymbol{E}} - \widetilde{\boldsymbol{E}}\cdot\boldsymbol{n}\cdot\boldsymbol{n}\right)e^{j\omega t}\right)$ according to the generalized Helmholtz formula:

$$\boldsymbol{u}_{slip}(t) = -\frac{\varepsilon\zeta}{\eta}\boldsymbol{E}_t = -\frac{\varepsilon}{\eta}\mathrm{Re}\left(\widetilde{\zeta}e^{j\omega t}\right)\mathrm{Re}\left(\left(\widetilde{\boldsymbol{E}} - \widetilde{\boldsymbol{E}}\cdot\boldsymbol{n}\cdot\boldsymbol{n}\right)e^{j\omega t}\right) \tag{4}$$

where η is the dynamic viscosity of the liquid medium.

For analytical convenience, we take advantage of the time-averaged counterpart of Equation (4):

$$\begin{aligned}\left\langle \boldsymbol{u}_{slip}(t)\right\rangle &= -\tfrac{\varepsilon}{2\eta}\mathrm{Re}\left(\widetilde{\zeta}\cdot\left(\widetilde{\boldsymbol{E}} - \widetilde{\boldsymbol{E}}\cdot\boldsymbol{n}\cdot\boldsymbol{n}\right)^*\right)\\ &= \tfrac{\varepsilon}{2\eta(1+\delta)}\mathrm{Re}\left(\left(\widetilde{\phi}_E - \widetilde{\phi}\right)\cdot\left(\nabla\widetilde{\phi} - \nabla\widetilde{\phi}\cdot\boldsymbol{n}\cdot\boldsymbol{n}\right)^*\right)\end{aligned} \tag{5}$$

where <A> denotes the time-average of A, and asterisk * the complex conjugate operator.

The time-averaged ICEO slipping $\left\langle \boldsymbol{u}_{slip}(t)\right\rangle$ is inserted to the steady-state full Stokes equation by subjecting these ideally polarizable surfaces to slip-wall boundary conditions, so as to numerally describe electroconvection from AC field-effect flow control:

$$-\nabla p + \eta\nabla^2\boldsymbol{u} = 0 \tag{6a}$$

$$\nabla \cdot \boldsymbol{u} = 0 \tag{6b}$$

where p denotes the scalar field of hydraulic pressure.

The standard convection-diffusion equation is utilized in current analysis to obtain the concentration distribution of analyte injected from the left entrance:

$$\nabla \cdot (\boldsymbol{u}c - D\nabla c\,) = 0 \tag{7}$$

where D represents the thermal diffusivity, and c the concentration field of fluorescein samples that ought to be well mixed before performing any following analysis.

2.3. Numerical Simulation

We use a commercial software package, Comsol Multiphysics (version 5.3a, COMSOL, Stockholm, Sweden), to analyze the ICEO fluid motion with field-effect flow control and its application to sample mixing in microchannels. The simulation procedure of electroosmotic flow field and convective mass transfer in the fluidic channel is as follows. Firstly, we compute the Laplace equation (Equation (1)) to get the AC potential phasor within the buffer solution. RC charging condition Equation (2) is imposed to the electrode/electrolyte interface, where $\widetilde{\phi}_E = V_D$, $\widetilde{\phi}_E = V_G$, and $\widetilde{\phi}_E = 0$ for the left DE, central GE and right DE, respectively, to delineate electrochemical ion relaxation within the IDL. The normal current vanishes on other insulating surfaces, i.e., $\boldsymbol{n} \cdot \nabla\widetilde{\phi} = 0$.

Next, the full Stokes equation (Equation (6)) is solved for obtaining the synthetic flow field, incorporating an axial Poiseuille flow due to a pressure difference externally applied across the inlet and outlet of the fluidic channel, and the transversal ICEO vortex streaming on application of an ac voltage wave. On one hand, an inlet flow velocity u_0 is designated at the channel entrance, and zero hydrodynamic pressure is assumed at the channel exit, so as to mimic the pressure-driven flow for downstream transport of the incoming nanoparticles along channel length direction. On the other hand, the ICEO fluid motion is embodied by inserting the time-averaged electrokinetic slip expression Equation (5) as a leaking-wall boundary condition on all the blocking electrodes, while other channel sidewalls are strictly subjected to no slip and no penetration.

Finally, the mass-transfer equation (Equation (7)) is computed in the fluidic channel, any normal flux is inhibited at all the solid/liquid interfaces. We use fluorescein spheres of 40 nm in diameter with Brownian diffusivity $D = 10^{-11}$ m^2/s as the test particles for mixing, the concentration value of which is $c = 1$ mol/m^3 at the left inlet (red color in Figure 1) and 0 mol/m^3 (blue part in Figure 1) at the right entrance, respectively, coinciding with the realistic situation of continuous sample mixing. In addition, normal diffusive mass transfer approaches zero at the channel exit.

Stationary solvers are employed for all the governing equations subjected to given boundary conditions. The AC potential phasor, fluid dynamics and sample delivery are solved sequentially with PARDISO algorithm, and grid-independence is scrutinized for each calculation result.

2.4. Development of the Mathematical Model

In a standard Cartesian coordinate system with three orthogonal axis (x, y, z), all the fundamental equations and boundary conditions possess explicit mathematical expressions, complying with the simulation method depicted in Section 2.3.

As for governing equations, we have:

$$\frac{\partial^2\widetilde{\phi}}{\partial x^2} + \frac{\partial^2\widetilde{\phi}}{\partial y^2} + \frac{\partial^2\widetilde{\phi}}{\partial z^2} = 0 \tag{8}$$

$$\frac{\partial u_x}{\partial x} + \frac{\partial u_y}{\partial y} + \frac{\partial u_z}{\partial z} = 0 \tag{9}$$

$$-\frac{\partial p}{\partial x}+\eta\left(\frac{\partial^2 u_x}{\partial x^2}+\frac{\partial^2 u_x}{\partial y^2}+\frac{\partial^2 u_x}{\partial z^2}\right) = 0 \tag{10}$$

$$-\frac{\partial p}{\partial y}+\eta\left(\frac{\partial^2 u_y}{\partial x^2}+\frac{\partial^2 u_y}{\partial y^2}+\frac{\partial^2 u_y}{\partial z^2}\right) = 0 \tag{11}$$

$$-\frac{\partial p}{\partial z}+\eta\left(\frac{\partial^2 u_z}{\partial x^2}+\frac{\partial^2 u_z}{\partial y^2}+\frac{\partial^2 u_z}{\partial z^2}\right) = 0 \tag{12}$$

$$u_x\frac{\partial c}{\partial x}+u_y\frac{\partial c}{\partial y}+u_z\frac{\partial c}{\partial z}-D\left(\frac{\partial^2 c}{\partial x^2}+\frac{\partial^2 c}{\partial y^2}+\frac{\partial^2 c}{\partial z^2}\right)=0 \tag{13}$$

To close the boundary-value problem, we analyze the integral form of above partial differential equations (PDE) to obtain the rational boundary condition at different structural interfaces:

At the channel inlets, we have:

$$\frac{\partial\widetilde{\phi}}{\partial \mathrm{x}}n_x+\frac{\partial\widetilde{\phi}}{\partial \mathrm{y}}n_y+\frac{\partial\widetilde{\phi}}{\partial \mathrm{z}}n_z=0;\ u_x=u_0(y,z);\ c = c_0(y,z) \tag{14}$$

At the channel exit:

$$\frac{\partial\widetilde{\phi}}{\partial \mathrm{x}}n_x+\frac{\partial\widetilde{\phi}}{\partial \mathrm{y}}n_y+\frac{\partial\widetilde{\phi}}{\partial \mathrm{z}}n_z=0;\ p = 0;\ \frac{\partial \mathrm{c}}{\partial \mathrm{x}}n_x+\frac{\partial \mathrm{c}}{\partial y}n_y+\frac{\partial \mathrm{c}}{\partial y}n_y=0 \tag{15}$$

where $\boldsymbol{n}$ = (n_x, n_y, n_z) represents the local unit normal vector on the surface of interest.

At the electrode/electrolyte interface, including both DE and GE:

$$\sigma\left(\frac{\partial\widetilde{\phi}}{\partial \mathrm{x}}n_x+\frac{\partial\widetilde{\phi}}{\partial \mathrm{y}}n_y+\frac{\partial\widetilde{\phi}}{\partial \mathrm{z}}n_z\right)=j\omega\frac{C_D}{1+\delta}(\widetilde{\phi}-V_{D/G});$$

$$u_x=\frac{\varepsilon}{2\eta(1+\delta)}\mathrm{Re}\left((\widetilde{\phi}_E-\widetilde{\phi})\cdot\left(\frac{\partial\widetilde{\phi}}{\partial x}-\left(\frac{\partial\widetilde{\phi}}{\partial \mathrm{x}}n_x+\frac{\partial\widetilde{\phi}}{\partial \mathrm{y}}n_y+\frac{\partial\widetilde{\phi}}{\partial \mathrm{z}}n_z\right)\cdot n_x\right)^*\right);$$

$$u_{\mathrm{y}}=\frac{\varepsilon}{2\eta(1+\delta)}\mathrm{Re}\left((\widetilde{\phi}_E-\widetilde{\phi})\cdot\left(\frac{\partial\widetilde{\phi}}{\partial y}-\left(\frac{\partial\widetilde{\phi}}{\partial \mathrm{x}}n_x+\frac{\partial\widetilde{\phi}}{\partial \mathrm{y}}n_y+\frac{\partial\widetilde{\phi}}{\partial \mathrm{z}}n_z\right)\cdot n_y\right)^*\right); \tag{16}$$

$$u_{\mathrm{z}}=\frac{\varepsilon}{2\eta(1+\delta)}\mathrm{Re}\left((\widetilde{\phi}_E-\widetilde{\phi})\cdot\left(\frac{\partial\widetilde{\phi}}{\partial z}-\left(\frac{\partial\widetilde{\phi}}{\partial \mathrm{x}}n_x+\frac{\partial\widetilde{\phi}}{\partial \mathrm{y}}n_y+\frac{\partial\widetilde{\phi}}{\partial \mathrm{z}}n_z\right)\cdot n_z\right)^*\right);$$

$$\frac{\partial \mathrm{c}}{\partial \mathrm{x}}n_x+\frac{\partial \mathrm{c}}{\partial y}n_y+\frac{\partial \mathrm{c}}{\partial y}n_y=0$$

At other insulating surfaces:

$$\frac{\partial\widetilde{\phi}}{\partial \mathrm{x}}n_x+\frac{\partial\widetilde{\phi}}{\partial \mathrm{y}}n_y+\frac{\partial\widetilde{\phi}}{\partial \mathrm{z}}n_z=0;u_x=u_y=u_z=0;\ \frac{\partial \mathrm{c}}{\partial \mathrm{x}}n_x+\frac{\partial \mathrm{c}}{\partial y}n_y+\frac{\partial \mathrm{c}}{\partial y}n_y=0 \tag{17}$$

Equations (8)–(13) subjected to boundary conditions Equations (14)–(17) met the definite solution condition of boundary value problem. That is, our mathematical model invariably has a unique solution under a given set of experimental parameters.

2.5. Evaluation of the Mixing Performance

The mixing index γ can correctly quantify the device performance once the concentration distribution of nanoparticle samples at the channel outlet is known:

$$\begin{aligned}\gamma &= \left(1 - \frac{\iint_S |c - 0.5[\mathrm{mol/m^3}]|\,\mathrm{d}A}{\iint_S 0.5[\mathrm{mol/m^3}]\,\mathrm{d}A}\right) \times 100\% \\ &= \left(1 - \frac{\int_{0<z<H}\int_{0<y<W_C} |c - 0.5[\mathrm{mol/m^3}]|\,\mathrm{d}y\mathrm{d}z}{\int_{0<z<H}\int_{0<y<W_C} 0.5[\mathrm{mol/m^3}]\,\mathrm{d}y\mathrm{d}z}\right) \times 100\%\end{aligned} \tag{18}$$

In this equation, the area integral performed on the channel exit S is transformed into a double integral, since $\mathrm{d}A = \mathrm{d}y\mathrm{d}z$ for a plane of interest that is perpendicular to the x axis.

3. Results and Discussion

3.1. A Comparative Study of ICEO Micromixers with 2D and 3D Electrode Layouts

An investigation on ICEO streaming reconfigurable through field-effect flow control may provide a theoretical foundation for developing high-efficiency active micromixers. At the very beginning, we focus on the traditional ICEO vortex flow pattern with central GE free from external wiring, i.e., $V_G = V_D/2$. A suitable parametric space is selected for the numerical simulation: W_C = 400 μm, W_D = 50 μm, W_G = 200 μm. W_{DG} = 50 μm, f = 200 Hz, $L_D = L_G$ = 2 mm, L_C = 3.3 mm, H = 250 μm. To make a fair comparison between micromixers of 2D (Figure 1a) and 3D electrode layouts (Figure 1b), V_D = 6 V and V_D = 8 V are imposed to the 2D (Figure 2a,c) and 3D DE pair (Figure 2b,d), respectively.

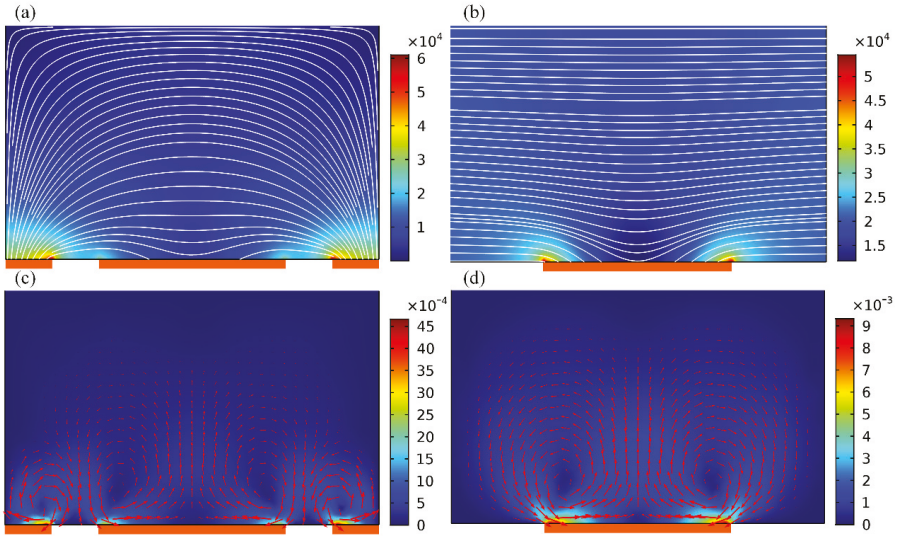

Figure 2. Under identical electric field intensity, a comparison of the basic trait of unbiased ICEO eddies above one central GE in the flow-FET configuration with 2D and 3D driving electrodes at given field frequency f = 200 Hz. For 3D electrode layouts in (**b**,**d**), $V_D = 2V_G$ = 8 V; while for the 2D counterpart in (**a**,**c**), $V_D = 2V_G$ = 6 V, such that they share a same magnitude of background electric field of E_b = 20,000 V/m. (**a**) A surface and arrow plot of electric field distribution (unit: V/m) in the 2D, and (**b**) 3D electrokinetic micromixer. (**c**) Transversal ICEO fluid motion (unit: m/s) with GE floating in the 2D, and (**d**) 3D device design.

In ICEO, a background electric field acts on its own induced Debye screening charge within the EDL, resulting in time-averaged electroosmotic streaming on ideally polarizable surfaces even in oscillating AC fields (Figure 2). In the early stage, the buffer solution is supposed to have an ionic strength of 0.001 S/m, resulting in a bulk charge relaxation frequency $f_{\text{bulk}} = \sigma/2\pi\varepsilon$ = 225 kHz. In the device of 2D electrodes, strong electric field is produced at the corner-field-singularity of DE on both sides, indirectly weakening the potential gradient across the planar surface of GE strip (Figure 2a). On application of a low-frequency ac signal, ICEO streaming appears and behaves as two pairs of counter-rotating micro-vortices above the three parallel electrode bars (Figure 2c). Focusing on one of the electrode spacings, ICEO vortex flow field resembles ACEO induced on a single coplanar electrode pair. That is, ICEO whirlpool in 2D flow-transistor cascades within interelectrode gaps, sweeps across the ideally polarizable surface, then streams upward, giving rise to four recirculating fluid loops (Figure 2c).

In stark contrast, as to the 3D layout Figure 2b,d, a relatively large area of the sidewall DE pair makes the electric field distribution much more uniform, and a local maximum intensity exists in the immediate vicinity of two edges of GE (Figure 2b), rather than the corner of DE pair in 2D configuration (Figure 2a). At the price of same energy dissipation, the usage of 3D sidewall electrodes enhances electrochemical polarization at GE/electrolyte interface (Figure 2b), and therefore produces stronger ICEO fluid motion inside the microchamber (Figure 2d). For this special device design, however, it is not possible for the ACEO convection to occur with no tangential field component on the DE surface, so that there is merely one pair of counter-rotating ICEO micro-vortices on GE along the transversal direction (Figure 2d). Even so, both the flow velocity and actuating range of ICEO vortex are greatly enhanced by exploiting 3D sidewall DE (Figure 2d) in comparison to coplanar arrangement (Figure 2c).

Above results about electro-convective streaming suggests that the 3D device design (Figure 1b) is of more superiority in developing high-performance micromixer than its 2D counterpart (Figure 1a). We then need to make a test validation on this inference. As shown Figure 3, the incoming pressure-driven laminar stream has a parabolic profile, with flow velocity of u_0 = 3 mm/s at the channel entrance. Without external powering, any mixing effect in a straight fluidic channel is in essence caused by molecular diffusion across the phase boundary. At the channel exit, the vertical contact interface stretches little in the absence of lateral perturbation, generating a very poor mixing efficiency γ = 22.83% (not shown). On switching the signal generator on, with the GE strip floating, symmetric ICEO vortex flow pattern appears on the surface of GE along channel width direction, and the lateral electro-convective perturbation intersects perpendicularly the axial Poiseuille flow, giving rise to rotating streamlines on top of the metal strips (Figure 3a,c). As a result, not only does thermal diffusion takes effect, but also transversal electroconvection of the nanoparticle samples contributes to expanding the phase boundary of a sharp concentration gradient (Figure 3b,d). Because of a higher efficiency in electromechanical energy conversion, as has been demonstrated in Figure 2, the 3D device design (Figure 3d) performs much better, in terms of producing a higher mixing performance γ = 50.1% than the 2D electrode configuration (Figure 3b) with γ = 26.48%.

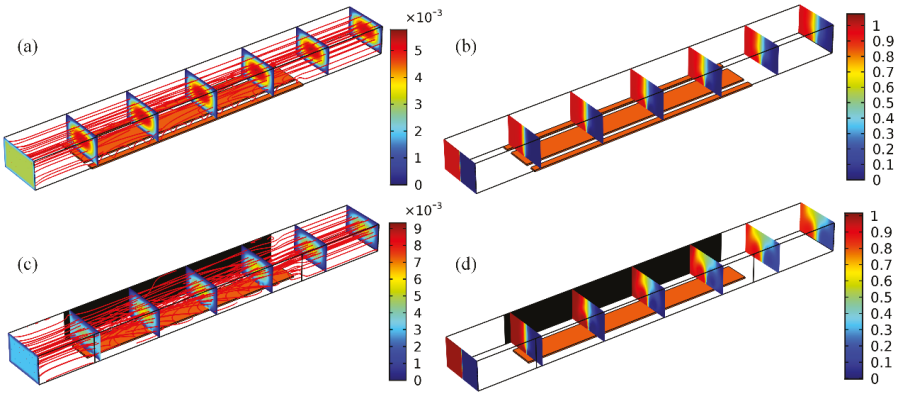

Figure 3. Simulation result of ICEO sample mixing in axial continuous flow of inlet flow rate u_0 = 3mm/s and solution conductivity 0.001 S/m in the fundamental configuration of single floating gate terminal under given frequency f = 200 Hz and field intensity E_B = 20,000 V/m. (**a**,**b**) With 2D electrode layouts, symmetrically circulating ICEO vortex flow induced on the surface of gate strip intersects perpendicularly with the incoming sample stream, resulting in a mixing performance of γ = 26.48% by lateral electroconvection which extends the phase interface without any hydrodynamic torque, (**c**) a streamline and multi-slice surface plot of flow field (unit: m/s), (**d**) a multi-slice surface plot of analyte concentration distribution affected by symmetric electroosmotic whirlpools in the transverse plane (unit: mol/m^3). (**c**,**d**) Corresponding simulation results in 3D electrode configuration, with an enhanced device efficiency of γ = 50.1%, albeit still not ideal.

Though the contact interface is simultaneously extruded by molecular diffusion and circulatory ICEO streamlines, it does not undergo any rotating motion because of the geometric symmetry in field-induced Debye screening on GE surface even in 3D electrode configuration. Since the rate of substance exchange across the phase boundary has a limitation without electrohydrodynamic torques, sample mixing above a floating gate is still unsatisfactory using sidewall DE (Figure 3d). Achieving further improvement through the AC field-effect control on ICEO is urgently needed.

3.2. Mixing with AC Field-Effect Flow Control in the 3D Device Design

It has been demonstrated that the 3D electrode layout is an improved device design in terms of developing microfluidic mixers. In this sense, unless otherwise noted, all the subsequent analysis is concentrated on the 3D microdevice. When the central GE is exempt from external wiring (Figure 2b), electroosmotic eddies in reverse rotating directions encounter and counterbalance one another at the center of GE surface, developing an in-situ flow stagnation line (FSL) (Figure 2d). Symmetrically-distributed stagnation areas can be fully exploited for preconcentration of colloidal particles, but are not efficient in steering the motion of two-phase contact interface for sample stirring.

Prompted by the previous work on field-effect flow control in microfluidic networks [53], a biased gate voltage V_G can help adjust electro-convective mass transport along channel transverse direction. As exhibited in Figure 4a,c, corresponding to a negatively- or positively- polarized gate terminal, the electric field intensity augments on the left or right side of gate strip surface, but decreases on the other side. This directly results in asymmetric distribution of the electrostatic potential gradient, which interplays with enhanced electrochemical polarization at the same site to induce biased ICEO vortex flow field (Figure 4b,d). The flow velocity and rotating direction can be arbitrarily reconfigured by adjusting the gate voltage amplitude V_G. For this reason, AC field-effect control on ICEO circulation opens up new opportunities for handling nanoscale entities in dilute electrolyte in the context of microfluidics.

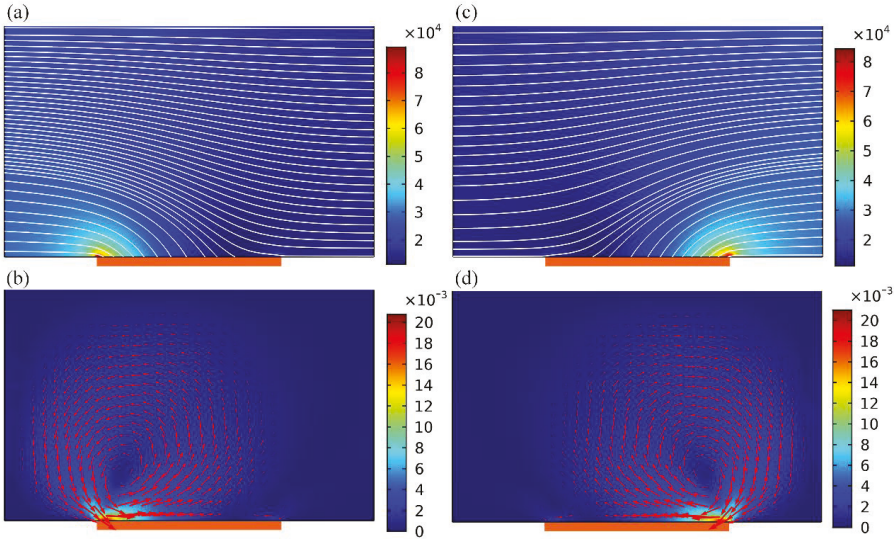

Figure 4. Simulation result of AC field-effect control on ICEO with non-neutral gate voltages in 3D electrode configurations, i.e., $V_G \neq V_D/2 = 4$ V, reconfigurable vortex flow pattern can be induced across channel width direction. (**a**,**b**) When the gate polarity is negative $V_G < V_D/2$ ($V_D = 8$ V, $V_G = 2$ V), electrochemical polarization becomes more significant adjacent to the left side of gate terminal, giving rise to a single large-scale ICEO vortex flow rotating counterclockwise, (**a**) a surface and streamline plot of the asymmetric electric field distribution (unit: V/m), (**b**) a surface and arrow plot of ICEO flow field, in which an anticlockwise eddy overwhelms the fluid motion within the entire fluidic channel (unit: m/s). (**c**,**d**) As GE is positively polarized $V_G > V_D/2$ ($V_D = 8$ V, $V_G = 6$ V), gradients of both the electric field and flow field variables reverse in the horizontal direction with respect to (**a**,**b**), respectively. Most importantly, the rotating direction of ICEO vortex is inverted, and the clockwise electroosmotic micro-vortex near the right rim of GE governs the transverse electroconvection.

As shown in Figure 5, by imposing a sufficiently large offset voltage $|V_G - 0.5V_D|$ to the gate terminal, biased ICEO whirlpool twirling in either anticlockwise (Figure 5a, for negative gate polarity) or clockwise direction (Figure 5c, for positively-polarized GE) can be generated above the metal strip. The asymmetric electroosmotic vortex flow exerts a time-averaged electrohydrodynamic torque on the buffer solution, rendering the phase boundary revolve in pace with the transversal electrokinetic circulation. The additional rotating motion twists and expands the two-phase contact interface in a more effective manner than the unbiased situation for an identical longitudinal distance. So, swapping of substance between the co-flowing buffer streams is sped up, irrespective of the rotating direction of ICEO vortex flow field (Figure 5b,d), leading to an elevated mixing efficiency $\gamma = 76.1\%$ compared to the symmetric configuration of $\gamma = 50.1\%$. The incoming laminar streams intersect perpendicularly with the asymmetric ICEO eddy, resulting in helical streamlines rolling forward above the GE surface (Figure 5a,c). Although the forward helix in Figure 5a,c rotates in opposite directions, however, there is not a clear difference in mixing of nanoparticles on account of symmetry in the magnitude of gate voltage offset.

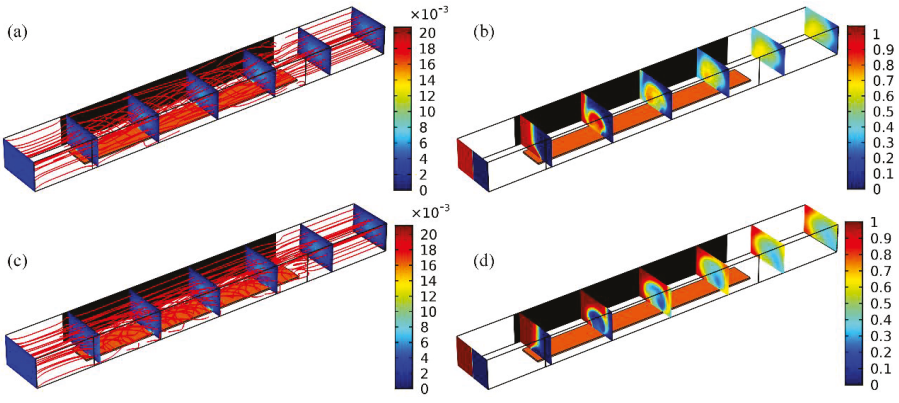

Figure 5. Calculation result of sample mixing behavior via field-effect-reconfigurable ICEO vortex flow field under distinct gate polarities and a fixed driving voltage V_D = 8 V, the device performance is improved greatly, taking into consideration an additional electrohydrodynamic torque exerted on the phase boundary. (**a**,**b**) Nanoparticle mixing reinforced by a single dominating ICEO vortex with anticlockwise recirculation as the gate voltage V_G = 2 V is lower than the balance potential $V_D/2$ = 4 V ($V_G - V_D/2 = -2$ V, negatively polarized GE), with mixing performance γ = 76.1%, (**a**) a streamline and cross-sectional magnitude plot of the helical flow field rolling counterclockwise (unit: m/s), (**b**) a multi-slice magnitude plot of sample concentration distribution (unit: mol/m^3). (**c**,**d**) Mixing behavior with clockwise ICEO vortex as the gate voltage V_G = 6 V is beyond the neutral one $V_D/2$ = 4 V ($V_G - V_D/2$ = 2 V, positive gate polarity), with same device efficiency γ = 76.1% owing to a mirror image of the gate voltage offset, (**c**) a streamline and cross-sectional magnitude plot of the helical streamlines in clockwise rotating direction (unit: m/s), (**d**) a multi-slice surface plot of nanoparticle concentration distribution (unit: mol/m^3).

3.3. Effect of Different Experimental Parameters on the 3D ICEO Micromixer

Based upon the above simulation studies, asymmetric ICEO whirlpool is more efficient in engendering active mixing in microfluidics than the symmetric case in which the central gate terminal floats in potential. It is then essential to elucidate how the different experimental parameters including the harmonic frequency, gate potential offset and inlet flow velocity, can exert an impact on device performance of the 3D ICEO micromixer

3.3.1. Frequency-Dependence

Since both DE and FE undergo electrode polarization that is strongly affected by electrochemical ion relaxation in alternating fields, the frequency-dependence of ICEO flow velocity with field-effect control must be quite complex. In DC limit, with the field frequency much lower than the inverse double-layer relaxation time on DE pair, i.e., $f \ll f_{DE}^{RC} = (1+\delta)\sigma\lambda_D/2\pi\varepsilon W_C$, most of the applied AC voltage drops across the IDL at the DE/electrolyte interface due to complete Debye screening, leaving no electric field in the bulk to force the mobile ions into ICEO streaming. For frequency well beyond the characteristic relaxation frequency of the blocking surface of GE, i.e., $f \gg f_{GE}^{RC} = (1+\delta)\sigma\lambda_D/\pi\varepsilon W_G$, there is not enough time for the counterionic charge to accumulate in the IDL at the GE/electrolyte interface within each harmonic cycle, resulting in null ICEO fluid motion once again due to incomplete Debye screening on GE. So, the best mixing behavior should take place in the intermediate frequency range, i.e., $f_{DE}^{RC} < f_{ideal} < f_{GE}^{RC}$.

As indicated by the calculation results in Figure 6a with a positive gate polarity chosen in priority, there is single peak of mixing performance of γ = 80% around f = 100 Hz, either increase or decrease the field frequency would abate the device efficiency, in good accordance with this simple physical

argument. Besides, the worst performance is lower than 25%, implying that sample mixing is chiefly induced by diffusive mass transfer for $f \leq 10$ Hz and $f \geq 5$ kHz. As a consequence, to acquire perfect mixing behavior with AC field-effect control of ICEO, we should carefully seek the ideal operation frequency, with reference to the reciprocal double-layer relaxation time of both DE and GE, which has a strong dependence on the ionic strength of the buffer medium.

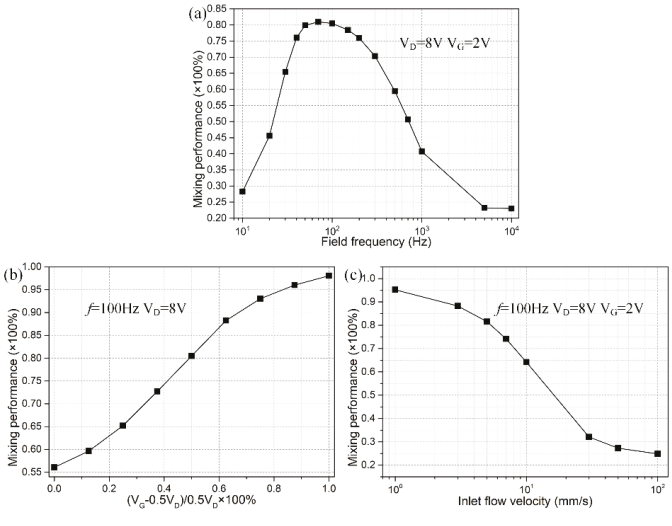

Figure 6. A parametric study of the 3D ICEO micromixer with ac field-effect control of lateral ICEO convection. (**a**) Frequency-dependence of mixing performance, for V_D = 8 V and V_G = 2 V; (**b**) Effect of gate potential offset on the device mixing behavior at frequency f = 100 Hz and driving voltage V_D = 8 V; (**c**) Effect of inlet flow rate on the mixing efficiency under given frequency f = 100 Hz, driving voltage V_D = 8 V, and gate voltage V_G = 1.5 V, being equivalent to an offset ratio of 0.625.

3.3.2. Influence of the Gate Voltage Offset

For practical applications, it is of great importance to quantify how the specific value of gate potential offset affects field-effect-reconfigurable ICEO mixing at a given field frequency, e.g., f = 100 Hz in current device geometry. With the definition of absolute offset voltage $V_G - 0.5V_D$, a nondimensional mathematical expression $|V_G - 0.5V_D|/0.5V_D$ is extractable, and its value is bounded between zero and unit in *real situations* where $0 \leq V_G \leq V_D$. When the offset ratio $|V_G - 0.5V_D|/0.5V_D$ of gate potential becomes zero, the GE strip floats in external fields and no symmetry breaking in ICEO vortex flow pattern takes place. As the value of $|V_G - 0.5V_D|/0.5V_D$ approaches one, the voltage offset reaches the peak magnitude for $V_G = V_D$ or V_G = 0, resulting in the largest electroosmotic whirlpool regardless of the specific rotating direction. So, the value of $|V_G - 0.5V_D|/0.5V_D$ is able to correctly evaluate the extent of symmetry breaking in transversal electroconvection. Theoretically, as $|V_G - 0.5V_D|/0.5V_D$ becomes larger, AC field-effect control on ICEO becomes more evident and thereby ICEO vortex has a propensity to roll in a preferential direction, as demonstrated by the increasing trend of field-effect-reconfigurable device performance with $|V_G - 0.5V_D|/0.5V_D$ (Figure 6b). The best mixing efficiency emerges at the largest offset voltage, in which the most asymmetric ICEO vortex exerts the most potent electro-rotational torque on the fluidic sample, but this would take a lot of energy. Accordingly, application of a moderate gate potential offset, which can well enhance convective mixing at no cost of severe power dissipation, ought to be our first choice. For this reason, a specific offset ratio $|V_G - 0.5V_D|/0.5V_D = 0.625$ is chosen for further theoretical studies (V_G = 1.5 V for negative and 6.5 V for positive gate polarity with V_D = 8 V).

3.3.3. Effect of Inlet Flow Rate

A square crossing of the axial laminar streams and lateral ICEO vortex on top of GE gives rise to forward helical streamlines, which is responsible for improving the mixing dynamics in the fluidic channel. For this reason, the flow velocity at the channel entrance fiercely influences the device efficiency. When the inlet flow velocity is slow and the Reynolds number is small, there is sufficient time for the incoming colloidal particles to get well mixed along the channel length direction as they are slowly delivered toward the outlet, producing a high mixing performance while greatly sacrificing the sample flux. On the contrary, at a high inlet flow rate, there is almost no chance for the helical streamlines to rotate a circle on the surface of gate terminal, and consequently the mixing dynamics is suppressed but high-throughput is obtainable at the channel exit, as verified by the calculation result in Figure 6c where the mixing efficiency declines as the inlet flow velocity increases.

Then, we have to address the issue about how to mingle fluidic samples efficiently without loss of throughput.

3.4. 3D High-Throughput Mixing with AC Field-Effect Flow Control

To accomplish sample mixing at a relatively large Reynolds number, electroconvection in the lateral direction must be promoted to compete against the axial pressure-driven flow. A scaling analysis of Equation (16) indicates the flow velocity of ICEO abides by a general scaling law:

$$\left|u_y^{\mathrm{ICEO}}\right| \approx C \cdot \frac{\varepsilon V_{\mathrm{D}}^2 W_G}{4\eta(1+\delta)W_C^2\left(1+(\omega\tau_{RC})^2\right)} \tag{19}$$

where C is a geometry-dependent prefactor, and $\tau_{RC} = \varepsilon W_G/2(1+\delta)\sigma\lambda_{\mathrm{D}}$ the RC charge relaxation time of interfacial capacitance. From Equation (19), once all the geometric and physicochemical properties are preset values, it is possible to improve the device performance by adjusting the applied voltage V_D and chip structure C. Accordingly, we then focus on AC field-effect nonlinear electroosmosis control for high-throughput mixing, in terms of adjusting either the background field intensity or the discrete layouts of central GE strips.

3.4.1. Voltage-Dependence

According to Equation (19), the transversal electrokinetic turbulence is linearly proportional to the input voltage squared, implying it is a utilitarian method to rectify the mixing behavior by just increasing the magnitude of the background field strength $E_B = V_D/W_C$, as shown in Figure 7a with a given gate voltage offset ratio of 0.625, inlet flow velocity of 10 mm/s, and signal frequency of 100 Hz. Besides, it is noteworthy that for the peak voltage V_D = 20 V, the electrical field intensity reaches 20 [V]/200 [μm] = 100 [V/mm] within the electrode spacing. This order of magnitude of driving voltage indicates there is a potential drop of 1V across a gap of 10 μm in size, which is no less than the common situation of 0.5–1.5 V used in experimental observation of ACEO. In addition, there is always a dead zone of ICEO vortex flow field at the upper left (or upper right, Figure 7b) of the channel cross section with a unipolar gate terminal, which is positively (or negatively) polarized.

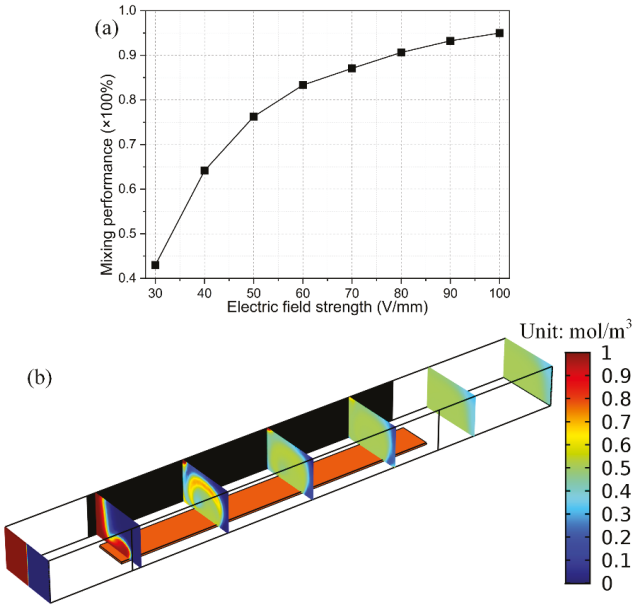

Figure 7. Effect of the imposed voltage magnitude on the device mixing efficiency under given voltage offset ratio 0.625, inlet flow velocity 10 mm/s, and field frequency 100 Hz. (**a**) Voltage-dependence of the mixing performance; (**b**) High-throughput mixing at V_D = 20 V and V_G = 3.75 V, while there is still a dead zone of ICEO turbulence on the upper right of the channel cross section.

3.4.2. Integrated 3D ICEO Micromixer with Bipolar Gate Terminals

To enlarge the actuating range of ICEO mixing streamlines, we propose a more advanced discrete electrode layouts for field-effect-reconfigurable sample mixing, as shown in Figure 8. In this integrated device design, an array of GE with four coplanar metal bars subjected to different gate voltage polarities is arranged consecutively along the centerline of the insulating substrate surface. To further miniaturize the device, the length of all the GE strips is reduced to L_G = 500 μm, and the separation between adjacent GE is W_{GG} = 100 μm. The ion conductivity of the suspension medium is 0.001 S/m, low enough to evade any steric effect. Because of a decrease in the dead zone of transversal electroconvection, an AC voltage signal of moderate amplitude V_D = 14 V at f = 100 Hz is imposed to the 3D sidewall DE. The four sequential GE strips are labelled as G_1, G_2, G_3 and G_4, and are imposed with gate potentials of V_{G1}, V_{G2}, V_{G3} and V_{G4}, respectively. We herein utilize two opposite gate polarities for convenience of simulation analysis, V_{Gi} = 11.375 V for the positive gate bias "+", and V_{Gi} = 2.625 V for the negative counterpart "−", where $1 \leq i \leq 4$ represents the i-th gate electrode from upstream to downstream. To test the feasibility of the integrated device structure in high-throughput sample mixing, the inlet flow velocity is enhanced to u_0 = 10 mm/s.

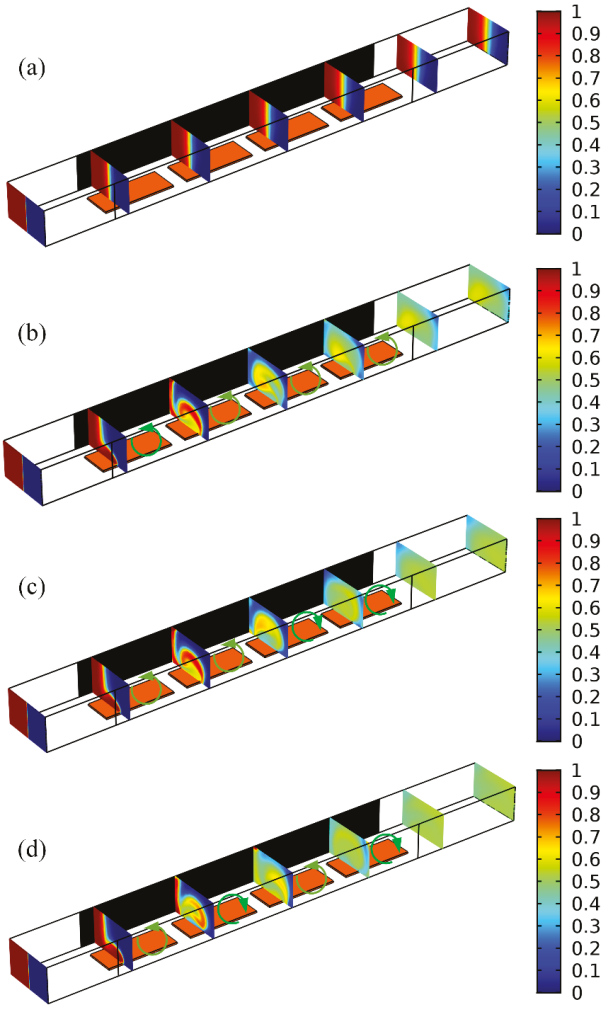

Figure 8. At an inlet flow velocity u_0 = 10 mm/s and ion conductivity 0.001 S/m, a simulation study on the influence of different combinations of ICEO vortex polarity on mixing improvement in the integrated tandem device structure with four sequential GE strips subjected to various of gate voltage sequence. (**a**) In the absence of external powering, the phase boundary between the co-flowing laminar streams is stretched only by diffusive mass transfer with γ = 23.54%. (**b**,**c**) For V_D = 14 V, (**b**) and V_{G1} = V_{G2} = V_{G3} = V_{G4} = 2.625 V are imposed on the four sequential GE, respectively, ICEO vortex in anticlockwise direction appears on the ideally polarizable surface of all the GE strips, which twists and stretches the phase interface in synergy with mass diffusion, resulting in an nonideal device performance of γ = 88.67%, (**c**) with a given gate potential sequence of V_{G1} = V_{G2} = 2.625 V and V_{G3} = V_{G4} = 11.375 V, ICEO eddy rotates anticlockwise on the surface of two GE upstream, but polarity of the electroosmotic vortex makes a reversal on the two GE downstream, so the distance scale of electrochemical polarization equals two gate length, and the transformation in rolling direction of the phase boundary at such a longitudinal displacement leads to better mixing efficiency γ = 92.41% than (**b**); (**d**) An more frequent alternation in flow direction of lateral ICEO vortex at a shorter distance (one GE length) gives rise to even more superior device performance γ = 95.233% than (**c**).

Without input of external electrical energy to the microdevice, there is no ICEO turbulence for electro-convective mixing, and the sole action of molecular diffusion produces a poor mixing efficiency of γ = 23.32% even using an GE array (Figure 8a and Table 1). On switching the multichannel function generator on, as the four GE in the strip array share an identical polarity, e.g., with a gate potential sequence $-/-/-/-$, anticlockwise ICEO micro-vortices of consistent flow direction appear on the ideally polarizable surface of the four GE, which convectively stretch and twist the phase boundary in synergy with diffusive mass transfer, giving rise to a modest device performance of γ = 88.67% (Figure 8b).

Table 1. Device efficiency for the integrated 3D high-throughput micromixer (Figure 8) with the central GE array subjected to different gate voltage sequence.

Specific Gate Voltage Sequence for the Ge Array	Mixing Performance
No Electric Field Supplied	23.54%
$-/-/-/-$	88.67%
$-/-/+/+$	92.41%
$-/+/-/+$	95.233%

Notes: The driving potential amplitude is V_D = 14 V, while the gate voltage is V_G = 11.375 V for positive gate polarity "+" and V_G = 2.625 V for its negative counterpart "−".

If we make use of two gate terminals of opposite polarities rather than a single, although there are numerous combinations of vortex-flow direction, two symmetric powering conditions are studied preferentially, as shown in Figure 8c,d, since they can best represent AC field-effect control on ICEO sample mixing. With a potential sequence $-/-/+/+$ of two reversed gate polarities, anticlockwise and clockwise ICEO eddies are produced above the upstream and downstream two gate strips, respectively (Figure 8c). In other words, electro-convective fluid motion reverses in lateral flow direction at the downstream end of the 2nd GE, which alters the direction of rotation of the two-phase contact interface on a distance scale of double GE length, leading to an improved mixing efficiency γ = 92.41% from double gate polarity (Figure 8c) than γ = 88.67% with unipolar gate terminal (Figure 8b).

This astonishing result encourages us to adjust the polarity of electrochemical polarization with an even shorter repeating length, as shown in Figure 8d, where the specific sequence of gate potential $-/+/-/+$ is imposed on the GE array. In this situation, the circulatory ICEO whirlpool changes the sense of rotation even more frequently (Figure 8d) than the "$-/-/+/+$" condition (Figure 8c), and inversion of electroconvection takes place on every adjacent GE of reversed gate polarity, further boosting the device performance to 95.233% (Figure 8d). To our best knowledge, an optimum distance scale in reverse of electrode polarization always exists in practical experiment, which should be the longitudinal displacement need for the phase boundary to rotate an entire circle of 360° as the fluidic samples are transported downstream. Accordingly, we can optimize field-effect-reconfigurable ICEO mixing by pursuing the best gate voltage sequence for a preset GE array in the integrated 3D high-throughput micromixer, which could help diminish the dead zones of transverse ICEO turbulence to great extent (Figure 8d).

3.4.3. Conductivity-Dependence of the Integrated Micromixer

The simulation analysis above has mainly concentrated on the influence of a variety of electric field parameters and the discrete electrode layout on the mixing dynamics due to AC field-effect control on ICEO. Nevertheless, medium conductivity is also a pivotal factor that greatly affects the functionality of sample mixing in the 3D micromixer. Generally speaking, a decrease in solution conductivity can extend the thickness of IDL, so the diffuse layer becomes much more important than the Stern layer in dilute electrolyte, resulting in an enhancement of ICEO flow velocity for convective mixing in low-conductivity suspension. In this way, the optimum mixing performance boosts with decreasing liquid conductivity (Figure 9b).

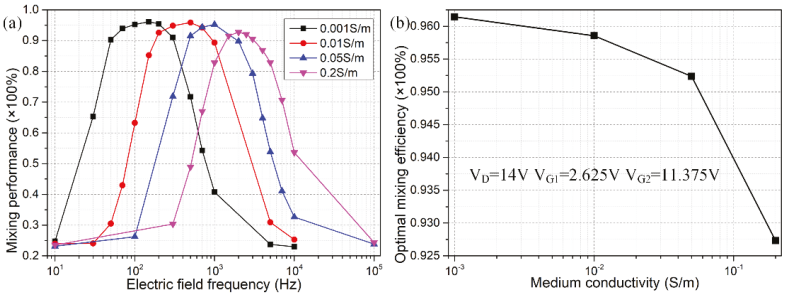

Figure 9. Effect of liquid conductivity on mixing efficiency of the integrated micromixer. (**a**) Frequency-dependent mixing performance for different ionic strength; (**b**) Conductivity-dependent optimum mixing efficiency at corresponding ideal operation frequencies.

At the same time, the rise in ionic strength increases the double-layer relaxation frequency, since the IDL capacitance and resistor of the bulk fluid are connected in series to comprise the whole electric circuit system. The ideal operating frequency of the micromixer f_{ideal}, which is bounded between f_{DE}^{RC} and f_{GE}^{RC}, then makes a change for different solution conductivities. Specifically, the ideal frequency f_{ideal} increases from 100 Hz to 2 KHz, as the ionic conductivity grows from 0.001 S/m to 0.2 S/m (Figure 9a), while the mixing efficiency at corresponding peak frequencies decays due to a shrink in Debye screening length. For analytical convenience, however, we have disregarded the possible action of nonlinear diffuse charge dynamics beyond the Debye-Huckel limit. In fact, when the medium conductivity surpasses a threshold value on the order of O(0.01) S/m, ionic species would overcrowd inside the IDL at the electrode/electrolyte interface, and this steric effect severely exacerbates as the ion concentration further increases, which is prone to evaporate the fluid motion of ICEO with ionic strength exceeding ~0.05 S/m. As a consequence, the integrated 3D device design is eligible for convective mixing of dilute electrolyte at the micrometer dimension.

4. Conclusions

In summary, we have put forward the physical concept of AC field-effect flow control on nonlinear electroosmosis, where arbitrary symmetry breaking in transversal ICEO vortex flow pattern can be realized via adjusting the AC voltage imposed to the central gate terminal immersed in buffer solution. A rigid mathematical model is established in the framework of 3D Cartesian coordinate system to study the feasibility of this unique device structure for field-effect electro-convective mixing in straight microchannels, and the earliest comparison studies indicate the 3D electrode configuration with arrangement of sidewall DE is able to achieve better field-effect mixing control than its 2D counterpart using coplanar metal strips in microsystems. The effect of various experimental parameters, such as the driving frequency, ratio of gate voltage offset and inlet flow velocity, on the performance of this 3D micromixer is investigated by direct numerical modeling. To suppress the dead zone of ICEO turbulence within the channel cross section, an integrated 3D micromixer with high-throughput is developed by employing an array of bipolar GE, in which ICEO vortex streaming on the surface of each GE can be separately addressed. With double gate terminals of reverse polarities, alternation in circulating direction of ICEO whirlpool at modest space intervals can rotate and extend the diffusing phase boundary more intensively, giving rise to even better mixing performance in the context of dilute electrolyte. The mathematical model of AC field-effect mixing control developed in this work is merely valid under Debye-Huckel approximation, and the action of nonlinear diffuse charge dynamics is excluded in this work. On account of this limitation, possible extensions of current work may include the investigation of using more complex electrode structures for controlling the field-effect-tunable mixing behavior and the coupling of asymmetric electrode polarization with effects of a relatively large

Dukhin number, including bipolar Faradaic reactions, nonlinear surface capacitance, non-uniform surface conduction, ion concentration polarization, steric effect and so on. Under such situations, the linear asymptotic analysis applied herein would malfunction, and alternative mathematical models are pursued to account for the influence of nonlinear diffuse charge dynamics on AC field-effect mixing control. We believe that AC-flow-FET would inspire interdisciplinary research focusing on condensed matter, electrokinetic phenomena, and micro/nanofluidics in the near future.

Author Contributions: K.D. wrote the paper and made the analysis; W.L. developed the mathematical model and carried out the numerical simulations; Y.R. guided this project; T.J. and J.S. conceived and designed the simulation experiment; Q.W. and Y.T. did the literature retrieval.

Funding: This project is financially supported by the National Natural Science Foundation of China (No. 11702035, No. 11672095, No. 11702075), the Chang'an University Fundamental Research Funds for the Central Universities (No. 310832171008, No. 300102328201, No. 300102328501), Shaanxi kefa [2018] No. 9 key industrial innovation chain (group)-industrial field (No. 2018ZDCXL-GY-05-04, No. 2018ZDCXL-GY-05-07-02), and Self-Planned Task (SKLRS201803B) of State Key Laboratory of Robotics and System (HIT).

Conflicts of Interest: The authors declare no conflict of interest.

References

1. Lee, C.Y.; Chang, C.L.; Wang, Y.N.; Fu, L.M. Microfluidic mixing: A review. *Int. J. Mol. Sci.* **2011**, *12*, 3263–3287. [CrossRef] [PubMed]
2. Green, J.; Holdø, A.; Khan, A. A review of passive and active mixing systems in microfluidic devices. *Int. J. Multiphys.* **2009**, *1*, 1–32. [CrossRef]
3. Chen, L.; Wang, G.; Lim, C.; Seong, G.H.; Choo, J.; Lee, E.K.; Kang, S.H.; Song, J.M. Evaluation of passive mixing behaviors in a pillar obstruction poly(dimethylsiloxane) microfluidic mixer using fluorescence microscopy. *Microfluid. Nanofluid.* **2009**, *7*, 267–273. [CrossRef]
4. Shilton, R.J.; Yeo, L.Y.; Friend, J.R. Quantification of surface acoustic wave induced chaotic mixing-flows in microfluidic wells. *Sens. Actuators B* **2011**, *160*, 1565–1572. [CrossRef]
5. Rida, A.; Gijs, M.A. Manipulation of self-assembled structures of magnetic beads for microfluidic mixing and assaying. *Anal. Chem.* **2004**, *76*, 6239–6246. [CrossRef] [PubMed]
6. Sasaki, N.; Kitamori, T.; Kim, H.B. Fluid mixing using ac electrothermal flow on meandering electrodes in a microchannel. *Electrophoresis* **2012**, *33*, 2668–2673. [CrossRef] [PubMed]
7. Liu, W.; Ren, Y.; Tao, Y.; Chen, X.; Yao, B.; Hui, M.; Bai, L. Control of two-phase flow in microfluidics using out-of-phase electroconvective streaming. *Phys. Fluids* **2017**, *29*, 112002. [CrossRef]
8. Jia, Y.; Ren, Y.; Hou, L.; Liu, W.; Deng, X.; Jiang, H. Microreactions: Sequential coalescence enabled two-step microreactions in triple-core double-emulsion droplets triggered by an electric field (small 46/2017). *Small* **2017**, *13*, 1702188. [CrossRef] [PubMed]
9. Ramos, A. *Electrokinetics and Electrohydrodynamics in Microsystems*; Springer Science & Business Media: Berlin/Heidelberg, Germany, 2011; Volume 530.
10. Morgan, H.; Green, N.G. *AC Electrokinetics: Colloids and Nanoparticles*; Research Studies Press: Birmingham, UK, 2003.
11. Yariv, E. "Force-free" electrophoresis? *Phys. Fluids* **2006**, *18*, 031702. [CrossRef]
12. Xuan, X.; Li, D. Electroosmotic flow in microchannels with arbitrary geometry and arbitrary distribution of wall charge. *J. Colloid Interface Sci.* **2005**, *289*, 291–303. [CrossRef] [PubMed]
13. Hu, G.; Li, D. Multiscale phenomena in microfluidics and nanofluidics. *Chem. Eng. Sci.* **2007**, *62*, 3443–3454. [CrossRef]
14. Olesen, L.H.; Bruus, H.; Ajdari, A. Ac electrokinetic micropumps: The effect of geometrical confinement, faradaic current injection, and nonlinear surface capacitance. *Phys. Rev. E* **2006**, *73*, 056313. [CrossRef] [PubMed]
15. García-Sánchez, P.; Ramos, A.; González, A.; Green, N.G.; Morgan, H. Flow reversal in traveling-wave electrokinetics: An analysis of forces due to ionic concentration gradients. *Langmuir* **2009**, *25*, 4988–4997. [CrossRef] [PubMed]
16. García-Sánchez, P.; Ramos, A.; Green, N.; Morgan, H. Traveling-wave electrokinetic micropumps: Velocity, electrical current, and impedance measurements. *Langmuir* **2008**, *24*, 9361–9369. [CrossRef] [PubMed]

17. Harnett, C.K.; Templeton, J.; Dunphy-Guzman, K.A.; Senousy, Y.M.; Kanouff, M.P. Model based design of a microfluidic mixer driven by induced charge electroosmosis. *Lab Chip* **2008**, *8*, 565–572. [CrossRef] [PubMed]
18. Gunda, N.S.K.; Bhattacharjee, S.; Mitra, S.K. Study on the use of dielectrophoresis and electrothermal forces to produce on-chip micromixers and microconcentrators. *Biomicrofluidics* **2012**, *6*, 034118. [CrossRef] [PubMed]
19. Cao, J.; Cheng, P.; Hong, F. A numerical study of an electrothermal vortex enhanced micromixer. *Microfluid. Nanofluid.* **2008**, *5*, 13–21. [CrossRef]
20. Mavrogiannis, N.; Desmond, M.; Ling, K.; Fu, X.; Gagnon, Z. Microfluidic mixing and analog on-chip concentration control using fluidic dielectrophoresis. *Micromachines* **2016**, *7*, 214. [CrossRef]
21. Liu, W.; Ren, Y.; Tao, Y.; Yao, B.; Li, Y. Simulation analysis of rectifying microfluidic mixing with field-effect-tunable electrothermal induced flow. *Electrophoresis* **2018**, *39*, 779–793. [CrossRef] [PubMed]
22. Wu, J.; Lian, M.; Yang, K. Micropumping of biofluids by alternating current electrothermal effects. *Appl. Phys. Lett.* **2007**, *90*, 234103. [CrossRef]
23. Stubbe, M.; Holtappels, M.; Gimsa, J. A new working principle for ac electro-hydrodynamic on-chip micro-pumps. *J. Phys. D Appl. Phys.* **2007**, *40*, 6850. [CrossRef]
24. Bazant, M.Z.; Squires, T.M. Induced-charge electrokinetic phenomena: Theory and microfluidic applications. *Phys. Rev. Lett.* **2004**, *92*, 066101. [CrossRef] [PubMed]
25. Yossifon, G.; Frankel, I.; Miloh, T. Symmetry breaking in induced-charge electro-osmosis over polarizable spheroids. *Phys. Fluids* **2007**, *19*, 068105. [CrossRef]
26. Yossifon, G.; Frankel, I.; Miloh, T. On electro-osmotic flows through microchannel junctions. *Phys. Fluids* **2006**, *18*, 117108. [CrossRef]
27. Gimsa, J.; Stubbe, M.; Gimsa, U. A short tutorial contribution to impedance and ac-electrokinetic characterization and manipulation of cells and media: Are electric methods more versatile than acoustic and laser methods? *J. Electr. Bioimpedance* **2014**, *5*, 74–91. [CrossRef]
28. Li, Y.; Ren, Y.; Liu, W.; Chen, X.; Tao, Y.; Jiang, H. On controlling the flow behavior driven by induction electrohydrodynamics in microfluidic channels. *Electrophoresis* **2017**, *38*, 983–995. [CrossRef] [PubMed]
29. Williams, S.J. Enhanced electrothermal pumping with thin film resistive heaters. *Electrophoresis* **2013**, *34*, 1400–1408. [CrossRef] [PubMed]
30. González, A.; Ramos, A.; Morgan, H.; Green, N.G.; Castellanos, A. Electrothermal flows generated by alternating and rotating electric fields in microsystems. *J. Fluid Mech.* **2006**, *564*, 415–433. [CrossRef]
31. Liu, W.; Ren, Y.; Tao, Y.; Chen, X.; Wu, Q. Electrode cooling effect on out-of-phase electrothermal streaming in rotating electric fields. *Micromachines* **2017**, *8*, 327. [CrossRef]
32. Salari, A.; Navi, M.; Dalton, C. A novel alternating current multiple array electrothermal micropump for lab-on-a-chip applications. *Biomicrofluidics* **2015**, *9*, 014113. [CrossRef] [PubMed]
33. Loire, S.; Kauffmann, P.; Mezić, I.; Meinhart, C. A theoretical and experimental study of ac electrothermal flows. *J. Phys. D Appl. Phys.* **2012**, *45*, 185301. [CrossRef]
34. Gao, J.; Sin, M.L.; Liu, T.; Gau, V.; Liao, J.C.; Wong, P.K. Hybrid electrokinetic manipulation in high-conductivity media. *Lab Chip* **2011**, *11*, 1770–1775. [CrossRef] [PubMed]
35. Boettcher, M.; Schmidt, S.; Latz, A.; Jaeger, M.; Stuke, M.; Duschl, C. Filtration at the microfluidic level: Enrichment of nanoparticles by tunable filters. *J. Phys. Condens. Matter* **2011**, *23*, 324101. [CrossRef] [PubMed]
36. Liu, W.; Ren, Y.; Shao, J.; Jiang, H.; Ding, Y. A theoretical and numerical investigation of travelling wave induction microfluidic pumping in a temperature gradient. *J. Phys. D Appl. Phys.* **2014**, *47*, 075501. [CrossRef]
37. Squires, T.M.; Bazant, M.Z. Induced-charge electro-osmosis. *J. Fluid Mech.* **2004**, *509*, 217–252. [CrossRef]
38. Schnitzer, O.; Yariv, E. Induced-charge electro-osmosis beyond weak fields. *Phys. Rev. E* **2012**, *86*, 061506. [CrossRef] [PubMed]
39. Boymelgreen, A.; Yossifon, G. Observing electrokinetic janus particle–channel wall interaction using microparticle image velocimetry. *Langmuir* **2015**, *31*, 8243–8250. [CrossRef] [PubMed]
40. Prabhakaran, R.A.; Zhou, Y.; Zhao, C.; Hu, G.; Song, Y.; Wang, J.; Yang, C.; Xuan, X. Induced charge effects on electrokinetic entry flow. *Phys. Fluids* **2017**, *29*, 42–48. [CrossRef]
41. Ren, Y.; Liu, W.; Wang, Z.; Tao, Y. Induced-charge electrokinetics in rotating electric fields: A linear asymptotic analysis. *Phys. Fluids* **2018**, *30*, 062006. [CrossRef]

42. Liu, W.; Shao, J.; Jia, Y.; Tao, Y.; Ding, Y.; Jiang, H.; Ren, Y. Trapping and chaining self-assembly of colloidal polystyrene particles over a floating electrode by using combined induced-charge electroosmosis and attractive dipole–dipole interactions. *Soft Matter* **2015**, *11*, 8105–8112. [CrossRef] [PubMed]
43. Liu, W.; Ren, Y.; Tao, Y.; Yao, B.; Liu, N.; Wu, Q. A universal design of field-effect-tunable microfluidic ion diode based on a gating cation-exchange nanoporous membrane. *Phys. Fluids* **2017**, *29*, 112001. [CrossRef]
44. Liu, W.; Shao, J.; Ren, Y.; Wu, Y.; Wang, C.; Ding, H.; Jiang, H.; Ding, Y. Effects of discrete-electrode arrangement on traveling-wave electroosmotic pumping. *J. Micromech. Microeng.* **2016**, *26*, 095003. [CrossRef]
45. Li, Z.; Liu, W.; Gong, L.; Zhu, Y.; Gu, Y.; Han, J. Accurate multi-physics numerical analysis of particle preconcentration based on ion concentration polarization. *Int. J. Appl. Mech.* **2017**, *9*, 1750107. [CrossRef]
46. Ren, Y.; Liu, W.; Jia, Y.; Tao, Y.; Shao, J.; Ding, Y.; Jiang, H. Induced-charge electroosmotic trapping of particles. *Lab Chip* **2015**, *15*, 2181–2191. [CrossRef] [PubMed]
47. Bhatt, K.H.; Grego, S.; Velev, O.D. An ac electrokinetic technique for collection and concentration of particles and cells on patterned electrodes. *Langmuir* **2005**, *21*, 6603–6612. [CrossRef] [PubMed]
48. Chen, X.; Ren, Y.; Liu, W.; Feng, X.; Jia, Y.; Tao, Y.; Jiang, H. A simplified microfluidic device for particle separation with two consecutive steps: Induced charge electro-osmotic prefocusing and dielectrophoretic separation. *Anal. Chem.* **2017**, *89*, 9583–9592. [CrossRef] [PubMed]
49. Tao, Y.; Ren, Y.; Liu, W.; Wu, Y.; Jia, Y.; Lang, Q.; Jiang, H. Enhanced particle trapping performance of induced charge electroosmosis. *Electrophoresis* **2016**, *37*, 1326–1336. [CrossRef] [PubMed]
50. Ren, Y.; Liu, W.; Liu, J.; Tao, Y.; Guo, Y.; Jiang, H. Particle rotational trapping on a floating electrode by rotating induced-charge electroosmosis. *Biomicrofluidics* **2016**, *10*, 054103. [CrossRef] [PubMed]
51. Ren, Y.; Liu, J.; Liu, W.; Lang, Q.; Tao, Y.; Hu, Q.; Hou, L.; Jiang, H. Scaled particle focusing in a microfluidic device with asymmetric electrodes utilizing induced-charge electroosmosis. *Lab Chip* **2016**, *16*, 2803–2812. [CrossRef] [PubMed]
52. Van Der Wouden, E.; Hermes, D.; Gardeniers, J.; Van Den Berg, A. Directional flow induced by synchronized longitudinal and zeta-potential controlling ac-electrical fields. *Lab Chip* **2006**, *6*, 1300–1305. [CrossRef] [PubMed]
53. Schasfoort, R.B.; Schlautmann, S.; Hendrikse, J.; van den Berg, A. Field-effect flow control for microfabricated fluidic networks. *Science* **1999**, *286*, 942–945. [CrossRef] [PubMed]
54. Van Der Wouden, E.; Heuser, T.; Hermes, D.; Oosterbroek, R.; Gardeniers, J.; Van Den Berg, A. Field-effect control of electro-osmotic flow in microfluidic networks. *Colloids Surf. A* **2005**, *267*, 110–116. [CrossRef]
55. Liu, W.; Shao, J.; Ren, Y.; Liu, J.; Tao, Y.; Jiang, H.; Ding, Y. On utilizing alternating current-flow field effect transistor for flexibly manipulating particles in microfluidics and nanofluidics. *Biomicrofluidics* **2016**, *10*, 034105. [CrossRef] [PubMed]
56. Soni, G.; Squires, T.; Meinhart, C. Microfluidic pumps based on induced charge electroosmosis and flow field effect transistor phenomena. In Proceedings of the APS March Meeting, Baltimore, MD, USA, 13–17 March 2006; p. 8004.
57. García-Sánchez, P.; Ren, Y.; Arcenegui, J.J.; Morgan, H.; Ramos, A. Alternating current electrokinetic properties of gold-coated microspheres. *Langmuir* **2012**, *28*, 13861–13870. [CrossRef] [PubMed]
58. Green, N.G.; Ramos, A.; Gonzalez, A.; Morgan, H.; Castellanos, A. Fluid flow induced by nonuniform AC electric fields in electrolytes on microelectrodes. III. Observation of streamlines and numerical simulation. *Phys. Rev. E* **2002**, *66*, 026305. [CrossRef] [PubMed]

micromachines

MDPI

Article

Tunable-Focus Liquid Lens through Charge Injection

Shizhi Qian [1,*], Wenxiang Shi [2], Huai Zheng [2] and Zhaohui Liu [3]

[1] Department of Mechanical and Aerospace Engineering, Old Dominion University, Norfolk, VA 23529, USA
[2] School of Power and Mechanical Engineering, Wuhan University, Wuhan 430072, China; 2017302650020@whu.edu.cn (W.S.); huai_zheng@whu.edu.cn (H.Z.)
[3] School of Energy and Power Engineering, Huazhong University of Science and Technology, Wuhan 430074, China; zliu@mail.hust.edu.cn
* Correspondence: sqian@odu.edu; Tel.: +1-757-683-3304

Received: 25 December 2019; Accepted: 12 January 2020; Published: 20 January 2020

Abstract: Liquid lenses are the simplest and cheapest optical lenses, and various studies have been conducted to develop tunable-focus liquid lenses. In this study, a simple and easily implemented method for achieving tunable-focus liquid lenses was proposed and experimentally validated. In this method, charges induced by a corona discharge in the air were injected into dielectric liquid, resulting in "electropressure" at the interface between the air and the liquid. Through a 3D-printed U-tube structure, a tunable-focus liquid lens was fabricated and tested. Depending on the voltage, the focus of the liquid lens can be adjusted in large ranges ($-\infty$ to -9 mm and 13.11 mm to ∞). The results will inspire various new liquid-lens applications.

Keywords: tunable focus; liquid lens; electrohydrodynamics; charge injection

1. Introduction

There has been a long history since liquid surfaces were adopted as optical lenses [1,2]. Liquid lenses have many advantages over traditional solid lenses, including simplicity, low cost, smoothness, and flexibility [3,4]. Additionally, liquid lenses can be easily integrated into the optical system or the observed objects [5,6]. As liquid surfaces can be flexibly adjusted and form various geometries, liquid lenses can realize many optical functions, such as in varying the focus [7], optical waveguides [8,9], gratings [10,11], liquid lenses [12–14], optical switches [15], optical attenuators [16], and optofluidic prisms [17].

In order to utilize the advantages, it is essential to manipulate the liquid surface morphology. Thus, various efforts have been devoted to controlling liquid surfaces [18,19]. Due to the surface tension effect, liquid surfaces usually present a spherical shape and capillary pressure exists on the surfaces. The capillary pressure varies with the surface morphology [20]. Thus, external forces are introduced to balance the capillary pressure, and the liquid surface morphologies are tuned by the imposed external forces [21]. Hydraulic force is the most common one, actuated by mechanical pumps [22]. However, this technique needs complex liquid transfer systems [23]. A thermal stimulus can be introduced into the manipulation mechanism [24,25]. Thermal actuation can lead to liquid expansion and change the liquid surface [24]. Additionally, thermal actuation can change the surface tension and, consequently, the capillary pressure [25]. However, it is difficult to precisely control liquid surfaces through the thermal method. In addition, for evaporable liquid, the thermal stimulus has some adverse effects. Stimuli-responsive hydrogel can also be employed as a viable tool for manipulating the curvature of the water–oil interface to produce micro lenses with variable focal lengths [26].

Apart from the above methods, the electrically driven method is the most common technique used for manipulating liquid lenses [27–29]. The electrically driven mechanism mainly consists of electrowetting [27,28] and dielectrophoresis [29]. Owing to high accuracy and flexibility, the electrically

driven method has been widely investigated for many applications, such as adaptive optics, optical switching, and displays. It shows the greatest potential for becoming the dominant technique. However, the current electrically driven methods need complex electrode configurations, which increase the fabrication cost and limit their application.

In this study, we proposed a simple and easily implemented electrically driven method for the liquid lens through charge injection. A prototype was designed and fabricated with a 3D printer, and the proposed method was experimentally validated. The optical performance of the tunable-focus lens by charge injection was characterized and analyzed.

2. Principle and Experiments

Figure 1 schematically depicts the principle of the proposed tunable-focus liquid lens by charge injection. A U-shaped tube with ends of different heights was used to connect the dielectric liquid. A needle-plate electrode configuration was placed in the higher tube end (the right-hand end in Figure 1) and at the bottom of the channel. When a high voltage was applied between the two electrodes, a corona discharge phenomenon occurred. Positive ions generated by the needle drifted toward the plate electrode, were deposited, and accumulated at the interface of the air and the dielectric liquid within the right-hand end of the tube due to the lower electrical conductivity of the liquid. Interactions between the imposed electric field and the ions that had accumulated at the interface generated a Coulomb force, which induced pressure at the interface. We named the induced pressure electropressure, P_e. Under electropressure, liquid flowed to the left-hand, lower tube end, as schematically shown in Figure 1. With an increase in voltage (i.e., $U_3 > U_2 > U_1$), the electropressure increased. The initial liquid morphology in the left-hand end of the tube had a concave shape, and its capillary pressure, P_c, was negative. The flow created by the induced electropressure pushed the liquid outside and pinned it to the left-hand tube end. Then, the liquid morphology in the left-hand end of the tube became convex in shape and its radius decreased. As the voltage increased, the capillary pressure turned from negative to positive and its value increased to balance the increasing electropressure.

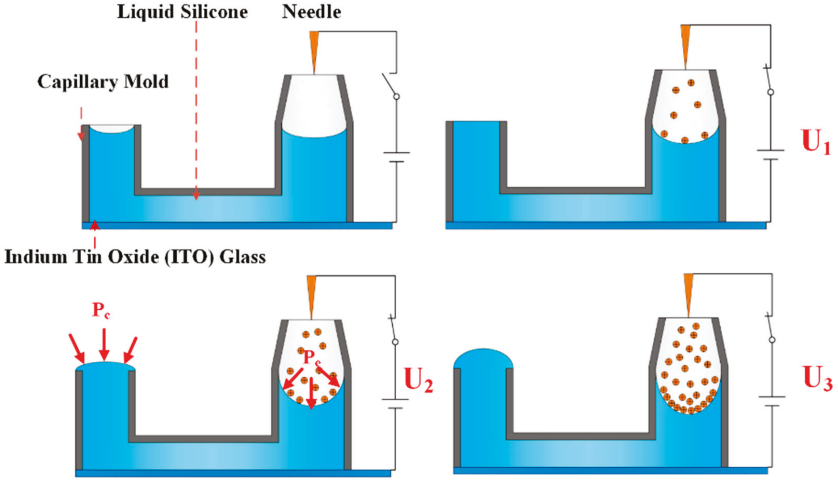

Figure 1. Principle of tunable-focus liquid lens by charge injection. As the imposed voltage increased (i.e., $U_3 > U_2 > U_1 > 0$), more positive ions accumulated at the air/liquid interface in the right-hand end of the tube, and the induced electropressure pushed the fluid toward the left-hand end of the tube.

Figure 2a schematically shows our experimental setup. A needle-plate electrode configuration was applied to generate a corona discharge. The curvature radius of the needle electrode made of steel was about 30 μm. The indium tin oxide (ITO) glass plate with a thickness of 2 mm was used as the

plate electrode and to support the 3D-printed U-tube and the dielectric liquid. The 3D-printed U-tube was made of a kind of curing polymer using the stereolithography method on ITO glass. The curing polymer was a dielectric material. We used 3D-printing equipment (Form2, Formlabs, Somerville, MA, USA) to print the U-shaped tube. The thickness of the tube wall was 0.5 mm. The left-hand end of the tube had an inner diameter of 3 mm, an outer diameter of 4 mm, and a height of 6 mm, while the other larger end had an inner diameter of 6 mm. A high-voltage direct current (DC) power source (DW-P303-5ACCC, Dongwen Corp., Tianjin, China) connected the two electrodes with the needle as the anode and the ITO plate as the cathode. The voltage could be changed from 0 to 30.0 kV continuously. The distance between the needle electrode tip and the ITO electrode was controlled by a micro motion frame during all the experiments. A digital camera (C13440, Hamamatsu, Japan) was adopted to record the liquid surface and measure the lens focus. When the camera was placed vertically, it was used to record the image of the object; when it was placed horizontally, it took photographs of the liquid morphologies. A LED lamp was used to illuminate the object, and a low-voltage power was applied to light the lamp.

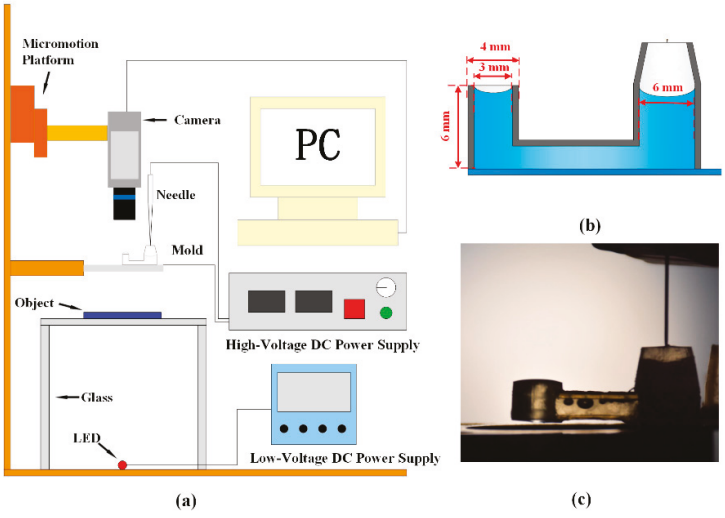

Figure 2. Experimental setup. (**a**) Schematic of experimental setup. (**b**) Schematic of U tube. (**c**) Picture of needle and U tube.

A dielectric fluid, silicone (OE-6650, Dow Corning, Midland, MI, USA), was adopted in all experiments. Its viscosity, electrical conductivity, and surface tension are about 4.0 Pa·s, 10^{-8} μS/cm, and 0.021 N/m, respectively. Its refractive index is 1.47. The liquid silicone with a volume of 25 μL was first injected using a microliter syringe with a needle into the U-tube, as shown in Figure 2. There were some air bubbles trapped in the U-tube during the injection process. Due to the low density of the bubbles, some of them moved toward the upper ends of the liquid and escaped at the open surfaces in the two ends of the tube. However, some bubbles were trapped near the upper wall of the center part of the U-tube, as shown in Figure 2c. These bubbles, however, did not affect the lens performance, because they remained almost at the same locations and were far away from the light and charge transfer paths. After loading the liquid into the tube, the high-voltage DC power source was turned on and the corona discharge phenomenon occurred.

3. Results and Discussion

We first measured the corona discharge characteristics. Figure 3 shows the corona current as a function of the corona voltage imposed between the needle-plate electrodes in the log-log format. From this figure, we can see that the relationship between the current (I) and the voltage (V) almost follows $I \propto V^n$. In our experiments, different voltages ranging from 0 to 9.2 kV were applied to the two electrodes and the resulting corona currents were measured. The corona discharge occurred at about 2.0 kV with a current of 0.01 μA. The corona current increased slowly with an increasing voltage from 2.0 to 7.0 kV and increased rapidly with an increasing voltage from 7 to 9.2 kV. At a voltage of 9.2 kV, the current reached 0.54 μA. An arcing appeared when the voltage was larger than 9.2 kV. During the whole corona discharge process, power consumption was less than 5 mW.

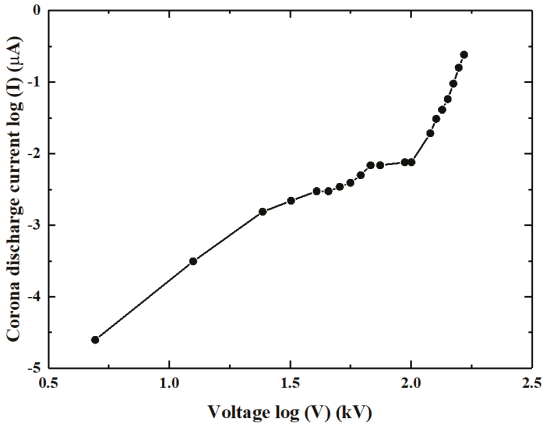

Figure 3. Corona discharge characteristics of the needle-plate electrode configuration.

We measured the temperatures of the two electrodes, the needle, the ITO glass, and the liquid silicone using an infrared camera (FLIR, E6, Wilsonville, OR, USA) at a room temperature of 12.5 °C. Figure 4 shows the temperatures at the applied voltages of 2 kV and 9.2 kV, respectively. Within the range of the applied voltages, the temperatures of the electrodes and the liquid silicone did not deviate significantly from the room temperature. The maximum temperature occurred at the needle tip when the applied voltage was 9.2 kV. Thus, the corona discharge did not introduce an obvious thermal effect, due to very low power consumption and heat dissipation to the environment by natural convection.

The side-view images of the liquid lens were recorded by the digital camera. The liquid surface morphologies are shown in Figure 5. Due to the low transparence of the 3D-printed tube, we could not observe the liquid surface inside the tube. Figure 5 only shows the liquid surface morphologies when the liquid was bulged outside the tube. The liquid was pinned at the outer edge of the tube and presented a convex shape. With an increase in voltage, the height of the liquid lens increased. Through imaging processing software, Image J (version 1.8.0, National Institutes of Health, Bethesda, MD, USA), the height could be measured based on the obtained images. For example, when the voltage was 8.2 kV, the height was 0.82 mm.

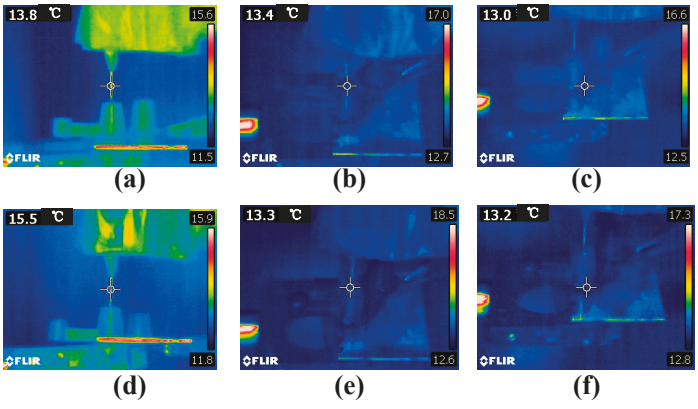

Figure 4. Temperatures of the two electrodes and the liquid silicone at the applied voltages of 2 kV and 9.2 kV: (**a**–**c**) are the infrared images of the needle, liquid, and indium tin oxide (ITO) glass at the voltage of 2.0 kV, while (**d**–**f**) are the infrared images of the needle, liquid, and ITO glass at the voltage of 9.2 kV.

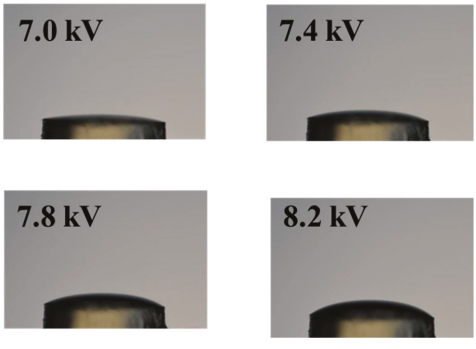

Figure 5. Surface evolution of the liquid lens with an increasing voltage, which shows the liquid silicone bulging outside of the tube.

The liquid surface morphologies in Figure 5 assumed spherical shapes. The radius of the spherical cap can be calculated by

$$R_s = (h^2 + \frac{D^2}{4})/2h \quad (1)$$

where R_s is the radius of the spherical cap and h is the height of the liquid lens. D is the outer diameter of the tube, and its value is 4 mm. The capillary pressure of the liquid lens can be calculated according to Laplace's law,

$$P_c = 2\gamma/R_s, \quad (2)$$

where γ is the surface tension of the liquid silicone with a value of 0.021 N/m. Based on Equations (1) and (2), we can obtain the curvature radiuses and the capillary pressures of the liquid lens at different voltages. The results are shown in Figure 6. The dots are the measured or calculated data. The two solid lines were obtained by fitting the data according to the B-spline algorithm, which shows the dependence of capillary pressures and curvature radiuses on voltages. As the voltage increased from 7.6 to 9.2 kV, the curvature radius decreased from 10.3 to 5.5 mm, while the capillary pressure increased from 4.0 to 7.6 Pa.

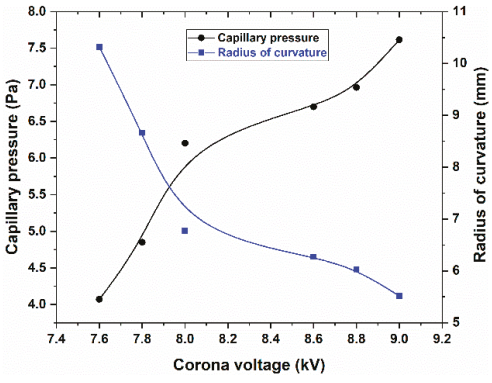

Figure 6. Capillary pressure and curvature radius of the liquid lens as a function of the voltage when the liquid silicone bulged outside of the tube.

Figure 7 depicts the images of the characters "WHU" through the tunable-focus lens. The characters were clear in all the images. With an increasing voltage, the images of the characters enlarged. When the voltage was larger than 7.6 kV, the images of the characters were inverted. As the voltage increased further, the characters became smaller. Pincushion distortion was not observed in the images, which suggests that the surface curvature was uniform.

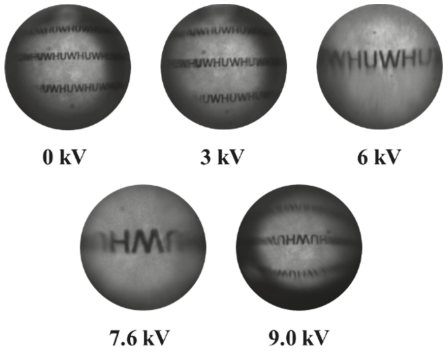

Figure 7. Recorded images of the characters "WHU" through the tunable-focus lens at different voltages.

If the liquid surfaces assume a spherical shape, the focal length of the liquid lens can be calculated based on the curvature radius, R_s, as follows:

$$F = R_s/(n_l - 1) \tag{3}$$

where F is the focal length and n_l is the refractive index of the liquid silicone with a value of 1.47.

The focal length of the liquid lens can also be calculated from the images shown in Figure 6. Considering the droplet as a thin lens, F was calculated using the following equation:

$$F = h_i l/(h_i + h_0) \tag{4}$$

where h_i is the image size of the object with the liquid lens, l is the distance between the lens and the test object, and h_0 is the image size of the object without the liquid lens.

Figure 8 shows the focal length of the liquid lens calculated by Equation (3) (black line with solid squares) and Equation (4) (red line with solid circles). The two solid lines were also obtained by fitting the calculated data according to the B-spline algorithm. The results from Equation (3) show that the

focal length decreased from 22.9 to 12.2 mm with the increasing voltage, while the focal length ranged from 23.1 to 13.1 mm based on the results from Equation (4). The results from both equations are in good agreement, and the largest deviation of 7.3% occurred at a voltage of 9.0 kV. Therefore, the morphologies of the liquid lens were very close to a spherical shape.

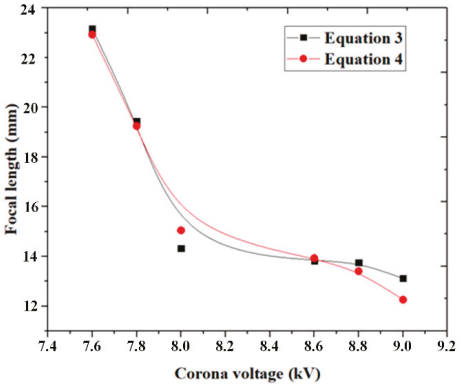

Figure 8. Focal length of the convex liquid lens as a function of the voltage.

Figure 7 shows the detailed information of the images that we obtained using the Image J software. By comparing the images with and without the liquid lens, we could calculate the focal length of the liquid lens according to Equation (4). For example, we obtained the pixel length of the character "H" with and without the liquid lens and then measured the distance between the lens and the test object. From these measurements, we could get a focal-length value. If the images with and without the lens had a same-direction arrangement, the focal length was negative, which means that the lens interface was concave. When the images with and without the lens had an inverted arrangement, the focal length was positive, suggesting that the lens interface was convex. Based on this method, we could calculate the whole focus range of the liquid lens when the voltage was varied from 0 to 9.2 kV. Figure 9 presents the relationship between the focal length and the applied voltages. When the voltage increased from 0 to 6.25 kV, the focal length declined from −10 mm to negative infinity. When the voltage was further increased to about 7 kV, it turned into a convex lens and the focal length decreased from positive infinity to 10 mm.

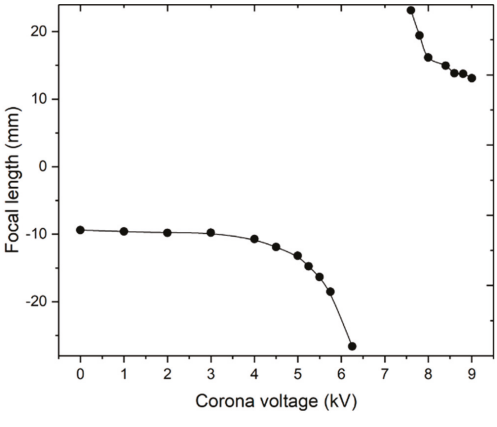

Figure 9. Focus range of the liquid lens with the voltage varying from 0 to 9.2 kV.

We conducted three experiments to test the robustness of this liquid-lens manipulation technique. The voltages of 8.4 kV and 9.0 kV were chosen, and at each voltage three experiments were repeated. Figure 10 shows three different experiments at voltages of 8.4 kV and 9.0 kV. At a voltage of 8.4 kV, the focal lengths were 14.9, 14.7, and 15.2 mm and their deviation was 0.5 mm. For a voltage of 9.0 kV, the focal lengths of the three experiments were, respectively, 11.1, 11.6, and 11.9 mm and their deviation was 0.8 mm.

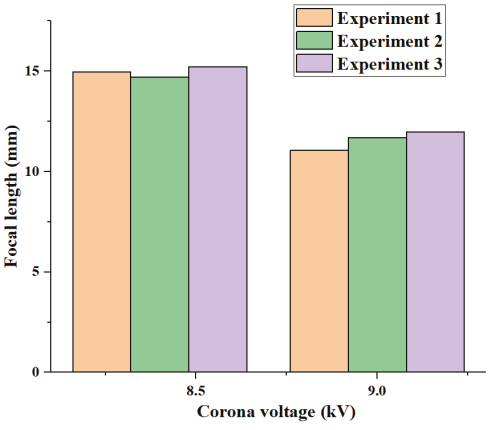

Figure 10. Focal length at two different voltages in three repeated experiments.

Figure 11 illustrates the focal length as a function of the voltage when we cyclically increased (solid squares) and decreased (solid circles) the voltage. A little hysteresis existed in the cycle. The majority of the focal lengths could be restored to their original state within a deviation of 2.5% after the corona voltage was increased from 0 to 9.2 kV and then returned to 0 kV.

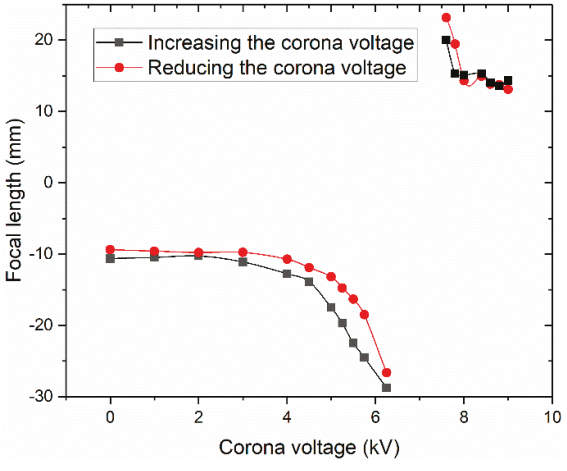

Figure 11. Focal length as a function of the voltage, which was gradually increased from 0 to 9.2 kV and then gradually decreased to 0 kV.

4. Conclusions

In summary, a new method of realizing tunable-focus liquid lenses through charge injection was proposed and demonstrated. By a corona discharge in the air, electropressure with a magnitude of

10 Pa was generated at the interface between the liquid silicone and the air. Using only a 3D-printed U-tube and liquid silicone, the focus of the liquid lens varied from $-\infty$ to -9 mm and from 13.11 mm to ∞. The robustness of this liquid-lens manipulation method was examined by testing the focus with an increasing–decreasing voltage loop. Such a simple and easily implemented liquid-lens manipulation method can be applied in many potential fields.

Author Contributions: S.Q. supervised and drafted the manuscript, H.Z. fabricated and set up the experiments, W.S. conducted the experiments, and Z.L. analyzed the data. All authors have read and agreed to the published version of the manuscript.

Funding: This research was funded by the Foundation of the State Key Laboratory of Coal Combustion (FSKLCCA1802) and the National Natural Science Foundation of China (51975423 and 51605341).

Conflicts of Interest: The authors declare no conflict of interest.

References

1. Miller, N.A. Investigation of the tension mechanisms responsible for lens formation and a new method for measuring the angles of liquid lenses. *J. Phys. Chem.* **1941**, *45*, 1025–1045. [CrossRef]
2. Paget, R.A.S. A primitive lens. *Nature* **1923**, *112*, 326. [CrossRef]
3. Erickson, D.; Sinton, D.; Psaltis, D. Optofluidics for Energy Applications. *Nat. Photonics* **2011**, *5*, 583–590. [CrossRef]
4. Fan, X.D.; White, I.M. Optofluidic microsystems for chemical and biological analysis. *Nat. Photonics* **2011**, *5*, 591–597. [CrossRef] [PubMed]
5. Psaltis, D.; Quake, S.R.; Yang, C. Developing optofluidic technology through the fusion of microfluidics and optics. *Nature* **2006**, *442*, 381–386. [CrossRef] [PubMed]
6. Monat, C.; Domachuk, P.; Eggleton, B.J. Integrated optofluidics: A new river of light. *Nat. Photonics* **2007**, *1*, 106–114. [CrossRef]
7. Berge, B.; Peseux, J. Variable focal lens controlled by an external voltage: An application of electrowetting. *Eur. Phys. J. E* **2000**, *3*, 159–163. [CrossRef]
8. Shopova, S.I.; Zhou, H.; Fan, X.; Zhang, P. Optofluidic ring resonator based dye laser. *Appl. Phys. Lett.* **2007**, *90*, 221101. [CrossRef]
9. Schmidt, H.; Hawkins, A.R. Optofluidic waveguides: I. Concepts and implementations. *Microfluid. Nanofluid.* **2008**, *4*, 3–16. [CrossRef]
10. Yang, Y.; Liu, A.Q.; Chin, L.K.; Zhang, X.M.; Tsai, D.P.; Lin, C.L.; Lu, C.; Wang, G.P.; Zheludev, N.I. Optofluidic waveguide as a transformation optics device for lightwave bending and manipulation. *Nat. Commun.* **2012**, *3*, 651. [CrossRef]
11. Chin, L.K.; Liu, A.Q.; Soh, Y.C.; Lim, C.S.; Lin, C.L. A reconfigurable optofluidic michelson interferometer using tunable droplet grating. *Lab Chip* **2010**, *10*, 1072–1078. [CrossRef] [PubMed]
12. Yu, J.Q.; Yang, Y.; Liu, A.Q.; Chin, L.K.; Zhang, X.M. Microfluidic droplet grating for reconfigurable optical diffraction. *Opt. Lett.* **2010**, *35*, 1890–1892. [CrossRef]
13. Song, C.; Nguyen, N.T.; Tan, S.H.; Asundi, A.K. Modelling and optimization of micro optofluidic lenses. *Lab Chip* **2009**, *9*, 1178–1184. [CrossRef]
14. Seow, Y.C.; Lim, S.P.; Lee, H.P. Optofluidic variable-focus lenses for light manipulation. *Lab Chip* **2012**, *12*, 3810–3815. [CrossRef] [PubMed]
15. Zhao, Y.; Stratton, Z.S.; Guo, F.; Lapsley, M.I.; Chan, C.; Lin, S.C.S.; Huang, T.J. Optofluidic imaging: Now and beyond. *Lab Chip* **2013**, *13*, 17–24. [CrossRef] [PubMed]
16. Song, W.; Psaltis, D. Pneumatically tunable optofluidic 2×2 switch for reconfigurable optical circuit. *Lab Chip* **2011**, *11*, 2397–2402. [CrossRef]
17. Müller, P.; Kloss, A.; Liebetraut, P.; Mönch, W.; Zappe, H. A fully integrated optofluidic attenuator. *J. Micromech. Microeng.* **2011**, *21*, 125027. [CrossRef]
18. Brown, C.V.; Wells, G.G.; Newton, M.I.; McHale, G. Voltage-programmable liquid optical interface. *Nat. Photonics* **2009**, *3*, 403–405. [CrossRef]

19. Heikenfeld, J.; Zhou, K.; Kreit, E.; Raj, B.; Yang, S.; Sun, B.; Milarcik, A.; Clapp, L.; Schwartz, R. Electrofluidic displays using young-laplace transposition of brilliant pigment dispersions. *Nat. Photonics* **2009**, *3*, 292–296. [CrossRef]
20. Moran, P.M.; Dharmatilleke, S.; Khaw, A.H.; Tan, K.W.; Chan, M.L.; Rodriguez, I. Fluidic lenses with variable focal length. *Appl. Phys. Lett.* **2006**, *88*, 041120. [CrossRef]
21. Roy, A.C.; Ghatak, A. Design of an adaptable optofluidic aspherical lens by using the elastocapillary effect. *Adv. Opt. Mater.* **2014**, *2*, 874–878. [CrossRef]
22. Lee, S.Y.; Tung, H.W.; Chen, W.C.; Fang, W. Novel micro lens with tunable astigmatism. In Proceedings of the TRANSDUCERS 2007—International Solid-State Sensors, Actuators and Microsystems Conference, Lyon, France, 10–14 June 2007; pp. 2147–2150.
23. Liebetraut, P.; Petsch, S.; Liebeskind, J.; Zappe, H. Elastomeric lenses with tunable astigmatism. *Light Sci. Appl.* **2013**, *2*, e98. [CrossRef]
24. Zhang, W.; Zappe, H.; Seifert, A. Wafer-scale fabricated thermo-pneumatically tunable microlenses. *Light Sci. Appl.* **2014**, *3*, e145. [CrossRef]
25. Malyuk, A.Y.; Ivanova, N.A. Varifocal liquid lens actuated by laser-induced thermal Marangoni forces. *Appl. Phys. Lett.* **2018**, *112*, 103701. [CrossRef]
26. Dong, L.; Agarwal, A.K.; Beebe, D.J.; Jiang, H.R. Adaptive liquid microlenses activated by stimuli-responsive hydrogels. *Nature* **2006**, *442*, 551–554. [CrossRef]
27. Li, L.; Yuan, R.; Wang, J.; Li, L.; Wang, Q. Optofluidic lens based on electrowetting liquid piston. *Sci. Rep.* **2019**, *9*, 1–7. [CrossRef]
28. Lee, J.; Lee, J.; Won, Y.H. Nonmechanical three-dimensional beam steering using electrowetting-based liquid lens and liquid prism. *Opt. Express* **2019**, *27*, 36757–36766. [CrossRef]
29. Chen, Q.; Li, T.; Zhu, Y.; Yu, W.; Zhang, X. Dielectrophoresis-actuated in-plane optofluidic lens with tunability of focal length from negative to positive. *Opt. Express* **2018**, *26*, 6532–6541. [CrossRef]

micromachines

MDPI

Article

Dynamics Behaviors of Droplet on Hydrophobic Surfaces Driven by Electric Field

Jie Liu [1] and Sheng Liu [1,2,*]

[1] The Laboratory of Transients in Hydraulic Machinery, School of Power and Mechanical Engineering, Wuhan University, Wuhan 430072, China; lll202087@whu.edu.cn
[2] Electronic Manufacturing and Packaging Laboratory, the Institute of Technological Sciences, Wuhan University, Wuhan 430072, China
* Correspondence: victor_liu63@vip.126.com; Tel.: +86-138-7125-1668

Received: 28 October 2019; Accepted: 12 November 2019; Published: 14 November 2019

Abstract: Droplet microfluidic technology achieves precise manipulation of droplet behaviors by designing and controlling the flow and interaction of various incompatible fluids. The electric field provides a non-contact, pollution-free, designable and promising method for droplet microfluidics. Since the droplet behaviors in many industrial and biological applications occur on the contact surface and the properties of droplets and the surrounding environment are not consistent, it is essential to understand fundamentally the sessile droplet motion and deformation under various conditions. This paper reports a technique using the pin-plate electrode to generate non-uniform dielectrophoresis (DEP) force to control sessile droplets on hydrophobic surfaces. The electrohydrodynamics phenomena of the droplet motion and deformation are simulated using the phase-field method. It is found that the droplet moves along the substrate surface to the direction of higher electric field strength, and is accompanied with a certain offset displacement. In addition, the effect of pin electric potentials, surface contact angles and droplet volumes on the droplet motion and deformation are also studied and compared. The results show that higher potentials, more hydrophobic surfaces and larger droplet volumes exhibit greater droplet horizontal displacement and offset displacement. But for the droplet vertical displacement, it is found that during the first revert process, the release of the surface tension can make the droplet with low potentials, small contact angles or small droplet volumes span from negative to positive. These results will be helpful for future operations encountered in sessile droplets under non-uniform electric fields towards the droplet microfluidics applications.

Keywords: dielectrophoresis; droplet; electrohydrodynamics; phase field method; non-uniform electric field

1. Introduction

Recently the dynamic behavior of sessile droplets on substrate surfaces have received considerable attention, especially for superhydrophobic surfaces with low adhesion resistance and ultra-low surface energy [1]. The research results of dynamic behaviors of droplets have been widely used in broad applications, such as self-cleaning [2,3], anti-icing [4], heat transfer [5,6], electronics [7–9], and microelectromechanical systems [10], etc. Typically, there are two types of ways to drive the dynamic behavior of sessile droplets. One is to make full use of the droplets' own gravity or surface tension. The gravity can play a major role when the droplet volume is large enough. The dynamic behavior of droplets can be enhanced by increasing tilt angles of substrate surfaces or using a more hydrophobic substrate structure and so on. On the other hand, surface tension plays a major role when the droplet volumes are small enough to ignore their own gravity, which are mainly manifested in promoting the droplet coalescence-driven jump [11,12]. Another method is to apply an external

force to drive the dynamic behavior of sessile droplets. The existing methods include applied electric fields [13–17], magnetic fields [18], pressure [19], air flow [20–22], laser [23] and so on. In these methods, the electric field driving the dynamic behavior of sessile droplets has been developed as a relatively technology exhibiting promising perspective for the droplet control [24,25]. Takeda et al. [13] experimentally studied the effects of direct current (DC) and alternating current (AC) electric fields on water droplets on superhydrophobic surfaces, demonstrating that superhydrophobic surfaces are beneficial for controlling water droplets through small electric fields. Sakai et al. [14] developed a particle image velocimetry (PIV) system to evaluate the internal fluidity of water droplets moving on a superhydrophobic surface by electric fields. Zhu Y et al. [15] experimentally studied the water droplet behaviors on superhydrophobic surfaces under an increasing AC voltage, and numerically simulated the electrification characteristics of water droplets deposited on hydrophobic surfaces and their influence on a driven discharge in an AC electric field. Wei et al. [16] experimentally conducted the rolling behavior of the water droplet on superhydrophobic surfaces under electrical fields, and built a finite element modeling (FEM) simulation model to indicate that an electrostatic force produced by electrical fields drove a water droplet to roll. Adamiak [17] numerically simulated the deformation of an ideally conducting liquid droplet deposited on the flat dielectric surfaces by solving the capillary Laplace–Young equation. Liu [26] conducted numerical simulations and experiments on the dynamic mechanism of water droplet formation with different applied voltages and droplet distribution, and drove surface discharges on the insulator surface under an AC electric field. However, existing research on electric fields driven dynamic behaviors of sessile droplets is mainly experimental, and the simulation research efforts are few and mainly focused on the polarization analysis of stationary droplets [2,5,27]. In addition, since sessile droplets constitute the three-phase contact line, the simulation research on the dynamic behavior of sessile droplets is naturally complicated [28,29]. The polarization effect during the electric-driven motion and deformation of sessile droplets remains unclear. There is still a need for a robust model of an electric-driven droplet to predict changes in droplet dynamic behaviors.

In this study, therefore, a phase-filed two-phase flow model under simplified non-uniform electric fields is developed to simulate the electrohydrodynamic behaviors of sessile droplets on hydrophobic surfaces. With this model, the electro-driven motion and deformation of water droplets in the oil phase are analyzed, and the horizontal displacement, vertical displacement and offset displacement of droplets are quantified to express the effect of non-uniform electric fields. In addition, the effects of pin electric potentials, surface contact angles and droplet volumes on the droplet motion and deformation are also studied and compared. This characterization will help the optimization of the electro-driven deformation and motion of sessile droplets for a variety of engineering and technological applications.

2. Construction of Dynamic Model

2.1. Model Description

The two-dimensional simulation model and corresponding boundary conditions based on previous experimental conditions and theoretical research [13–16] is developed as shown in Figure 1a. The computation area contains the droplet and oil phase. A droplet with a certain volume is placed in the middle of substrate surfaces and forms a certain contact angle θ. The substrate bottom surface is considered to be in a wetted wall condition, the top and side surfaces of the computational domain are considered to be pressure outlet boundaries to ensure there are no pressure and velocity gradient effects. In order to simplify the problem and highlight the effect of a non-uniform electric field, the electric field structure is simplified to a pin-plate electrode structure that locates at the left and right sides, respectively. Specific model sizes and parameter values used in these simulations are listed in Table 1.

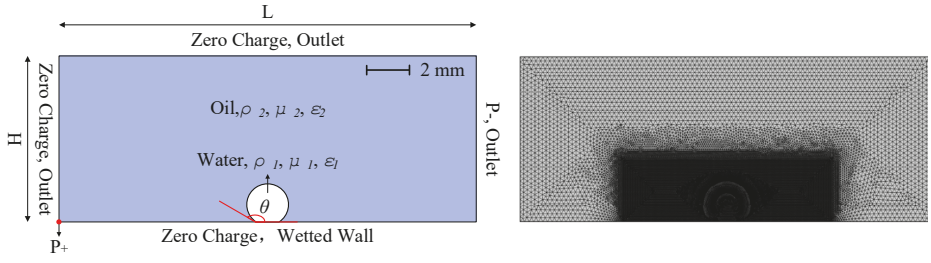

Figure 1. (**a**) Computational domain and boundary conditions with (**b**) the example of mesh used in simulations.

Table 1. Simulation parameter setting.

Parameter	Symbol	Value	Units
Plate electrode potential	V_-	0	kV
Pin electrode potential	V_+	0–20	kV
Droplet volume	Z	2–6	mm^3
Droplet contact angle	θ	90–170	°
Length of air domain	L	20	mm
Height of air domain	H	8	mm
Permittivity of vacuum	ε_0	8.85×10^{-12}	F/m
Acceleration of gravity	g	9.81	m^2/s
Density of water	ρ_1	998	kg/m^3
Dynamic viscosity of water	μ_1	0.001	Pa·s
Relative permittivity of water	ε_1	80	-
Conductivity of water	σ_1	1×10^{-5}	S/m
Density of oil	ρ_2	884	kg/m^3
Dynamic viscosity of oil	μ_2	0.474	Pa·s
Relative permittivity of oil	ε_2	2.2	-
Conductivity of oil	σ_2	1×10^{-4}	S/m
Surface tension	α	0.03	N/m

The model is divided by free triangle meshes and there is the refined meshes in and near the droplet region. By using virtual operations and mesh controlled edges, a rectangular virtual domain with higher resolution than the remaining domain is introduced to decrease the number of elements and thus reduces the computational load considerably. An example of such a mesh is shown in Figure 1b and a mesh independence study is performed to validate the numerical stability of the simulation. The conditions of V_+ = 15 kV, Z = 4 mm^3 and θ =150° are used as a mesh correction benchmark. By changing the number of meshes from 46,646 (mesh 1) to 60,996 (mesh 2), the final horizontal displacement of the droplet with 3 s is less than 2.77%. The error caused by finite mesh is relatively small and the mesh 1 is sufficiently precise for the present model. Therefore, the structure of the mesh 1 above is adopted for all cases in this study.

2.2. Two-Phase Flow Equations

The whole system can be considered as an isothermal and incompressible laminar flow due to small changes in temperature and velocity. Based on mass and momentum conservation, the governing equations for both phases are the incompressible Navier–Stokes equations:

$$\nabla \cdot \vec{u} = 0 \tag{1}$$

$$\rho\frac{\partial\vec{u}}{\partial t}+\rho\left(\vec{u}\cdot\nabla\right)\vec{u}=\nabla\cdot\left[-p\mathrm{I}+\mu\left(\nabla\vec{u}+\left(\nabla\vec{u}\right)^{\mathrm{T}}\right)\right]+\rho g+F_{st}+F_e \tag{2}$$

where $\vec{u}$ (m/s) is the velocity, ρ (kg/m^3) is the density, p (Pa) is the pressure, μ (Pa·s) is the dynamic viscosity, I is the unit matrix, g (m^2/s) is the acceleration of gravity, F_{st} (N/m^3) is the surface tension per unit volume on the water–oil interface, and F_e (N/m^3) is the electric stress per unit volume respectively.

Phase field method, an effective tool for exploring the multiphase flow behaviors and interfacial phenomena, used in this paper is relatively effective in multiphase flow research efforts. The water–oil phase interface is described by a phase field variable, φ, whose evolution is governed by the Cahn–Hilliard equation [19]:

$$\frac{\partial\phi}{\partial t}+\vec{u}\cdot\nabla\phi=\nabla\gamma\nabla G \tag{3}$$

where γ (m^3·s/kg) is the mobility parameter that controls the diffusion scale, and (Pa) is the chemical potential at the phase interface respectively. The formulas of γ and G are depicted as follows:

$$\gamma=\chi{e_{pf}}^2 \tag{4}$$

$$G=\lambda\left[-\nabla^2\phi+\frac{\phi\left(\phi^2-1\right)}{{e_{pf}}^2}\right] \tag{5}$$

where χ (m·s/kg) is the mobility tuning parameter and set to 1 m·s/kg that is a good starting point for current models, e_{pf} (m) is capillary width that scales with the thickness of the interface and is set to R/20 (R is the droplet radius), and λ (N) is the mixing energy density respectively. λ and e_{pf} are related to the surface tension coefficient, α (N/m), through the equation:

$$\alpha=\frac{2\sqrt{2}}{3}\frac{\lambda}{e_{pf}} \tag{6}$$

The parameters appearing in equations are determined by the phases. These quantities are modeled as global variables that vary across the interface with respect to volume fraction. Therefore, the density and dynamic viscosity in the two-phase flow are defined as:

$$\rho=\rho_1V_{f1}+\rho_2V_{f2} \tag{7}$$

$$\mu=\mu_1V_{f1}+\mu_2V_{f2} \tag{8}$$

where subscript 1 and 2 represent the water phase and oil phase respectively. The volume fraction V_f of phase 1 and phase 2 is calculated as:

$$\begin{cases} V_{f1}=\frac{1-\phi}{2} \\ V_{f2}=\frac{1+\phi}{2} \end{cases} \tag{9}$$

Phase 1 corresponds to the domain where $\varphi = -1$, and phase 2 corresponds to the domain where $\varphi = 1$. The interface between the two fluids is evolved by a fixed contour of a phase field function $\varphi = 0$.

The surface tension force F_{st} is added to the Navier-Stokes equations as a body force by multiplying the chemical potential of the system by the gradient of the phase field variable.

$$F_{st}=G\nabla\phi \tag{10}$$

2.3. Electric Field Equations

An idealized case that the both phases (the droplet and the oil) are leaky dielectrics in a DC electric field is considered. Therefore, the governing equation for the electric field is expressed by Maxwell's equation [30]:

$$-\nabla \cdot \left(\varepsilon_0 \varepsilon \vec{E}\right) = 0 \tag{11}$$

where ε_0 (F/m) is the free space permittivity, and ε is the relative permittivity, and $\vec{E}$ (V/m) is the electric field strength, which can be expressed as the gradient of electric potential, V (V):

$$\vec{E} = -\nabla V \tag{12}$$

The relative permittivity ε can be calculated similarly to the density and viscosity:

$$\varepsilon = \varepsilon_1 V_{f1} + \varepsilon_2 V_{f2} \tag{13}$$

The electric force F_e, as a source term of the Navier-Stokes equations, can be calculated by the divergence of the Maxwell stress tensor, τ^M (SI unit: N/m^2) [31,32]. Under the conditions of the perfect dielectric model and incompressible fluid, the electric force per unit volume is given as:

$$F_e = \nabla \cdot \tau^M = \nabla \varepsilon_0 \varepsilon \left[\vec{E}\vec{E} - \frac{1}{2}E^2 \mathrm{I}\right] \tag{14}$$

The electric force is along the normal direction of two-phase interface. In the case of non-uniform electric fields, the electric force of the polarized dielectric is referred to as the DEP force.

3. Results and Discussion

The motion and deformation of droplets on the substrate surface under electric fields are mainly affected by the inertial force, viscous force, electric field force, surface tension and substrate adhesion. The characteristic phenomena are determined by the relative importance of the forces in the flow. It is useful to calculate several dimensionless numbers based on the relative magnitudes of key physical parameters before performing full time-dependent simulations, which characterize fluid behavior in multiphase and microfluidic flows. In many cases it is not necessary to calculate dimensionless numbers accurately, and just simply estimating its magnitude is sufficient [33]. The two-phase characteristic flow under the electric field is mainly determined by the Reynolds number (*Re*), capillary number (*Ca*) [34,35] and electric Bond number (Bo_E) [33]:

$$Re = \frac{\rho_1 u R}{\mu_1} \tag{15}$$

$$Ca = \frac{\mu_1 u}{\alpha} \tag{16}$$

$$Bo_E = \frac{\varepsilon_0 \varepsilon R E^2}{\alpha} \tag{17}$$

here the characteristic length of the two-phase flow is represented by the droplet radius, R (mm), which can be calculated at the given droplet volume and contact angle:

$$R = \left(Z/(\frac{4\pi}{3} - \frac{\pi}{3}(1+\cos\theta)^2(3-(1+\cos\theta)))\right)^{\frac{1}{3}} \tag{18}$$

The Re number, *Ca* number and Bo_E number are, respectively, the ratio of inertial forces to viscous forces, viscous forces to surface tension forces and electric forces to surface tension forces. Using these definitions, the Re number varies between about 0.9 and 1.5, which means viscous forces are sufficiently

strong to prevent the flow from becoming turbulent; the *Ca* number ranges between about 0.014 and 0.024, which means the interface shape and velocity distribution are driven by the surface tension; the Bo_E number varies between about 3.3 and 5.6, which means electric field force can overcome the surface tension and change the interface shape and velocity distribution. Therefore, the above assumptions and equations are applicable to the numerical simulation study of this paper.

In this paper, COMSOL Multiphysics 5.4 (COMSOL, Inc., Burlington, MA, USA), the multiphysical field coupling software, is employed to perform the numerical simulations. The second-order quadratic basic functions used for the phase-field varies, the velocity is filed, and the electric potential is recorded, while the pressure is solved using linear basic functions. The transient solver PARDISO is adopted with phase initialization. The time step is set to 0.01 s and 0.02 s according to the degree of the droplet movements. The time step 0.01 s is used to calculate the droplet movement within 0 to 0.2 s, and the time step 0.01 s is used to calculate the remaining time period. The fully coupled system is solved by the backwards Euler method.

3.1. Deformation and Motion of the Droplet

The droplet with the condition of V_+ = 15 kV, Z = 4 mm^3 and θ = 150° is considered first, whose angle is the demarcation contact angle between hydrophobic and superhydrophobic structures. The time-lapse evolutions and local velocity field inside the droplet are shown in Figure 2. As can be seen that under the effect of non-uniform electric fields, the droplet deforms to the left offset and slides to the left side along the substrate. During the motion, the droplet offset is becoming larger, corresponding to this is the gradually increasing advancing angle and the gradually deceasing receding angle. The droplet finally moves to the left side, which is the direction of increasing electric field strength.

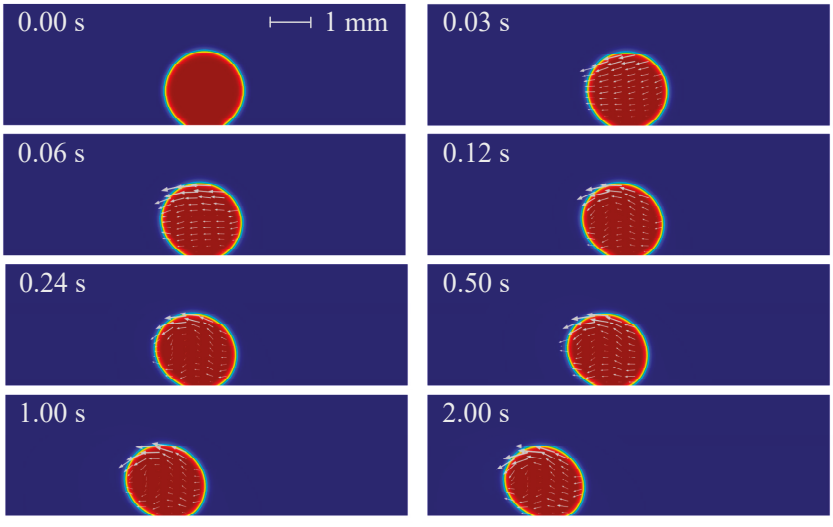

Figure 2. Time-lapse evolutions of droplet morphology (V_+ = 15 kV, Z = 4 mm^3 and θ = 150°).

The above phenomenon can be explained by the non-uniform DEP force of droplets under non-uniform electric fields [36]. In the absence of electric fields, the stationary sessile droplet on substrate surfaces maintains its spherical cap shape and forms a certain contact angle because of the effect of interfacial tension. The droplet is polarized under the effect of electric fields: the electric dipole moments are generated along the direction of the electric field inside the droplet, and polarization charges are generated on both sides of droplet surface. As the electric field strength increases, the charge

density on both sides of the droplet increases, which means the electric field force on both sides of the droplet also increases. When electric fields are non-uniform, the electric dipole is subjected to an uneven electric field force, so that the force on both sides of the droplet is uneven. When the electric field force on both sides of the droplet is large enough, the droplet can be deformed against the surface tension, and even moves against the substrate adhesion. When the polarization degree of the droplet is higher than that of the surrounding phase, the positive DEP force occurs, resulting in a net DEP force pointing to the direction of increasing electric field strength; by contrast, when the polarization degree of the droplet is lower than that of the surrounding phase, the negative DEP force occurs, resulting in a net DEP force pointing to the direction of decreasing electric field strength. In this paper, the relative permittivity of the droplet phase ($\varepsilon_1 = 80$) is much larger than that of the oil phase ($\varepsilon_2 = 2.2$), so that there is a positive DEP force acting on the droplet under non-uniform electric fields. In addition, there is an adhesion force on the contact surface between the droplet and the substrate, resulting in sluggish motions of the bottom surface of the droplet, thus causing droplet offset. In summary, under the combined action of the gravity, surface tension, non-uniform DEP force and substrate adhesion, the droplet deforms and moves to the left side, which is the direction of increasing electric field strength.

The electric polarization degree of the droplet, represented by the norm of polarization charge, is shown in Figure 3, in which the black line is electric field lines around the droplet. As can be seen that the electric polarization degree and electric lines vary with the droplet motion and deformation pattern. There is a greater polarization degree inside the droplet and electric field lines shrink in the droplet phase. More specifically, the polarization degree of the droplet increases with time, and the polarization degree on both sides of the droplet is different: the left is higher and the right is lower. The reason for these phenomena is due to the fact that the droplet is more easily polarized than the oil ($\varepsilon_1 > \varepsilon_2$) and the polarization degree increases with the increase of electric field strength. As time increases, the droplets is closer to the pin electrode with higher electric field strength, so that the polarization degree inside the droplet increases and the difference in the polarization degree on both sides of the droplet is more distinct. The velocity and pressure distributions are shown in Figures 4 and 5, respectively.

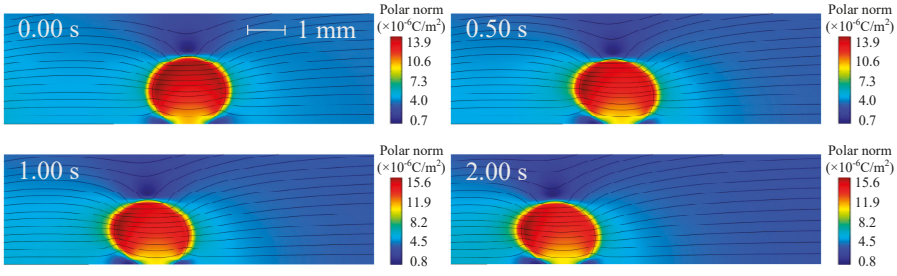

Figure 3. Electric polarization and electric field lines around the droplet ($V_+ = 15$ kV, $Z = 4$ mm^3 and $\theta = 150°$).

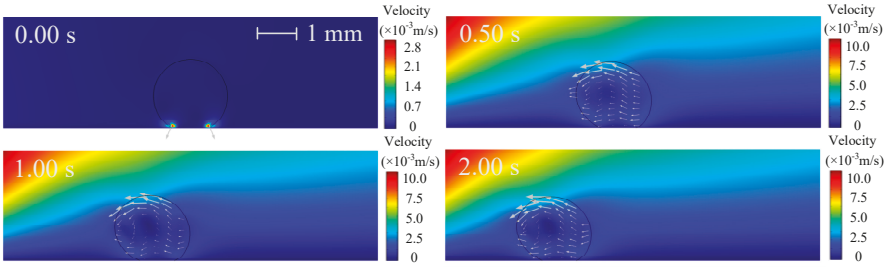

Figure 4. Velocity distribution around the droplet ($V_+ = 15$ kV, $Z = 4$ mm^3 and $\theta = 150°$).

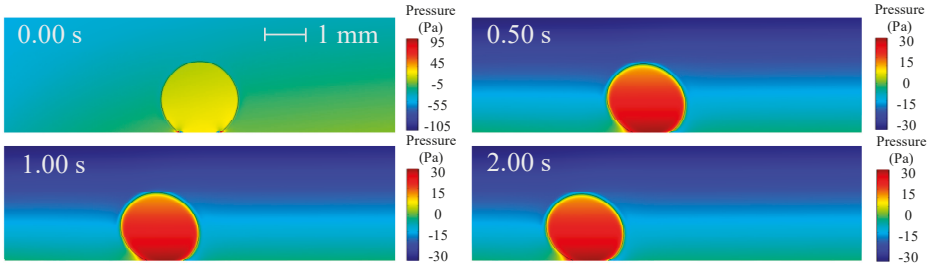

Figure 5. Pressure distribution around the droplet (V_+ = 15 kV, Z = 4 mm^3 and θ = 150°).

In order to quantitatively show the effects of electric fields on the droplet motion, variations of the droplet horizontal displacement d_x (mm) and vertical displacement d_y (mm) of droplet centroids are shown in Figure 6a,b. The droplet centroid is the value of the two-dimensional coordinates x and y of the droplet, which are calculated as $\iint\left(x \times V_{f1}\right) / \iint V_{f1}$ and $\iint\left(y \times V_{f1}\right) / \iint V_{f1}$, respectively. It can be seen from Figure 6a that the droplet horizontal displacement value increases with time and is nearly linear. The negative sign represents the horizontal displacement direction of the droplet from the right to the left. Within 3 s, the horizontal displacement value of droplet centroids reaches 3.4106 mm. Comparing the horizontal displacement curves of droplet centroids and contact surface centers, the former responds to the DEP force relatively quickly about 0.02 s. This means that under the effects of non-uniform electric fields, the droplet first deforms against the surface tension, that is, the droplet centroid begins to move first; then the droplet is driven to move against the substrate adhesion, this is, the droplet-substrate contact surface center moves later. In addition, there is always a difference between the droplet centroid horizontal displacement and the contact surface horizontal displacement, indicating that the droplet is deformed. It can be seen from Figure 6b that the vertical displacement of the droplet centroid firstly moves downward quickly under the non-uniform DEP force, and then reverts upward due to the release of the surface tension caused by the droplet deformation. The maximum revert displacement of the droplet is 0.0082 mm at 0.7 s. The negative sign represents the vertical displacement direction of the droplet from the up to the down. This is because the pin electrode is located below the droplet, so that the vertical component of the non-uniform DEP force makes the droplet move vertically downward. After that, the vertical displacement of the droplet centroid gradually moves downward due to the enhancement of the electric field strength as the droplet gets closer to the pin electrode.

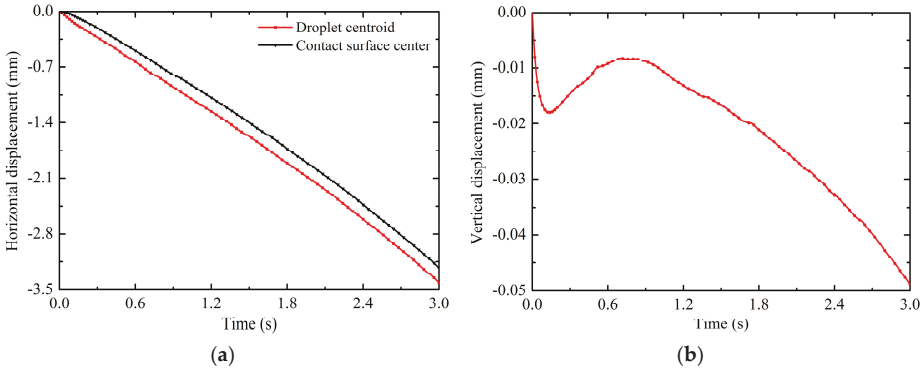

Figure 6. Variations in (**a**) the horizontal displacement and (**b**) vertical displacement (V_+ = 15 kV, Z = 4 mm^3 and θ = 150°).

In order to show the effects of electric fields on the droplet deformation, the droplet offset displacement d_o (mm) is defined as the horizontal displacement difference between the contact surface center and the droplet centroid, $d_o = d_{\text{center}} - d_x$. The variation of the droplet offset displacement is shown in Figure 7. As displayed, the droplet offset displacement is sharply increased within 0.3 s. This is due to the fact that the droplet centroid moves faster in response to the non-uniform DEP force relative to the contact surface center. Then the increase in the droplet offset displacement becomes slow because the motive of the contact surface center is gradually synchronized with the droplet centroid. Finally the droplet offset displacement continues to increase almost steadily and keeps oscillating around 0.0091 mm. In the process of a non-uniform electric field driving droplet motion, the droplet does not maintain a constant deformation state, but the deformation relaxation occurs with a slight oscillation phenomenon due to its own inertia. By contrast with the one-time revival phenomenon of the vertical displacement, the oscillation phenomenon of the horizontal offset displacement exists all the time. In summary, the non-uniform electric fields can induce positive electrophoresis motion and deformation of the droplet.

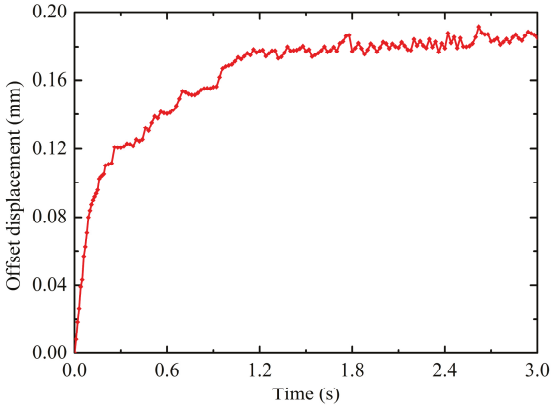

Figure 7. Variations in the offset displacement (V_+ = 15 kV, Z = 4 mm^3 and θ = 150°).

3.2. Effects of the Potential

It has been revealed that the electrohydrodynamic phenomenon of the droplet with the contact angle of 150° under non-uniform electric fields, which the non-uniform polarization force can cause droplets to offset deform and move along substrate surfaces. Therefore, the electric field potential has an important impact on the droplet electro-driven deformation and motion. In this section, the effects of different pin electrode potentials on the deformation and motion are discussed. The droplet volume is 4 mm^3 and the contact angle is maintained at 150°. There is the same droplet radius of 0.9890 mm which is calculated according to Equation (18). The results on the droplet motion of different pin potentials are shown in Figure 8a,b. It is observed from Figure 8a that the horizontal displacement is increased when increasing the potential. This is because the electric field intensity and its gradient increase with the increase in the pin electrode potential at the same pin-plate electrode distance. According to Equation (12) and Equation (14), the non-uniform DEP force on the droplet also increases. Therefore, the horizontal displacement is increased with increasing the potential. Moreover, as shown in Figure 8b, there are some differences in the patterns of the droplet vertical displacement for different potentials. The vertical displacement of the first revert of the droplet increases as the potential increases. For the low potential, the droplet vertical motion direction can change. For example, the droplet vertical displacement changes from negative to positive at about 0.45 s for the potential of 5 kV, and at about 0.57 s for the potential of 10 kV. But for the potentials of 15 kV and 20 kV, the droplet vertical displacement are always negative. The smaller the potential, the lower the vertical component

of the non-uniform DEP force, and the smaller the binding effect on the droplet. Therefore, for the low potential, the release of the surface tension caused by the droplet deformation not only makes the droplet revert, but also makes the droplet vertical displacement span from negative to positive. In this paper, the vertical displacement for the low potential does not change from positive to negative. In addition, the results on the droplet deformation of different pin potentials are shown in Figure 9. The horizontal component of the DEP force causes the horizontal displacement of the droplet. As can been seen, because the non-uniform DEP force increases with the increase in the pin electrode potential at the same pin-plate electrode distance, the offset displacement is increased with the increase in the potential. The closer the droplet moves to the pin electrode, the greater the effect of the non-uniform DEP force, resulting in a rapid increase in droplet offset displacement, such as the droplet for the potential of 20 kV.

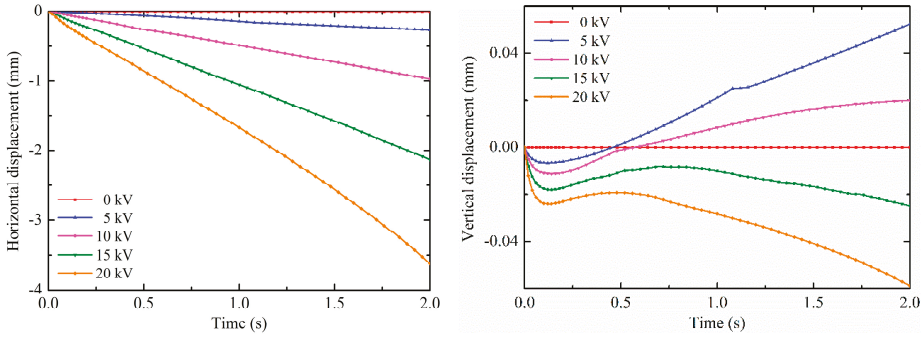

Figure 8. Effects of the potential on (**a**) the horizontal displacement and (**b**) vertical displacement.

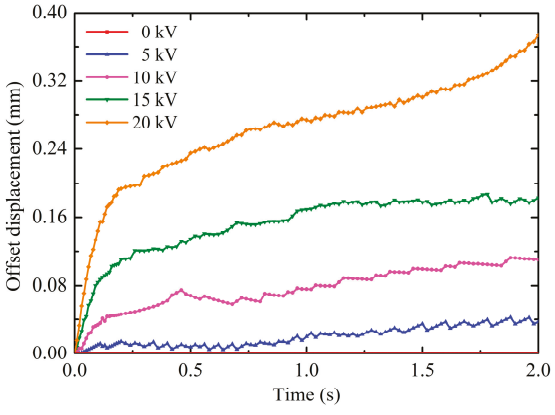

Figure 9. Effects of the potential on the offset displacement.

3.3. Effects of the Contact Angle

The contact angle is a measure of substrate wettability, that is, hydrophilic or hydrophobic. Typically, the contact angle less than 90° is referred to as hydrophilic; the contact angle greater than 90° is referred to as hydrophobic; and the contact angle greater than 150° is referred to as superhydrophobic. The contact angle is related to the surface tension and the substrate adhesion; thus, it can also affect the droplet deformation motion under non-uniform electric fields. Therefore, the effect of the contact angle is discussed in this section. The pin potential is set to 15 kV and the droplet volume is 4 mm^3. According

to Equation (18), the droplet radii are calculated as shown in Table 2. The results on the droplet motion of different contact angles are shown in Figure 10a,b. For ease of analysis, the calculated contact angles are divided into two categories: hydrophobic, which is 90° and 120°, and superhydrophobic, which is 150°, 160° and 170°. It is observed from Figure 10a that the horizontal displacement is increased by increasing the contact angle. The larger the contact angle, the more obvious the effect of non-uniform electric fields, as evidenced by the gap of the horizontal displacement curve. This is because the droplet with larger contact angles has the smaller contact area with the substrate surface, which means that the substrate adhesion is relatively small. Under the effect of same non-uniform electric fields, the droplet with larger contact angles are more susceptible to motion. Therefore, the horizontal displacement is increased with increasing the contact angle. Moreover, as shown in Figure 8b, there are great differences in the patterns of the droplet's vertical displacement for different potentials. For the droplet with hydrophobic contact angles, 90° and 120°, the vertical displacement direction first changes at about 0.14 s and 0.21 s, respectively. The vertical displacement of the droplet with the contact angle of 90° changes from negative to positive after the revert. For the droplet with superhydrophobic contact angles, 150°, 160° and 170°, the vertical displacement direction first changes at about 0.13 s, 0.15 s and 0.18 s, respectively. The droplet vertical displacement is always negative. The smaller the contact angle, the lower the vertical component of the non-uniform DEP force, and the smaller the binding effect on the droplet. Therefore, the vertical displacement of the droplet with the contact angle of 90° changes from negative to positive after the revert. The stronger vertical component of the non-uniform DEP force results in the large revert vertical displacement and longer revert duration time, like d_y (90°) < d_y (120°), d_y (150°) < d_y (160°) < d_y (170°). The reason why all contact angles cannot be compared is that there is an important factor affecting the droplet motion and deformation when the contact angle changes to cause a large change in the droplet radius, the additional pressure, $\Delta p = 2\alpha/R$. It is caused by the interfacial tension and toward the inside of the droplet. Among them, the radius of the droplet with contact angles of 90° and 120° varies greatly, so that the effect of the additional pressure is quite different from the other three. Furthermore, the results on the droplet deformation of different contact angles are shown in Figure 11. As can been seen, the same as the comparison of the horizontal displacement between contact angles, the offset displacement is increased with increasing the contact angle. As mentioned above, the droplets are more susceptible to motion and deformation as the contact angle increases under the effect of non-uniform electric fields.

Table 2. Relations between droplet contact angles and radius at the same droplet of 4 mm^3.

θ (°)	90	120	150	160	170
R (mm)	1.2407	1.0421	0.9890	0.9856	0.9848

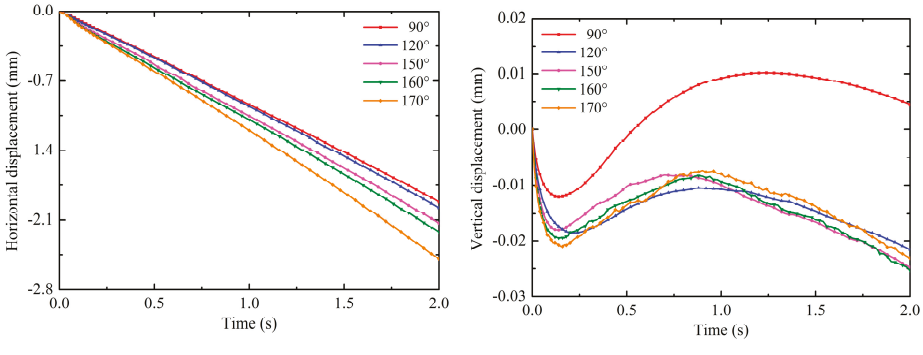

(**a**) (**b**)

Figure 10. Effects of the contact angle on (**a**) the horizontal displacement and (**b**) vertical displacement.

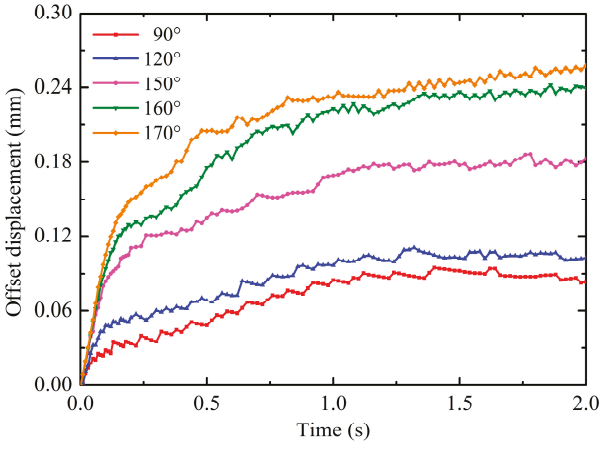

Figure 11. Effects of the contact angle on the offset displacement.

3.4. Effects of the Droplet Volume

The droplet volumes on substrate surfaces are not all the same in practice; therefore, they can also affect the droplet deformation and motion under non-uniform electric fields. For this reason, the effects of the droplet volume are discussed in this section. The pin potential is set to 15 kV and the contact angle is maintained at 150°. The droplet radius is calculated according to Equation (18) at different volumes as shown in Table 3. The results on the droplet motion of different droplet volumes are shown in Figure 12a,b. It is observed from Figure 12a that the horizontal displacement is increased as the droplet volume increases. The enhancement effect of non-uniform electric fields decreases as the droplet volume increases, as evidenced by the gap of the horizontal displacement curve. This is because the non-uniform DEP force is increased as the droplet volume increases, which has more polarization charges. On the other hand, the additional pressure decreases with increasing the droplet volume, which has larger droplet radii. At this time, the increase of the substrate adhesion due to the increase of the droplet volume can be ignored, so that the droplet with larger volume has larger horizontal displacement under the effect of the same electric fields. Moreover, as shown in Figure 12b, there are some differences in the patterns of the droplet vertical displacement for different droplet volumes. The vertical displacement of the first revert of the droplet increases as the droplet volume increases. For the small droplet volume, the droplet vertical displacement can change from negative to positive, such as the droplet with the volume of 2 mm^3 and 3 mm^3. For the droplet with the volume of 4 mm^3, 5 mm^3 and 6 mm^3, the droplet vertical displacement are always negative. This is because the effect of gravity decreases as the droplet volume decreases, the release of the surface tension caused by the droplet deformation is sufficient to cause the droplet vertical displacement to change from negative to positive. Furthermore, the results on the droplet deformation of different droplet volumes are shown in Figure 13. As can been seen, the same as the comparison of the horizontal displacement between droplet volumes, the offset displacement is increased with increasing the droplet volume. As mentioned above, the droplets are more susceptible to motion and deformation as the contact angle increases under the effect of non-uniform electric fields. As mentioned above, the droplets are more susceptible to motion and deformation as the droplet volume increases under the effect of non-uniform electric fields.

Table 3. Relations between droplet volumes and radius at the same contact angle of 150°.

Z (mm^3)	2	3	4	5	6
R (mm)	0.7850	0.8986	0.9890	1.0654	1.1321

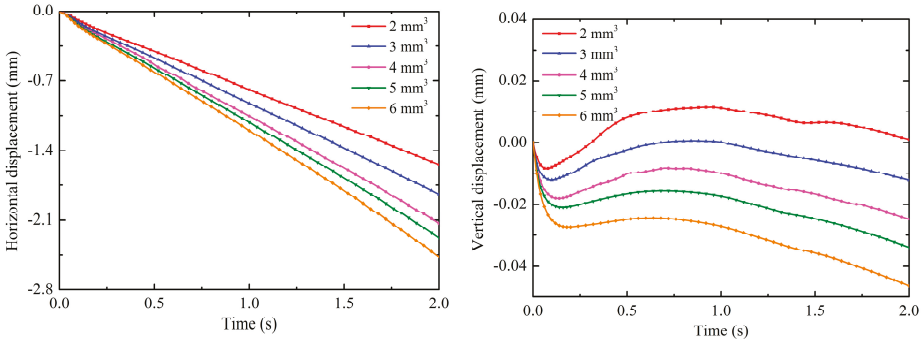

Figure 12. Effects of the droplet volume on (**a**) the horizontal displacement and (**b**) vertical displacement.

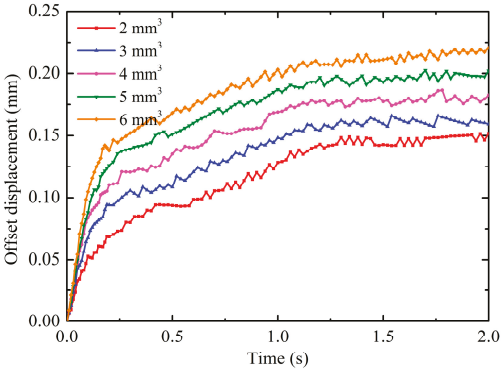

Figure 13. Effects of the droplet volume on the offset displacement.

4. Conclusions

In this study, the electrohydrodynamics phenomena of sessile droplets on hydrophobic surfaces under non-uniform electric fields are simulated using the phase field method. Dynamics behaviors of the electro-driven deformation and motion of water droplets in the oil phase are analyzed. The results show that under the effect of non-uniform DEP force, the droplet moves along the substrate surface to the direction of increasing electric field strength, and is accompanied with a certain deformation of the offset displacement. More specifically, the horizontal displacement of the droplet increases with time; and a revival phenomenon occurs in the direction of the vertical displacement; for droplet offset displacement, it first increases sharply and then slowly rises to a relatively stable value. The slight oscillation phenomenon in the horizontal offset of the droplet always occurs due to the deformation relaxation and its own inertia. In addition, the effect of pin electric potentials, surface contact angles and droplet volumes on the droplet motion and deformation are also studied and compared. The results show that the horizontal displacement and offset displacement of the droplet increase with the increase of pin potentials, contact angles and droplet volumes. For the vertical displacement, it is found that during the first revert process, the release of the surface tension caused by the droplet deformation can make the droplet with low potentials, small contact angles or small droplet volumes span from negative to positive. On the contrary, due to the effect of the non-uniform DEP force, the vertical displacement of the droplet with high potentials, and larger contact angles or large droplet volumes is always negative although it reverts. The results obtained in this study will be helpful for the future

operation encountered in the electro-driven deformation and motion of droplets on hydrophilic and hydrophobic surfaces.

Author Contributions: S.L. and J.L. performed simulations and discussions; J.L. wrote the manuscript; S.L. revised and polished the manuscript.

Funding: This work was supported by the Hubei Provincial Major Program of Technological Innovation (No. 2017AAA121).

Conflicts of Interest: The authors declare no conflict of interest.

References

1. Chen, L.; Wang, X.; Yang, T.; Ping, H.; Bennett, P.; Zheng, Z.; Yang, Q.B.; Perrie, W.; Edwardson, S.P.; Dearden, G.; et al. Superhydrophobic micro-nano structures on silicone rubber by nanosecond laser processing. *J. Phys. D Appl. Phys.* **2018**, *51*, 445301. [CrossRef]
2. Li, J.; Wei, Y.; Huang, Z.; Wang, F.; Yan, X.; Wu, Z. Electrohydrodynamic behavior of water droplets on a horizontal super hydrophobic surface and its self-cleaning application. *Appl. Surf. Sci.* **2017**, *403*, 133–140. [CrossRef]
3. Fürstner, R.; Barthlott, W.; Neinhuis, C.; Walzel, P. Wetting and self-cleaning properties of artificial superhydrophobic surfaces. *Langmuir* **2005**, *21*, 956–961. [CrossRef] [PubMed]
4. Wang, N.; Xiong, D.S.; Li, M.T.; Deng, Y.L.; Shi, Y.; Yang, K. Superhydrophobic surface on steel substrate and its anti-icing property in condensing conditions. *Appl. Surf. Sci.* **2015**, *355*, 226–232. [CrossRef]
5. Miljkovic, N.; Enright, R.; Nam, Y.; Lopez, K.; Dou, N.; Sack, J. Jumping-droplet-enhanced condensation on scalable superhydrophobic nanostructured surfaces. *Nano Lett.* **2013**, *13*, 179–187. [CrossRef]
6. Ölçeroğlu, E.; Hsieh, C.Y.; Rahman, M.M.; Lau, K.K.S.; Carthy, M.M. Full-field dynamic characterization of superhydrophobic condensation on biotemplated nanostructured surfaces. *Langmuir* **2014**, *30*, 7556–7566. [CrossRef]
7. Zeng, J.; Korsmeyer, T. Principles of droplet electrohydrodynamics for lab-on-a-chip. *Lab. Chip* **2004**, *4*, 265–277. [CrossRef]
8. Boreyko, J.B.; Zhao, Y.; Chen, C.H. Planar jumping-drop thermal diodes. *Appl. Phys. Lett.* **2011**, *99*, 234105. [CrossRef]
9. Tian, L.; Gao, M.; Gui, L. A Microfluidic Chip for Liquid Metal Droplet Generation and Sorting. *Micromachines* **2017**, *8*, 39. [CrossRef]
10. Mugele, F.; Baret, J.C. Electrowetting: From basics to applications. *J. Phys. Condens. Matter.* **2005**, *17*, R705–R774. [CrossRef]
11. Nam, Y.; Kim, H.; Shin, S. Energy and hydrodynamic analyses of coalescence-induced jumping droplets. *Appl. Phys. Lett.* **2013**, *103*, 161601. [CrossRef]
12. Liu, X.; Cheng, P.; Quan, X. Lattice Boltzmann simulations for self-propelled jumping of droplets after coalescence on a superhydrophobic surface. *Int. J. Heat Mass Tran.* **2014**, *73*, 195–200. [CrossRef]
13. Takeda, K.; Nakajima, A.; Murata, Y.; Hashimoto, K.; Watanabe, T. Control of water droplets on superhydrophobic surfaces by static electric field. *Jpn. J. Appl. Phys.* **2002**, *41*, 287–291. [CrossRef]
14. Sakai, M.; Kono, H.; Nakajima, A.; Sakai, H.; Abe, M.; Fujishima, A. Water droplets' internal fluidity during horizontal motion on a superhydrophobic surface with an external electric field. *Langmuir* **2010**, *26*, 1493–1495. [CrossRef] [PubMed]
15. Zhu, Y.; Haji, K.; Otsubo, M.; Honda, C.; Hayashi, N. Electrohydrodynamic behaviour of water droplet on an electrically stressed hydrophobic surface. *J. Phys. D Appl. Phys.* **2016**, *39*, 1970. [CrossRef]
16. Wei, Y.; Li, J.; Huang, Z.; Yan, X. Electrical driven rolling behavior of water droplet on a super hydrophobic surface. In Proceedings of the ICHVE International Conference on High Voltage Engineering and Application, Poznan, Poland, 8–11 September 2014; pp. 1–4.
17. Adamiak, K. Capillary and electrostatic limitations to the contact angle in electrowetting-on-dielectric. *Microfluid. Nanofluidics* **2006**, *2*, 471–480. [CrossRef]
18. Bacri, J.C.; Salin, D.; Massart, R. Study of the deformation of ferrofluid droplets in a magnetic field. *J. Phys. Lett.* **1982**, *43*, 179–184. [CrossRef]

19. Adzima, B.J.; Velankar, S.S. Pressure drops for droplet flows in microfluidic channels. *J. Micromech. Microeng.* **2006**, *16*, 1504–1510. [CrossRef]
20. Moghtadernejad, S.; Tembely, M.; Jadidi, M.; Esmail, N.; Dolatabadi, A. Shear driven droplet shedding and coalescence on a superhydrophobic surface. *Phys. Fluids* **2015**, *27*, 032106. [CrossRef]
21. Moghtadernejad, S.; Mohammadi, M.; Jadidi, M.; Tembely, M.; Dolatabadi, A. Shear Driven Droplet Shedding on Surfaces with Various Wettabilities. *SAE Int. J. Aerosp.* **2013**, *6*, 459–464. [CrossRef]
22. Barwari, B.; Burgmann, S.; Janoske, U. Hydrodynamic instabilities of adhering droplets due to a shear flow in a rectangular channel. *Chem. Ing. Tech.* **2019**, *91*, 991–1000. [CrossRef]
23. Karsch, S.; Düsterer, S.; Schwoerer, H.; Ewald, F.; Habs, D.; Hegelich, M. High-intensity laser induced ion acceleration from heavy-water droplets. *Phys. Rev. Lett.* **2003**, *91*, 015001. [CrossRef] [PubMed]
24. Rowland, S.M.; Lin, F.C. Stability of alternating current discharges between water drops on insulation surfaces. *J. Phys. D Appl. Phys.* **2006**, *39*, 3067–3076. [CrossRef]
25. Nudurupati, S.; Janjua, M.; Aubry, N.; Singh, P. Concentrating particles on drop surfaces using external electric fields. *Electrophoresis* **2008**, *29*, 1164–1172. [CrossRef] [PubMed]
26. Liu, Y.; Kong, X.; Wu, Y.; Du, B. Dynamic behavior of droplets and flashover characteristics for CFD and experimental analysis on SiR composites. *IEEE Access* **2019**, *31*, 052107. [CrossRef]
27. Nakajima, A. Design of hydrophobic surfaces for liquid droplet control. *NPG Asia Mater.* **2011**, *3*, 49–56. [CrossRef]
28. Li, J.; Wei, Y.; Huang, Z.; Wang, F.; Yan, X.Z. Investigation of the electric field driven self-propelled motion of water droplets on a superhydrophobic surface. *IEEE Trans. Dielect. Electr. Insul.* **2016**, *23*, 3007–3015. [CrossRef]
29. Bansal, L.; Sanyal, A.; Kabi, P.; Pathak, B.; Basu, S. Engineering interfacial processes at mini-micro-nano scales using sessile droplet architecture. *Langmuir* **2018**, *34*, 8423–8442. [CrossRef]
30. Lin, Y. Two-phase electro-hydrodynamic flow modeling by a conservative level set model. *Electrophoresis* **2013**, *34*, 736–744. [CrossRef]
31. Barman, J.; Shao, W.; Tang, B.; Yuan, D.; Groenewold, J.; Zhou, G.F. Wettability manipulation by interface-localized liquid dielectrophoresis: Fundamentals and applications. *Micromachines* **2019**, *10*, 329. [CrossRef]
32. Zhou, T.; Yeh, L.H.; Li, F.C.; Mauroy, B.; Joo, S.W. Deformability-based electrokinetic particle separation. *Micromachines* **2016**, *7*, 170. [CrossRef] [PubMed]
33. Du, W.; Chaudhuri, S. A multiphysics model for charged liquid droplet breakup in electric fields. *Int. J. Multiph. Flow* **2017**, *90*, 46–56. [CrossRef]
34. Taylor, G.I. The Viscosity of a fluid containing small drops of another fluid. *Proc. R. Soc. Lond. Ser. A* **1932**, *138*, 41–48. [CrossRef]
35. Vlahovska, P.M. Electrohydrodynamics of Drops and Vesicles. *Annu. Rev. Fluid Mech.* **2019**, *51*, 305–330. [CrossRef]
36. Ji, X.; Xu, L.; Zhou, T.; Shi, L.; Deng, Y.; Li, J. Numerical investigation of DC dielectrophoretic deformable particle–particle interactions and assembly. *Micromachines* **2018**, *9*, 260. [CrossRef] [PubMed]

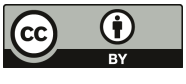

micromachines

MDPI

Article

Characterization of the Dielectrophoretic Response of Different Candida Strains Using 3D Carbon Microelectrodes

Monsur Islam [1,2], Devin Keck [1], Jordon Gilmore [1,3] and Rodrigo Martinez-Duarte [1,*]

[1] Multiscale Manufacturing Laboratory, Mechanical Engineering Department, Clemson University, Clemson, SC 29634, USA; monsur.islam@kit.edu (M.I.); dkeck@g.clemson.edu (D.K.); jagilmo@clemson.edu (J.G.)
[2] Institute for Microstructure Technology, Karlsruhe Institute of Technology, Hermann-von-Helmholtz-Platz 1, 76344 Eggenstein-Leopoldshafen, Germany
[3] Department of Bioengineering, 301 Rhodes Engineering Research Center, Clemson University, Clemson, SC 29634, USA
* Correspondence: rodrigm@clemson.edu; Tel.: +1-864-656-5634

Received: 3 February 2020; Accepted: 26 February 2020; Published: 28 February 2020

Abstract: Bloodstream infection with *Candida* fungal cells remains one of the most life-threatening complications among hospitalized patients around the world. Although most of the cases are still due to *Candida albicans*, the rising incidence of infections caused by other *Candida* strains that may not respond to traditional anti-fungal treatments merits the development of a method for species-specific isolation of *Candida*. To this end, here we present the characterization of the dielectrophoresis (DEP) response of *Candida albicans*, *Candida tropicalis* and *Candida parapsilosis*. We complement such characterization with a study of the *Candida* cells morphology. The *Candida* strains exhibited subtle differences in their morphology and dimensions. All the *Candida* strains exhibited positive DEP in the range 10–500 kHz, although the strength of the DEP response was different for each *Candida* strain at different frequencies. Only *Candida tropicalis* showed positive DEP at 750 kHz. The current results show potential for manipulation and enrichment of a specific *Candida* strain at specific DEP conditions towards aiding in the rapid identification of *Candida* strains to enable the effective and timely treatment of *Candida* infections.

Keywords: characterization; dielectrophoresis; carbon electrodes; three-dimensional (3D); diagnostics; *Candidiasis*

1. Introduction

Candida species are one of the most prevalent fungal pathogens in hospitals around the world. In the United States alone, 5%–10% of hospitalized patients will acquire a nosocomial infection and 80% of such infections are caused by *Candida* species [1]. As early as 1995, *Candida* species became recognized as the fourth most common cause of nosocomial bloodstream infections in the United States, and most recently reported as the 3rd most common cause of nosocomial bloodstream infections in the intensive care unit (ICU) [2]. Concerningly, nosocomial bloodstream infections from *Candida* have a crude mortality rate of 39% overall, and this figure can be as high as 47% for patients infected in the ICU [2]. More than 17 different *Candida* species have been identified as responsible for invasive candidiasis (IC), an umbrella term referring to various severe diseases resulting from *Candida* infection [3]. While *Candida albicans* remains the most frequently isolated *Candida* strains from infected blood [4], the incidence of the infections caused by other species has increased significantly worldwide. For example, a survey in European countries showed that around 50% infection was caused by *Candida albicans*, whereas incidence rates were 14% for each *Candida glabrata* and *Candida parapsilosis*, 7% for *Candida tropicalis*

and 2% for *Candida krusei* [5]. In Chile, the most frequently isolated non-*albicans* species was *Candida parapsilosis*, followed by *Candida tropicalis* and *Candida glabrata* [6]. The emergence of non-*albicans* species as pathogens is concerning because many of them do not respond to conventional anti-fungal therapy, which are generally targeted for *Candida albicans*. For example, *Candida tropicalis* is less susceptible to fluconazole, a common anti-fungal medication, when compared to *Candida albicans* [7]. Hence, with an increased incidence of infections with different *Candida* species, there is a need for a method that allows for rapid identification of the *Candida* species, so that timely measures can be taken towards species-specific treatment of *Candida* infections.

Dielectrophoresis (DEP) is a technique that offers the potential for sorting different *Candida* species in a label-free fashion towards a rapid and affordable assay. DEP is a relatively simple procedure that works by exploiting the specific response of different cells to an electric field gradient [8–12], and has been used for the manipulation, separation, and enrichment of many bioparticles that include bacteria and other bloodborne pathogens [13–20] including *Candida albicans* [21–27]. The fact that DEP has been demonstrated in the sorting of cells featuring minor observable differences between them [9,28–30] encourages the study of DEP to isolate specific *Candida* strains. However, till date, no DEP characterization of *Candida* strains other than *Candida albicans* is available. Hence, there is a knowledge gap preventing the wider use of DEP as a method to sort *Candida* strains. Methodical characterization of the DEP response of *Candida* strains can enable the use of different DEP platforms towards a more rapid way to identify the type of *Candida* causing an infection and an informed approach to combat it. For example, specific *Candida* strains can be isolated and enriched from a dilute sample in a timely manner in a DEP-based sample preparation protocol previous published by the authors [8], which can increase sensitivity of common detection techniques [31].

In this work, we present the morphological characteristics and a first study on the DEP response of three different *Candida* strains: *Candida albicans*, *Candida parapsilosis*, and *Candida tropicalis*; which are three of the most frequently isolated *Candida* strains from infected samples. We used 3D carbon microelectrode arrays to obtain the results presented here due to their improved performance over more traditional planar electrodes [13,32,33].

2. Materials and Methods

2.1. Cell Culture and Sample Preparation

Candida albicans (ATCC 18804), *Candida parapsilosis* (ATCC22019), and *Candida tropicalis* (ATCC750) were cultured in dynamic conditions at 37 °C and 215 rpm in yeast malt broth (YMB) and passed regularly to maintain a healthy culture. To prepare the sample for DEP experiments, 100 µL of 4-day old cell culture were mixed with 2.5 mL of an optimized DEP buffer solution composed of 8.6 wt% sucrose, 0.3 wt% dextrose and 0.1 wt% bovine serum albumin to achieve a concentration of around 10^6 cells/mL. The electrical conductivity of this DEP buffer solution was 20 µS/cm. Cells were then pelleted through centrifugation at 5000 rpm for 5 min and then resuspended into fresh DEP buffer solution. This centrifugation and re-suspension protocol were repeated three times to ensure complete removal of any remaining YMB culture media.

2.2. Device Fabrication

The microfluidic DEP device used in this study featured 3D carbon microelectrode arrays. The fabrication of the carbon microelectrodes has been reported several times in our previous work [8–12,31,34–37]. Briefly, the fabrication process included two-step photolithography of SU-8 (Gersteltec, Switzerland), a negative tone photoresist, on a Si/SiO_2 substrate. The SU-8 microstructures were carbonized at 900 °C in a nitrogen environment using a heating rate of 5 °C/min to obtain carbon microstructures. The resultant carbon electrode array (3161 electrodes total) featured intercalated 3D electrodes as shown in Figure 1a; each carbon microelectrode had a height of 100 µm and diameter of 50 µm while the spacing between them was around 58 µm in all directions. A thin layer of SU-8 was

then patterned around the 3D carbon electrodes to insulate the connecting planar leads and planarize the channel bottom. On a parallel process, a 1.8 mm-wide and 32 mm-long channel was patterned from 127 µm-thick sheet of double sided pressure sensitive adhesive, or PSA (Switchmark 212R, Flexcon, Spencer, MA, USA), using xurography and adhered to a previously machined polycarbonate (PC) piece. The details of this method are detailed in our previous publication [38]. The DEP chip was then assembled by manually positioning the PC/PSA arrangement around the carbon microelectrode array, followed by sealing using a rolling press. The cross-section of the assembly of the microfluidic device is illustrated in Figure 1b.

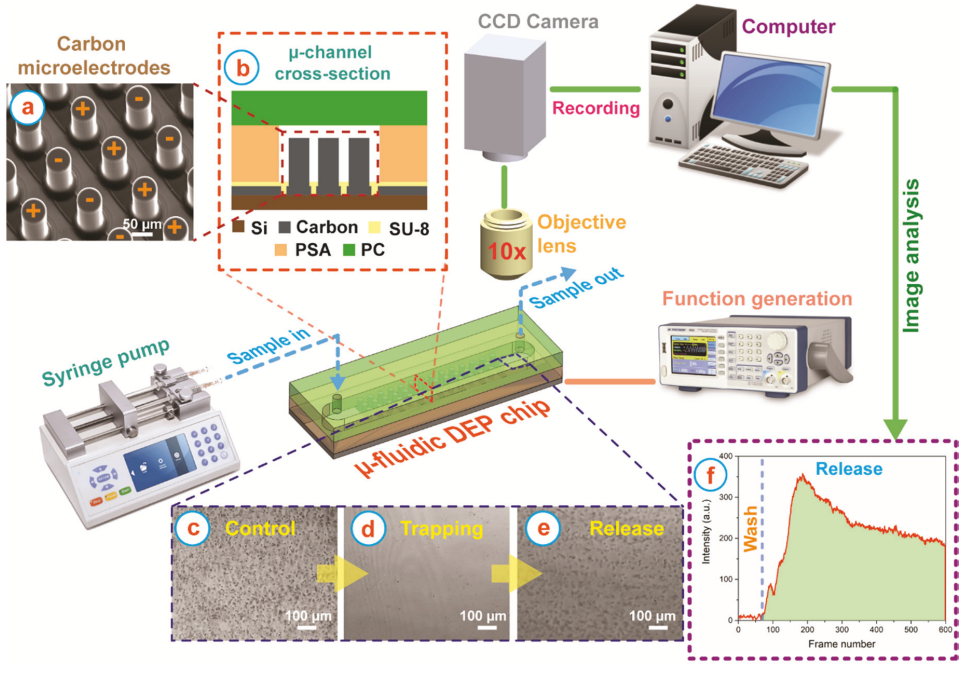

Figure 1. Experimental set up for the characterization of DEP response of the *Candida* strains using 3D carbon microelectrodes. (**a**) Scanning Electron Microscope (SEM) image of the 3D carbon microelectrodes. (**b**) Cross section of the microchannel showing the different elements of the DEP device. The polarity of the 3D carbon electrodes to induce the non-uniform electric field for DEP is also illustrated. The region of interest (ROI) during experiments was immediately after the last column of the electrode array. The ROI for (**c**) the control experiment (no field applied); (**d**) during the trapping stage when cells displayed a strong DEP trapping behavior; and (**e**) immediately after turning the field off to release any previously trapped cells. The black dots in these images are *Candida* cells. (**f**) An indicative plot of the normalized intensity obtained after computational analysis of the ROI throughout an experiment. The blue dashed line denotes the time when the electric field was turned off, and marks the transition between the wash and release stages. The area under the curve in the "Release" section is identified by the green area, which is reported here as the DEP trapping response of the cells in each experiment. At least three experiments were conducted for each data point, i.e., a given *Candida* strain and frequency. See text for further details.

2.3. Experimental Protocol

Experiments revolved around characterizing: (1) cell morphology and (2) DEP response. Few studies are available regarding the morphological characterization of few *Candida* strains [39,40] and a morphology study was performed here to better understand how the unique morphology of the

cells from each species may contribute to a difference in their response to an electric field. To this end, 4-day cell cultures were observed under an optical microscope (Nikon Eclipse LV100, Tokyo, Japan) to measure the dimensions of at least 30 cells per strain. Images were recorded through an Andor Zyla CMOS camera.

The experimental set up for characterization of the DEP response of the cells at different frequencies is illustrated in Figure 1. The experimental protocol followed can be separated into 3 stages: (1) cell trapping, (2) washing, and (3) cell release. Of note, cell release only occurred in the frequencies that lead to cell trapping due to positive DEP: this is when the cells were attracted to the regions of high field gradient that are around the carbon electrodes in this work. The desired flow rate in the experimental device was implemented using a syringe pump (FusionTouch 200, Chemyx, Stafford, TX, USA). The electrode array was polarized as illustrated in Figure 1a using a function generator (BK Precision 4052, Yorba Linda, CA, USA). During the first experimental stage, trapping, 20 μL of the sample containing the cells was flowed at 10 μL/min through the electrode array polarized at specific frequency (10 kHz–1 MHz) and magnitude of 20 V_{pp}. In the second stage, washing, a cell-free DEP buffer solution was flowed with a flow rate of 10 μL/min through the still polarized electrode array for 5 min to wash any non-trapped cells. In the last stage, release, the polarizing signal was turned off while maintaining the same flow rate. This last stage lasted for 110 s. The entire experiment was monitored through a 10× objective lens in a Nikon Eclipse LV100 microscope. However, only the release stage and the last 10 s of the wash stage were recorded using an Andor Zyla CMOS camera running at a frame rate of 5 frames per second. Hence, each of the video recordings used for data analysis was 120 s, or 600 frames, long. The electric field was turned off at frame 50.

2.4. Data Analysis

Images of cell cultures were manually analyzed in the NIS Element Basic software native to the microscope to measure the major (x) and minor axes (y) of at least 30 cells per strain. The major and minor axes were identical for a perfect circle. The average values and standard deviation for all measurement were calculated using built-in mathematical functions in Microsoft Excel.

The videos obtained during DEP experiments were analyzed with ImageJ (National Institutes of Health, Bethesda, MD, USA) to plot the average pixel intensity at a region of interest (ROI), with area 830 μm × 700 μm and established immediately after the electrode array, throughout each experiment done for a particular cell strain and frequency of interest (Figure 1c–e). The analysis was designed such that a difference in the intensity of the ROI before and after turning the field off can be directly correlated to the strength of the trapping DEP force acting on a given sample at that specific frequency. To this end, the average intensity in the ROI was measured for a total of 600 frames, where frames 1–50 were for the frames recorded before turning the field off and frame 51–600 were recorded after the field was turned off. In order to properly isolate the DEP response from each experiment, all the intensity values after turning the field off were normalized against the average intensity before the field was off. These normalized values were then plotted using Origin Pro software (OriginPro 2016, Northampton, MA, USA). An example of such plot is shown in Figure 1f for an experiment that exhibited cell trapping and release. The larger the curve would denote a larger number of cells trapped, and released, and thus a stronger DEP trapping response. No DEP trapping resulted in no curve, i.e., a flat line after turning the field off. Here, we report the area under the curve in frames 51–600 to represent the DEP trapping response of the *Candida* strains.

3. Results

3.1. Morphology of the Candida Strains

Candida albicans (Figure 2a) displayed an average spherical morphology, which means the major axis diameter (x) of Candida albicans is identical to the minor axis diameter (y). Candida albicans featured an average diameter of $x = y = 5.12 \pm 0.75$ μm, as depicted in Figure 2d. In addition to their

largely spherical morphology, Candida albicans were commonly found in their budding phase of reproduction offering an alternate morphology of two or more attached spheres, as indicated by the dashed circles in Figure 2a. Such morphologies of the Candida albicans cells are in agreement with previous reports [39,40].

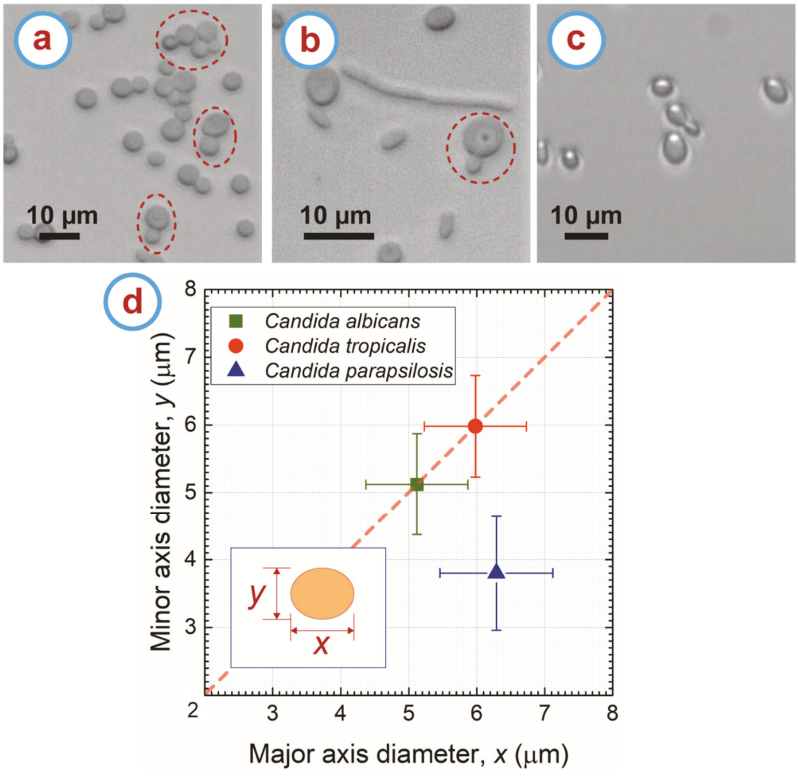

Figure 2. Morphology of (**a**) Candida albicans, (**b**) Candida tropicalis, and (**c**) Candida parapsilosis. The dashed circles indicate the budding behavior of the cells. (**d**) Plot of the major (x) vs minor diameter (y) of the different Candida strains. The diameters in the major and minor axes of a cell are illustrated in the inset. For a spherical cell, x is identical to y as denoted by the red dashed line. Each data point represents the average from at least 30 cells for each strain. The error bar represents the standard deviation from all measurements.

Candida tropicalis exhibited multiple morphologies. The first was a spherical morphology similar to that of Candida albicans but with larger diameter of $x = y = 5.98 \pm 0.75$ µm, which is consistent with previous findings by other authors [39]. As in the case for Candida albicans, Candida tropicalis also displayed spherical morphology in its budding phase of reproduction. The second shape is referred to as pseudohyphae [39,41,42] and resulted when cells began to bud but instead of separating the membranes of the cell merged to become one elongated cell. This happened multiple times in our observations, leading the pseudohyphae to have elongated ellipsoidal morphology and even beginning to resemble a tree when multiple branches of elongated ellipsoids formed. The length of the pseudohyphae ranged from 7 µm to 27 µm with an average width of 1.89 ± 0.4 µm as seen in Figure 2b.

Candida parapsilosis shown in Figure 2c displayed an ellipsoidal morphology. The diameters of each of the two axes were found to be $x = 6.29 \pm 0.83$ µm and $y = 3.8 \pm 0.84$ µm, and these values are in the range of the dimensions reported elsewhere for this strain [39]. Although less frequent

than in *Candida albicans*, *Candida parapsilosis* was also found in its budding stage but with a featuring morphology that resembled two or more attached ellipsoids instead of spheres.

3.2. Trap, Wash and Release of Candida Cells

We were able to trap, wash and release different *Candida* strains at will. Upon applying the electric field at specific frequencies, the *Candida* cells experienced positiveDEP force and got trapped in the regions of high field gradient around the carbon microelectrodes (Figure 3). Our DEP device has a capacity of trapping around 4000 cells as previously reported [8]. In our DEP experiments, the microchannel was loaded with an experimental sample featuring a cell concentration of 10^6 cells/mL, which translates to a total number of cells ~7000 present in the microchannel to start with. Hence, upon applying the electric field, our device could trap the *Candida* cells to its capacity, and the wash protocol ensured carrying away the untrapped cells, enabling purification of the trapped cells. Due to the cell trapping, no cells were seen in the flow in the recording area at the end of the electrode array before the cell release (Figure 1d). Upon turning off the electric field, the trapped cells on the electrodes were eluted through the recording area (Figure 1e). Of note, a small number of cells was observed to be non-specifically adhered to the electrodes after turning off the polarizing signal. The number of such cells was significantly smaller than those released. Furthermore, this non-specific adhesion was observed for all strains studied in this work. Hence, the effect of such adhesion on the characterization of the DEP response for the different strains, and the differences between them, was deemed not significant. This non-specific adhesion may be detrimental to future assays where the recovery of targeted cells would be required but this out of the scope of the work presented here.

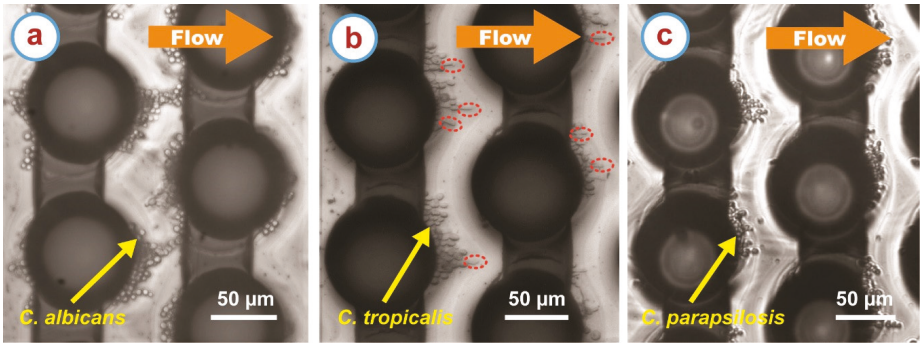

Figure 3. Examples of trapping of (**a**) *Candida albicans*, (**b**) *Candida tropicalis*, and (**c**) *Candida parapsilosis* cells on the carbon microelectrodes (the dark circles and connecting lines) due to positive dielectrophoresis. These specific examples are when the frequency of the applied electric field is 100 kHz. Note that for *Candida tropicalis*, few short length pseudohyphae cells were also trapped and indicated with the red dotted ellipse in (b).

3.3. DEP Response of the Candida Strains

The DEP trapping response for the different *Candida* species characterized in this work is plotted in Figure 4. *Candida albicans* and *Candida parapsilosis* exhibited a trapping DEP response in the frequency range 10–500 kHz. *Candida tropicalis* also showed a trapping positive DEP response at 750 kHz. No positive DEP was observed beyond 750 kHz for any of the *Candida* strains. Although all the three strains showed positive DEP response in the range 10–500 kHz, the strength of the DEP response was different for each strain. The highest DEP trapping response for *Candida tropicalis* and *Candida albicans* was at 50 kHz, whereas *Candida parapsilosis* showed the peak DEP response at 100 kHz. *Candida albicans* exhibited relatively weak DEP trapping compared to the other two strains of *Candida* in the frequency

range 50–500 kHz. However, at 10 kHz, the positive DEP response was strongest for *Candida albicans* among the three *Candida* strains.

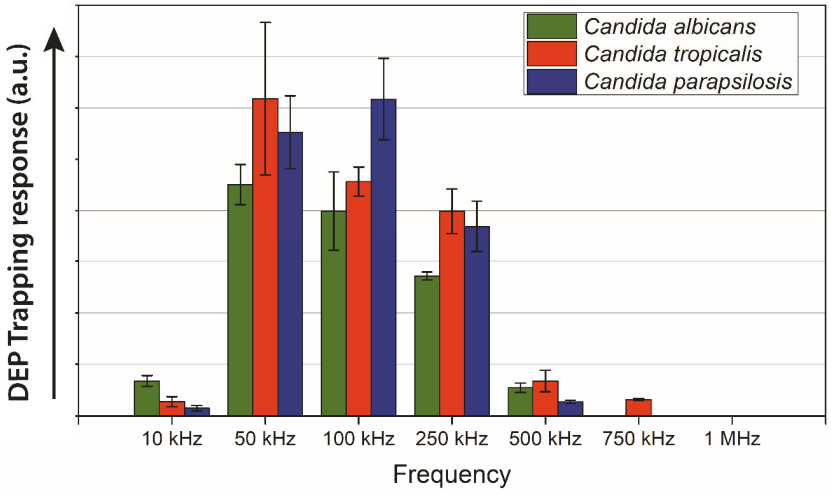

Figure 4. The DEP trapping response of *Candida albicans*, *Candida tropicalis*, and *Candida parapsilosis* at frequencies ranging from 10 kHz to 1 MHz. At least three experiments were carried out for each data point, bars denote the average values while the bars represent standard deviation. The upward arrow indicates that the higher value represents higher cell trapping due to DEP.

4. Discussion

The *Candida* strains studied here showed subtle differences in cell morphologies. Figure 2d shows how the cells dimensions overlap for all the strains, making it difficult to sort *Candida* strains solely based on their sizes. The dimensional overlap is more prevalent when comparing *Candida albicans* and *Candida tropicalis*. Moreover, both *Candida albicans* and *Candida tropicalis* exhibited spherical morphology, further complicating differentiation based on shape. Although pseudohyphae forms of *Candida tropicalis* exhibits different shape than the spherical cells, *Candida albicans* is also known to transform to hyphal state during infectious process [43–45] and this must be taken into account even when we did not observe hyphal forms in our handling of *C. albicans*. Although size and shape are not enough for cell separation, these can be complemented with the DEP response of specific strains.

All the *Candida* strains exhibited positive DEP response in the frequency range 10–500 kHz. However, *Candida tropicalis* and *Candida parapsilosis* consistently exhibited higher positive DEP response than *Candida albicans* in the frequency range 50–250 kHz. Such behavior might be a result of the budding behavior of *Candida albicans*. *Candida albicans* were more commonly found in their budding stage as a group of multiple attached spheres. The drag force created by a conglomeration of attached spherical entities would have a higher magnitude than the drag force of a smaller spherical entity [46]. If the drag force becomes larger than the DEP force created from the electrical field gradient, the cells would not attract to the electrodes [30]. However, at 10 kHz, different DEP behavior was observed, where *Candida albicans* exhibited strongest DEP response. Our hypothesis is that different *Candida* strains might feature different cell membrane potential, which resulted in different behaviors in different frequency range. However, the cell membrane potentials for *Candida* strains are unknown at present. A separate, more extensive study to determine the cell membrane potential of these *Candida* strains is ongoing and will be reported in a future work.

Candida tropicalis shows both spherical and pseudohyphae morphology in the media studied here as shown in Figure 2b. However, mostly spherical *Candida tropicalis* cells were observed on the carbon

microelectrodes during trapping (Figure 3b). A small amount of short ranged pseudohyphae cells with length ranging from 7 μm to 12 μm were also trapped on the carbon electrodes. No long range pseudohyphae cells were trapped on the carbon microelectrodes. We speculate that as the *Candida tropicalis* cells transforms to pseudohyphae cells, the cell membrane potential might also change. The difference in the cell membrane potential of the spherical and pseudohyphae cells might be in direct proportion of the length of the pseudohyphae cells. For example, the short pseudohyphae cells might feature a cell membrane potential close to that of the spherical cells. This may lead to trapping of short length pseudohyphae cells in the current DEP conditions along with the spherical cells, whereas the long pseudohyphae cells did not experience any positive DEP force and flow with media during the washing step.

The current results indicate a potential for DEP to be utilized to distinguish between different types of *Candida* strains from an already purified blood sample and help diagnose the specific strain causing disease. One of the important results in this direction is that *Candida tropicalis* was the only *Candida* strain to show a positive response at 750 kHz. In terms of strain identification, a sample could be subjected to an electric field with frequency of 750 kHz to only trap *C. tropicalis* while eluting *Candida albicans* and *Candida parapsilosis*. Further separation between *C. albicans* and *C. parapsilosis* could be done in a second stage, i.e., polarized at 10 kHz to emphasize trapping of *C. albicans*, in a multi-stage carbon-electrode DEP device as previously reported [47]. Furthermore, each *Candida* strain exhibited a difference in the strength of the positive DEP response, which can be also utilized for diagnosis purposes. This characteristic could be used in multiple ways. One potential method would be to tailor the strength of the electric field within the DEP device to be strong enough to attract one type of cell, but too weak to trap another *Candida* strains allowing these *Candida* strains to be eliminated as the cause of infection. The trap and wash protocol demonstrated here can be used to enrich desired *Candida* cells in a small sample volume for further analysis. Using the current DEP set up, it is possible to enrich a cell sample up to 150 folds within a few hours as we previously reported [8]. This rich enrichment can lead to a timely detection of the *Candida* cells by enabling concentrated and purified samples to improve the sensitivity of common detection protocols such as PCR [31]. Another approach might be using streaming DEP for rapid cell sorting, where cells are focused into specific streams of elution instead of trapping cells on the electrodes. Streaming DEP can enable focusing of different *Candida* cells into different streams utilizing the different strength of DEP on the different *Candida* strains [11,30]. The streams can be collected separately at the outlet of the microfluidic system and used for cell detection. Such timely detection of the *Candida* cells can enable timely initiation of medical treatment specific to the responsible *Candida* strains.

It should be noted that the value of DEP in a practical solution for rapid diagnosis of *Candida* infection is envisioned to be the isolation of different strains of *Candida* from each other, but not directly from blood. A multi-stage protocol is preferred when attempting to isolate potential targets of interest from a blood sample in clinical diagnostics. For example, centrifugation can enable a first rapid coarse separation of serum, buffy coat and red blood cells (RBC) [48], with the *Candida* cells expected to be in the buffy coat [49]. Buffer exchange protocols common in clinical diagnostics can then be implemented to re-suspend the cellular content of the buffy coat in a buffer optimized for DEP and any other downstream processing. Further stages in the process can include size exclusion to further isolate *Candida* cells from other blood cells until only particles that may resemble *Candida* are present in the sample. At this stage, a DEP assay for fine separation could be used to perform isolation and purification of specific strains to increase the performance of detection assays such as PCR as detailed above. If necessary, the DEP properties of blood cells with similar sizes than *Candida* have been characterized [9,50,51] and such knowledge could be used to aid in their separation. Such a multi-stage process can be readily implemented in a clinical setting. However, the details of such integrated assay are out of the scope of this paper. Of note, the integration of DEP with centrifugal microfluidics towards enabling such integrated assay has been reported by one of us [13,35].

5. Conclusions

The characterization of the morphology and DEP response of three frequently isolated *Candida* strains from infected samples: *Candida albicans*, *Candida tropicalis*, and *Candida parapsilosis* was presented here. The studied *Candida* strains only exhibited subtle differences in morphology that makes direct observation an incomplete method to sort them. 3D carbon electrode DEP was implemented for characterizing the DEP response of the *Candida* cells. All three *Candida* strains showed a strong positive DEP response in the frequency range 10–500 kHz. However, positive DEP at 750 kHz was only observed for *Candida tropicalis*. Furthermore, the *Candida* strains exhibited the positive DEP at different strength. *Candida tropicalis* and *Candida parapsilosis* showed relative high DEP response than *Candida albicans* in the frequency range 50–250 kHz, whereas at 10 kHz, the DEP response was strongest for *Candida albicans*. Together, the morphological and DEP differences among the different strains could provide a framework to enable sorting different strains.

This is to the best of our knowledge the first study reporting the DEP responses of different *Candida* strains. The current results show promise towards using DEP as a tool to enable separation of different *Candida* species. Ongoing work focuses on characterizing the membrane capacitance of the strains presented here and expanding this study to other relevant strains such as *Candida glabrata* and *Candida krusei*. The results presented here indicate that one can potentially manipulate and enrich a specific *Candida* strain at specific DEP conditions and encourages further work towards rapid identification to the enable effective and timely treatment of candidiasis.

Author Contributions: Conceptualization, M.I. and R.M.-D.; Data curation, M.I. and J.G.; Formal analysis, M.I., D.K., J.G. and R.M.-D.; Investigation, M.I. and J.G.; Methodology, M.I. and R.M.-D.; Project administration, R.M.-D.; Supervision, R.M.-D.; Validation, M.I.; Writing—original draft, M.I., D.K. and J.G.; Writing—review & editing, M.I. and R.M.-D. All authors have read and agreed to the published version of the manuscript.

Funding: This research received no external funding.

Acknowledgments: The authors thank Mark Blenner and his laboratory from the Department of Chemical & Biomolecular Engineering at Clemson University for facilitating the culture of Candida cells.

Conflicts of Interest: The authors declare no conflict of interest.

References

1. Capoor, M.R.; Nair, D.; Deb, M.; Verma, P.K.; Srivastava, L.; Aggarwal, P. Emergence of non-albicans Candida species and antifungal resistance in a tertiary care hospital. *Jpn. J. Infect. Dis.* **2005**, *58*, 344–348.
2. Sandhu, R.; Dahiya, S.; Sayal, P.; Budhani, D. Increased role of nonalbicans Candida, potential risk factors, and attributable mortality in hospitalized patients. *J. Health Res. Rev.* **2017**, *4*, 78. [CrossRef]
3. Pfaller, M.A.; Diekema, D.J.; Procop, G.W.; Rinaldi, M.G. Multicenter comparison of the VITEK 2 antifungal susceptibility test with the CLSI broth microdilution reference method for testing amphotericin B, flucytosine, and voriconazole against Candida spp. *J. Clin. Microbiol.* **2007**, *45*, 3522–3528. [CrossRef] [PubMed]
4. Chakravarthi, S.; Haleagrahara, N. A comprehensive review of the occurance and management of systematic candidiasis as an opportunistic infection. *Microbiol. J.* **2011**, *1*, 1–7.
5. Tortorano, A.M.; Kibbler, C.; Peman, J.; Bernhardt, H.; Klingspor, L.; Grillot, R. Candidaemia in Europe: Epidemiology and resistance. *Int. J. Antimicrob. Agents* **2006**, *27*, 359–366. [CrossRef] [PubMed]
6. Sardi, J.C.O.; Scorzoni, L.; Bernardi, T.; Fusco-Almeida, A.M.; Mendes Giannini, M.J.S. Candida species: Current epidemiology, pathogenicity, biofilm formation, natural antifungal products and new therapeutic options. *J. Med. Microbiol.* **2013**, *62*, 10–24. [CrossRef] [PubMed]
7. Pereira, G.H.; Müller, P.R.; Szeszs, M.W.; Levin, A.S.; Melhem, M.S.C. Five-year evaluation of bloodstream yeast infections in a tertiary hospital: The predominance of non-C. albicans Candida species. *Med. Mycol.* **2010**, *48*, 839–842. [CrossRef]
8. Islam, M.; Natu, R.; Larraga-Martinez, M.F.; Martinez-Duarte, R. Enrichment of diluted cell populations from large sample volumes using 3D carbon-electrode dielectrophoresis. *Biomicrofluidics* **2016**, *10*. [CrossRef]
9. Yildizhan, Y.; Erdem, N.; Islam, M.; Martinez-Duarte, R.; Elitas, M. Dielectrophoretic separation of live and dead monocytes using 3D carbon-electrodes. *Sensors* **2017**, *17*, 2691. [CrossRef]

10. Gilmore, J.; Islam, M.; Duncan, J.; Natu, R.; Martinez-Duarte, R. Assessing the importance of the root mean square (RMS) value of different waveforms to determine the strength of a dielectrophoresis trapping force. *Electrophoresis* **2017**, *38*, 2561–2564. [CrossRef]
11. Natu, R.; Islam, M.; Martinez-duarte, R. Nondimensional Streaming Dielectrophoresis Number for a System of Continuous Particle Separation. *Anal. Chem.* **2019**. [CrossRef] [PubMed]
12. Elitas, M.; Yildizhan, Y.; Islam, M.; Martinez-Duarte, R.; Ozkazanc, D. Dielectrophoretic characterization and separation of monocytes and macrophages using 3D carbon-electrodes. *Electrophoresis* **2018**. [CrossRef] [PubMed]
13. Martinez-Duarte, R. *Label-Free Cell Sorting Using Carbon-Electrode Dielectrophoresis and Centrifugal Microfluidics*; University of California: Irvine, CA, USA, 2010.
14. Dharmasiri, U.; Witek, M.A.; Adams, A.A.; Soper, S.A. Microsystems for the capture of low-abundance cells. *Annu. Rev. Anal. Chem.* **2010**, *3*, 409–431. [CrossRef] [PubMed]
15. Gascoyne, P.R.C.; Noshari, J.; Anderson, T.J.; Becker, F.F. Isolation of rare cells from cell mixtures by dielectrophoresis. *Electrophoresis* **2009**, *30*, 1388–1398. [CrossRef]
16. Lapizco-Encinas, B.H.; Davalos, R.V.; Simmons, B.A.; Cummings, E.B.; Fintschenko, Y. An insulator-based (electrodeless) dielectrophoretic concentrator for microbes in water. *J. Microbiol. Methods* **2005**, *62*, 317–326. [CrossRef]
17. Gascoyne, P.; Mahidol, C.; Ruchirawat, M.; Satayavivad, J.; Watcharasit, P.; Becker, F.F. Microsample preparation by dielectrophoresis: Isolation of malaria. *Lab Chip* **2002**, *2*, 70–75. [CrossRef]
18. Chou, C.-F.; Tegenfeldt, J.O.; Bakajin, O.; Chan, S.S.; Cox, E.C.; Darnton, N.; Duke, T.; Austin, R.H. Electrodeless dielectrophoresis of single- and double-stranded DNA. *Biophys. J.* **2002**, *83*, 2170–2179. [CrossRef]
19. Gagnon, Z.; Chang, H.-C. Aligning fast alternating current electroosmotic flow fields and characteristic frequencies with dielectrophoretic traps to achieve rapid bacteria detection. *Electrophoresis* **2005**, *26*, 3725–3737. [CrossRef]
20. Hölzel, R.; Calander, N.; Chiragwandi, Z.; Willander, M.; Bier, F.F. Trapping single molecules by dielectrophoresis. *Phys. Rev. Lett.* **2005**, *95*, 18–21. [CrossRef]
21. Cheng, I.F.; Chang, H.C.; Hou, D.; Chang, H.C. An integrated dielectrophoretic chip for continuous bioparticle filtering, focusing, sorting, trapping, and detecting. *Biomicrofluidics* **2007**, *1*, 1–15. [CrossRef]
22. Cai, D.; Xiao, M.; Xu, P.; Xu, Y.-C.; Du, W. An integrated microfluidic device utilizing dielectrophoresis and multiplex array PCR for point-of-care detection of pathogens. *Lab Chip* **2014**, *14*, 3917–3924. [CrossRef] [PubMed]
23. Cheng, I.F.; Han, H.W.; Chang, H.C. Dielectrophoresis and shear-enhanced sensitivity and selectivity of DNA hybridization for the rapid discrimination of Candida species. *Biosens. Bioelectron.* **2012**, *33*, 36–43. [CrossRef]
24. Jesús-Pérez, N.M.; Lapizco-Encinas, B.H. Dielectrophoretic monitoring of microorganisms in environmental applications. *Electrophoresis* **2011**, *32*, 2331–2357. [CrossRef] [PubMed]
25. Cheng, I.-F.; Chang, H.-C.; Chung, C.C. Microbial Identification and Manipulation of Nanoscale Biomolecules. U.S. Patent 8808518B2, 19 August 2014.
26. Bisceglia, E.; Cubizolles, M.; Mallard, F.; Vinet, F.; Français, O.; Le Pioufle, B. Micro-organism extraction from biological samples using DEP forces enhanced by osmotic shock. *Lab Chip* **2013**, *13*, 901. [CrossRef] [PubMed]
27. Cheng, I.F.; Liu, S.L.; Chung, C.C.; Chang, H.C. Stepwise gray-scale light-induced electric field gradient for passive and continuous separation of microparticles. *Microfluid. Nanofluid.* **2012**, *12*, 95–105. [CrossRef]
28. Low, W.S.; Wan Abas, W.A.B. Benchtop technologies for circulating tumor cells separation based on biophysical properties. *Biomed Res. Int.* **2015**, *2015*. [CrossRef]
29. Meighan, M.M.; Staton, S.J.R.; Hayes, M.A. Bioanalytical separations using electric field gradient techniques. *Electrophoresis* **2009**, *30*, 852–865. [CrossRef]
30. Natu, R.; Martinez-Duarte, R. Numerical Model of Streaming DEP for Stem Cell Sorting. *Micromachines* **2016**, *7*, 217. [CrossRef]
31. Jaramillo, M.D.C.; Martínez-Duarte, R.; Hüttener, M.; Renaud, P.; Torrents, E.; Juárez, A. Increasing PCR sensitivity by removal of polymerase inhibitors in environmental samples by using dielectrophoresis. *Biosens. Bioelectron.* **2013**, *43*, 297–303. [CrossRef]

32. Martinez-Duarte, R.; Renaud, P.; Madou, M.J. A novel approach to dielectrophoresis using carbon electrodes. *Electrophoresis* **2011**, *32*, 2385–2392. [CrossRef]
33. Martinez-duarte, R.; Cito, S.; Collado-arredondo, E.; Martinez, S.O.; Madou, M.J. Fluido-Dynamic and Electromagnetic Characterization of 3D Carbon Dielectrophoresis with Finite Element Analysis. *Sens. Transducers J.* **2008**, *3*, 25–36.
34. Islam, M.; Natu, R.; Martinez-Duarte, R. Carbon MEMS for Selected Lab-on-a-Chip Applications. In *Carbon: The Next Silicon? Book-2 Applications*; Madou, M.J., Perez-Gonzalez, V.H., Pramanick, B., Eds.; Momentum Press: New York, NY, USA, 2015; pp. 79–100. ISBN 13:978-1-60650-884-8.
35. Martinez-Duarte, R.; Gorkin, R.A.; Abi-Samra, K.; Madou, M.J. The integration of 3D carbon-electrode dielectrophoresis on a CD-like centrifugal microfluidic platform. *Lab Chip* **2010**, *10*, 1030–1043. [CrossRef] [PubMed]
36. Martinez-Duarte, R.; Camacho-Alanis, F.; Renaud, P.; Ros, A. Dielectrophoresis of lambda-DNA using 3D carbon electrodes. *Electrophoresis* **2013**, *34*, 1113–1122. [CrossRef] [PubMed]
37. Elitas, M.; Martinez-Duarte, R.; Dhar, N.; McKinney, J.D.; Renaud, P. Dielectrophoresis-based purification of antibiotic-treated bacterial subpopulations. *Lab Chip* **2014**, *14*, 1850–1857. [CrossRef]
38. Islam, M.; Natu, R.; Martinez-Duarte, R. A study on the limits and advantages of using a desktop cutter plotter to fabricate microfluidic networks. *Microfluid. Nanofluid.* **2015**. [CrossRef]
39. Silva, S.; Negri, M.; Henriques, M.; Oliveira, R.; Williams, D.W.; Azeredo, J. Candida glabrata, Candida parapsilosis and Candida tropicalis: Biology, epidemiology, pathogenicity and antifungal resistance. *FEMS Microbiol. Rev.* **2012**, *36*, 288–305. [CrossRef]
40. Staniszewska, M.; Bondaryk, M.; Siennicka, K.; Sygitowicz, G. Candida albicans morphologies revealed by scanning electron microscopy analysis. *Braz. J. Microbiol.* **2013**, *44*, 813–821. [CrossRef]
41. Odds, F.C.; Rinaldi, M.G.; Cooper, J.; Fothergill, A.; Pasarell, L.; McGinnis, M.R. Candida and Torulopsis: A blinded evaluation of use of pseudohypha formation as basis for identification of medically important yeasts. *J. Clin. Microbiol.* **1997**, *35*, 313–316. [CrossRef]
42. Suzuki, T.; Imanishi, Y.; Iwaguchi, S.I.; Kamihara, T. Depolarized cell growth precedes filamentation during the process of ethanol-induced pseudohyphal formation in the yeast Candida tropicalis. *Microbiology* **1998**, *144*, 403–410. [CrossRef]
43. Urban, C.F.; Reichard, U.; Brinkmann, V.; Zychlinsky, A. Neutrophil extracellular traps capture and kill Candida albicans and hyphal forms. *Cell. Microbiol.* **2006**, *8*, 668–676. [CrossRef]
44. Desai, J.V. Candida albicans hyphae: From growth initiation to invasion. *J. Fungi* **2018**, *4*, 10. [CrossRef] [PubMed]
45. Hernández, R.; Nombela, C.; Diez-Orejas, R.; Gil, C. Two-dimensional reference map of Candida albicans hyphal forms. *Proteomics* **2004**, *4*, 374–382. [CrossRef] [PubMed]
46. Cichocki, B.; Hinsen, K. Stokes drag on conglomerates of spheres. *Phys. Fluids* **1995**, *7*, 285–291. [CrossRef]
47. Martinez-Duarte, R.; Andrade-Roman, J.; Martinez, S.O.; Madou, M.J. A High Throughput Multi-stage, Multi-frequency Filter and Separation Device based on Carbon Dielectrophoresis. In Proceedings of the 11th Annual NSTI Nanotechnology Conference and Trade Show, Boston, MA, USA, 1–5 June 2008; Volume 3, pp. 316–319.
48. Piao, L.; Park, H.; Jo, C.H. Theoretical prediction and validation of cell recovery rates in preparing platelet-rich plasma through a centrifugation. *PLoS ONE* **2017**, *12*, e0187509. [CrossRef] [PubMed]
49. Nam, J.; Jang, W.S.; Hong, D.H.; Lim, C.S. Viscoelastic Separation and Concentration of Fungi from Blood for Highly Sensitive Molecular Diagnostics. *Sci. Rep.* **2019**, *9*, 1–12. [CrossRef] [PubMed]
50. Pethig, R.; Menachery, A.; Pells, S.; De Sousa, P. Dielectrophoresis: A review of applications for stem cell research. *J. Biomed. Biotechnol.* **2010**, *2010*, 182581. [CrossRef]
51. Borgatti, M.; Altomare, L.; Baruffa, M.; Fabbri, E.; Breveglieri, G.; Feriotto, G.; Manaresi, N.; Medoro, G.; Romani, A.; Tartagni, M.; et al. Separation of white blood cells from erythrocytes on a dielectrophoresis (DEP) based "Lab-on-a-chip" device. *Int. J. Mol. Med.* **2005**, *15*, 913–920. [CrossRef]

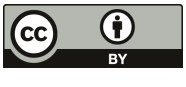

micromachines

MDPI

Article

Analysis of Bacteriophages with Insulator-Based Dielectrophoresis

Adriana Coll De Peña [1,2], Nurul Humaira Mohd Redzuan [2], Milky K. Abajorga [2], Nicole Hill [1], Julie A. Thomas [2,*] and Blanca H. Lapizco-Encinas [1,*]

[1] Microscale Bioseparations Laboratory and Biomedical Engineering Department, Rochester Institute of Technology, Rochester, NY 14623, USA
[2] Thomas H. Gosnell School of Life Sciences, Rochester Institute of Technology, Rochester, NY 14623, USA
* Correspondence: jatsbi@rit.edu (J.A.T.); bhlbme@rit.edu (B.H.L.-E.); Tel.: +1-585-475-2375 (J.A.T.); +1-585-475-2773 (B.H.L.-E.)

Received: 23 May 2019; Accepted: 30 June 2019; Published: 4 July 2019

Abstract: Bacterial viruses or phages have great potential in the medical and agricultural fields as alternatives to antibiotics to control nuisance populations of pathogenic bacteria. However, current analysis and purification protocols for phages tend to be resource intensive and have numbers of limitations, such as impacting phage viability. The present study explores the potential of employing the electrokinetic technique of insulator-based dielectrophoresis (iDEP) for virus assessment, separation and enrichment. In particular, the application of the parameter "trapping value" (*Tv*) is explored as a standardized iDEP signature for each phage species. The present study includes mathematical modeling with COMSOL Multiphysics and extensive experimentation. Three related, but genetically and structurally distinct, phages were studied: *Salmonella enterica* phage SPN3US, *Pseudomonas aeruginosa* phage ϕKZ and *P. chlororaphis* phage 201ϕ2-1. This is the first iDEP study on bacteriophages with large and complex virions and the results illustrate their virions can be successfully enriched with iDEP systems and still retain infectivity. In addition, our results indicate that characterization of the negative dielectrophoretic response of a phage in terms of *Tv* could be used for predicting individual virus behavior in iDEP systems. The findings reported here can contribute to the establishment of protocols to analyze, purify and/or enrich samples of known and unknown phages.

Keywords: bacteriophage; dielectrophoresis; electric field; electrophoresis; electrokinetics; virus

1. Introduction

Bacteriophages, estimated to have a total population of 10^{31}, are possibly the most abundant and genetically diverse biological entities on earth [1,2]. Over the past decade, there has been an increase in observations of antibiotic resistance leading to the need for alternative treatments for bacterial infections. Phage therapy possesses great potential to control multi-drug resistant organisms, such as in the medical and agricultural fields [2]. To employ phages safely for such purposes it is important to have an in-depth knowledge of a representative for each phage group. Our research focuses on understanding the biology of unusually large, so-called "giant" phages, with >200 kb dsDNA genomes, such as *Salmonella enterica* phage SPN3US (240 kb). Increasing numbers of phages that share a core set of genes with SPN3US have recently been isolated, most for the goal of using them for phage therapy purposes. Despite their obvious potential for biocontrol applications, in reality little is known about the biology of these phages. For instance, the virions of giant phages related to SPN3US are comprised of many (>70) different proteins ranging in copy numbers from just a few to 1560 copies per virion,

a large proportion of which (~80%) have no known specific function. These characteristics have led us to conduct genetic studies on SPN3US as a model for related "giant" phages.

To conduct characterization studies on SPN3US, or any phage, requires the use of techniques to purify and enrich particles from a non-homogenous sample containing bacterial cells, cellular debris, and virions, as illustrated in Figure 1. Traditional bacteriophage purification methods, developed for model phages, such as T4 and T7, have numbers of limitations, including being time and labor intensive and often involving a complex series of steps (e.g., CsCl gradient ultracentrifugation) [3]. However, due to the great variability in virion composition between different phages, traditional procedures are frequently not suitable for the purification of many of the newer "environmental" phages, damaging their virions and causing loss of viability. For instance, CsCl gradient purification causes the virions of *Bacillus* virus, phageG to completely disintegrate, and those of *B. thuringiensis* phage 0305ϕ8-36 to lose infectivity by several orders of magnitude [4]. Similarly, even environmental phages that are related to model phages, such as T4, can respond very differently to the protocols employed for the model phage (e.g., [5]). To further complicate matters, standard purification protocols often do not completely remove all bacterial debris, such as cell wall proteins and endotoxins, which can impede downstream analyses (e.g., mass spectrometry) and represents a major problem for therapeutic preparations of phages [6,7]. Given these limitations of traditional phage purification techniques, alternative separation and enrichment processes are being explored [6–8].

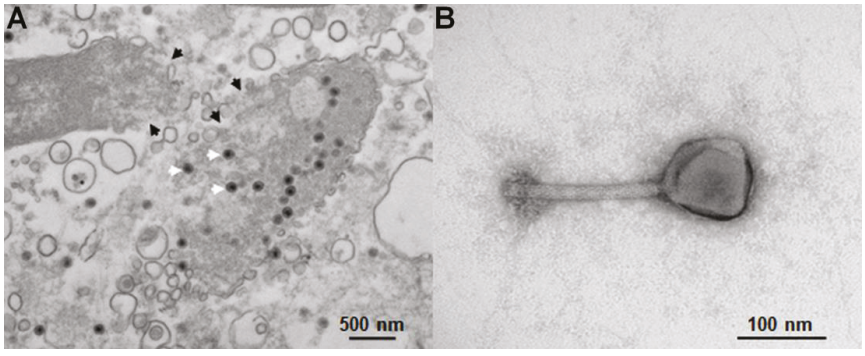

Figure 1. Transmission electron microscopy (TEM) of SPN3US-infected *Salmonella* and purified SPN3US. (**A**) Negatively stained thin section showing two *Salmonella* cells in the process of being lysed at the end of infection by SPN3US. Regions of the cell walls undergoing rupture due to phage enzymes are indicated with black arrowheads. Particles of SPN3US progeny are indicated with white arrowheads. Note the extensive amount of cell debris in the sample. (**B**) Negatively stained image of a single SPN3US virion from a preparation that has undergone purification via CsCl gradient ultracentrifugation to remove cellular debris from the sample. SPN3US virions consist of a head (which contains the dsDNA genome) and tail which ends in a complex baseplate that attaches to a *Salmonella* cell to initiate infection.

Microfluidics has revolutionized the manner in which many bioanalytical assessments are performed. It has opened the doors to perform high resolution and sensitivity purification assays [9]. Electrokinetics (EK), electric field-driven techniques, is one of the main pillars of microfluidics due to its great flexibility and simplicity of application. Dielectrophoresis (DEP) has proven to be a robust platform for the separation, sorting and enrichment of a wide array of biological particles ranging from macromolecules to parasites [10–14]. Dielectrophoresis is the migration of particles under the influence of a non-uniform electric field. Unlike electrophoresis (EP), DEP exploits particle polarization effects, not the electrical charge, leading to a greater flexibility since it works with both DC and AC electric potentials [15]. Insulator-based DEP (iDEP) is a technique where non-uniform electric fields are produced employing insulating structures, usually embedded in a microchannel, creating a truly 3-dimensional dielectrophoretic effect [16]. Is it important to note that iDEP systems can suffer from

electrolysis and Joule heating effects [17] due to the requirement of high voltages. Therefore, operating conditions need to be carefully selected.

Microorganisms have been extensively studied in dielectrophoretic-based systems, including both electrode-based DEP (eDEP) and iDEP systems [18]. A challenge in the dielectrophoretic manipulation of viral particles is the inherently small size as larger applied electric potentials are required to generate sufficient dielectrophoretic forces [19]. Some of the first studies were focused on the assessment of viruses that are pathogenic to humans. In 1996 the Furh research group demonstrated the enrichment and stable trapping of influenza and Sendai viruses in an eDEP system with two sets of planar electrodes that allowed for the creation of 3D field cages [20,21]. This work was later extended by Grom et al. demonstrating the ability to transport and accumulate hepatitis A virus in a field cage consisting of eight microelectrodes. [19]. Hughes et al. reported a series of studies on the characterization of herpes simplex virus with DEP [22–24]. Akin et al. reported an iDEP system with an interdigitated electrode array for real-time trapping and imaging of vaccinia virus [25]. Masuda et al. presented a 3-dimensional iDEP system that allowed the filtration and selective transportation of a single influenza to promote single-virus cell infection [8]. Prakash et al. employed a droplet-based system for the detection of influenza viruses using PCR; illustrating the potential of DEP for diagnostics [26]. Ding et al. utilized gradient iDEP to concentrate Sindbis virus to increase the concentration of the virus from two to six times within the channel using voltages as low as 70 V [12]. Other recent reports have focused on the development of sensors. Singh et al. created a sensor for influenza virus employing carbon nanotubes that were electrodeposited by means of DEP [27]. Madiyar et al. reported the capture and detection of vaccinia virus with DEP by using carbon nanoelectrode arrays [28]. Some earlier studies involved plant viruses. Morgan and Green demonstrated the first application of eDEP for the manipulation of tobacco mosaic virus (TMV) using AC electric fields [29]. Ermolina et al. characterized the dielectric properties of cow pea mosaic virus and TMV in a system with castellated electrodes [30,31]. Lapizco-Encinas reported the enrichment of TMV in an iDEP system with cylindrical insulating posts [32].

In contrast to human and plant viruses, there have been few studies on the suitability of DEP for phage enrichment. Sonnenberg et al developed an eDEP system for the isolation detection of T7 bacteriophage from whole blood [33], illustrating the potential of DEP for clinical applications. Madiyar et al. demonstrated single virus and large ensemble trapping of T4r and T1 bacteriophages from a dilute solution under conditions with a nanoelectrode array made of carbon nanofibers [34].

The contributions mentioned above are excellent examples of some of the latest advancements in the dielectrophoretic manipulation of viral particles. However, it is evident that systems capable of purifying newer "environmental" phages, including giant phages, are still an unexplored area. Similarly, unexplored are systems capable of handling a larger throughput containing several viral species which would be of potential value in phage therapy as typically cocktails or mixtures of different types of phages are employed. In this contribution, we present the first report on the assessment and enrichment of *Salmonella* phage SPN3US, and for comparison purposes, two related giant *Pseudomonas* phages: ϕKZ and 201ϕ2-1, in two distinct iDEP systems. In particular, the application of the parameter "trapping value" (*Tv*) is explored as a standardized iDEP signature for each virus species. This work includes mathematical modeling with COMSOL Multiphysics®(version 4.4, COMSOL Inc., Stockholm, Sweden) and experimentation with iDEP devices containing an array of circular or oval-shaped insulating posts. For model information, please see the supplementary material. The dielectrophoretic trapping of viral particles under the influence of DC electric potentials was fully characterized in order to discern the specific trapping conditions ("sufficient" trapping) for each one of the distinct viral species. All viruses in this study exhibited negative dielectrophoretic behavior. The results illustrating virus trapping and enriching allowed the identification of the specific Trapping value (*Tv*, Equation (3)) for each type of phage [35,36]. This is the first iDEP study on large bacteriophages and these findings could be used for the design of new iDEP systems aimed to separate and enrich samples of both known and unknown phages.

2. Theory

Particles can exhibit either positive or negative DEP, depending on their relative polarizability with respect to the suspending media [37]. Positive DEP (pDEP) occurs when the particle is more polarizable than the medium, resulting in particle attraction to the regions with higher electric field gradient. Negative DEP (nDEP) is the opposite effect. In our iDEP channels (Figure 2A,B), the constrictions between posts are the areas of high field gradients. Under nDEP, all virus species in this study could be trapped in the constriction regions. In iDEP systems particles are captured when the effects of DEP and linear EK forces, which are opposite, are balanced [38]. For a particle to become trapped the following condition has been identified [39,40]:

$$\frac{\mu_{DEP}\nabla E^2 \cdot \vec{E}}{\mu_{EK}\, E \cdot \vec{E}} \leq -1, \tag{1}$$

Separating the above expression into system-dependent and particle-dependent parameters:

$$\frac{\nabla E^2 \cdot \vec{E}}{E^2} \leq -\frac{\mu_{EK}}{\mu_{DEP}}, \tag{2}$$

where the left-hand side of the equation is the Trapping value which is independent of particle properties, as it only depends on the electric field magnitude ($\vec{E}$) and gradient of the electric field squared (∇E^2). This parameter, identified by the Casals-Terré [35] and Hayes [36] groups, characterizes the condition required to trap a specific type of particle:

$$Tv = \frac{\nabla E^2 \cdot \vec{E}}{E^2}. \tag{3}$$

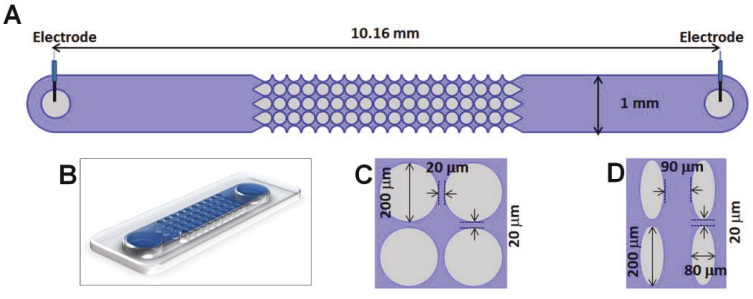

Figure 2. Schematic representation of one insulator-based dielectrophoresis (iDEP) channel employed in this study. (**A**) Top view of a full channel for design Circle-200-220. (**B**) 3D representation of the channel. For the two designs analyzed in this study, an illustration of four insulating posts with dimensions is included: (**C**) Circle-200-220, (**D**) Oval-200-220&80-170. Design names illustrate post size and post spacing.

3. Materials and Methods

3.1. Microdevices, Viral Samples and Suspending Medium

Experiments were conducted in two distinct microchannel designs made from PDMS employing standard soft lithography techniques; microfabrication information is included here [40]. The microchannels were 10.16 mm long, 40 µm deep and 880 µm wide, specific post dimensions are included in Figure 2C,D. This study employed high titer stocks (10^{10}–10^{12} pfu (plaque-forming units)/mL) of three related viruses: *Salmonella* Typhimurium phage SPN3US [41], *Pseudomonas aeruginosa*

phage ϕKZ [42] and *P. chlororaphis* phage 201ϕ2-1 [43]. These phage stocks underwent a low speed clarification spin (~8000 g, 10 min, 4 °C) to remove large bacterial debris. All virus samples were fluorescently labeled as follows: 1 mL of a phage stock was spun down at 13,000 rpm for 10 min, after discarding the supernatant the pellet was resuspended in 0.5 mL of distilled water. Then, 2 µL of SYTO 11 dye (Invitrogen, Carlsbad, CA, USA) was added to the sample and incubated for 20 min. After removing the excess dye, the sample was resuspended in 0.5 mL of the suspending medium. The suspending medium was sterilized deionized water with a conductivity of 14 µS/cm and a pH of 7.07; under these conditions the zeta potential of the PDMS channel was approximately −108.57 mV.

Phage samples were assayed for viability via plaque assays in triplicate using the standard double overlay technique using LB agar bottom plates and overlays made from LB broth and 0.34% agar. Briefly, each phage sample underwent a 10-fold dilution series in SM buffer and these were spotted onto overlays made containing 100 µL of a fresh overnight culture of the appropriate bacterial strain. Plaques were enumerated after overnight incubation at 30 °C.

3.2. Equipment and Experimental Procedure

Phage response was observed and recorded as videos with a Leica DMi8 inverted microscope (Wetzlar, Germany). Direct current (DC) electric potentials were applied with a high voltage supply (Model HVS6000D, LabSmith, Livermore, CA, USA). COMSOL Multiphysics®4.4 was used to predict the magnitude of the trapping value (*Tv*, Equation (3)). Each experiment started with a clean channel to which a 5–10 µL sample of the corresponding labeled virus was added, followed by the application of DC electric potentials. For the purpose of this study, a "sufficient" trapping voltage was determined as the required voltage to obtain a visually observable band or cluster of trapped viral particles.

4. Results and Discussion

4.1. Experimental Characterization of the Dielectrophoretic Trapping of Phage Virions

A series of experiments were carried out to characterize the required voltage to trap and enrich each type of phages in both iDEP devices with nDEP. After a sample of the fluorescently labelled virus was introduced into the channel, the applied voltage was manually increased until "sufficient" trapping of the viral species was observed. Each experiment was repeated at least five times to ensure reproducibility, a summary of these results is included in Table S1 (supplementary material). Figure 3A,C illustrate images of the trapping of all three phage species in the circle-shaped iDEP channel at applied potentials between 1100 and 1200 V. Lower voltages, in the range of 750–800 V, were required with the oval-shaped posts, as depicted in Figure 3D,F. Figure 3G shows a plot of the required trapping voltage necessary to achieve "sufficient" trapping. As expected, for all viral species, the required voltages are lower with the oval-shaped posts, since narrower posts generate higher electric field gradients (∇E^2), producing greater dielectrophoretic forces [40]. The characteristic trapping voltage and *Tv* for each viral species is a strong function of the size, shape and polarizability of the viral species. As demonstrated by Hughes et al. [44] the total conductivity of a particle depends on the conductivity of the bulk material, and the individual conductances of the compact and diffuse layers of the electrical double layer (EDL). This group successfully extended this analysis with the dielectrophoretic characterization of simplex virus-1 capsids [45]. In a later contribution, Ermolina et al. [30] illustrated that surface conductance, which is directly related to polarizability, is a dominant parameter in the EP response of submicron particles, such as viruses.

4.2. Modeling Predictions for the Trapping of Phage Virus

The trapping value (*Tv*), which characterizes the conditions required to trap a specific type of particle [35,36], was determined using COMSOL Multiphysics®software (Table S1). The geometries of interest were imported into COMSOL along with trapping voltage (Figure 3G) associated for each species in order to predict the parameters ∇E^2, $\vec{E}$ and E^2. These values were estimated across a cutline

located at the centerline of one constriction between two posts. Images depicting the cutlines used in these estimations are illustrated in Figure S1.

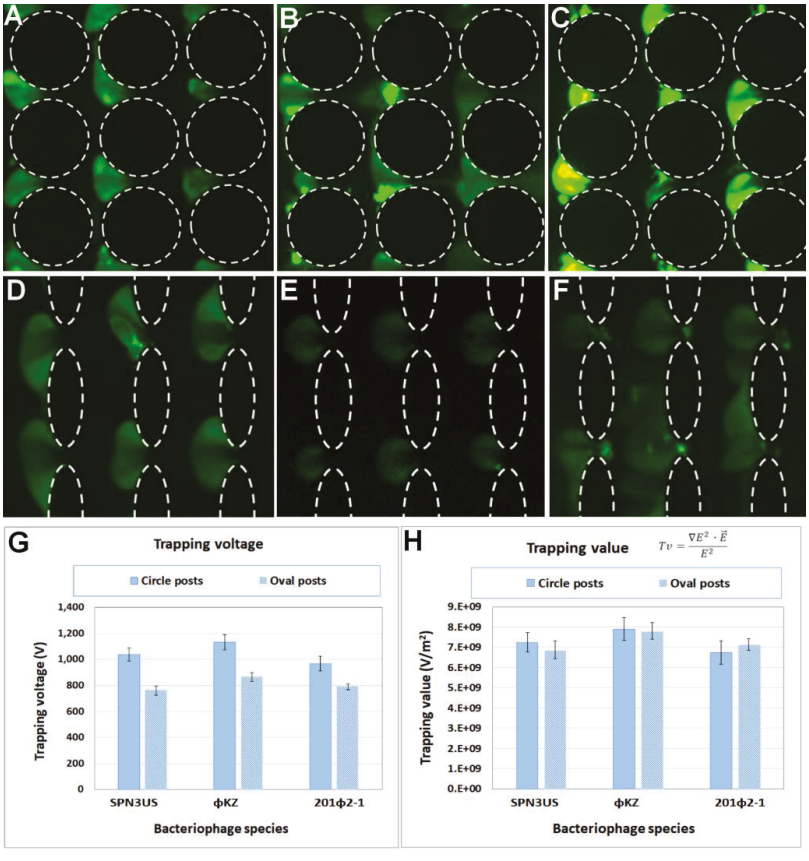

Figure 3. Results of the dielectrophoretic trapping of all three phages. Circle-shaped posts: (**A**) SPN3US at 1200 V, (**B**) ϕKZ at 1100 V and (**C**) 201ϕ2-1 at 1100 V. Oval-shaped posts: (**D**) SPN3US at 800 V, (**E**) ϕKZ at 750 V and (**F**) 201ϕ2-1 at 750 V. (**G**) Experimental characterization of the trapping voltage, and (**H**) Estimation of the trapping value (*Tv*) in both iDEP channel designs for the three types of bacteriophages in this study. Table S1 in the Supplementary Material includes a summary of the trapping voltage and *Tv* estimations.

As defined by Casals-Terré [35] and Hayes [36] groups, the *Tv* parameter normalizes the required conditions for trapping a specific type of particles for any type of iDEP design. The results in Figure 3H confirm the applicability of *Tv*. It can be observed for each one of the three viral species that the *Tv* values for both iDEP designs are quite similar, a finding which is consistent with our previous analyses that each of these three phages has a large virion composed of mostly homologous proteins and very similar dimensions [46]. Notably, the trapping voltage (Figure 3G) for each phage was unique, which indicates that if, in future studies, the separation of a mixture of similarly related viruses was required, we should focus on the trapping voltages, not the trapping values. In addition, our results indicate that devices with wider posts might be more suitable for such separation purposes (i.e., wider posts (circles) produced trapping voltages with a larger distribution between the three virus species than obtained with narrow posts (ovals)). Furthermore, these findings open the exciting

possibility of using *Tv* for the designing of iDEP devices with distinct post geometries; and also for predicting the trapping conditions of different types of particles (from viruses to cells) in a given iDEP device. Consequently, these findings will be relevant for future studies on mixtures of phages, even those including related phages, as found in phage therapy cocktails.

4.3. Viability Assessments after Dielectrophoretic Trapping

To evaluate the potential of iDEP for bacteriophage purification and enrichment, the phage samples were assessed for viability after exposing them to high voltages. To do this, the stained input samples that had been previously fluorescently stained for the trapping voltage experiments were run on a circle post design in triplicates, and exposed to the following sequence of voltages: 400 V for 30 s, 800 V for 20 s and 400 V for 10 s. The voltages were chosen to represent the experimental conditions with an initial voltage to move the sample to the post array, followed by a trapping voltage and a release voltage to move the sample to the outlet reservoir prior to extraction. While some sample did reach the outlet reservoir without experiencing the total magnitude of the electric field gradient within the constrictions at 800 V, all viruses retrieved were still exposed to high voltages for at least one minute. Upon extraction of the samples from their respective channels, the samples of each phage were plated on their respective bacterial host. The clearings in the bacterial lawns observed in Figure 4A represent bacterial cell lysis generated by the presence of viable bacteriophages. Remarkably, the two *Pseudomonas* phages, ϕKZ and 201ϕ2-1, had titers in the high range after trapping (Figure 4B, Table S2), a finding which supports that iDEP can indeed be used as a purification technique and not only as an analytical tool for bacteriophages.

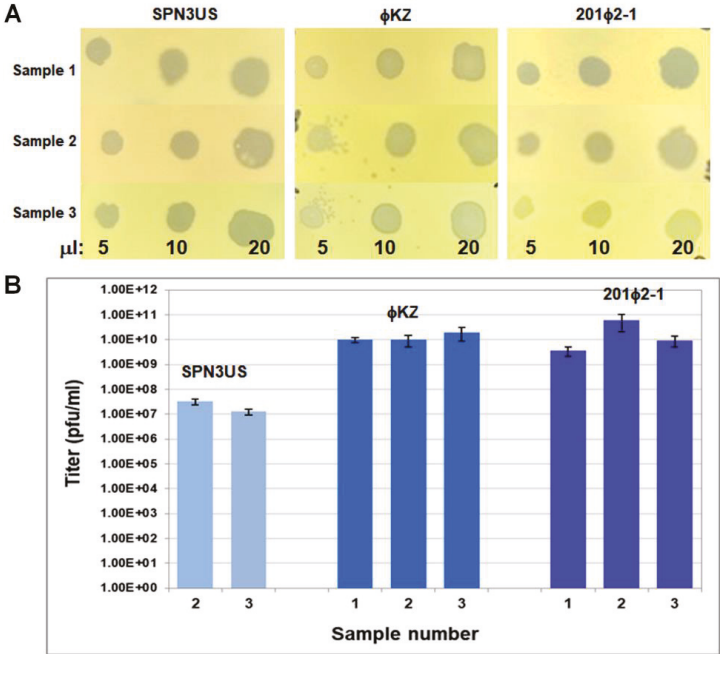

Figure 4. Qualitative viability assessments for all three phages studied here. (**A**) Three samples of phages SPN3US, ϕKZ and 201ϕ2-1 that had been fluorescently labelled and treated were spotted onto the lawns of their respective bacterial hosts in three replicate experiments. Volumes of phage spotted are indicated at the bottom of the image. (**B**) Enumeration of viable particles (plaque-forming units, pfu) of the samples in (A) for phages SPN3US, ϕKZ and 201ϕ2-1, with the exception of SPN3US sample 1 which was not able to be titered.

The titers of SPN3US after iDEP were more variable despite comparable trapping magnitudes of its virions in the iDEP channels relative to ϕKZ and 201ϕ2-1 (Figure 4). Potential causes for the SPN3US titer variability include that certain parts of its virion may be more susceptible to damage during trapping after virions have been treated with SYTO 11 than similar structures in ϕKZ and 201ϕ2-1. This seems highly likely as our analyses indicate that each phage has a reduced viability immediately after SYTO 11 treatment (Table S3). It is also feasible that some of the variation in the viability of the SPN3US sample extracted from iDEP may have been the consequence of variation within the channel to the outlet reservoir. Potential future research directions could focus on increasing the yield of enriched phages, and quantification of iDEP relative to existing phage purification techniques with regard the amount of bacterial contaminants removed.

5. Conclusions

Presented here is the assessment of three phages: SPN3US, ϕKZ and 201ϕ2-1 in two distinct iDEP devices, one with circle-shaped and one with oval-shaped insulator posts. Experimental work demonstrated the successful trapping of all three phage species, where the voltage requirement to achieve trapping of virions was lower in devices with circular insulating posts, since these produce lower dielectrophoretic forces than the oval-shaped posts. A mathematical model created with COMSOL was then employed to estimate the trapping value (Tv) for each phage type. This parameter, as identified by other research groups, normalizes the required conditions, in terms of electric field and electric field gradient, for trapping a specific type of particle. The results demonstrated that the Tv for a specific species is reasonably constant within the two distinct designs studied here, opening the exciting possibility of using Tv for the designing of iDEP devices targeting specific viral species, and also for predicting the required voltage for trapping a specific type of particle, including viruses, in distinct iDEP devices. In addition, these findings suggest that iDEP has potential for analyses of mixtures of phages, even those including related phages, such as found in phage therapy cocktails.

Supplementary Materials: The following are available online at http://www.mdpi.com/2072-666X/10/7/450/s1. Figure S1: Representation of the cutline employed in COMSOL for the determination of Tv. Table S1: Comparison between trapping voltages and Tv of SPN3US, ϕKZ, and 201ϕ2-1 in the circle and oval post channel designs. Table S2: Enumeration of viable particles of phages SPN3US, ϕKZ, and 201ϕ2-1 after trapping in the circle designs. Table S3: Enumeration of viable particles of phages SPN3US, ϕKZ, and 201ϕ2-1 before and immediately after staining with SYTO 11.

Author Contributions: A.C.D.P, J.A.T and B.H.L.-E conceived and designed the experiments, and contributed reagents/materials; A.C.D.P performed the microfluidics experiments; N.H.M.R and M.K.A. prepared virus stocks and performed viability experiments; A.C.D.P and N.H. performed mathematical model analysis; A.C.D.P, J.A.T, and B.H.L.-E. analyzed the data and wrote the paper; A.C.D.P, J.A.T, N.H. and B.H.L.-E. reviewed and edited the paper.

Funding: A.C.D.P., N.H. and B.H.L.-E would like to acknowledge the financial support provided by the National Science Foundation (CBET-1705895). J.A.T., N.H.M.R. and M.K.A. acknowledge support by the National Institutes of Health (UA5GM126533).

Acknowledgments: We thank Ru-ching Hsia for transmission electron microscopy (TEM) of SPN3US and SPN3US-infected *Salmonella*. TEM was performed at the UMB Electron Microscopy Core Imaging Facility. We thank Roberto Gallo-Villanueva for providing Figure 2B.

Conflicts of Interest: The authors declare no conflict of interest.

References

1. Comeau, A.M.; Hatfull, G.F.; Krisch, H.M.; Lindell, D.; Mann, N.H.; Prangishvili, D. Exploring the prokaryotic virosphere. *Res. Microbiol.* **2008**, *159*, 306–313. [CrossRef] [PubMed]
2. Keen, E.C. A century of phage research: Bacteriophages and the shaping of modern biology. *BioEssays* **2015**, *37*, 6–9. [CrossRef]
3. Nasukawa, T.; Uchiyama, J.; Taharaguchi, S.; Ota, S.; Ujihara, T.; Matsuzaki, S.; Murakami, H.; Mizukami, K.; Sakaguchi, M. Virus purification by CsCl density gradient using general centrifugation. *Arch. Virol.* **2017**, *162*, 3523–3528. [CrossRef]

4. Thomas, J.A.; Hardies, S.C.; Rolando, M.; Hayes, S.J.; Lieman, K.; Carroll, C.A.; Weintraub, S.T.; Serwer, P. Complete genomic sequence and mass spectrometric analysis of highly diverse, atypical Bacillus thuringiensis phage 0305phi8-36. *Virology* **2007**, *368*, 405–421. [CrossRef] [PubMed]
5. Bourdin, G.; Schmitt, B.; Marvin Guy, L.; Germond, J.E.; Zuber, S.; Michot, L.; Reuteler, G.; Brüssow, H. Amplification and purification of T4-like Escherichia coli phages for phage therapy: From laboratory to pilot scale. *Appl. Environ. Microbiol.* **2014**, *80*, 1469–1476. [CrossRef]
6. Castro-Mejía, J.L.; Muhammed, M.K.; Kot, W.; Neve, H.; Franz, C.M.; Hansen, L.H.; Vogensen, F.K.; Nielsen, D.S. Optimizing protocols for extraction of bacteriophages prior to metagenomic analyses of phage communities in the human gut. *Microbiome* **2015**, *3*, 64. [CrossRef]
7. Bonilla, N.; Rojas, M.I.; Cruz, G.N.F.; Hung, S.H.; Rohwer, F.; Barr, J.J. Phage on tap-a quick and efficient protocol for the preparation of bacteriophage laboratory stocks. *Peer J* **2016**, *4*, e2261. [CrossRef]
8. Masuda, T.; Maruyama, H.; Honda, A.; Arai, F. Virus enrichment for single virus infection by using 3d insulator based dielectrophoresis. *PLoS ONE* **2014**, *9*, e94083. [CrossRef] [PubMed]
9. Whitesides, G.M. The origins and the future of microfluidics. *Nature* **2006**, *442*, 368–373. [CrossRef] [PubMed]
10. Nakano, A.; Camacho-Alanis, F.; Ros, A. Insulator-based dielectrophoresis with [small beta]-galactosidase in nanostructured devices. *Analyst* **2015**, *140*, 860–868. [CrossRef] [PubMed]
11. Jones, P.V.; Salmon, G.L.; Ros, A. Continuous separation of DNA molecules by size using insulator-based dielectrophoresis. *Anal. Chem.* **2017**, *89*, 1531–1539. [CrossRef] [PubMed]
12. Ding, J.; Lawrence, R.M.; Jones, P.V.; Hogue, B.G.; Hayes, M.A. Concentration of sindbis virus with optimized gradient insulator-based dielectrophoresis. *Analyst* **2016**, *141*, 1997–2008. [CrossRef] [PubMed]
13. LaLonde, A.; Romero-Creel, M.F.; Lapizco-Encinas, B.H. Assessment of cell viability after manipulation with insulator-based dielectrophoresis. *Electrophoresis* **2015**, *36*, 1479–1484. [CrossRef] [PubMed]
14. Su, Y.H.; Tsegaye, M.; Varhue, W.; Liao, K.T.; Abebe, L.S.; Smith, J.A.; Guerrant, R.L.; Swami, N.S. Quantitative dielectrophoretic tracking for characterization and separation of persistent subpopulations of cryptosporidium parvum. *Analyst* **2014**, *139*, 66–73. [CrossRef] [PubMed]
15. Romero-Creel, M.; Goodrich, E.; Polniak, D.; Lapizco-Encinas, B. Assessment of sub-micron particles by exploiting charge differences with dielectrophoresis. *Micromachines* **2017**, *8*, 239. [CrossRef] [PubMed]
16. Polniak, D.V.; Goodrich, E.; Hill, N.; Lapizco-Encinas, B.H. Separating large microscale particles by exploiting charge differences with dielectrophoresis. *J. Chromatogr. A* **2018**, *1545*, 84–92. [CrossRef]
17. Gallo-Villanueva, R.C.; Perez-Gonzalez, V.H.; Cardenas-Benitez, B.; Jind, B.; Martinez-Chapa, S.O.; Lapizco-Encinas, B.H. Joule heating effects in optimized insulator-based dielectrophoretic devices: An interplay between post geometry and temperature rise. *Electrophoresis* **2019**, *40*, 1408–1416. [CrossRef]
18. Jesús-Pérez, N.M.; Lapizco-Encinas, B.H. Dielectrophoretic monitoring of microorganisms in environmental applications. *Electrophoresis* **2011**, *32*, 2331–2357. [CrossRef]
19. Grom, F.; Kentsch, J.; Müller, T.; Schnelle, T.; Stelzle, M. Accumulation and trapping of hepatitis a virus particles by electrohydrodynamic flow and dielectrophoresis. *Electrophoresis* **2006**, *27*, 1386–1393. [CrossRef]
20. Schnelle, T.; Muller, T.; Fiedler, S.; Shirley, S.G.; Ludwig, K.; Herrmann, A.; Fuhr, G.; Wagner, B.; Zimmermann, U. Trapping of viruses in high-frequency electric field cages. *Naturwissenschaften* **1996**, *83*, 172–176. [CrossRef]
21. Müller, T.; Fiedler, S.; Schnelle, T.; Ludwig, K.; Jung, H.; Fuhr, G. High frequency electric fields for trapping of viruses. *Biotechnol. Tech.* **1996**, *10*, 221–226. [CrossRef]
22. Hughes, M.P.; Morgan, H.; Rixon, F.J. Characterization of herpes simplex virus particles by dielectrophoretic crossover methods. In Proceedings of the 20th Annual International Conference of the IEEE Engineering in Medicine and Biology Society, Hong Kong, China, 1 November 1998; pp. 2816–2819.
23. Hughes, M.P.; Morgan, H.; Rixon, F.J.; Burt, J.P.H.; Pethig, R. Manipulation of herpes simplex virus type 1 by dielectrophoresis. *Biochim. Biophys. Acta (BBA) Gen. Subj.* **1998**, *1425*, 119–126. [CrossRef]
24. Hughes, M.P.; Morgan, H.; Rixon, F.J. Measuring the dielectric properties of herpes simplex virus type 1 virions with dielectrophoresis. *Biochim. Biophys. Acta (BBA) Gen. Subj.* **2002**, *1571*, 1–8. [CrossRef]
25. Akin, D.; Li, H.; Bashir, R. Real-time virus trapping and fluorescent imaging in micro-fluidic devices. *Nano Letters.* **2004**, *4*, 257–259. [CrossRef]
26. Prakash, R.; Pabbaraju, K.; Wong, S.; Wong, A.; Tellier, R.; Kaler, K. Multiplex, quantitative, reverse transcription pcr detection of influenza viruses using droplet microfluidic technology. *Micromachines* **2015**, *6*, 63. [CrossRef]

27. Singh, R.; Sharma, A.; Hong, S.; Jang, J. Electrical immunosensor based on dielectrophoretically-deposited carbon nanotubes for detection of influenza virus h1n1. *Analyst* **2014**, *139*, 5415–5421. [CrossRef] [PubMed]
28. Madiyar, F.R.; Haller, S.L.; Farooq, O.; Rothenburg, S.; Culbertson, C.; Li, J. Ac dielectrophoretic manipulation and electroporation of vaccinia virus using carbon nanoelectrode arrays. *Electrophoresis* **2017**, *38*, 1515–1525. [CrossRef]
29. Morgan, H.; Green, N. Dielectrophoretic manipulation of rod-shaped viral particles. *J. Electrost.* **1997**, *42*, 279–293. [CrossRef]
30. Ermolina, I.; Milner, J.; Morgan, H. Dielectrophoretic investigation of plant virus particles: Cow pea mosaic virus and tobacco mosaic virus. *Electrophoresis* **2006**, *27*, 3939–3948. [CrossRef]
31. Ermolina, I.; Morgan, H.; Green, N.G.; Milner, J.J.; Feldman, Y. Dielectric spectroscopy of tobacco mosaic virus. *Biochim. Biophys. Acta (BBA) Gen. Subj.* **2003**, *1622*, 57–63. [CrossRef]
32. Lapizco-Encinas, B.H.; Davalos, R.; Simmons, B.A.; Cummings, E.B.; Fintschenko, Y. An insulator-based (electrodeless) dielectrophoretic concentrator for microbes in water. *J. Microbiol. Methods* **2005**, *62*, 317–326. [CrossRef] [PubMed]
33. Sonnenberg, A.; Marciniak, J.Y.; McCanna, J.; Krishnan, R.; Rassenti, L.; Kipps, T.J.; Heller, M.J. Dielectrophoretic isolation and detection of cfc-DNA nanoparticulate biomarkers and virus from blood. *Electrophoresis* **2013**, *34*, 1076–1084. [CrossRef] [PubMed]
34. Madiyar, F.R.; Syed, L.U.; Culbertson, C.T.; Li, J. Manipulation of bacteriophages with dielectrophoresis on carbon nanofiber nanoelectrode arrays. *Electrophoresis* **2013**, *34*, 1123–1130. [CrossRef] [PubMed]
35. Mohammadi, M.; Zare, M.J.; Madadi, H.; Sellarès, J.; Casals-Terré, J. A new approach to design an efficient micropost array for enhanced direct-current insulator-based dielectrophoretic trapping. *Anal. Bioanal. Chem.* **2016**, *408*, 5285–5294. [CrossRef] [PubMed]
36. Crowther, C.V.; Hayes, M.A. Refinement of insulator-based dielectrophoresis. *Analyst* **2017**, *142*, 1608–1618. [CrossRef] [PubMed]
37. Jones, T.B. *Electromechanics of Particles*; Cambridge University Press: New York, NY, USA, 1995; p. 265.
38. Gencoglu, A.; Olney, D.; LaLonde, A.; Koppula, K.S.; Lapizco-Encinas, B.H. Dynamic microparticle manipulation with an electroosmotic flow gradient with low frequency alternating current dielectrophoresis. *Electrophoresis* **2014**, *35*, 363–373. [CrossRef]
39. Saucedo-Espinosa, M.A.; Lapizco-Encinas, B.H. Experimental and theoretical study of dielectrophoretic particle trapping in arrays of insulating structures: Effect of particle size and shape. *Electrophoresis* **2015**, *36*, 1086–1097. [CrossRef] [PubMed]
40. Saucedo-Espinosa, M.A.; Lapizco-Encinas, B.H. Design of insulator-based dielectrophoretic devices: Effect of insulator posts characteristics. *J. Chromatogr. A* **2015**, *1422*, 325–333. [CrossRef]
41. Lee, J.H.; Shin, H.; Kim, H.; Ryu, S. Complete genome sequence of salmonella bacteriophage spn3us. *J. Virol.* **2011**, *85*, 13470–13471. [CrossRef]
42. Mesyanzhinov, V.V.; Robben, J.; Grymonprez, B.; Kostyuchenko, V.A.; Bourkaltseva, M.V.; Sykilinda, N.N.; Krylov, V.N.; Volckaert, G. The genome of bacteriophage φKZ of Pseudomonas aeruginosa. *J. Mol. Biol.* **2002**, *317*, 1–19. [CrossRef]
43. Thomas, J.A.; Rolando, M.R.; Carroll, C.A.; Shen, P.S.; Belnap, D.M.; Weintraub, S.T.; Serwer, P.; Hardies, S.C. Characterization of Pseudomonas chlororaphis myovirus 201phi2-1 via genomic sequencing, mass spectrometry, and electron microscopy. *Virology* **2008**, *376*, 330–338. [CrossRef] [PubMed]
44. Hughes, M.P.; Morgan, H.; Flynn, M.F. The dielectrophoretic behavior of submicron latex spheres: Influence of surface conductance. *J. Colloid Interface Sci.* **1999**, *220*, 454–457. [CrossRef] [PubMed]
45. Hughes, M.P.; Morgan, H.; Rixon, F.J. Dielectrophoretic manipulation and characterization of herpes simplex virus-1 capsids. *Eur. Biophys. J.* **2001**, *30*, 268–272. [CrossRef] [PubMed]
46. Thomas, J.A.; Benítez Quintana, A.D.; Bosch, M.A.; Coll De Peña, A.; Aguilera, E.; Coulibaly, A.; Wu, W.; Osier, M.V.; Hudson, A.O.; Weintraub, S.T.; et al. Identification of essential genes in the Salmonella phage SPN3US reveals novel insights into giant phage head structure and assembly. *J. Virol.* **2016**, *90*, 10284–10298. [CrossRef] [PubMed]

micromachines

MDPI

Article

Multi-Stage Particle Separation based on Microstructure Filtration and Dielectrophoresis

Danfen Yin, Xiaoling Zhang, Xianwei Han, Jun Yang and Ning Hu *

Key Laboratory of Biorheological Science and Technology, Chongqing University, Ministry of Education, Bioengineering College, Chongqing University, Chongqing 400030, China; yindf@cqu.edu.cn (D.Y.); zhangxiaoling@cqu.edu.cn (X.Z.); 20161901019@cqu.edu.cn (X.H.); bioyangjun@cqu.edu.cn (J.Y.)
* Correspondence: huning@cqu.edu.cn; Tel.: +86-23-6510-2291

Received: 30 December 2018; Accepted: 29 January 2019; Published: 31 January 2019

Abstract: Particle separation is important in chemical and biomedical analysis. Among all particle separation approaches, microstructure filtration which based particles size difference has turned into one of the most commonly methods. By controlling the movement of particles, dielectrophoresis has also been widely adopted in particle separation. This work presents a microfluidic device which combines the advantages of microfilters and dielectrophoresis to separate micro-particles and cells. A three-dimensional (3D) model was developed to calculate the distributions of the electric field gradient at the two filter stages. Polystyrene particles with three different sizes were separated by micropillar array structure by applying a 35-Vpp AC voltage at 10 KHz. The blocked particles were pushed off the filters under the negative dielectrophoretic force and drag force. A mixture of Haematococcus pluvialis cells and Bracteacoccus engadinensis cells with different sizes were also successfully separated by this device, which proved that the device can separate both biological samples and polystyrene particles.

Keywords: Microfilter; Dielectrophoresis; Particle separation, micropillar

1. Introduction

Microfluidic technology involves the control and manipulation of small amount of fluid confined in micron-sized geometry [1,2]. Microfluidic operations have many advantages, including faster analyses, minimum consumption of samples and reagents, shorter reaction times, and high-throughput screenings [3]. Moreover, miniaturization makes it possible to develop portable devices, which means that miniaturized laboratory equipment can be taken where it is needed. The influence of microfluidic technology in the academic community has rapidly increased over the last ten years because it has a number of potential applications in such areas as biological analysis [4], clinical examination [5], and food safety inspection [6,7].

Particle separation is important in chemical and biomedical analysis [7], and microfluidic techniques have been effective at separating particles. Many microfluidic methods have been developed to separate particles [8] using the flow field, microstructure, or forces created by electricity [9], optics [10–13], acoustics [14,15], magnetics [16–18], hydrodynamics [9,19,20], or gravity [20,21]. Some of these methods require fluorescent immunolabeling or magnetic labeling of the targeted or non-targeted particles, which is not only complicated but also possibly pollutes the reactants [22]. Other methods do not require label and separate particles by their intrinsic qualities, such as dielectric properties, deformability, size, deterministic lateral displacement, etc.

Microfilters, which are frequently used in many fields for tasks such as particle capture, enrichment and separation, have a controllable pore size and distribution. Microfilters do not need sophisticated injection systems, which make them efficient, fast, and simple.

Wilding et al. [23] demonstrated a micropillar array structure to separate blood cells and particles from nanoliter samples. However, the use of micropillar array structures to separate cells can lead to blockages in the flow path, limiting the development of the structure. Recently, different kinds of microfluidic chips were developed to avoid blockages, such as independent micropillars based filter, etc. Mohamed et al. [24] designed a sorting chip consisting of four channel segments. The channel's width sequentially contracts from 20 μm to 15 μm, then to 10 μm, and ends at 5 μm, while the height remains constant. Cells injected into the chip were captured at different segments according to their sizes. Tan et al. [25] proposed another filtering structure to separate cancer cells. On the microfluidic device, each filter element consists of three independent micropillars arranged in a circular arc with a 5 μm gap, which ensured that only larger cancer cells cannot pass and other cells can bypass from the side due to the increased flow resistance. McFaul et al. [26] developed a funnel-shaped micropillar array with a large gap in upstream and a small gap in downstream to reduce the influence of blockages. These methods can alleviate the degree of clogging to a certain extent, but they cannot completely prevent blockages.

Dielectrophoresis (DEP) is also a useful and simple technology for particle separation [27]. Positive dielectrophoresis (pDEP) and negative dielectrophoresis (nDEP) are both used to separate blood cells, tumor cells (including CTCs), algae cells, etc. The DEP force is a net force caused by the non-uniform electric field around the particles, which could be generated by the geometry of the electrodes or insulators [28]. The most frequently used DEP approaches are electrode-based DEP and insulator-based DEP [8,29,30]. The electric field gradient in iDEP is produced by using insulator micropillars, which in eDEP is produced by complex shaped electrodes. Particle separation using iDEP can avoid many problems that may occur in eDEP. Mohammadi et al. [31] developed an efficient micropost array to capture particles using insulator-based dielectrophoretic generated by a DC voltage source, and did numerical simulation to find the most efficient design of the post array, which demonstrated the effectiveness of the combination of micropost array and dielectrophoresis

However, the blockage problem frequently occurs in particle separation by using microfilter devices. Recently, our group developed a new microfluidic device made of a series of filters to separate particles using AC voltages. AC voltages were chosen to generate iDEP because the electrodes in AC voltages were less likely to be electrolyzed than in the DC voltages. Compared with the proposed methods, our device combined the advantages of microfilters and dielectrophoresis. Under the manipulation of dielectrophoretic force, the blocked particles were pushed off from filters to ensure that the particles can be separated continuously. This device can separate particles of three or more different sizes simultaneously, by adding more separation stages. More importantly, all filter stages can work at a constant frequency and voltage, by adjusting the geometry parameters of micropillars and ITO electrodes.

2. Materials and Methods

2.1. Related Theories

The DEP technology is an electrokinetic transport mechanism driven by polarization [32] that could be a useful tool to control the motion of particles. When surrounded by an electric field, homogeneous dielectric particles will be polarized [33,34] and the time-averaged DEP force can be expressed as [35,36]:

$$F_{DEP} = 2\pi\varepsilon_m a^3 \mathrm{Re}[K(\omega)]\nabla|E_{rms}|^2 \quad (1)$$

where ε_m is the permittivity of the medium, a is the particle radius, $\nabla|E_{rms}|^2$ is the gradient of the square of the RMS electric field, and $K(\omega)$ is the Clausius–Mossotti factor. For a particular sphere,

the real part of $K(\omega)$ ranges from -0.5 to 1, and is determined by the frequency of the applied field and the complex permittivity of the medium [37]. $K(\omega)$ can be calculated by:

$$K(\omega) = \frac{\widetilde{\varepsilon}_p - \widetilde{\varepsilon}_m}{\widetilde{\varepsilon}_p + 2\widetilde{\varepsilon}_m} \tag{2}$$

where ω is the angular field frequency, $\widetilde{\varepsilon}_p$ is the complex permittivity of the particle and $\widetilde{\varepsilon}_m$ is the complex permittivity of the medium. For isotropic homogeneous dielectrics [38], the complex permittivity can be expressed as:

$$\widetilde{\varepsilon} = \varepsilon - j\frac{\sigma}{\omega} \tag{3}$$

with $j = \sqrt{-1}$, ε and σ being the is permittivity and conductivity, respectively.

F_{DEP} is balanced with the drag force of particles in the fluid [39]. For a homogeneous spherical particle in a laminar flow regime, the Stokes drag force can be expressed as:

$$F_{drag} = 6\pi\eta a v \tag{4}$$

where η is the fluid viscosity, a is the radius of the particle, and v is the velocity of the particle relative to the fluid.

2.2. Experiment

2.2.1. Microfabrication

The microfilter device in the experiment was fabricated using the standard soft lithography technique [22,40,41]. To produce a 50 μm thickness structure, a positive mold was fabricated by using SU-8 3050 (Microchem, Westborough, MA, USA) spin-coated on a 3-inch silicon wafer (ePAK, Austin, TX, USA) at 3000 rpm for 30 s [42]. A mold was realized by using a photolithography aligner device (URE-2000/25, Institute of Optics and Electronics, Chengdu, China). Replicas of the mold were made in polydimethylsiloxane (PDMS, Dow Corning, Midland, MI, USA). As shown in Figure 1A, the microfluidic filter device had two reservoirs with a diameter of 4-mm and a long micro-channel with a length of 2.3 cm, a width of 6 mm, and a depth of 50 μm. Considering the convenience and reliability of connection between the signal generator and ITO electrodes, a 30 mm × 6 mm ITO glass was chosen to fabricate ITO electrodes. In addition, to integrate more separation stages and induced a high strength DEP force under a lower voltage, the distance between electrodes should be miniaturized. Finally, the distance between two ITO electrodes was 200 μm, which was wider than the micropillars (shown in Figure 1A). The filter consisted of a series of hexagonal micropillars (Figure 1C,D), which had two interval sizes inside the microchannel (25 μm and 14 μm). The injection port was fabricated using a 3-mm diameter puncher and the port to plug outlet tubing was fabricated using a 1-mm diameter puncher.

For better observation, indium-tin-oxide (ITO) [43] (220-nm ITO film thickness, 7 Ω/sq.) was used to fabricate the electrodes due to its good transparency. A bare ITO electrode should be carefully washed by using acetone, isopropanol, ethanol, and ultrapure water in turns before use. Then the ITO electrode was fabricated with a SU-8 2000 series negative resin using the standard soft lithography technology. Finally, the PDMS replica was sealed onto the ITO glass with electrodes via O_2-plasma activation (PDC-MG, Chengdu, China) of both surfaces.

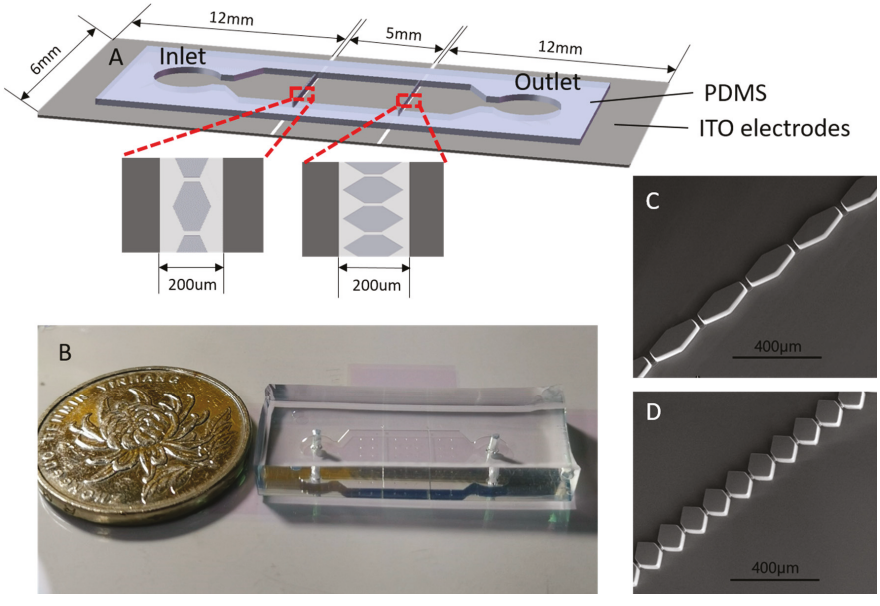

Figure 1. (**A**) Schematic illustration of the microfilter device, the distance of the two ITO electrodes is 200 μm; (**B**) a picture of the microfilter device; (**C**,**D**) scanning electron micrograph of micropillar structures with a height of 50 μm, and the gap of the micropillars are 25 μm and 14 μm, respectively.

2.2.2. Experimental Solutions

Polystyrene particles were suspended in a 1-mM phosphate-buffered saline (PBS) buffer with a low electrical conductivity of 0.17 S/m to minimize Joule heating in the filter region [8,44,45]. Polystyrene particles of 37-μm, 16.3-μm, and 9.7-μm diameters were suspended in the PBS buffer at a concentration of 10^4-10^5 particles per milliliter. To avoid the adhesion of particles to the channel walls and minimize the interactions between particles, Tween 20 (TP1379, Bomeibio, Hefei, China) was added to the mixture solution at a concentration of 0.1% *v*/*v* [41].

Haematococcus pluvialis (FACHB, Wuhan, China) and Bracteacoccus engadinensis (FACHB, Wuhan, China) were cultured in Blue-Green Medium (BG11, FACHB, Wuhan, China). A mixture of Haematococcus pluvialis and Bracteacoccus engadinensis were diluted in the culture medium at a concentration of 10^4-10^5 cells per milliliter, and 0.4 g/mL sorbitol was added to suspend the cells.

2.2.3. Experimental Manipulation and Visualization

A pipe connecting the outlet and the peristaltic pump was inserted into the outlet reservoir. The particle solution was added in the inlet reservoir by a pipette and introduced into the micro-channel by suction provided by the peristaltic pump. Serious leakage may occur during solution injection, but suction can help avoid this disadvantage because of the excessive pressure. Before the experiment, the microfluidic filter device was washed with 1-mM PBS buffer without particles for 5 min [46]. The inlet reservoir was brimmed with the particle mixture solution using a 100-μL pipette when the experiment began. As shown in the Figure 2, the sinusoidal signal used in the experiment was supplied by a function generator (SDG1020, Siglent, Solon, OH, USA) and a high-voltage amplifier (ATA-2042, Agitek, Xi'an, China) [41]. The AC electric field was fixed at 10 KHz and 35 V peak-to-peak value during polystyrene particles experiments. For algal cells, the AC electric field was fixed at 8 KHz and 100 V peak-to-peak value [47,48]. A microscope (IX73, Olympus, Tokyo, Japan) was used to monitor

particle motion, and a digital single lens reflex (Canon, Tokyo, Japan) was used to record videos and images in the microfluidic filter device through the microscope.

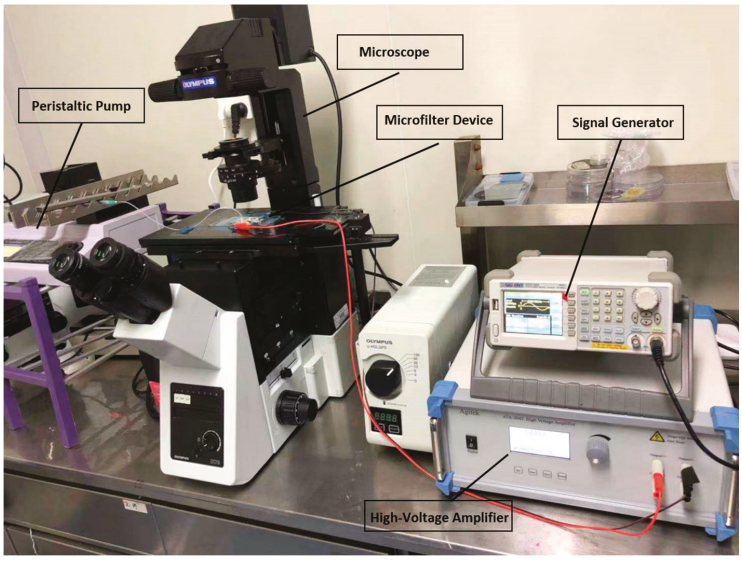

Figure 2. Experimental setup including the microfilter device, microscope, peristaltic pump, signal generator, and high-voltage amplifier.

3. Results and Discussion

3.1. Electric Field Gradient Distribution

Clausius-Mossotti factor value will determine whether the particles were subjected to positive dielectrophoresis (pDEP) or negative dielectrophoresis (nDEP). It depends on the parameters of particles, buffer solution, and applied electric signal. In our separation system, 1mM phosphate buffer was used as a buffer solution. The conductivity σm and permittivity of buffer solution are 0.17 S/m and 7.04×10^{-10} F/m, respectively. And the conductivity of polystyrene particles could be calculated by $\sigma_p = 2K_s/r$ (r: the radius of the particle). The recommended value of K_s for surface conductance is 10^{-9} S. The permittivity of polystyrene particles is 2.04×10^{-10} F/m. Clausius–Mossotti factor could be calculated by Equation (2) and Equation (3). The results showed that the value was always negative in the frequency range of 0–10^7 Hz. In addition, considering the ITO electrodes are easier for electrolysis at a frequency less than 10 KHz and the same DEP force can be induced by a lower voltage and higher frequency electric signal, 10 KHz was selected as the operating frequency.

To find a proper structure of the filter to separate particles of three sizes in two stages of filters by applying the same voltage, we developed a three-dimensional (3D) model in COMSOL Multiphysics 5.0 (COMSOL, Newton, MA, USA) to investigate the distributions of the electric field gradient and intensity. Figure 3 illustrates the distributions of the electric field gradient at the two stages. The strongest intensity is 9.46×10^{16} V^2/m^3 in Figure 3A and 1.65×10^{17} V^2/m^3 in Figure 3B. The electric field gradient at the second stage must be higher than that at the first stage because the DEP force is proportional to the cube of the particle radius (a^3).

The non-uniform electric field is generated by applying an AC electric field of 35 Vpp and 10 KHz using ITO electrodes placed as shown in Figure 1A [49,50]. The strongest intensity and gradients of the electric field exist near the edge of filter. The particle mixture was injected into the inlet well and flew through the two-stages filter in sequence due to pressure-driven flow. When entering into the

non-uniform electric field region, the trajectories of some particles change because of the nDEP force. When the particles passed the first stage filter, 37-μm particles moved to the opposite direction of the flow because of the strong DEP force, while 16.3-μm and 9.7-μm particles passed through the first stage filter. In the second stage filter, 16.3-μm particles were trapped before the second stage filter, while 9.7-μm particles passed through the second stage filter.

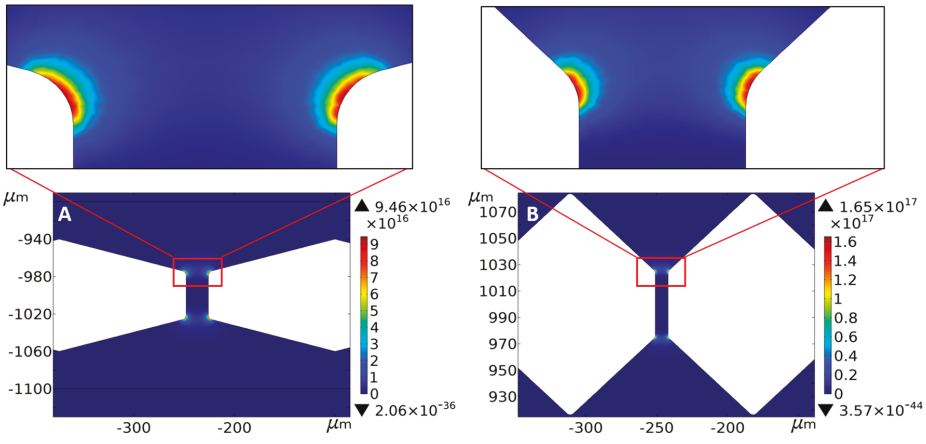

Figure 3. Distributions of $\nabla|E_{rms}|^2$ near the two stages microfilters (**A**,**B**), when 35 Vpp at 10 KHz is applied.

3.2. Separation of Three Different Particles

For particular particles and media, changing the AC frequency influenced the direction of the DEP force. A frequency of 10 KHz was chosen to ensure the particles experienced a negative DEP force. During the experiment, we found that if the flow velocity was fixed, the filters were easily clogged at low AC voltages; however, a strong DEP force generated at high AC voltages, which prevented all particles from passing through the first stage filter. Similarly, if the AC voltage was fixed, a high velocity caused congestion, while a low velocity influenced the separation efficiency. Thus, there is a balance between voltage and fluid velocity [51]. To achieve better continuous microfiltration, voltage and velocity should be optimized. Experiments were conducted with AC voltages ranging from 30−50 Vpp and flow velocities ranging from 0.5−2 μL/min [51]. The best separation condition for the particles was found to be 35 Vpp and 1 μL/min, where in the first stage the 16.3-μm and 9.7-μm particles can pass through and in the second stage the 9.7-μm particles can pass through the filter; none of them got trapped when the voltage was above 35 Vpp.

Figure 4 shows a continuous separation of 37-μm, 16.3-μm, and 9.7-μm polystyrene particles in the microchannel (The complete separation process is recorded in Video S1 and Video S2). The AC voltage and frequency imposed were 35 Vpp and 10 KHz, respectively, and the flow velocity was 1 μL/min. As seen in Figure 4A1–A4, in the first stage, only the 16.3-μm and 9.7-μm particles could pass through the filter, while 37-μm particles were stopped by the filter (25-μm interval). Figure 4B1–B4 show results near the second stage; the filter (14 μm interval) stopped the 16.3-μm particles and pushed them to the roof of hexagon and only allows the 9.7-μm particles to pass through. It can be seen from Figure 4B1–B4 that not all 9.7-μm particles can pass through the second stage filter at once. Some particles were bunched to form a pearl chain and suddenly pass through the filter as a group.

The microfilter would be blocked right after the 50-μL particle mixture is pumped into the micro-channel without applying AC field [51], which limits the popularization and application of microstructure filtration methods. Figure 4 demonstrate that the device kept working when the AC

field (35 Vpp, 10 KHz) was applied, indicating the microfluidic device solved the blockage problem successfully, which makes continuous separation possible.

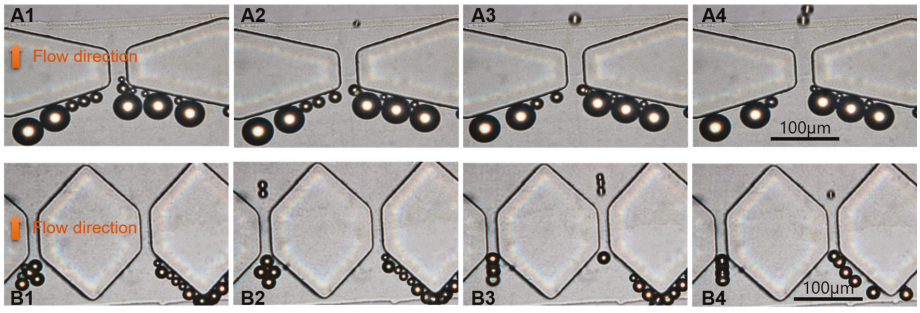

Figure 4. The separation process of 37-μm, 16.3-μm and 9.7-μm particles. (**A1**–**A4**) The first stage. (**B1**–**B4**) The second stage.

3.3. Separation of Algae Cells

Haematococcus pluvialis and Bracteacoccus engadinensis were also used to verify the feasibility of the device. Haematococcus pluvialis is famous for its high content of astaxanthin, which is the strongest antioxidant in nature and plays an important role in aquaculture, health care, and cosmetics industries [52]. Haematococcus pluvialis cells are often mixed with other algae cells in nature, thus, it is necessary to sort and purify Haematococcus pluvialis. Bracteacoccus engadinensis cells were mixed with Haematococcus pluvialis cells to mimic the natural condition.

The sizes of Haematococcus pluvialis cells are between 15 and 30 μm, and the sizes of Bracteacoccus engadinensis cells are 10 to 15 μm. In this study, we applied an AC signal with a voltage of 100 V and a frequency of 8 KHz, and the flow velocity is the same as the particle separation. As shown in Figure 5A1–A4, all of the Bracteacoccus engadinensis cells and some of the smaller Haematococcus pluvialis cells can pass through the filter unimpededly in first stage with a pore size of 25 μm, but larger Haematococcus pluvialis cells larger than 25 μm cannot pass. Like the 37-um particles, large Haematococcus pluvialis cells were pushed away by the negative dielectrophoretic force near the entrance of the first stage filter. The results of the second stage are depicted in Figure 5B1–B4. Smaller Bracteacoccus engadinensis cells can pass through the filter with the size of 14 μm, while Haematococcus pluvialis cells and large Bracteacoccus engadinensis cells were trapped before the filter under dielectrophoretic force. The complete separation process is recorded in Video S3 and Video S4.

Due to large size, only a few Haematococcus pluvialis cells can pass the first stage since more Haematococcus pluvialis cells can been seen before the entrance of the first stage filter (Figure 5A1–A4), while only a few Haematococcus pluvialis cells can be seen in the second stage (Figure 5B1–B4). Accordingly, because of the small size, all of the Bracteacoccus engadinensis cells can pass through the first stage, and most of them can pass through the second stage and reach the outlet directly. After separation, there are only Haematococcus pluvialis cells left in the channel before the first stage, Bracteacoccus engadinensis cells in the outlet, and merely a small amount of these two algae cells with similar sizes in the channel between the first stage and the second stage. Thus different sizes of Haematococcus pluvialis cells and Bracteacoccus engadinensis cells were separated.

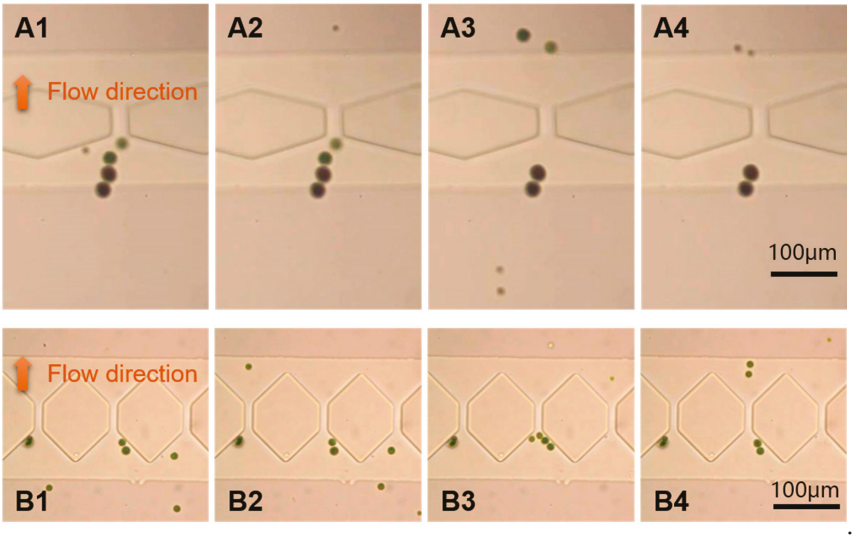

Figure 5. Separation process of Haematococcus pluvialis cells and Bracteacoccus engadinensis cells at a voltage amplitude of 100 V and a frequency of 8 KHz. (**A1**–**A4**) The first stage. (**B1**–**B4**) The second stage.

4. Conclusions

We presented a microfluidic filter device that combines the advantages of negative dielectrophoretic force and microfilters, to separate particles of different sizes. Microfilter is one of the most widely used particle/cell separation methods due to simple operation. However, blockages limit its popularization and applications. We were committed to solving the blockage problem of microfilter and purify Haematococcus pluvialis cells using the simplest filter structure in this study. A 3D model was developed to analyze electric field distribution. Based on the simulation results and particles size, micropillars based separation device was designed and fabricated. In addition, the geometry parameters of micropillars were optimized to ensure two separation stages work by using a generator. The feasibility of this method was demonstrated by the continuous flow separation of polystyrene particles with three different sizes. Haematococcus pluvialis cells and Bracteacoccus engadinensis cells were also separated in this device without blockages phenomenon.

Considering our device is based on the filtration theory, this microfluidic device could separate complex sample, which contains many kinds of (bio)particles with different size, by integrating several separation stage with appropriate micropillars and applying appropriate AC signal. By optimizing the geometry parameter of micropillars, and adjusting the distance between two adjacent micropillars, circulating tumor cells, white blood cells, red blood cells, or blood plasma could be separated from whole blood samples [53–55].

The developed microfluidic filter device can be conveniently fabricated and generates a strong dielectrophoretic force near the filter of each stage. The device can separate particles of different sizes efficiently with minimal Joule heating due to the use of pressure-driven flow and AC electric field. However, some particles, which should theoretically pass through the filter, were trapped due to the too strong DEP force and adhesion between particles. It reduces the separation efficiency [6]. Additionally, (bio) particles collection structures should be integrated, to avoid too much (bio) particles block the flow path.

Supplementary Materials: The following are available online at http://www.mdpi.com/2072-666X/10/2/103/s1, Video S1: The separation process of particles in the first stage, Video S2: The separation process of particles

in the second stage, Video S3: The separation process of Haematococcus pluvialis cells and Bracteacoccus engadinensis cells in the first stage, Video S4: The separation process of Haematococcus pluvialis cells and Bracteacoccus engadinensis cells in the second stage.

Author Contributions: N.H. conceived and designed the experiments; D.Y. built up the device and performed the experiments; X.Z. simulated the electric field gradient; X.H. contributed microchip fabrication; D.Y. wrote the paper; N.H. and J.Y. revised the paper.

Funding: National Natural Science Foundation of China: 21827812, 31571005, 81871450; Natural Science Foundation of Chongqing: cstc2018jcyjAX0389.

Conflicts of Interest: The authors declare no conflict of interest.

References

1. Pohl, H.A.; Pollock, K.; Crane, J.S. Dielectrophoretic force: A comparison of theory and experiment. *J. Biol. Phys.* **1978**, *6*, 133–160. [CrossRef]
2. Srivastava, S.K.; Bayloncardiel, J.L.; Lapizcoencinas, B.H.; Minerick, A.R. A continuous DC-insulator dielectrophoretic sorter of microparticles. *J. Chromatogr. A* **2011**, *1218*, 1780–1789. [CrossRef] [PubMed]
3. Chen, G.H.; Huang, C.T.; Wu, H.H.; Zamay, T.N.; Zamay, A.S.; Jen, C.P. Isolating and concentrating rare cancerous cells in large sample volumes of blood by using dielectrophoresis and stepping electric fields. *Biochip J.* **2014**, *8*, 67–74. [CrossRef]
4. Mohammed, A.; Nicholas, M.; Eva, J.P.; Fadi, A.; Fang, Y.; Xiaoming, Y.; Guiren, W. Separation of tumor cells with dielectrophoresis-based microfluidic chip. *Biomicrofluidics* **2013**, *7*, 11803.
5. Becker, F.F.; Wang, X.B.; Huang, Y.; Pethig, R.; Vykoukal, J. Separation of Human Breast Cancer Cells From Blood by Differential Dielectric Affinity. *Proc. Natl. Acad. Sci. USA* **1995**, *92*, 860. [CrossRef] [PubMed]
6. Whitesides, G.M. The origins and the future of microfluidics. *Nature* **2006**, *442*, 368. [CrossRef] [PubMed]
7. Zhu, J.; Canter, R.C.; Keten, G.; Vedantam, P.; Tzeng, T.R.J.; Xuan, X. Continuous-flow particle and cell separations in a serpentine microchannel via curvature-induced dielectrophoresis. *Microfluid. Nanofluid.* **2011**, *11*, 743–752. [CrossRef]
8. Kale, A.; Lu, X.; Patel, S.; Xuan, X. Continuous-flow dielectrophoretic trapping and patterning of colloidal particles in a ratchet microchannel. *J. Micromech. Microeng.* **2014**, *24*, 75007–75012. [CrossRef]
9. Jellema, L.C.; Mey, T.; Koster, S.; Verpoorte, E. Charge-based particle separation in microfluidic devices using combined hydrodynamic and electrokinetic effects. *Lab Chip* **2009**, *9*, 1914–1925. [CrossRef]
10. Zhang, Y.; Lei, H.; Li, Y.; Li, B. Microbe removal using a micrometre-sized optical fiber. *Lab Chip* **2012**, *12*, 1302–1308. [CrossRef]
11. Polynkin, P.; Polynkin, A.; Peyghambarian, N.; Mansuripur, M. Evanescent field-based optical fiber sensing device for measuring the refractive index of liquids in microfluidic channels. *Opt. Lett.* **2005**, *30*, 1273. [CrossRef] [PubMed]
12. Chiou, P.Y.; Ohta, A.T.; Wu, M.C. Massively parallel manipulation of single cells and microparticles using optical images. *Nature* **2005**, *436*, 370. [CrossRef] [PubMed]
13. Macdonald, M.P.; Spalding, G.C.; Dholakia, K. Microfluidic sorting in an optical lattice. *Nature* **2003**, *426*, 421–424. [CrossRef] [PubMed]
14. Shi, J.; Mao, X.; Ahmed, D.; Colletti, A.; Huang, T.J. Focusing microparticles in a microfluidic channel with standing surface acoustic waves (SSAW). *Lab Chip* **2008**, *8*, 221. [CrossRef] [PubMed]
15. Shi, J.; Huang, H.; Stratton, Z.; Huang, Y.; Huang, T.J. Continuous particle separation in a microfluidic channel via standing surface acoustic waves (SSAW). *Lab Chip* **2009**, *9*, 3354. [CrossRef] [PubMed]
16. Lee, H.; Xu, L.; Ahn, B.; Lee, K.; Oh, K.W. Continuous-flow in-droplet magnetic particle separation in a droplet-based microfluidic platform. *Microfluid. Nanofluid.* **2012**, *13*, 613–623. [CrossRef]
17. Zeng, J.; Chen, C.; Xuan, X.; Vedantam, P.; Tzeng, T.-R. Magnetic concentration of particles and cells in ferrofluid flow through a straight microchannel using attracting magnets. *Microfluid. Nanofluid.* **2013**, *15*, 49–55. [CrossRef]
18. Zeng, J.; Deng, Y.; Vedantam, P.; Tzeng, T.R.; Xuan, X. Magnetic separation of particles and cells in ferrofluid flow through a straight microchannel using two offset magnets. *J. Magn. Magn. Mater.* **2013**, *346*, 118–123. [CrossRef]

19. Chiu, Y.Y.; Huang, C.K.; Lu, Y.W. Enhancement of microfluidic particle separation using cross-flow filters with hydrodynamic focusing. *Biomicrofluidics* **2016**, *10*, 1–52. [CrossRef]
20. Nejad, H.R.; Samiei, E.; Ahmadi, A.; Hoorfar, M. Gravity-driven hydrodynamic particle separation in digital microfluidic systems. *RSC Adv.* **2015**, *5*, 35966–35975. [CrossRef]
21. Devendra, R.; Drazer, G. Gravity driven deterministic lateral displacement for particle separation in microfluidic devices. *Anal. Chem.* **2012**, *84*, 10621. [CrossRef] [PubMed]
22. Martinez-Duarte, R. Microfabrication technologies in dielectrophoresis applications—A review. *Electrophoresis* **2012**, *33*, 3110. [CrossRef] [PubMed]
23. Wilding, P.; Pfahler, J.; Bau, H.H.; Zemel, J.N.; Kricka, L.J. Manipulation and flow of biological fluids in straight channels micromachined in silicon. *Clin. Chem.* **1994**, *40*, 43–47. [PubMed]
24. Mohamed, H.; Mccurdy, L.D.; Szarowski, D.H.; Duva, S.; Turner, J.N.; Caggana, M. Development of a rare cell fractionation device: Application for cancer detection. *IEEE Trans. Nanobiosci.* **2004**, *3*, 251–256. [CrossRef] [PubMed]
25. Tan, S.J.; Yobas, L.; Lee, G.Y.; Ong, C.N.; Lim, C.T. Microdevice for the isolation and enumeration of cancer cells from blood. *BioMi* **2009**, *11*, 883–892. [CrossRef] [PubMed]
26. Mcfaul, S.M.; Lin, B.K.; Ma, H. Cell separation based on size and deformability using microfluidic funnel ratchets. *Lab Chip* **2012**, *12*, 2369–2376. [CrossRef] [PubMed]
27. Yang, J.; Huang, Y.; Wang, X.B.; Becker, F.F.; Gascoyne, P.R. Differential analysis of human leukocytes by dielectrophoretic field-flow-fractionation. *Biophys J.* **2000**, *78*, 2680–2689. [CrossRef]
28. Lewpiriyawong, N.; Yang, C.; Lam, Y.C. Electrokinetically driven concentration of particles and cells by dielectrophoresis with DC-offset AC electric field. *Microfluid. Nanofluid.* **2012**, *12*, 723–733. [CrossRef]
29. Baylon-Cardiel, J.L.; Jesús-Pérez, N.M.; Chávez-Santoscoy, A.V.; Lapizco-Encinas, B.H. Controlled microparticle manipulation employing low frequency alternating electric fields in an array of insulators. *Lab Chip* **2010**, *10*, 3235–3242. [CrossRef]
30. Hawkins, B.G.; Smith, A.E.; Syed, Y.A.; Kirby, B.J. Continuous-flow particle separation by 3D Insulative dielectrophoresis using coherently shaped, dc-biased, ac electric fields. *Anal. Chem.* **2007**, *79*, 7291–7300. [CrossRef]
31. Mohammadi, M.; Zare, M.J.; Madadi, H.; Sellarès, J.; Casals-Terré, J. A new approach to design an efficient micropost array for enhanced direct-current insulator-based dielectrophoretic trapping. *Anal. Bioanal. Chem.* **2016**, *408*, 5285–5294. [CrossRef] [PubMed]
32. Gascoyne, P.R.C.; Vykoukal, J. Particle separation by dielectrophoresis. *Electrophoresis* **2002**, *23*, 1973–1983. [CrossRef]
33. Sadeghian, H.; Hojjat, Y.; Soleimani, M. Interdigitated electrode design and optimization for dielectrophoresis cell separation actuators. *J. Electrostatics* **2017**, *86*, 41–49. [CrossRef]
34. Tang, S.Y.; Zhu, J.; Sivan, V.; Gol, B.; Soffe, R.; Zhang, W.; Mitchell, A.; Khoshmanesh, K. Creation of Liquid Metal 3D Microstructures Using Dielectrophoresis. *Adv. Funct. Mater.* **2015**, *25*, 4445–4452. [CrossRef]
35. Ramos, A.; Morgan, H.; Green, N.G.; Castellanos, A. Ac electrokinetics: A review of forces in microelectrode structures. *J. Phys. D Appl. Phys.* **1999**, *31*, 2338–2353. [CrossRef]
36. Jones, T.B. *Electromechanics of Particles: Dielectrophoresis and Magnetophoresis*; Cambridge University Press: Cambridge, UK, 1995.
37. Khoshmanesh, K.; Nahavandi, S.; Baratchi, S.; Mitchell, A.; Kalantar-Zadeh, K. Dielectrophoretic platforms for bio-microfluidic systems. *Biosens. Bioelectron.* **2011**, *26*, 1800–1814. [CrossRef] [PubMed]
38. Huang, L.R.; Cox, E.C.; Austin, R.H.; Sturm, J.C. Continuous particle separation through deterministic lateral displacement. *Science* **2004**, *304*, 987. [CrossRef]
39. Srivastava, S.K.; Gencoglu, A.; Minerick, A.R. DC insulator dielectrophoretic applications in microdevice technology: A review. *Anal. Bioanal. Chem.* **2011**, *399*, 301–321. [CrossRef]
40. Ng, J.M.; Gitlin, I.; Stroock, A.D.; Whitesides, G.M. Components for integrated poly(dimethylsiloxane) microfluidic systems. *Electrophoresis* **2002**, *23*, 3461–3473. [CrossRef]
41. Patel, S.; Qian, S.; Xuan, X. Reservoir-based dielectrophoresis for microfluidic particle separation by charge. *Electrophoresis* **2013**, *34*, 961–968. [CrossRef]
42. Li, M.; Li, W.H.; Zhang, J.; Alici, G.; Wen, W. A review of microfabrication techniques and dielectrophoretic microdevices for particle manipulation and separation. *J. Phys. D Appl. Phys.* **2014**, *47*, 63001–63029. [CrossRef]

43. Suga, M.; Kunimoto, A.; Shinohara, H. Non-invasive, electro-orientation-based viability assay using optically transparent electrodes for individual fission yeast cells. *Biosens. Bioelectron.* **2017**, *97*, 53. [CrossRef] [PubMed]
44. Hawkins, B.G.; Kirby, B.J. Electrothermal flow effects in insulating (electrodeless) dielectrophoresis systems. *Electrophoresis* **2010**, *31*, 3622–3633. [CrossRef]
45. Sridharan, S.; Zhu, J.; Hu, G.; Xuan, X. Joule heating effects on electroosmotic flow in insulator-based dielectrophoresis. *Electrophoresis* **2011**, *32*, 2274–2281. [CrossRef] [PubMed]
46. Lee, D.; Hwang, B.; Choi, Y.; Kim, B. A novel dielectrophoresis activated cell sorter (DACS) to evaluate the apoptotic rate of K562 cells treated with arsenic trioxide (As_2O_3). *Sens. Actuators A Phys.* **2016**, *242*, 1–8. [CrossRef]
47. Morgan, H.; Green, N.G. *AC Electrokinetics: Colloids and Nanoparticles*; Research Studies Press LTD: Hertfordshire, UK, 2003.
48. Gencoglu, A.; Olney, D.; Lalonde, A.; Koppula, K.S.; Lapizco-Encinas, B.H. Dynamic microparticle manipulation with an electroosmotic flow gradient in low-frequency alternating current dielectrophoresis. *Electrophoresis* **2014**, *35*, 362–373. [CrossRef] [PubMed]
49. Zhao, K.; Li, D. Continuous separation of nanoparticles by type via localized DC-Dielectrophoresis using asymmetric nano-orifice in pressure-driven flow. *Sens. Actuators B Chem.* **2017**, *250*, 274–284. [CrossRef]
50. Shi-Yang, T.; Wei, Z.; Sara, B.; Mahyar, N.; Kourosh, K.Z.; Khashayar, K. Modifying dielectrophoretic response of nonviable yeast cells by ionic surfactant treatment. *Anal. Chem.* **2013**, *85*, 6364–6371.
51. Douglas, T.A.; Cemazar, J.; Balani, N.; Sweeney, D.C.; Schmelz, E.M.; Davalos, R.V. A feasibility study for enrichment of highly-aggressive cancer subpopulations by their biophysical properties via dielectrophoresis enhanced with synergistic fluid flow. *Electrophoresis* **2017**, *38*, 1507–1514. [CrossRef]
52. Boussiba, S. Carotenogenesis in the green alga Haematococcus pluvialis: Cellular physiology and stress response. *Physiol Plant.* **2010**, *108*, 111–117. [CrossRef]
53. Mohammadi, M.; Madadi, H.; Casals-Terré, J. Microfluidic point-of-care blood panel based on a novel technique: Reversible electroosmotic flow. *Biomicrofluidics* **2015**, *9*, 131–138. [CrossRef] [PubMed]
54. Madadi, H.; Casalsterré, J.; Mohammadi, M. Self-driven filter-based blood plasma separator microfluidic chip for point-of-care testing. *Biofabrication* **2015**, *7*, 025007. [CrossRef] [PubMed]
55. Kersaudykerhoas, M.; Sollier, E. Micro-scale blood plasma separation: From acoustophoresis to egg-beaters. *Lab Chip* **2013**, *13*, 3323–3346. [CrossRef] [PubMed]

MDPI
St. Alban-Anlage 66
4052 Basel
Switzerland
Tel. +41 61 683 77 34
Fax +41 61 302 89 18
www.mdpi.com

Micromachines Editorial Office
E-mail: micromachines@mdpi.com
www.mdpi.com/journal/micromachines

MDPI
St. Alban-Anlage 66
4052 Basel
Switzerland

Tel: +41 61 683 77 34
Fax: +41 61 302 89 18

www.mdpi.com

ISBN 978-3-0365-0049-2